Probing the Dye-Semiconductor Interface in NiO Based p-type Dye Sensitized Solar Cells Using BODIPY

Nathan Potts

A thesis submitted for the degree of

Doctor of Philosophy in Chemistry

School of Natural and Environmental Sciences

Newcastle University

March 2020

Firstly, I would like to thank my supervisor, Dr. Elizabeth Gibson. From the first lecture I saw you present you inspired me to be a better scientist, the lessons you have taught me I will be forever grateful for. Thanks must to go Newcastle University for the funding to complete this project, Prof. Benjamin Dietzek at Universitat Jena, Institut für Physikalische Chemie and especially Ruri Wahyuono for his help on the fs-TA measurements carried out in Chapter 6. Thanks also go to Dr. Ute Cappel at KTH Royal Institute of Technology, Stockholm and Tamara Sloboda for their help with the X-ray PES measurements and the company on a long week at the Diamond beamline. Thanks also go to Prof. Melepurath Deepa and Ankita Kolay for their hospitable welcome to IIT Hyderabad, I hope you gained as much from working together as I have. To the many members of the Gibson group, past and present, thank you for the help, the good times and the company, I wish you all every success in life. To all my friends and family, and every person who told me I could do it along the way, this thesis is for you. To Kimi and Anouk, for welcoming me to a new city with open arms and supplying the caffine and laughter. To Beckie C and Marina, your encouragement and support made all this possible, I hope to spend many more hours in kitchens with you, where I do all my best thinking. To my cousin Marzi, your love and guidance helped make me the man I am today. To Becky H, thank you for always picking me up every time I fell down.

To Dave, who took a leap of faith with me and who never looked back, we've got this.

And finally to my father, who told me I could do anything, so I did. I wish you could have been here to see it.

In science, we stand on the shoulders of giants, but in life I have found we are uplifted by those around us. This PhD has shown me that happiness can be found in even the darkest of times, if one only remembers to turn on the light.

Love always,

Nathan.

Abstract A significant portion of the scientific community is focused on developing new approaches to fulfilling the energy demands of a growing population, whilst also minimising the damage to the environment. Chemistry has played a vital role in developing new molecular systems to turn solar energy into electricity. Dye-sensitized solar cells (DSSC) have gained significant attention by offering a versatile and tuneable molecular system as a promising alternative to traditional silicon devices. Single junction devices usually based around an n-type TiO_2 photoanode can be improved by pairing with a p-type photocathode to create a tandem device, which could potentially surpass the Shockley-Queisser limit of solar energy conversion over a single p-n junction. Although most of the research on DSSC focusses on TiO_2 based systems, improving the performance of the p-type photocathode is required in order to approach a tandem DSSC which outperforms the TiO_2 photoanode.

A series of BODIPY sensitizers with small structural modifications to the core of the chromophore were prepared by various synthetic pathways to create a robust and reliable system with different photophysical and electrochemical properties with which to investigate the underlying electron transfer pathways in p-type NiO DSSC. The properties of these dyes were studied using steady state UV-Visible and Fluorescence spectroscopy and coupled with cyclic voltammetry in order to create an energy level map of the system. Although all three dyes appeared to have sufficient driving force for electron injection from the VB on NiO into the HOMO of the dye, the three dyes showed modest performance which appeared to be limited by the efficient regeneration of the dye by the redox electrolyte. BOD2 showed the most promising results when used in a working p-type device (J_{SC} = 0.48 mA cm^{-2}) however these results did not agree with the calculated driving force for injection (ΔG_{inj} therefore the dye|semiconductor interface was studied using X-ray Photoelectron Spectroscopy (XPS) to create a new map of the energy levels inside the p-DSSC. Inspection of the valence photoelectron spectra at varied X-ray excitation energy allowed for probing of the energy levels in both the bulk semiconductor and at the dye|semiconductor interface. The HOMO energies for all three dyes adsorbed onto NiO were measured experimentally and these results confirm a shift in Fermi level for the

NiO upon dye adsorption. These results predict that BOD2 had the highest Ginj and the frontier orbitals of BOD2 were the most well placed to encourage efficient electron transfer between the dye and semiconductor. Femtosecond Transient Absorption Spectroscopy (fs-TAS) was utilized to study the kinetics of the electron transfer processes within the p-type device. Interestingly, the lifetime of the reduced dye appears to be increased in the presence of a redox electrolyte and we postulate this to result from catalytic activity of surface trap states NiO catalysing the conversion of Iodide to triiodide and deactivating a recombination pathway in the p-DSSC. This has implications on future design of dyes for p-type DSSC and outlines new methods on estimating driving forces for electron transfer within a p-DSSC.

Contents

II Small-Molecule BODIPYs for p-type DSC 41

List of Figures

List of Tables

Part I

Introduction

Chapter 1

Introduction

1.1 Solar Energy

Energy and energy consumption has played a pivotal role in the developed world and improvement of modern society. Since the industrial revolution, most of this energy has been generated by fossil fuels, a finite and non-renewable source of energy, which has been shown to cause harmful effects to the earth's atmosphere and subsequently, the lives of people around the globe.

With the global energy consumption estimated to be approximately 18 Terrawatts per year (TW/year), with estimates of growth to 27.6 TW/year by 2050, many are looking for alternatives means to generate clean sources of energy to fulfill the needs of a growing global population without causing irreparable damage to the planet.[1] 120 000 TW of solar energy strikes the earth's surface per year, making it a prime candidate to sate the growing energy demands of a growing planet. Despite being the most abundant energy source available, solar energy only provides less than 0.5% of the global energy demand. (Fig. 1.1).[2–4] At a pivotal time in the history of the developed world, in order to combat the irreversible effects of climate change, science has looked for new technologies to harness solar energy in order to power the future.

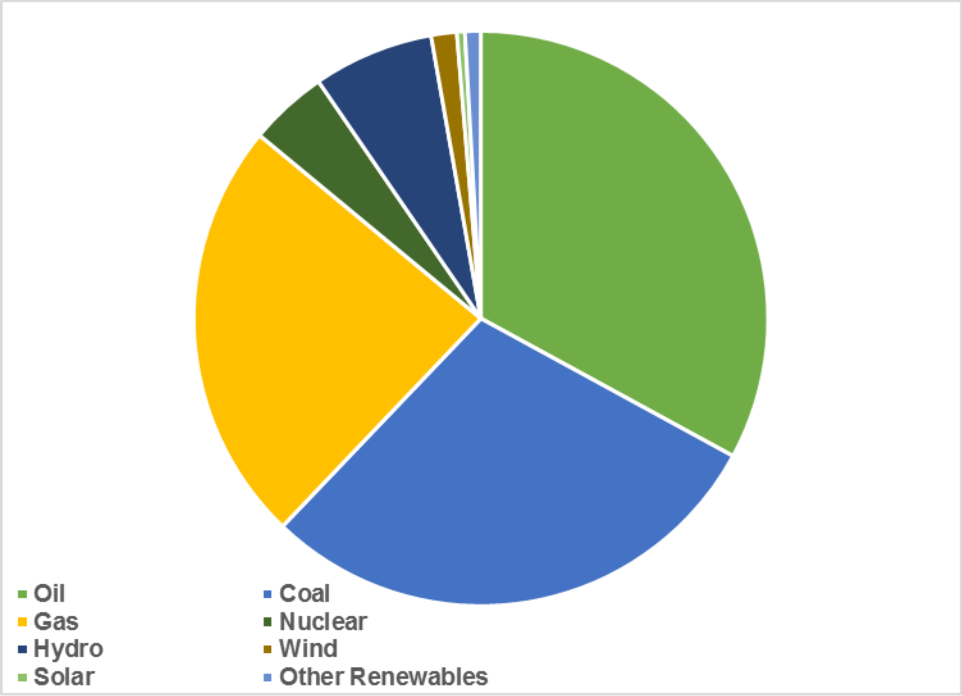

Figure 1.1: Global energy consumption, broken down by source 2015

1.2 Metals, Semiconductors and Insulators

1.2.1 Bonding in Materials

When a pair of atoms are brought together to form a molecule, the two atomic orbitals combine and then split to form a pair of molecular orbitals (bonding and anti-bonding) situated at higher and lower energies than that of the original atomic orbital pair (Fig. 1.2).

When a large number of orbitals come together to form a solid, the atomic orbitals split into multiple energy levels. These energy levels are situated so close together they form a continuum (or band) of energy levels that an electron may pass through freely. (Fig. 1.3) The distribution of these bands depend on many factors, including the specific electronic properties of the atoms involved in bonding and the strength of the bonds between these atoms. The highest occupied band in a material is termed the valence band (VB) and the lowest unoccupied band is known as the conduction band (CB). If the VB is partially full, or overlaps with the CB, we can describe the solid as a metal. The valence electrons

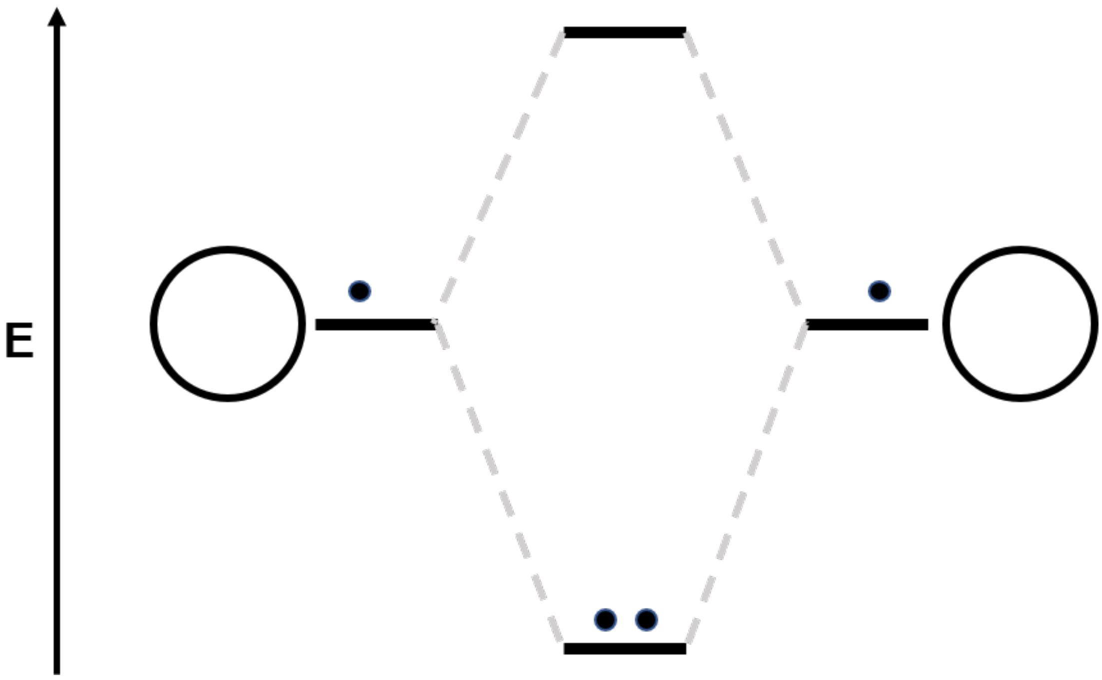

Figure 1.2: σ-Bonding in a diatomic molecule

are easy to excite due to the empty sites available at similar energies to the VB, and these electrons act as transporters of heat and charge through the material. This property allows for metals to be used as thermal or electrical conductors.

If the VB is full and completely separated from the CB by an energy gap (here defined as a region where no wavelike electron orbitals exist, meaning transitions of electrons from the VB to the band gap are forbidden) then the material is defined as a semiconductor. As the valence electrons are all involved in bonding and cannot be easily removed, they require energy equivalent or greater than the band gap in order to be removed. Semiconductors are classified as materials with a band gap in the range 0.5 - 3 eV. Semiconductors exhibit low conductivity in the dark, as a small number of valence electrons will have enough kinetic energy to be excited across the band gap into the conduction band, this intrinsic conductivity will decrease with increasing band gap energies.[5,6]

In metals the Fermi level E_F lies inside at least one band, for insulators and semiconductors the E_F lies inside a band gap. In semiconductors the E_F lies close enough to the band edge to be thermally populated by electrons or holes.

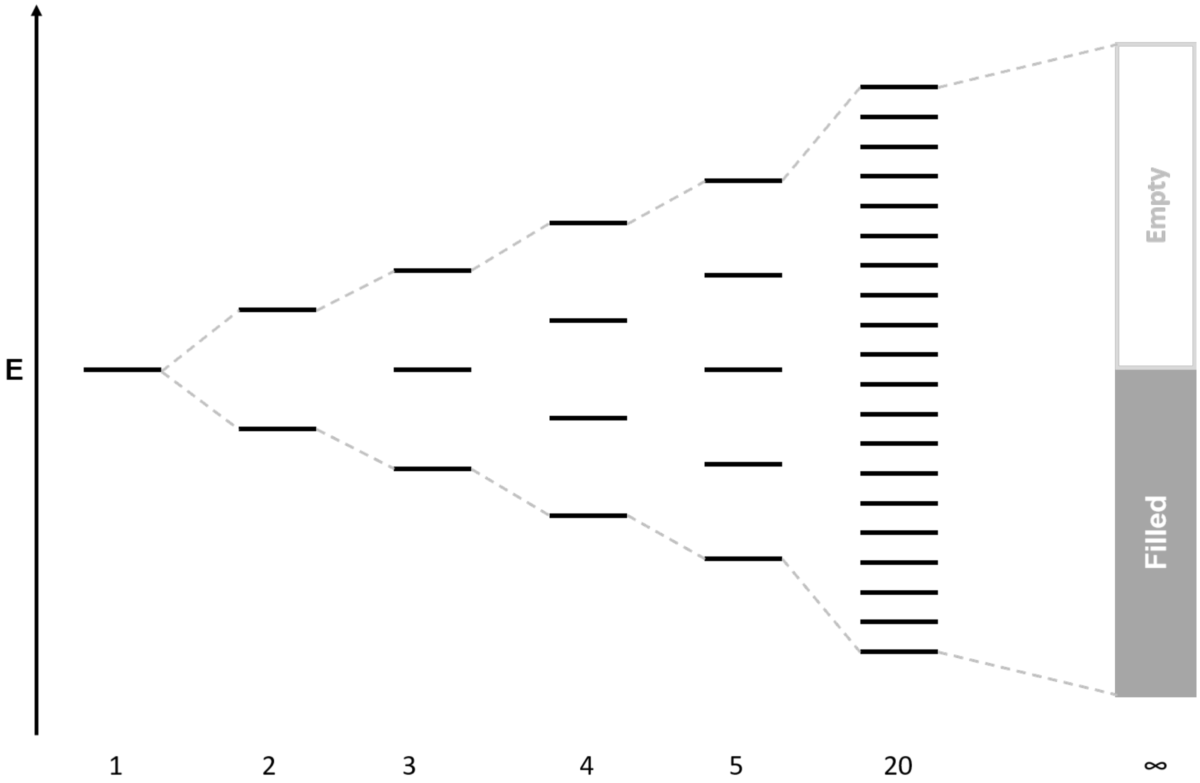

Figure 1.3: Schematic representation of atomic bonding in a diatomic molecule, (n = 2) to a metal (n = ∞)

Insulators are materials with wider band gaps than those found in semiconductors. Insulators have negligible conductivity at room temperature in the dark.

1.2.2 The Fermi Level

When a semiconductor is in thermal equilibrium, the electron distribution in the system can be defined by a Fermi-Dirac distribution function and the Fermi level is defined as the level where the probability of finding an electron is 1/2.[7]

For a distribution function f(k,r), where f is the probability that at point r the electron state of wavevector k is occupied, we can describe an electron in a semiconductor with Equation 1.1.

$$f(k, r) = f_0(E(k), E_F, T) \tag{1.1}$$

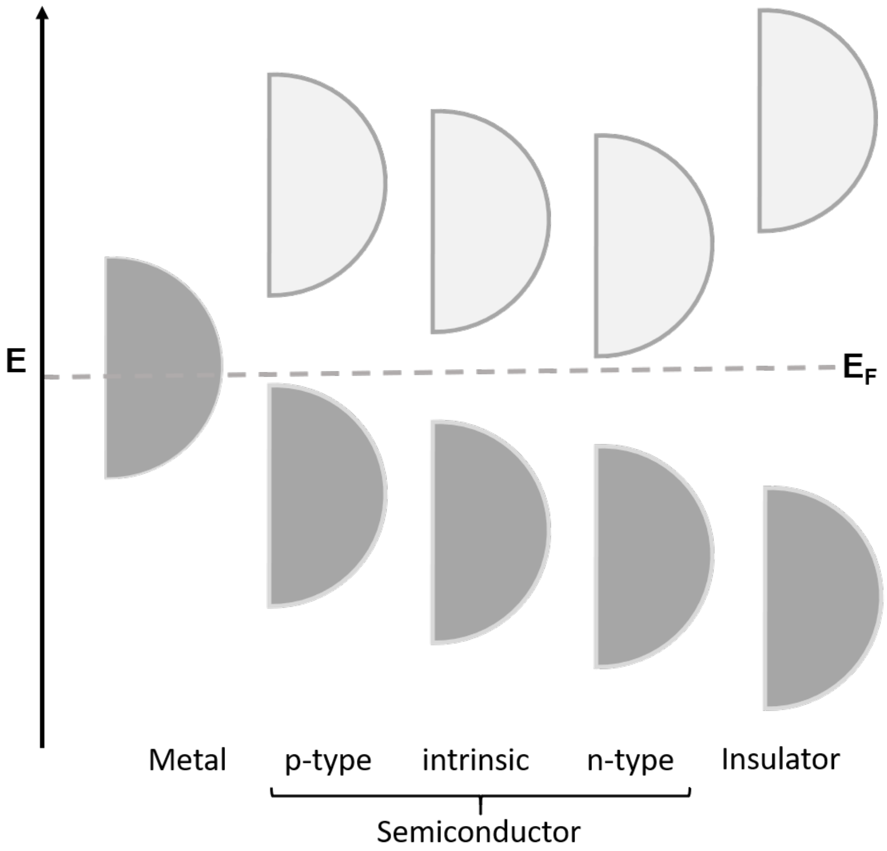

Figure 1.4: Band filling at equilibrium for various materials, E$_F$ (Fermi Level) denoted by dashed line.

Where f$_0$(E, E$_F$, T) is the Fermi Dirac distribution function, giving the probability of an electron state of energy E will be occupied, at temperature T. (Equation 1.2)

$$f_0(E, E_F, T) = \frac{1}{e^{(E-E_F)/k_BT+1}}(1.2)$$

Under thermal equilibrium, f is dependant on wavevector only implicitly through the electron energy, and is independent of position. When the thermal equilibrium is disturbed (ie. under illumination) the population of states in the valence and conduction bands change due to injection of electrons and holes in the system. In this case, the Fermi level splits into two quasi-Fermi levels (or imref), one for electrons and one for holes.[8] (Figure 1.5)

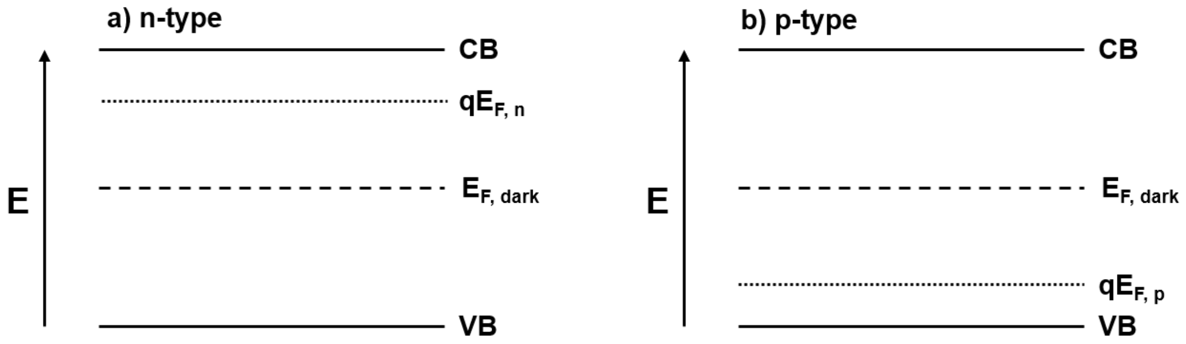

Figure 1.5: Energy level diagram of the Fermi energy of a semiconductor in the dark (E$_{F,dark}$) and quasi-Fermi level under illumination for an n-type (qE$_{F,n}$) and p-type (qE$_{F,p}$) semiconductor.

1.2.3 p-type and n-type semiconductors

Extrinsic semiconductors are materials doped with trace amounts of material during manufacture to introduce different electrical properties to the doped semiconductor than the pure semiconductor material.[9] The doping agents used can vary from semiconductor to semiconductor, however they can be classified into two types (electron donating or electron accepting), resulting in two types of extrinsic semiconductor.[10,11] Doping the semiconductor lattice with an electron donor results in an n-type semiconductor, with the majority charge carriers in the system being negatively charged electrons. Doping the semiconductor with an electron acceptor leads to the electron acceptor receiving an electron from the semiconductor lattice, resulting in a hole (a vacancy where an electron should be). The majority charge carriers are now positive resulting in a p-type semiconductor.

When placing two doped semiconductor crystals of p-type and n-type in contact, there is no resulting effect. The two conductive crystals both have the number of protons balanced with the number of electrons and therefore possess no net charge. A single crystal doped to create a p-type region at one side of the crystal, and an n-type region on the other side displays interesting properties. The p-type material has majority positive charge carriers (holes) whereas the n-type material has majority negative charge carriers (electrons), both free to move around the lattice. Near the junction, n-type material electrons diffuse across the junction, combining with the holes in the p-type material. This region of the p-type

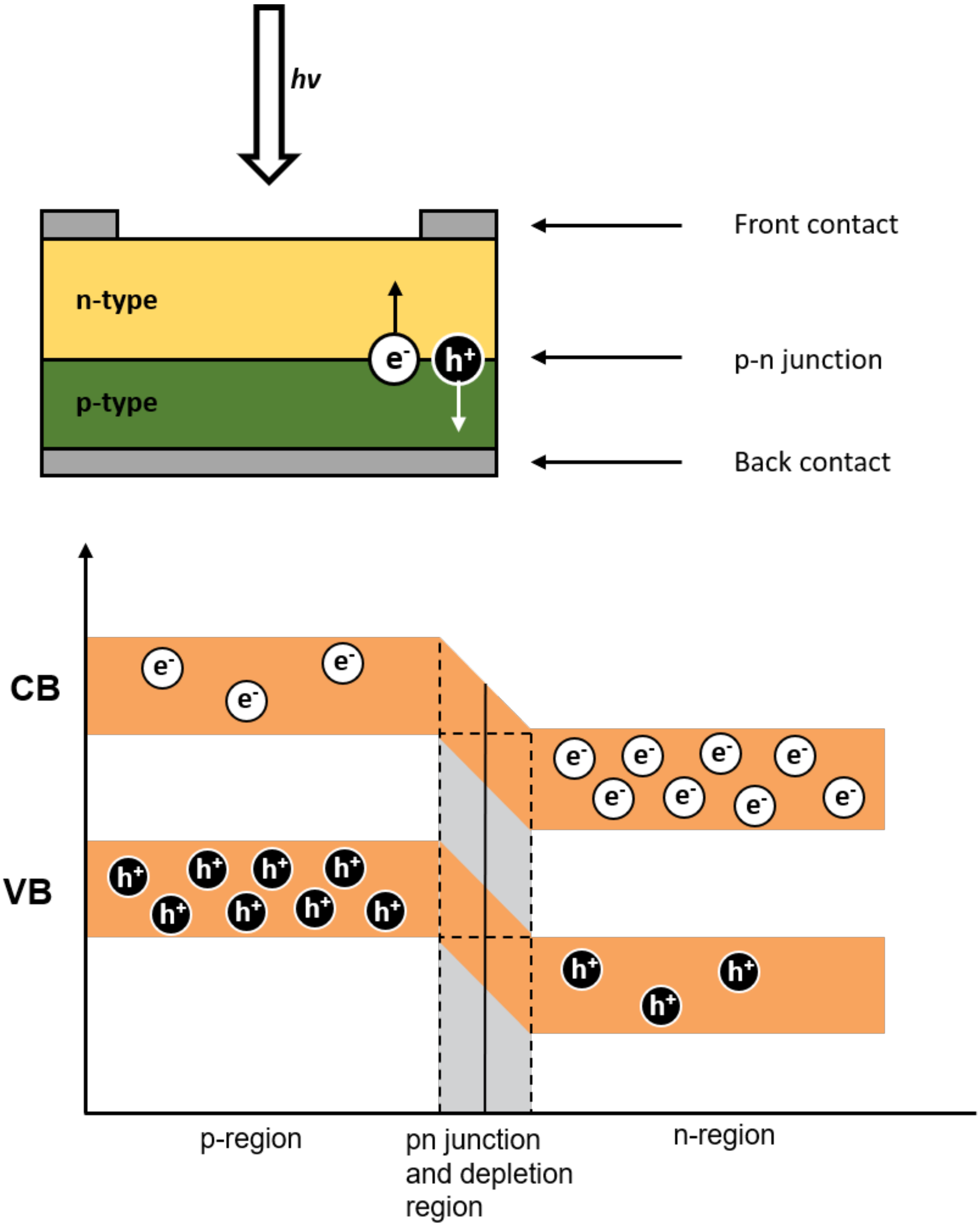

Figure 1.6: Schematic representation of a p-n junction (top), Energy level diagram of a pn-junction at equilibrium (bottom).

material takes on a net negative charge, due to the electrons attracted across the junction. As electrons also left the n-type region, that portion of the material close to the junction takes on a localized positive charge. The thin layer between these regions which has been depleted of majority carriers is known as the depletion region and effectively acts as an insulator between the conductive p- and n-doped regions. Figure 1.6 shows a schematic representation of a pn junction (top) and an energy level diagram describing the charge carriers in the semiconductors (bottom).

1.3 Photovoltaic Technologies

1.3.1 1st Generation

Currently the renewable energy market is dominated by single junction monocrystaline silicon devices (c-Si), a 1st generation photovoltaic technology.[12–14] These devices are comprised of multiple silicon wafers of high purity with thicknesses of 0.2 - 0.5 mm.[15] These wafers are doped with either phosphorous or boron to create n-type or p-type silicon respectively. The interface between the two domains form a p-n junction. At this junction, photons are absorbed and separated into an electron-hole pair. The electric field generated at the p-n junction aids in this charge separation and the two charges are collected at back contacts integrated into the device to complete the circuit and generate a photocurrent through the device. As the light harvesting and charge extraction processes occur in the same material, defects found in the bulk material drastically reduce the efficiency of the device.[16] High-purity materials are required, which incurs costly manufacturing procedures to make the pristine silicon wafers. As c-Si is an indirect band gap material, large amounts of material is required in order to absorb sufficient photons to produce efficient photovoltaic devices.[17] Despite these large manufacturing costs, these devices are generally robust and efficiencies are high (20% - 26.6%).[13]

1.3.2 2nd Generation

2nd Generation devices are typically defined as thin film technologies. These include amorphous silicon (a-Si), Cadmium Telluride (CdTe) and Copper Indium Gallium Selenide (CIGS).[12,18–20] These devices operate under the same working principles as a c-Si photovoltaic device, however, as these materials have direct band gaps, a smaller amount of material is required to generate high photocurrents. In turn, these devices are often cheaper to produce, and have limited degrees of flexibility enabling new engineering solutions like the popularized solar roof tiles from Tesla.[21] The use of rare earth elements, namely indium and tellurium, mean concerns have been raised about the viability of scaling up these types of devices.[22]

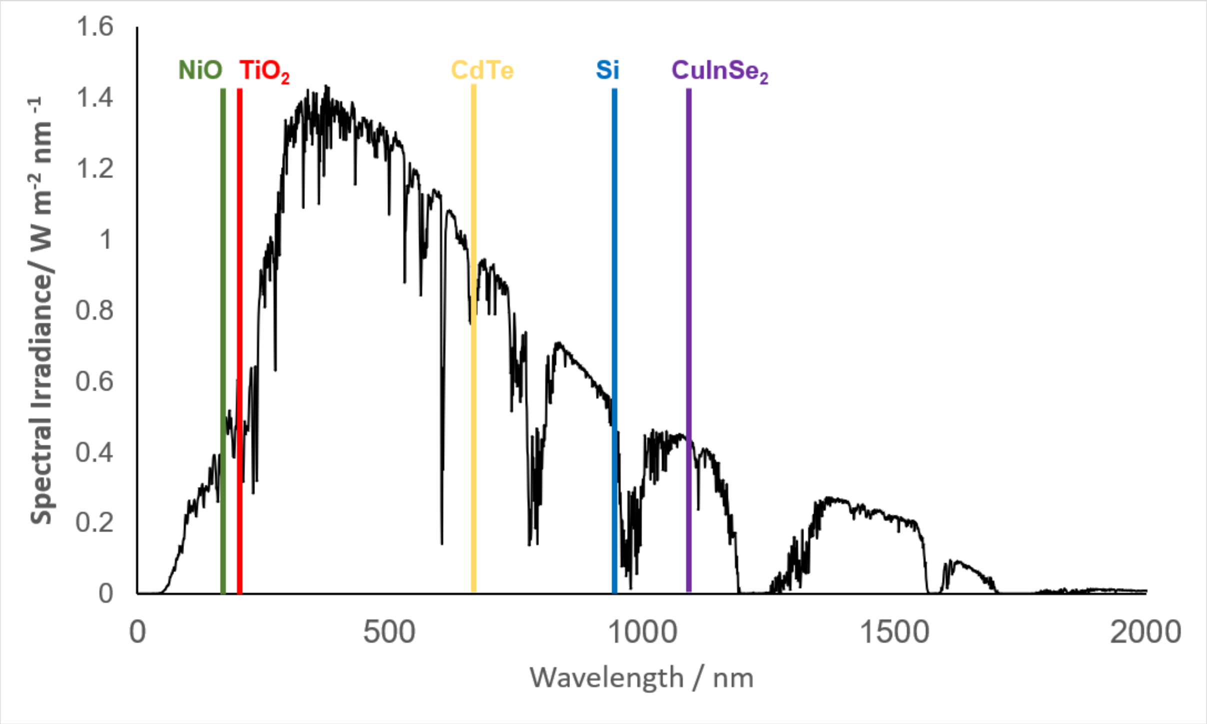

Figure 1.7: Band gaps of common thin film photovoltaic semiconductors against AM 1.5 solar spectrum

1st and 2nd generation devices both show encouraging efficiencies, however the theoretical maximum efficiencies for both technologies are defined by the Shockley-Queisser (SQ) limit.[23] For a single p-n junction, the maximum theoretical efficiency is approximately 34% under an AM 1.5 solar spectrum with a semiconductor of optimal band gap (1.34

eV).[24] A key limitation is the energy loss occurring when photons of greater energy then the semiconductor band gap are absorbed and require thermal relaxation to the band edge.[25] Inversely, the photons with lower energy than the semiconductor band gap do not create an electron-hole pair to generate a photocurrent.

1.3.3 3rd Generation

3rd generation devices are emerging technologies which aim to surpass the SQ limit. As previously stated the maximum efficiency for a single junction device at AM 1.5 is 34%. Multijunction devices can split the collection of high and low energy photons, reducing the thermal relaxation energy losses found in 1st and 2nd generation devices, and increasing the amount of usable photons which enter the device. This increases the maximum solar conversion of a single junction device from 34% (as stated by the SQ limit), to 45% for a two junction device, up to a maximum theoretical efficiency of 65% for an infinite number of p-n junctions.[26–28]

3rd generation devices based on nanotechnologies have experienced a surge in interest due to their relatively high efficiency and low processing costs. Lower processing costs and alternative materials enable cheaper manufacturing and bulk processing, which enables the cost of these PV technologies to be significantly lower than their c-Si counterparts. The device architectures also enable a wide and versatile range of molecules to be utilized in the device opening up a huge area of research interest.[12,29]

Three key 3rd generation technologies that have made significant improvements over a short period of time are dye sensitized solar cells (DSSC), quantum dot solar cells (QDSC) and perovskite solar cells. Although all three types of device have their problems, promising efficiencies of 14.3%,[30] 13.4%[31] and 23.7% have been achieved respectively, demonstrating the potential of 3rd generation devices to become future market leaders in the renewable energy sector.[32,33]

1.4 Dye-Sensitized Solar Cells

1.4.1 Working Principles

Dye sensitized solar cells are fabricated from a thin film of mesoporous semiconductor, acting as a support for dye molecules which bind to the surface and absorb photons. The difference in device architecture from a standard pn-junction separates the absorption of photons and extraction of charges into two separate materials allowing for the use of lower purity materials during manufacture, decreasing the cost of manufacture and sales dramatically.[8] Low cost processing methods, such as screen or ink-jet printing, have been developed in order to take these low purity materials forward to large scale production.[34,35] These methods are also favourable for roll-to-roll fabrication techniques, allowing for large scale devices to be assembled using flexible substrates.[36] Being semi-transparent allows for aesthetic integration into architectural designs for integrated photovoltaics.[37] A key benefit of the DSSC over c-Si devices is the relatively high efficiency of DSSC under low or diffuse light conditions (ie. indoors or overcast days). Technologies with up to 28.9% efficiency under these low light conditions have been achieved, opening up possibilities for powering small electronic devices within the home.[38]

1.4.2 n-type DSSC

The working principles of a classic n-type DSSC is outlined in Figure 1.8. Briefly, a thin layer of mesoporous metal oxide (typically n-type TiO_2) is deposited on a transparent conductive electrode supported on a suitable substrate (glass, plastic, fabric). The semiconductor is sensitized with a metallo-organic or organic chromophore to form the complete photoanode. The counter electrode is formed of a transparent conductive electrode on a suitable substrate, typically platinum deposited on fluorine doped tin oxide (FTO). Sandwiched between the two electrodes is a redox electrolyte which fills the pores of the mesoporous semiconductor photoanode, forming an electrical contact between the two electrodes. Figure 1.8 outlines the forward (productive) electron transfer pathway in

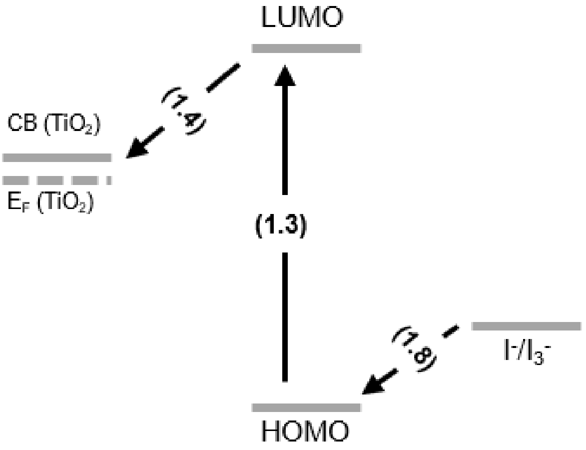

Figure 1.8: Representation of the relative energy levels and forward electron transfer processes in a TiO_2 DSSC. (1.3) dye excitation; (1.4) charge injection; (1.8) dye regeneration

an n-type TiO_2 DSSC leading to charge extraction to an external circuit. The electron transfer mechanism through a n-type DSSC has been researched extensively and has been shown to occur via a multi-step electron transfer pathway initiated by photoexcitation (Equation 1.3) of a dye molecule to an electronic excited state (D^*).[39]

$$D + hv \longrightarrow D^* \tag{1.3}$$

Following this photoexcitation, an electron is transferred from the now occupied LUMO of the excited dye molecule into the conduction band of the TiO_2 (Equation 1.4), assuming the energy levels are properly aligned sufficient Gibbs free energy is present for electron injection. (ΔG_{inj}). Upon injection of an electron, the excited dye is converted to the oxidized dye (D^+) and with the semiconductor forms a transient charge separated state (CSS).

$$D^*|TiO_2 \longrightarrow D^+|TiO_2^- \tag{1.4}$$

The electron diffuses through the semiconductor via a diffusion gradient to the back contact where it is collected and transferred to the external circuit. The dye is regenerated to the ground state by a redox electrolyte in order to repeat the process again (Equation

1.8). The iodide/triiodide redox couple has been extensively studied and used in DSSC, although much interest has been directed towards researching new electrolytes to facilitate the dye regeneration in DSSC.[40,41] The dye regeneration process in a n-type DSSC is believed to follow the mechanism outlined below.[42,43]

$$I_2 + I^- \longrightarrow I_3^- \tag{1.5}$$

$$I_3^- + 2e^- \longrightarrow 3I^- \tag{1.6}$$

$$D^+ + I^- \longrightarrow D - I \tag{1.7}$$

$$D - I + I^- \longrightarrow D + I_2^{\cdot -} \tag{1.8}$$

$$2I_2^{\cdot -} \longrightarrow I_3^- + I^- \tag{1.9}$$

Iodine and iodide ions in the electrolyte solution bind to form triidodide (Equation 1.5) with the equilibrium of this process limiting the quantities of free iodine present in the system.[44] Triiodide diffuses through the solution to the counter electrode and is reduced by electrons found in the platinised surface. The iodide can then regenerate the oxidised dye and forms the radical species $I_2^{\cdot -}$. Disproportionation of two of these transient radical species reforms iodide and triiodide. Hence the DSSC can be considered as a conservative photoelectrochemical cell, an electric current is generated by a cascade of electron transfer processes however, the chemical composition of the device remains unchanged. The aforementioned processes are favourable and contribute towards generation of a photocurrent between the two electrodes. In competition with these forward processes are negative recombination pathways within the cell leading to loss of efficiency. The main recombination pathways in n-type DSSC are outlined in Figure 1.9.

Relaxation of the dye from the electronic excited state back to the ground state (Equation 1.10) can occur via radiative or non-radiative decay pathways. For a device to work efficiently, the excited state lifetime (τ_{exc}) should be greater than the charge transfer lifetime (τ_{tr}) in order for the electrons to have sufficient time to diffuse through the electrode and be collected at the back contact. This step is in competition with recombination at the electrolyte/semiconductor interface.

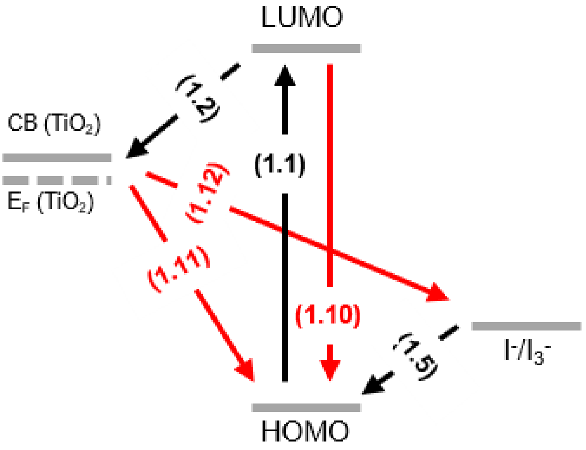

Figure 1.9: Representation of the forward electron transfer proceeses (black) and recombination processes (red) in a TiO_2 DSSC. (1.10) dye relaxation; (1.11) dye$^+$ $|TiO_2^-$ recombination; (1.12) electrolyte$^+$ $|TiO_2$ recombination.

$$D^* \longrightarrow D \tag{1.10}$$

Following the injection of charge to the conduction band of TiO_2, the charge pair can recombine to reduce the dye back to the ground state and terminate the electron transfer process within the DSSC (Equation 1.11). For this reason the charge separated state lifetime (τ_{css}) should be longer than τ_{tr}.

$$D^+|TiO_2^- \longrightarrow D|TiO_2 \tag{1.11}$$

Finally, the electron held inside the TiO_2 can recombine with species in the electrolyte to terminate the electron transfer (Equation 1.12). Recombination of this type is referred to in this work as *dark current*. Reduction of the dark current enhances the V_{OC} of a solar cell. Dark current mainly occurs at the TiO_2|electrolyte interface where no photosensitizer has been absorbed. The use of co-adsorbents such as di-tert butyl bipyridine (TBP) has been shown to reduce the dark current in a solar cell.[45]

$$I_2 + TiO_2^{2-} \longrightarrow 2I^- + TiO_2 \tag{1.12}$$

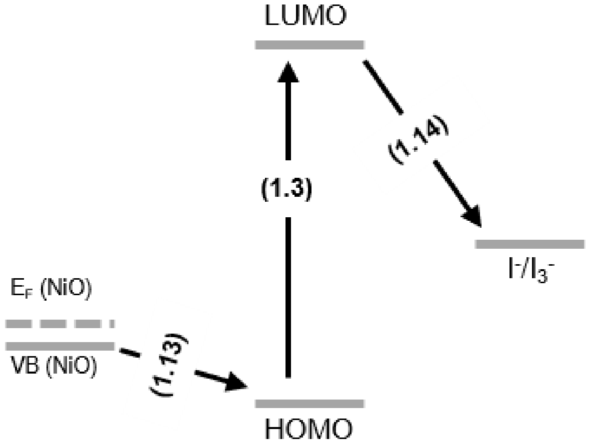

Figure 1.10: Representation of the relative energy levels and forward electron transfer processes in a NiO DSSC. (1.3) dye excitation; (1.13) charge injection; (1.14) dye regeneration.

1.4.3 p-type

P-type DSSC devices are comprised of a dye sensitized photocathode commonly containing p-type mesoporpous nickel oxide (NiO) as the p-type semiconductor. The multiple electron transfer processes are initiated, once again, by a photoexcitation of the dye, followed by electron injection from the valence band of the NiO into the HOMO of the excited dye molecule, producing a charge separated state (CSS) consisting of a reduced dye molecule and a hole in the VB of the semiconductor. (Equation 1.13)

$$D^*|NiO \longrightarrow D^-|NiO^+ \tag{1.13}$$

The hole diffuses to the back contact to be extracted to the external circuit. Dye regeneration by the iodide/triiodide redox electrolyte occurs from the triiodide species in solution (Equation 1.14).

$$D^- + I_3^- \longrightarrow D + I_2^{\cdot -} + I^- \tag{1.14}$$

The triiodide is then regenerated via an electron transfer reaction at the counter electrode. As with n-type DSSC there are several recombination processes, leading to the termination

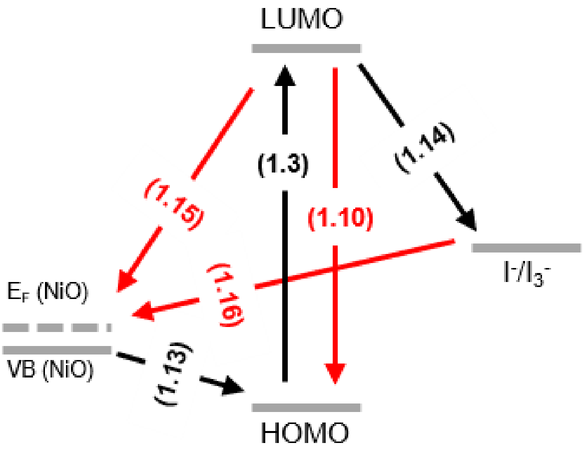

Figure 1.11: Representation of the forward electron transfer processes (black) and recombination processes (red) in a NiO DSSC. (1.10) dye relaxation; (1.15) dye$^-$ |NiO$^+$ recombination; (1.16) electrolyte$^-$ |NiO$^+$ recombination.

of the electron transfer processes in the device, that are in competition with the forward processes.

Dye relaxation occurs when τ_{exc} is smaller than τ_{tr}. The holes in the D$^-$|NiO$^+$ charge separated state can recombine with the reduced dye leading to a loss of the electron-hole pair (Equation 1.15). The holes in the valence band of NiO can also recombine with reduced species in the electrolyte (Equation 1.16).

$$D^-|NiO^+ \longrightarrow D|NiO \tag{1.15}$$

$$2[NiO^+] + 3I^- \longrightarrow NiO + I_3^- \tag{1.16}$$

1.4.4 Tandem pn-devices

Pairing an n-type photoanode and a p-type photocathode creates a tandem DSSC. The maximum V$_{OC}$ across the two junctions are additive (the V$_{OC}$ of the p-DSSC and the n-DSSC are added together) increasing the theoretical maximum voltage in the tandem device to the sum of both junctions. By pairing complimentary dyes on the photolectrodes, it is possible to harness a larger portion of the solar spectrum. Reduction of the spectral overlap of the dyes enables harvesting of the high energy photons on the n-type photoanode and lower energy photons on the p-type photocathode. Upon illumination of the device, both dyes are excited into an electronic excited state. At the photoanode the dye injects an electron into the conduction band of the n-type semiconductor. The electron can then move around the external circuit to regenerate the reduced dye attached to the p-type semiconductor. The redox electrolyte facilitates charge transport between the two electrodes.

The open circuit voltage (V_{OC}) of a DSSC is dictated by the relative energy levels found within the device. The V_{OC} of the device is calculated as the difference between the potential of the quasi-fermi level, close to the band edge of the semiconductor and the redox potential (E_{redox}) of the electrolyte at the counter electrode. The V_{OC} for n- and p-type devices are given by Equations 1.17 and 1.18 respectively.

$$V_{OC}(n) = E_{redox} - qE_{F,n} \tag{1.17}$$

$$V_{OC}(p) = qE_{F,p} - E_{redox} \tag{1.18}$$

$qE_{F,n}$ for TiO_2 is approximately -0.50 V vs. NHE and $qE_{F,p}$ for NiO is approximately 0.54 V vs. NHE.[46,47]

E_{redox} of the iodide/triiodide electrolyte is calculated from the Nernst equation:

$$E_{redox} = E^0_{redox} + \frac{RT}{2F} ln \frac{[I_3^-]}{[I^-]^3} \tag{1.19}$$

Where E^0_{redox} is the formal redox potential of the electrolyte, R is the ideal gas constant, T is the temperature and F is the Faraday constant. E_{redox} is 0.35 V vs. NHE for the iodide/triiodide in CH_3CN.[42,48]

Given the position of the quasi Fermi levels of TiO_2 (-0.50 V vs. NHE) and NiO (0.54 V vs. NHE), using equations 1.17 and 1.18, the maximum V_{OC} for a TiO_2 or NiO based DSSC are 0.85 V and 0.19 V respectively.

For a tandem pn-DSSC, the maximum V_{OC} available is calculated from the difference between the quasi fermi levels of both the n-type and p-type semiconductors.

$$V_{OC}(pn) = qE_{F,p} - qE_{F,n} \tag{1.20}$$

Therefore the maximum V_{OC} for a pn-tandem device can be described as the additive V_{OC} of the two separate cells, leading to a maximum V_{OC} in a TiO_2|NiO DSSC of approximately 1.04 V.

1.4.5 Organic Dyes

Currently, the highest certified efficiency n-type DSSC reached 14.3%. This device utilized two metal-free organic dyes (ADEKA-1 and LEG4, Figure 1.12) co-sensitized onto the surface of a TiO_2 electrode. Coupled with a cobalt (III/II) phenanthroline electrolyte and a graphitic nanoparticle (GNP) based counter electrode, the device showed impressive performance parameters, with Incident Photon-to-electron Conversion Efficiency (IPCE) values of 91% and V_{OC} above 1 V.[30]

Early p-type dyes

The first published working p-type DSSC was reported by Lindquist and co-workers and utilized a NiO electrode paired with an **Erythrosin B** sensitizer (Figure 1.13, left).[49] As a proof of concept, the dye produced a low efficiency (J_{SC} = 0.23 mA cm^{-2}; V_{OC} = 83 mV; η= 0.0076%). Following this **Coumarin-343** (**C343**) (Figure 1.13, right) was used as another small molecule sensitizer and once again, functioned as a proof of concept, however device efficiencies were low.[50] Upon inspection of the kinetic pathways of electron transfer within the device, it was shown that the main recombination pathway in a **C343**|NiO DSSC was the back electron transfer between the reduced dye and the hole in the NiO semiconductor valence band, leading to a low charge-separated state lifetime (20 ps).[50]

This work demonstrates the fundamental need for a long lived charge separated state

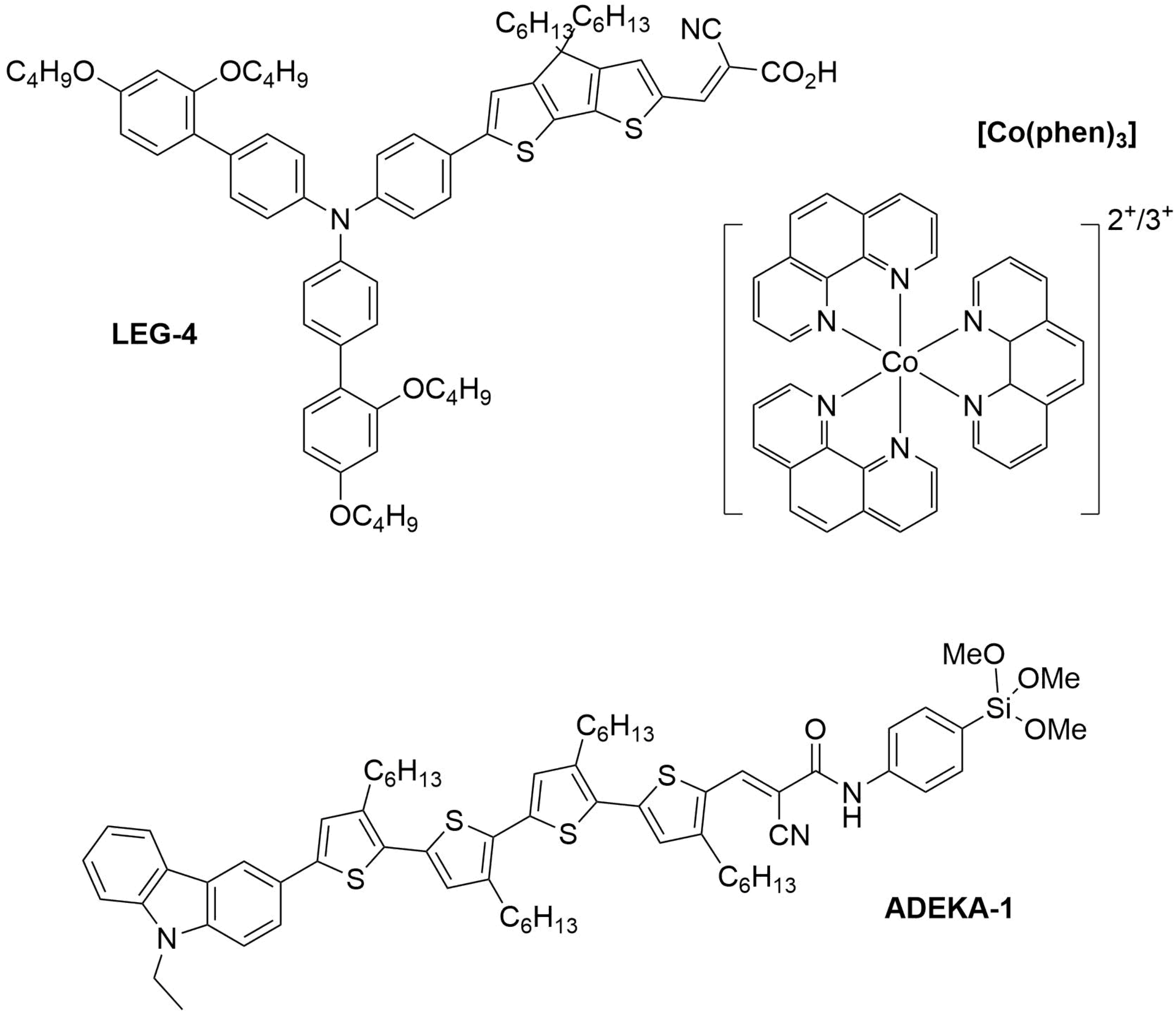

Figure 1.12: Molecular Structures of **LEG-4**, **ADEKA-1** and cobalt (III) phenanthroline

lifetime, and that slowing down the recombination is key to improving device performance going forward.

Push-pull dyes

PMI-NDI (Figure 1.14) was designed specifically to extend the CSS lifetime and adopted a "push-pull" structure. By separating the position of the electrons during the excited state of the dye to be localized on the electron acceptor, positioned on the periphery of the dye, the maximum separation of charges from the semiconductor surface was obtained and slower recombination rates were achieved. Le Pleux showed that the **PMI-NDI** dyad system achieved an external quantum efficiency three times greater than the PMI donor

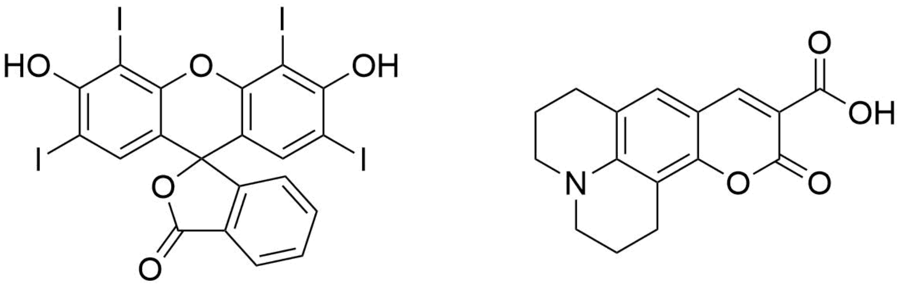

Erythrosin B **Coumarin-343**

Figure 1.13: Molecular structures of **Erythrosin B** and **Coumarin-343**

alone.[51]

The improvement in efficiency was attributed to the long lived charge separated state formed when the NDI acceptor was present. Other NDI and C_{60} acceptors were also screened in the system and each showed both an improvement in performance and an increase in the CSS lifetime when compared to the PMI donor alone. A common structural motif found in dyes for p-type DSSC are based on a triphenylamine donor with an anchor group and one or more electron acceptors. **P1** (Figure 1.15) combines a triphenylamine donor with two malonitrile acceptor units, linked by a thiophene bridge system and a carboxylic acid group to anchor the dye to the NiO. The initial reports published for **P1**|NiO based devices produced J_{SC} of 1.52 mA cm^{-2}, V_{OC} of 110 mV and IPCE of 18%, giving an overall efficiency of 0.05%.[52] Later these devices were optimised to give an IPCE of 68% and a PCE of 0.15%. Triphenylamine based dyes have recieved much interest in literature due to its strong electron donating character, ease of functionalization with a wide variety of groups and non-planar shape, which can prevent -stacking or aggregation. Most dye designs aim to modify the acceptor, linker or sometimes the anchor group, and to date, hundreds of arylamine based dyes have been reported in literature.[53,54]

Dyes with two acceptor units tend to produce higher J_{SC} values in p-DSSC. **CAD3** (Figure 1.16) was based on the **P1** structure, however replaced the two malonitrile acceptor groups with cationic indolium acceptors, achieving an impressive J_{SC} of 8.21 mA cm^{-2}.[55] The increased performance when compared to related dyes with only one acceptor (**CAD1**

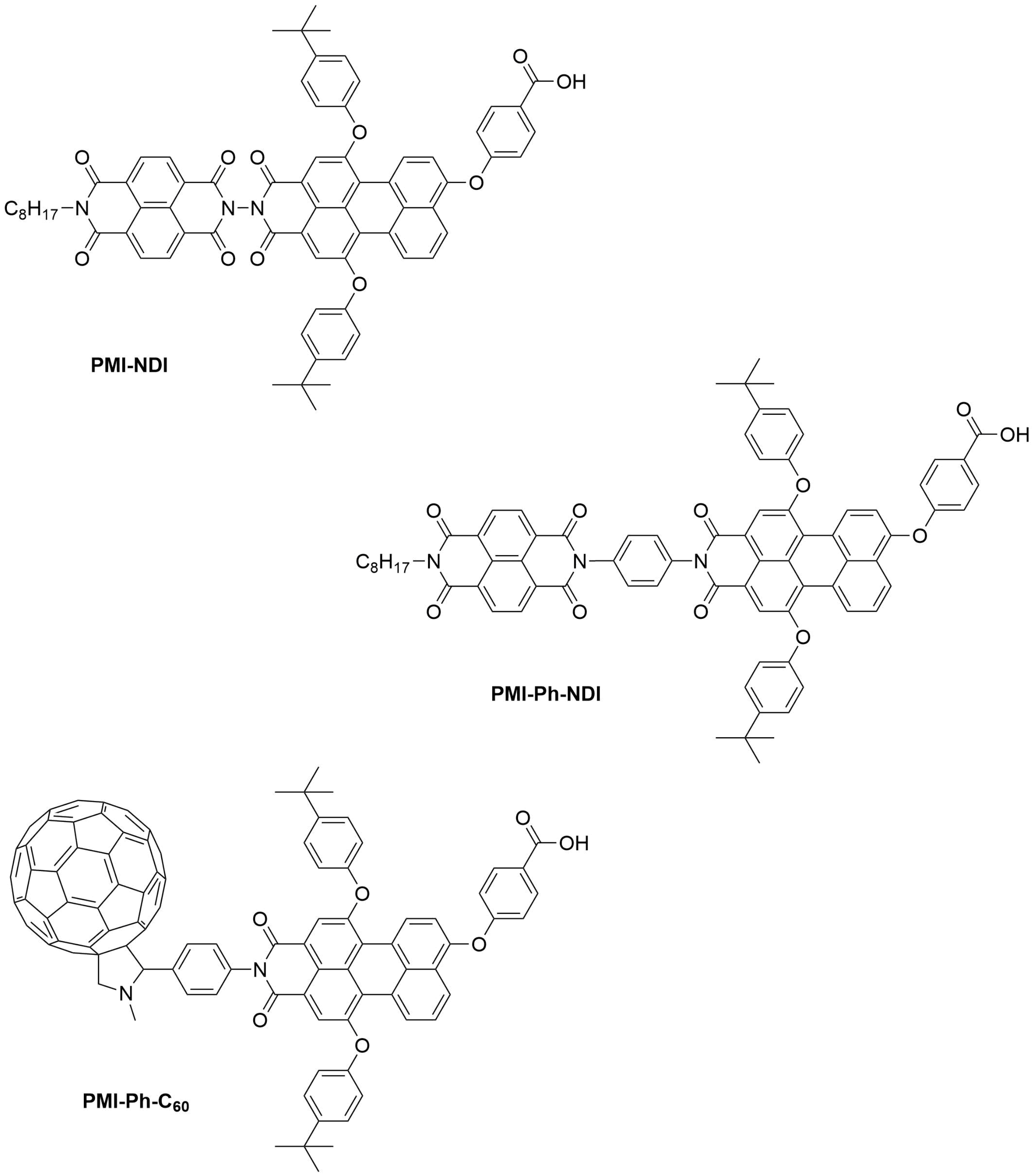

PMI-NDI

PMI-Ph-NDI

PMI-Ph-C_{60}

Figure 1.14: Molecular structures of the **PMI** dye series by Le Pleux.[51]

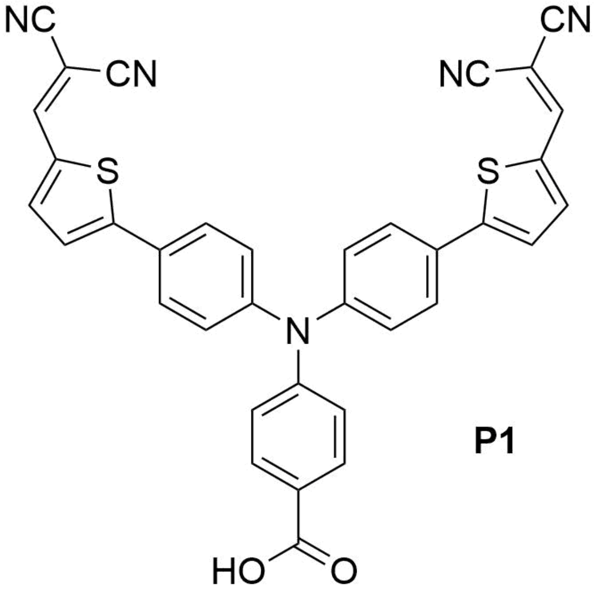
P1

Figure 1.15: Molecular structure of **P1** dye

and **CAD2**) was due to the stronger absorbance of the double-acceptor dye (**CAD3**; ϵ = 95 000 mol^{-1}dm^{3}cm^{-2}).[56]

Studies have also been conducted into the effects donor-acceptor separation within the push-pull dye system. Yang and co-workers modified the length of the thiophene chain of **P1** from 4 to 6 thiophene units, concluding that that the best performing dye in this series was **T3** featuring 4 thiophene units (Figure 1.17, top). (**T3**; $J_{SC} = 5.31$ mA cm^{-2}, $V_{OC} = 119$ mV, $\eta = 0.208$ %).[57,58] Extending the conjugation length of the oligothiophene chains resulted in slower charge recombination at the metal oxide/electrolyte interface, yet the conductace of the oligothiophene chain decreased with additional units (T4 (41.76 Ω) $<$ T3 (45.13 Ω) $\approx$ T5 (45.46 Ω) $<$ T6 (48.74 Ω)) indicating that the increase in thiophene chain length slowed down the hole transporting ability of the dye.

Furthering this work, Yang and co-workers replaced the malonitrile groups of **P1** with 1,3-diethyl-2-thiobarbituric acid (**T4H**) (Figure 1.17, bottom). The change in electron acceptor induced a broadening of the absorbance spectrum extending into the NIR, increasing the light harvesting ability of **T4H** in comparison to **T3**. As a result, T4H generated a higher J_{SC} then **T3** when incorporated into a p-type DSSC. (**T3**; $J_{SC} = 5.31$ mA cm^{-2}, **T4H**; $J_{SC} = 6.74$ mA cm^{-2}).[59]

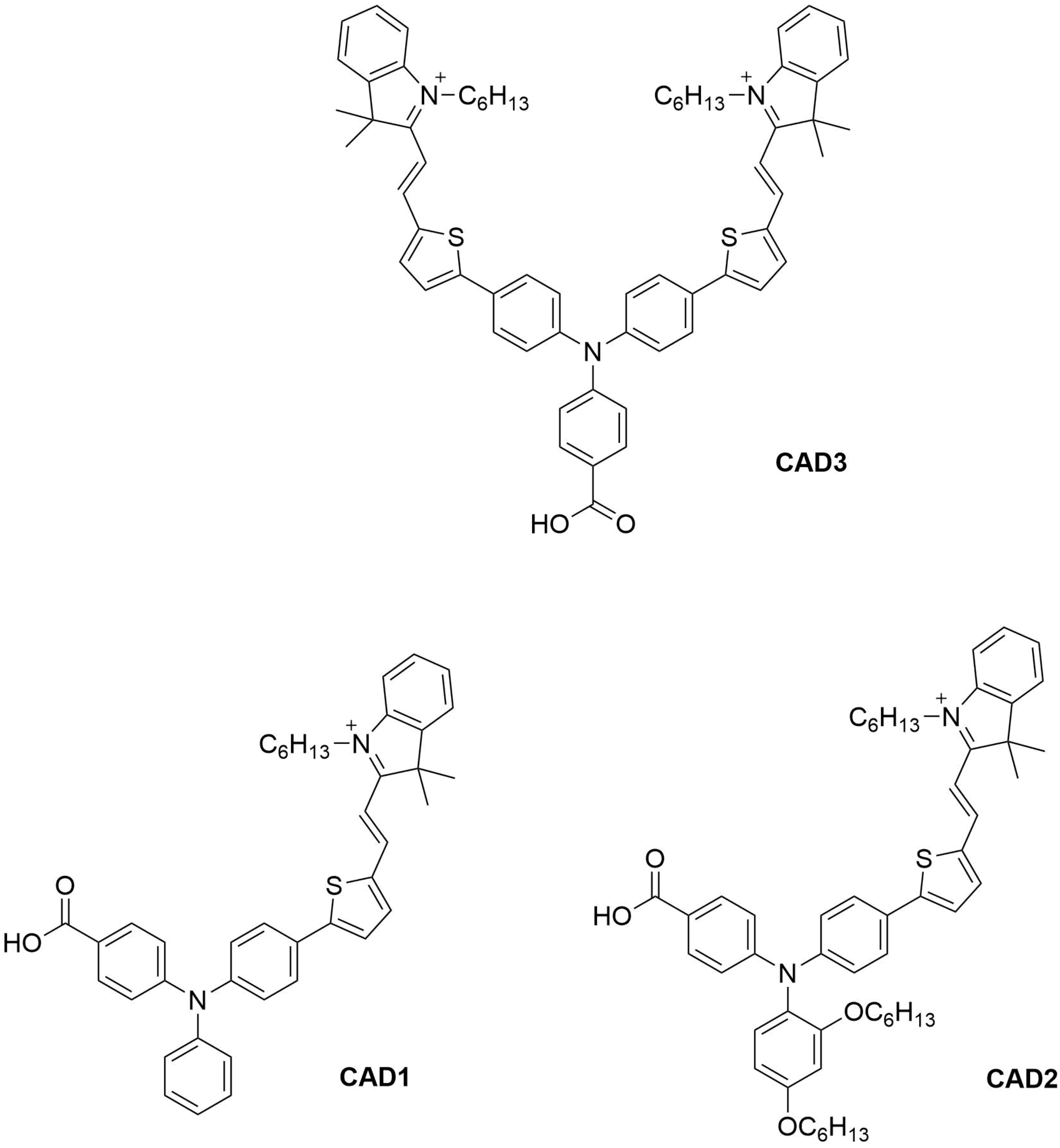

CAD3

CAD1

CAD2

Figure 1.16: Molecular structures of **CAD1-3**

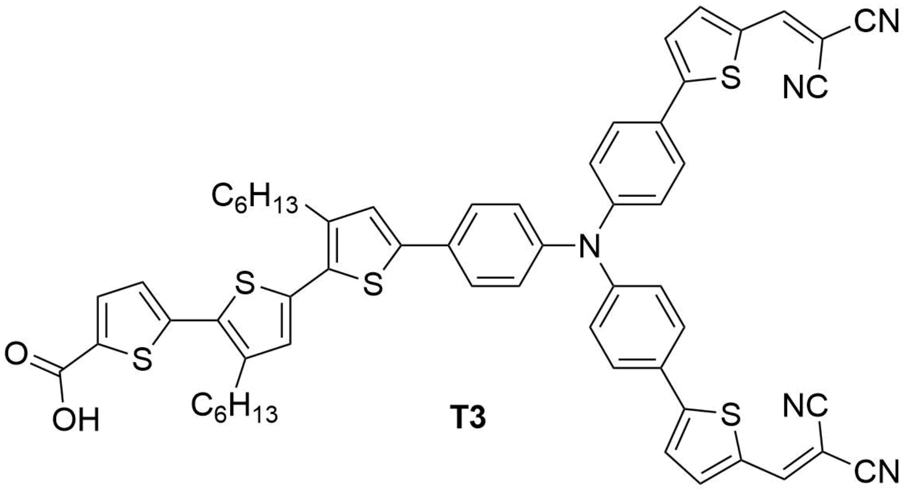

T3

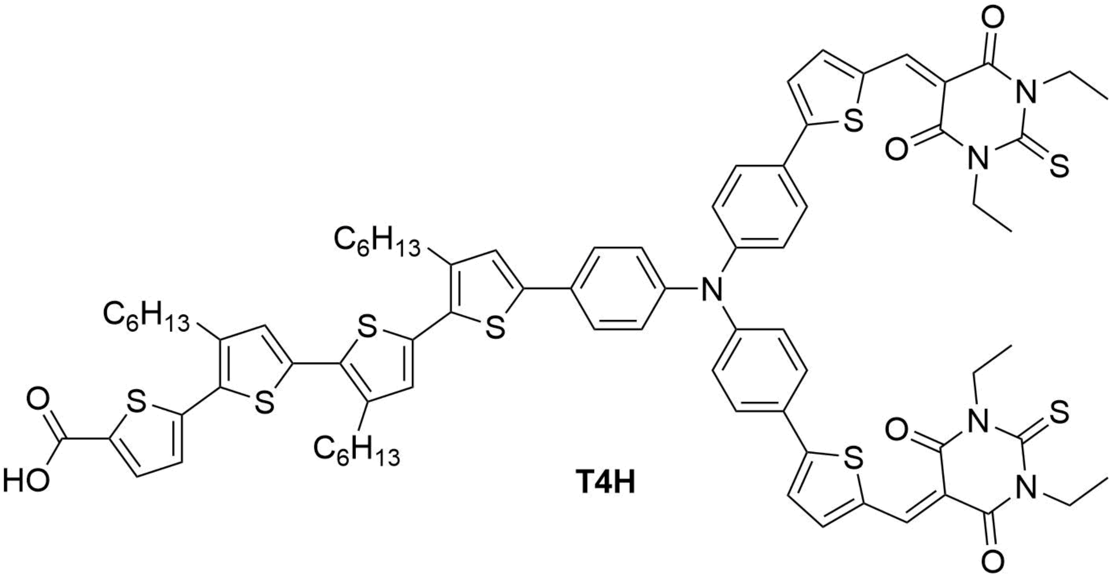

T4H

Figure 1.17: Molecular structures of **T3** and **T4H**, two triphenylamine-based, bis-acceptor dyes published by Yang.

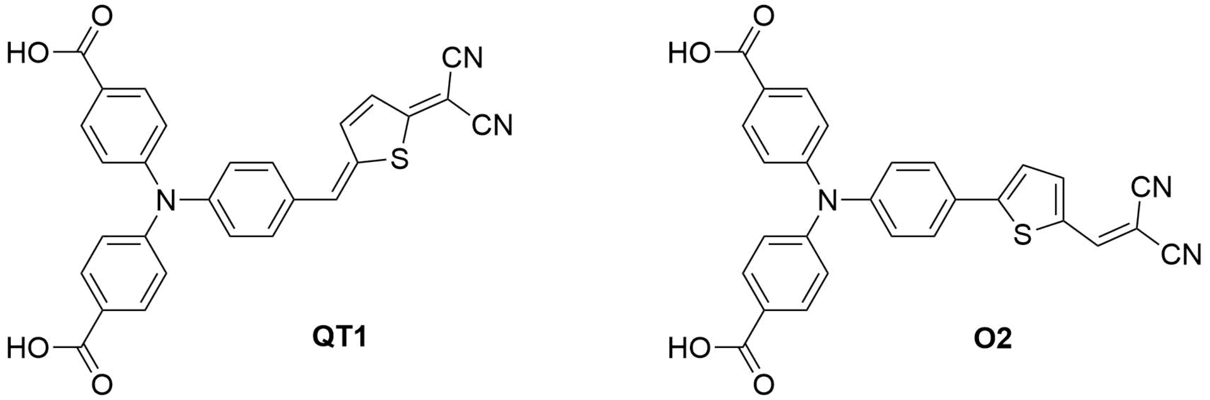

Figure 1.18: Molecular structures of **QT1** and **O2**

Bis-anchored dyes have also been investigated for use in p-type DSSC. Zhou and coworkers incorporated a doubly anchored triphenylamine type system with a single thienoquinodyl acceptor (**QT1**) (Figure 1.18, left) into a NiO DSSC. Despite the mono-acceptor design and small separation of the donor and acceptor units of the dye, it displayed an impressive photocurrent density (**QT1**; J_{SC} = 8.2 mA cm^{-2}).[60] There is little discussion on why the performance of this dye is so high, however it is mainly attributed to a high extinction coeffificent and small size, allowing for a high dye loading on the surface of the electrode. (**QT1**; ϵ = 54 000 $mol^{-1}dm^{3}cm^{-2}$).

Ji and coworkers reported another triphenylamine based double anchor dye, **O2** (Figure 1.18, right), which bears strong resemblance to **QT1**, notably a bis-carboxylic acid triphenylamine donor, however the thienoquinodyl bridge found in **QT1** is replaced with a more conventional thiophene in **O2**. **O2** performed worse in a working p-DSSC (**O2**; J_{SC} = 1.74 mA cm^{-2}, **QT1**; J_{SC} = 8.2 mA cm^{-2}). demonstrating how minor structural changes to a chromophore can cause drastic effects on the efficiency of the system.[61]

The **zzx-op** dye series (Figure 1.19) demonstrates a key factor when designing dyes for p-type DSSC. A series of triphenylamine-NDI donor-acceptor systems with two carboxylic acid anchor groups were synthesized. The linker groups were modified to fluorene (**zzx-op1**), fluorene-3,4-ethylene dioxythiophene (EDOT, **zzx-op2**) and fluorene-EDOT-thiophene (**zzx-op3**).[62] As expected the extended conjugation length from the π-system caused broadening of the absorbance spectrum. The increase in spectral coverage was

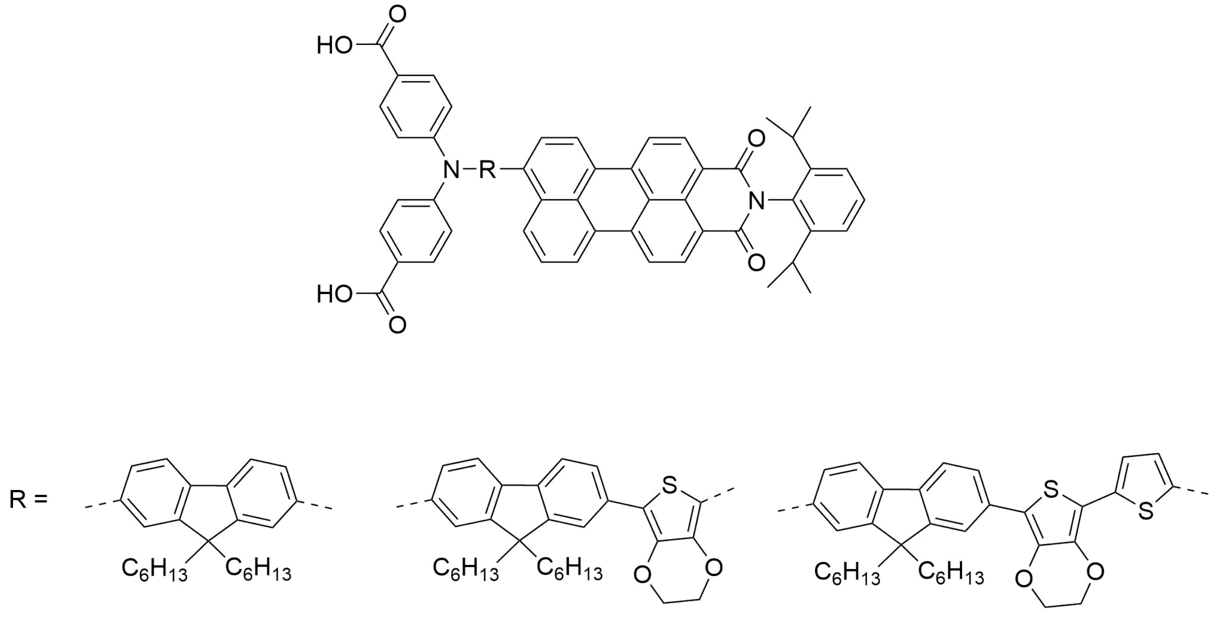

zzx-op1 **zzx-op2** **zzx-op3**

Figure 1.19: Molecular structures of the **zzx-op** dye series published by He, utilizing a double anchor and fluorene linker design.

expected to increase photocurrents produced by the devices, however, when implemented into working devices the J_{SC} values decreased with conjugation length (J_{SC}: **zzx-op1**; 4.36 mA cm^{-2}, **zzx-op2**; 4.00 mA cm^{-2}, **zzx-op3**; 3.80 mA cm^{-2}). The V_{OC} and fill factors of these devices remained consistent throughout the series.

The drop in J_{SC} upon increasing the conjugation length was rationalized by the lowering of the HOMO of the dye with increasing conjugation, causing the driving force for charge injection to decrease. The injection quantum yield for **zzx-op1**, **zzx-op2** and **zzx-op3** were calculated as 90%, 54% and 39% respectively. He and co-workers postulated that a driving force for charge injection should be ca. 0.80 eV to enable high charge transfer quantum yields between the dye and semiconductor. Further publications from He expanded the **zzx-op** series (Figure 1.20), incorporating 1-3 fluorenes into the π-bridge (**zzx-op1**, **zzx-op1-2** and **zzx-op1-3**). As the conjugation length increased, the driving force for charge injection was unaffected. However, the increase in spatial separation of the donor-acceptor caused a reduction in the charge recombination between the reduced dye and the hole on NiO.

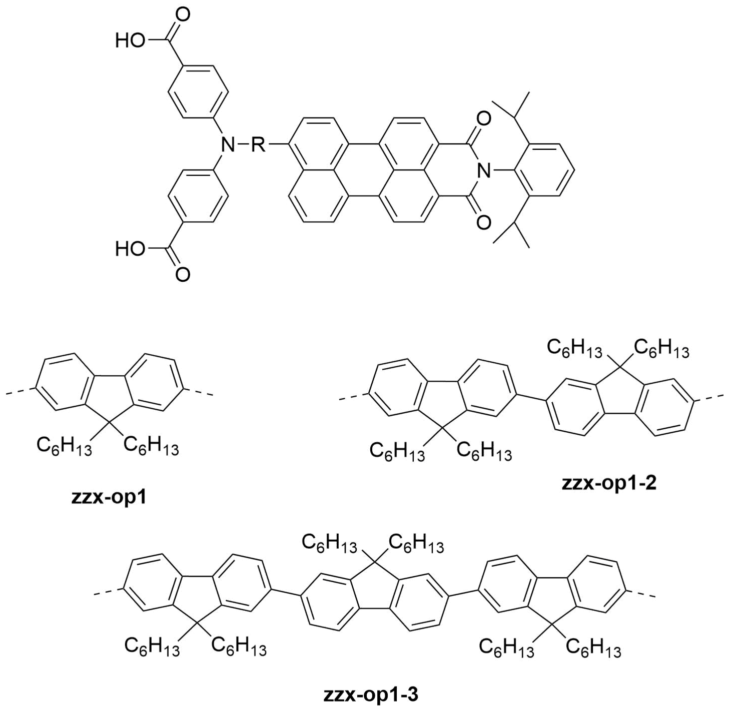

Figure 1.20: Molecular structures of the **zzx-op** dye series published by He, utilizing a double anchor and fluorene linker design.

zzx-op1-2 displayed the highest J$_{SC}$ in a working p-DSSC (**zzx-op1-2**; J$_{SC}$ = 7.57 mA cm^{-2}). He and co-workers suggested that this dye performed better than the other two dyes in the series due to a trade off between spatial separation of the donor and acceptor, and flexibility of the fluorene chain. The increased spatial separation reduced the charge recombination between the dye and NiO. The shorter and more flexible chains were described as forming a more compact layer over the semiconductor which protected the NiO surface from recombination with the I^-/I_3^- electrolyte. He et. al describe **zzx-op1-2** as a midpoint of these two factors in the dye series and therefore showed the best performance in a p-DSSC.

Although TPA-based dyes have dominated the field of p-type DSSC, recent publications have shown the promise of non-TPA sensitizers. Odobel and coworkers reported a series of diketopyrollopyrrole (**DPP**) dyes both with and without TPA donors (Figure 1.21).

The most effiicent dye in the series, **Th-DPP-NDI**, produced an impressive photocurrent density (**Th-DPP-NDI**; J_{SC} = 8.2 mA cm^{-2}), over two times that of the TPA-based

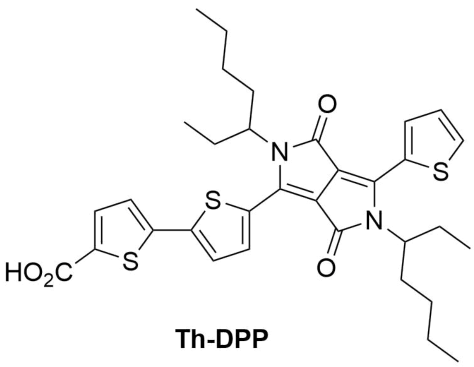

Th-DPP

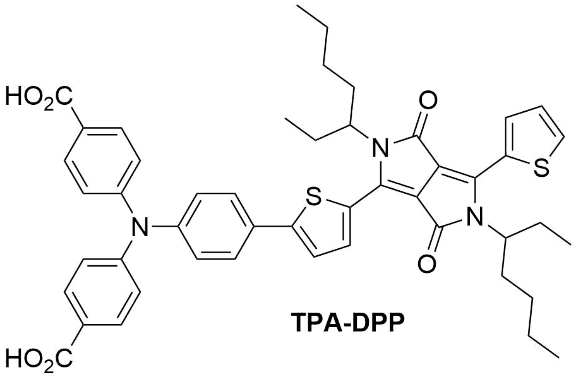

TPA-DPP

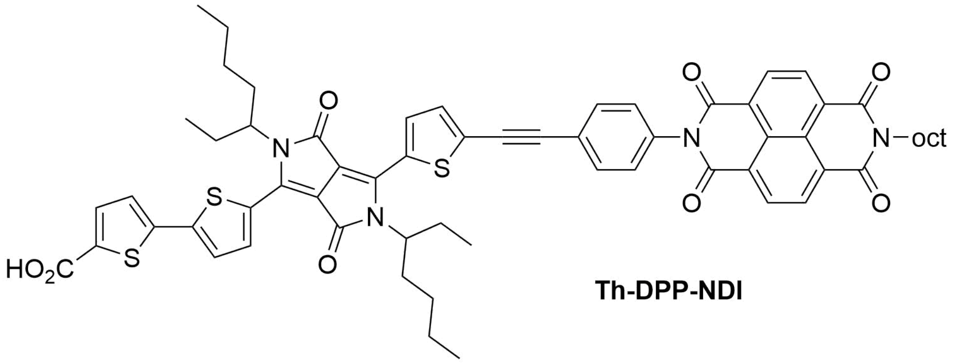

Th-DPP-NDI

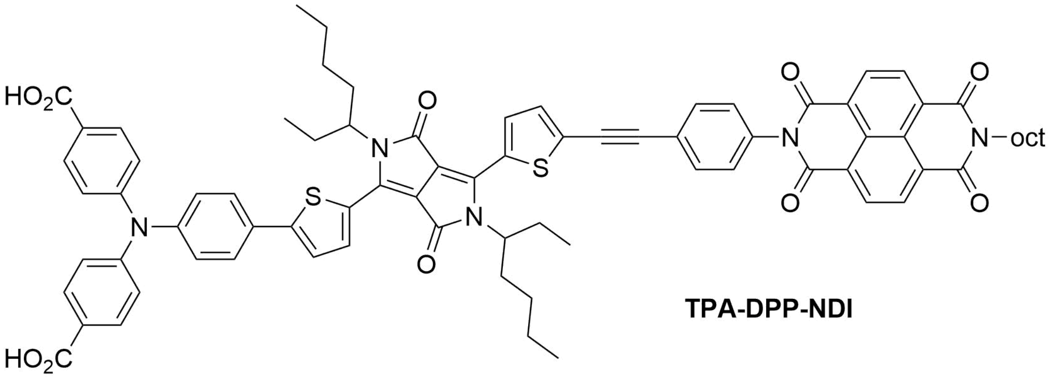

TPA-DPP-NDI

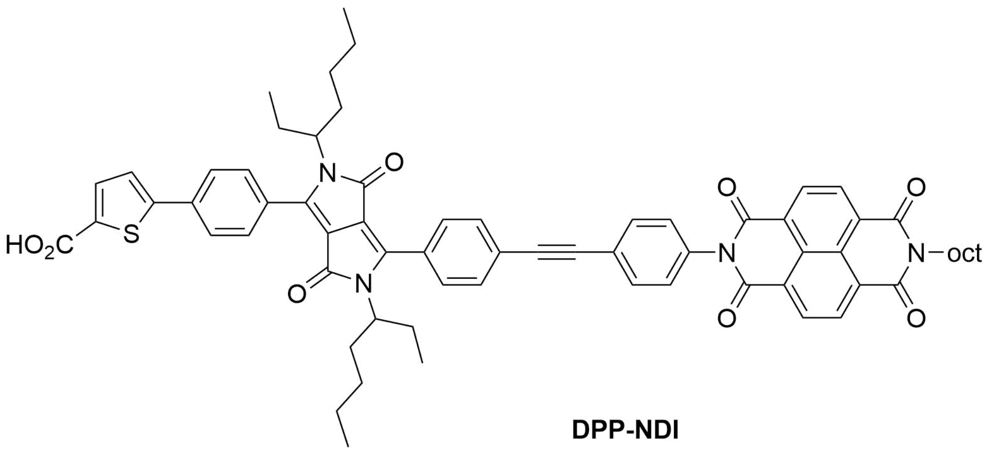

DPP-NDI

Figure 1.21: Molecular structures of the diketopyrrollopyrrole (**DPP**) dye series designed by Odobel.

senzitizer (**TPA-DPP-NDI**; J_{SC} = 4.04 mA cm^{-2}). In this system, the NDI acceptor is essential for high efficiencies. Both Th-DPP and TPA-DPP produced small photocurrent densities (**Th-DPP**; 0.26 mA cm^{-2}, **TPA-DPP**; 0.70 mA cm^{-2}). Previous iterations of these DPP-NDI dyes with mixed phenyl/thiophene bridges (**DPP-NDI**) produced only modest photocurrents (**DPP-NDI**; 1.79 mA cm^{-2}), again highlighting how minor structural changes in a sensitizer can yield dramatic improvements in device parameters. **Th-DPP-NDI** was also successfully incorporated into a tandem pn-DSSC. A TiO2|**D35** photoanode was paired with a **Th-DPP-NDI** photocathode and the tandem device produced a higher PCE than the two electrodes individually. This not only marks a significant step in the field of tandem DSSC, but will also encourage research on non-TPA based sensitizers for p-DSSC.

Cell	J_{SC} (mAcm^{-1})	V_{OC} (mV)	FF	η(%)
TiO_2 |**D35**	7.41	764	69	3.91
NiO|**Th-DPP-NDI**	7.85	150	30	0.35
Tandem	6.73	910	66	4.10

Table 1.1: Solar Cell performance parameters for the D35 n-type DSSC, Th-DPP-NDI p-type DSSC and D35/Th-DPP-NDI tandem DSSC produced by Odobel.

To date, the highest performing p-DSSC was published by Bäurle and co-workers and was constructed from a bis-anchored TPA donor, an oligothiophene spacer and a PMI acceptor. It was shown in the original publication that **PMI-6T-TPA** (Figure 1.22), containing 6 thiophenes, was the optimal oligothiophene chain length. Using an I^-/I_3^- redox electrolyte affords a PCE of 0.60%. Extensive research around this dye has led to efficiencies of 1.20% with a cobalt (III/II) redox couple and 2.51% with an iron (III/II) couple (Table 1.2).

The first tandem device was fabricated by Lindquist et. al and utilized a TiO_2 photoanode with the metallo-organic ruthenium dye N3, and a NiO photocathode with an **Erythrosine B** sensitizer.[27] The results showed that the open circuit voltage (V_{OC}) of the tandem device was close to the sum of the individual V_{OC} of the separated n- and

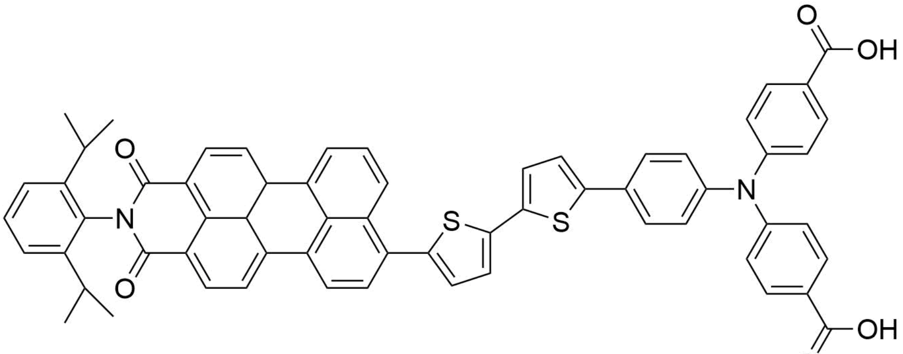
PMI-6T-TPA

Figure 1.22: Molecular structure of **PMI-6T-TPA** published by Bäurle and co-workers.

	I_3^-/I^-	$[Co(en)_3]^{3+/2+}$	$[Fe(acac)_3]^{0/1-}$
V_{OC} (mV)	243	724	645
J_{SC} (mA cm^{-2})	6.26	4.11	7.65
FF (%)	39	40	51
η (%)	0.60	1.20	2.51

Table 1.2: Solar cell performance parameters for the PMI-6T-TPA p-DSSC recorded with three redox electrolytes.

p-type DSSC. However, the efficiency of the tandem device was poor (0.39%) which was mainly attributed to the poor photocurrents of the photocathode (J_{SC} = 0.27 mA cm^{-2}). More recently, tandem devices have been fabricated which outperform the individual p- or n-type DSSC individually. Odobel reported a p DSSC with diketopyrollopyrrole sensitizers (**Th-DPP-NDI**) with an encouraging performance (J_{SC} = 7.38 mA cm^{-2}, V_{OC} = 0.147 V, FF = 0.32; η = 0.35%).[63]

When paired with a TiO_2|**D35** photoanode (Figure 1.23), the resulting pn-tandem device outperformed the individual p- and n-DSSC in isolation (J_{SC} = 6.73 mA cm^{-2}, V_{OC} = 0.91 V, η = 4.1 %) Although these results are promising, the highest recorded tandem efficiency has not yet reached the 14.3% efficiency of an n-type device. It appears the limiting factor is still the current at the photocathode, and without increasing the photocurrent at the photocathode to match that of the highest performing n-type devices, improvements to pn-tandem DSSC will be limited.

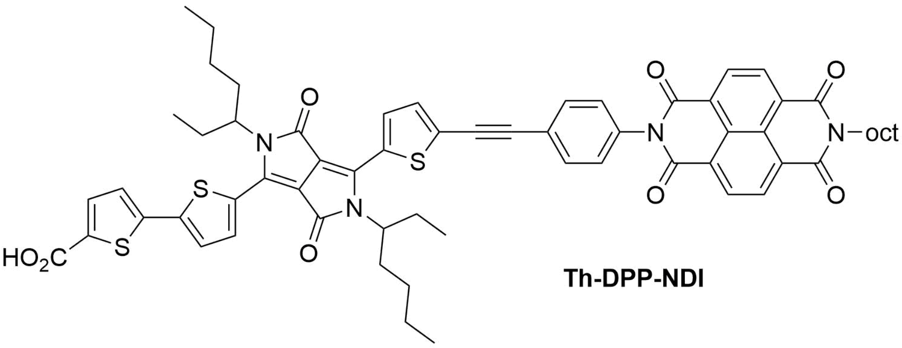

Th-DPP-NDI

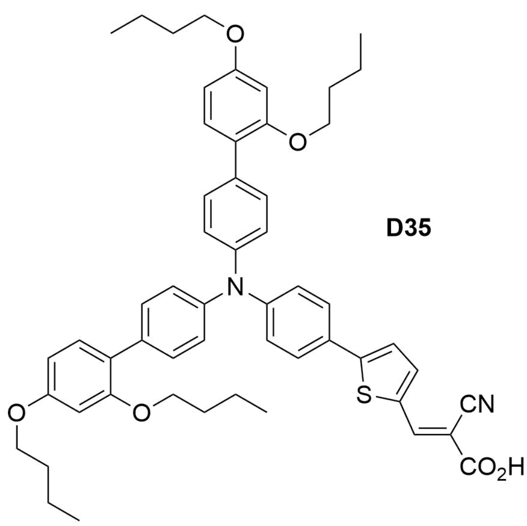

D35

Figure 1.23: Molecular structures of **Th-DPP-NDI** and **D35** used to make a high performance tandem DSSC by Odobel.[63]

1.5 p-type dyes

The main losses to the photocurrent in a p-DSSC are produced at the dye|semiconductor interface. Developing new sensitizers is a vital step needed to improve p-type DSSC. Improving the photocurrents generated in a p-DSSC opens possibilities to match the photocurrents generated between the photoelectrodes and solve a key limitation in tandem pn-DSSC devices.

When designing new dyes for p-type devices, a few criteria must be met:

- In order for a photocathode to operate efficiently in a tandem device, the two photosensitizers used must absorb at complimentary wavelengths.[64] As such, if the photosensitizer used for the TiO_2 photoanode absorbs at higher energies, it is favoured for the photocathode to absorb at lower energies, or vice versa. By minimising the spectral overlap between the two photosensitizers, the maximum number of available photons can be utilized over a larger portion of the solar spectrum.
- As the film thickness of the NiO electrode is small (c.a 1.5 μm), the dye requires a high absorption coefficient to maximise light harvesting with restricted surface area.[65]
- The dye must contain an anchor group to facilitate strong adsorption onto the semiconductor surface and to enable efficient charge transfer between the dye and semiconductor. Most commonly, the carboxylic acid moiety has been used.[51,63,66,67] However, a variety of other functionalities have been used including, phosphonates,[68] pyridyls[69] and alkoxysilane groups.[70,71]
- The energy levels of the frontier orbitals of the dye must be positioned for efficient charge transfer to occur. This requires both the HOMO of the dye to be positioned at a more positive potential than the valence band of the semiconductor for a p-type device, and the LUMO to be more negative than the redox potential of the electrolyte.[72,73]

References

(1) Nocera, D. G.; Nash, M. P. *PNAS* **2007**, *104*, 15729–15735.

(2) Lewis, N. S. *Science* **2007**, *315*, 798–801.

(3) Crabtree, G. W.; Lewis, N. S. *Physics Today* **2007**, *60*, 37–42.

(4) Grätzel, M. *Inorganic Chemistry* **2005**, *44*, 6841–6851.

(5) Brennan, K. F.; Brown, A. S., *Theory of Modern Electronic Semiconductor Devices*; John Wiley & Sons, Inc.: 2002.

(6) Zanatta, A. R. *Scientific Reports* **2019**, *9*, 11225–11230.

(7) Poole, C. P.; Prozorov, R.; Farach, H. A.; Creswick, R. J. In *Superconductivity*; Elsevier: 2014, pp 1–31.

(8) Nelson, J., *The Physics of Solar Cells*; Series on Properties of Semiconductor Materials; Imperial College Press: 2003.

(9) Shklovskii, B. I.; Efros, A. L., *Electronic Properties of Doped Semiconductors*; Springer Berlin Heidelberg: 1984.

(10) Schwingenschlögl, U.; Chroneos, A.; Schuster, C.; Grimes, R. W. *Journal of Applied Physics* **2012**, *112*, 046101.

(11) Raymond, C.; Ronca, S. In *Brydson's Plastics Materials*; Elsevier: 2017, pp 103–125.

(12) Nayak, P. K.; Mahesh, S.; Snaith, H. J.; Cahen, D. *Nature Reviews Materials* **2019**, *4*, 269–285.

(13) Liu, J.; Yao, Y.; Xiao, S. *Journal of Physical Chemistry D: Applied Physics* **2018**, *51*, 123001.

(14) Andreani, L. C.; Bozzola, A.; Kowalczewski, P.; Liscidini, M.; Redorici, L. *Advances in Physics: X* **2018**, *4*, 1548305.

(15) Wang, X.; Wang, Z. M., *High Efficiency Solar Cells - Physics, Materials and Devices*; Springer International Publishing: 2014.

(16) Park, J.-S.; Walsh, A. *Nature Energy* **2019**, *4*, 95–96.

(17) Goetzberger, A.; Knobloch, J., *Crystaline Silicon Solar Cells*, 2014, pp 87–131.

(18) Lee, T. D.; Ebong, A. U. *Renewable and Sustainable Energy Reviews* **2016**, *70*, 1286–1297.

(19) Green, M. A. *Journal of Materials Science: Materials in Electronics* **2007**, *18*, 15–19.

(20) Powalla, M.; Paetel, S.; Ahlswede, E.; Wuerz, R.; Wessendorf, C. D.; Friedlmeier, T. M. *Applied Physics Reviews* **2018**, *5*, 041602.

(21) TeslaUK Tesla Solar Roof., `https://www.tesla.com/en_GB/solarroof`, (accessed: 10.07.2020).

(22) Lee, T. D.; Ebong, A. U. *Renewable and Sustainable Energy Reviews* **2017**, *70*, 1286–1297.

(23) Shockley, W.; Queisser, H. J. *Journal of Applied Physics* **1961**, *32*, 510–519.

(24) Ruhle, S. *Solar Energy* **2016**, *130*, 139–147.

(25) Kahmann, S.; Loi, M. A. *Journal of Materials Chemistry C* **2019**, *7*, 2471–2486.

(26) Henty, C. H. *Journal of Applied Physics* **1980**, *51*, 4494–4500.

(27) He, J.; Lindstro, H.; Hagfeldt, A.; Lindquist, S.-e. *Solar Energy Materials and Solar Cells* **2000**, *62*, 265–273.

(28) Marti, A.; Arafijo, G. L. *Solar Energy Materials and Solar Cells* **1996**, *43*, 203–222.

(29) Benazzi, E.; Mallows, J.; Summers, G. H.; Black, F. A.; Gibson, E. A. *Journal of Materials Chemistry C* **2019**, *7*, 10409–10445.

(30) Kakiage, K.; Aoyama, Y.; Yano, T.; Oya, K.; Fujisawa, J.; Hanaya, M. *Chem Communication* **2015**, *51*, 15894.

(31) Sanehira, E. M.; Marshall, A. R.; Christians, J. A.; Harvey, S. P.; Ciesielski, P. N.; Wheeler, L. M.; Schulz, P.; Lin, L. Y.; Beard, M. C.; Luther, J. M. *Science Advances* **2017**, *3*, 4204.

(32) Brown, G.; Wu, J. *Laser & Photonics Review* **2009**, *3*, 394–405.

(33) Conibeer, G. *Materials Today* **2007**, *10*, 42–50.

(34) Hashmi, G.; Miettunen, K.; Peltola, T.; Halme, J.; Asghar, I.; Aitola, K.; Toivola, M.; Lund, P. *Renewable and Sustainable Energy Reviews* **2011**, *15*, 3717–3732.

(35) Ghufran, S.; Ozkan, M.; Halme, J.; Dimic, K.; Mohammed, S.; Paltakari, J.; Grätzel, M.; Lund, P. D. *Nano Energy* **2015**, *17*, 206–215.

(36) Pagliaro, M.; Ciriminna, R.; Palmisano, G. *ChemSusChem* **2008**, *1*, 880–891.

(37) Biyik, E.; Araz, M.; Hepbasli, A.; Shahrestani, M.; Yao, R.; Shao, L.; Essah, E.; Oliveira, A. C.; Rico, E.; Luis, J.; Andrade, L.; Mendes, A.; Baver, Y. *Engineering Science and Technology, an International Journal* **2017**, *20*, 833–858.

(38) Freitag, M.; Teuscher, J.; Saygili, Y.; Zhang, X.; Giordano, F.; Liska, P.; Hua, J.; Zakeeruddin, S. M.; Moser, J.; Grätzel, M.; Hagfeldt, A. *Nature Photonics* **2017**, 1–8.

(39) Listorti, A.; O'Regan, B.; Durrant, J. R. *Chemistry of Materials* **2011**, *23*, 3381–3399.

(40) Wu, J.; Lan, Z.; Lin, J.; Huang, M.; Huang, Y.; Fan, L.; Luo, G. *Chemical Reviews* **2015**, *115*, 2136–2173.

(41) Nakade, S.; Kanzaki, T.; Kubo, W.; Kitamura, T.; Wada, Y.; Yanagida, S. *The Journal of Physical Chemistry B* **2005**, *109*, 3480–3487.

(42) Hagfeldt, A.; Boschloo, G.; Sun, L.; Kloo, L.; Pettersson, H. *Chemical Reviews* **2010**, *110*, 6595–6663.

(43) Odobel, F.; Pellegrin, Y.; Gibson, E. A.; Hagfeldt, A.; Smeigh, A. L.; Hammarström, L. *Coordination Chemistry Reviews* **2012**, *256*, 2414–2423.

(44) Datta, J.; Bhattacharya, A.; Kundu, K. K. *Bulletin of the Chemical Society of Japan* **1988**, *61*, 1735–1742.

(45) Hara, K.; Tachibana, Y.; Ohga, Y. *Solar Energy Materials and Solar Cells* **2003**, *77*, 89–103.

(46) Zhu, H.; Hagfeldt, A.; Boschloo, G. *The Journal of Physical Chemistry C* **2007**, *111*, 17455–17458.

(47) Grätzel, M. *Accounts of Chemical Research* **2009**, *42*, 1788–1798.

(48) Boschloo, G.; Hagfeldt, A. *Accounts of Chemical Research* **2009**, *42*, 1819–1826.

(49) He, J.; Lindstro, H.; Hagfeldt, A.; Lindquist, S. *Journal of Physical Chemistry B* **1999**, 8940–8943.

(50) Morandeira, A.; Boschloo, G.; Hagfeldt, A.; Hammarstro, L. *Journal of Physical Chemistry C* **2008**, *112*, 9530–9537.

(51) Le Pleux, L.; Odobel, F.; Smeigh, A. L.; Gibson, E.; Pellegrin, Y.; Blart, E.; Boschloo, G.; Hagfeldt, A.; Hammarstr, L. *Energy and Environmental Science* **2011**, 2075–2084.

(52) Qin, P.; Zhu, H.; Edvinsson, T.; Boschloo, G.; Hagfeldt, A. *Journal of the American Chemical Society* **2008**, *130*, 8570–8571.

(53) Wang, J.; Liu, K.; Ma, L.; Zhan, X. *Chemical Reviews* **2016**, 14675–14725.

(54) Chen, J.; Liang, M. *Chem. Soc. Rev* **2013**, 3453–3488.

(55) Wood, C. J.; Summers, G. H.; Gibson, E. A. *Chem Commun* **2015**, *51*, 3915–3918.

(56) Wood, C. J.; Cheng, M.; Clark, C. A.; Horvath, R.; Clark, I. P.; Hamilton, M. L.; Towrie, M.; George, M. W.; Sun, L.; Yang, X.; Gibson, E. A. *Journal of Physical Chemistry C* **2014**, *118*, 16536–16546.

(57) Zhao, S.; Song, Q. L. *RSC Advances* **2015**, 93652–93658.

(58) Zhu, L.; Bin, H.; Zhong, C.; Ming, C. *Dyes and Pigments* **2014**, *105*, 97–104.

(59) Wu, F.; Zhu, L.; Zhao, S.; Song, Q.; Yang, C. *Dyes and Pigments* **2016**, *124*, 93–100.

(60) Zhang, Q.-Q.; Jiang, K.-J.; Huang, J.-H.; Zhao, C.-W.; Zhang, L.-P.; Cui, X.-P.; Su, M.-J.; Yang, L.-M.; Song, Y.-L.; Zhou, X.-Q. *Journal of Materials Chemistry A* **2015**, *3*, 7695–7698.

(61) Ji, Z.; Natu, G.; Huang, Z.; Wu, Y. *Energy Environ. Sci.* **2011**, *4*, 2818–2821.

(62) Liu, Z.; Xiong, D.; Xu, X.; Arooj, Q.; Wang, H.; Yin, L.; Li, W.; Wu, H.; Zhao, Z.; Chen, W.; Wang, M.; Wang, F.; Cheng, Y.-B.; He, H. *ACS Applied Materials & Interfaces* **2014**, *6*, 3448–3454.

(63) Ø, Y. F.; Raissi, M.; Fihey, A.; Pellegrin, Y.; Blart, E. *ChemSusChem* **2017**, *10*, 2618–2625.

(64) Gong, J.; Sumathy, K.; Qiao, Q.; Zhou, Z. *Renewable and Sustainable Energy Reviews* **2017**, *68*, 234–246.

(65) Li, B. L.; Gibson, E. A.; Qin, P.; Boschloo, G.; Gorlov, M.; Hagfeldt, A.; Sun, L. *Advanced Materials* **2010**, 1759–1762.

(66) Qin, P.; Wiberg, J.; Gibson, E. A.; Linder, M.; Li, L.; Brinck, T.; Hagfeldt, A.; Albinsson, B.; Sun, L. *Journal of Physical Chemistry C* **2010**, *114*, 4738–4748.

(67) Nattestad, A.; Mozer, A. J.; Fischer, M. K. R.; Cheng, Y.-B.; Mishra, A.; Bäuerle, P.; Bach, U. *Nature Materials* **2009**, *9*, 31–35.

(68) Brunner, F.; Marinakis, N.; Wobill, C.; Willgert, M.; Ertl, C. D.; Kosmalski, T.; Neuburger, M.; Bozic-Weber, B.; Glatzel, T.; Constable, E. C.; Housecroft, C. E. *Journal of Materials Chemistry C* **2016**, *4*, 9823–9833.

(69) Cui, J.; Lu, J.; Xu, X.; Cao, K.; Wang, Z.; Alemu, G.; Yuang, H.; Shen, Y.; Xu, J.; Cheng, Y.; Wang, M. *The Journal of Physical Chemistry C* **2014**, *118*, 16433–16440.

(70) Ladomenou, K.; Kitsopoulos, T. N.; Sharma, G. D.; Coutsolelos, A. G. *RSC Adv.* **2014**, *4*, 21379–21404.

(71) Zhang, L.; Cole, J. M. *ACS Applied Materials & Interfaces* **2015**, *7*, 3427–3455.

(72) Wei, L.; Yang, Y.; Wang, P. *RSC Advances* **2016**, *6*, 39972–39981.

(73) Alemu, G.; Cui, J.; Cao, K.; Li, J.; Shen, Y.; Wang, M. *RSC Advances* **2014**, *2*, 51374–51380.

Part II

Small-Molecule BODIPYs for p-type DSC

Chapter 2

Design and Synthesis of Red-Shifted BODIPY Dyes for p-type DSC

2.1 Aims

Building on previous work on BODIPY based sensitizers for p-type DSSC, two new dyes (BOD2 and BOD3) were synthesised to complete a new small molecule BODIPY series alongside previously published dye BOD1 which showed promising results when incorporated in a p-DSSC. By introducing small structural changes to the chromophore, wider implications of these changes can be studied using steady-state spectroscopy and differences in performance in a p-DSSC can be evaluated.

2.2 Introduction

BODIPY DSSC

4,4'-difluoro-4-bora-3a,4a-diaza-s-indacene dyes - referred to in this thesis as BODIPY (Figure 2.1) sensitizers are a class of organic heterocycles characterised by the boron chelated centre and pyrrolic units. These dyes have received wide attention in many areas of research and are used routinely in a range of applications.[12] The popularity of this class of dyes stems from their interesting photophysical properties (high absorption coeffi-

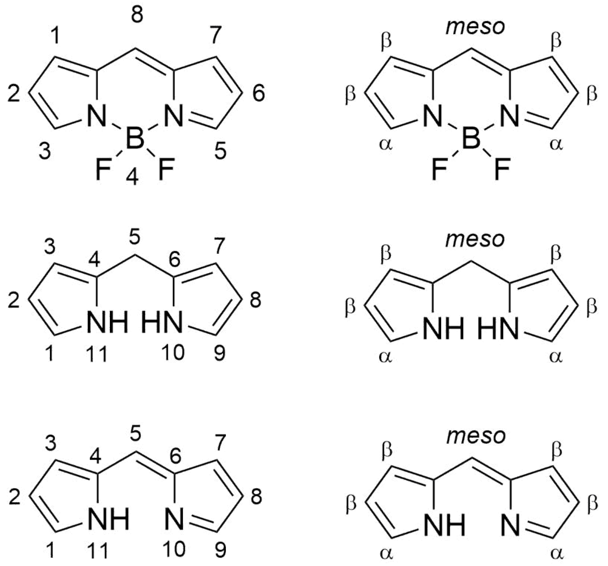

Figure 2.1: Structure of the BODIPY core (top) with IUPAC (left) and standard numbering systems (right), with two common synthetic precursors (dipyrromethane (middle) and dipyrromethene (bottom)). These numbering systems will be used throughout this thesis.

cients and fluoresence quantum yields) coupled with the ease of synthetic availability and versatility of synthetic methodologies available to fine tune the absorption and emission profiles.

The method for the synthesis of of the BODIPY core has not varied much from the initial publication by Triebs and co-workers.[3] Typically the BODIPY core is synthesized via condensation of two pyrroles with an aldehyde, acid choride or anhydride, mediated by the addition of catalytic amounts of acid, to form the dipyrromethene frame of the chromophore (Figure 2.2).[4] Reactions with an acid chloride or anhydride proceed directly to the dipyrromethene, whereas condensations around an aldehyde produce an intermediate dipyrromethane, requiring oxidation (usually by DDQ or p-chloranil) to form the dipyrromethene core. Complexation of the dipyrromethene with $BF_3.Et_2O$ in the presence of a base (typically a tertiary amine) yields the symmetric F-BODIPY.[5] The work demonstrated in this thesis uses synthetic procedures based on the condensation of aldehydes and pyrroles however it is important to highlight the huge variety of methods available in the synthetic library of BODIPY.

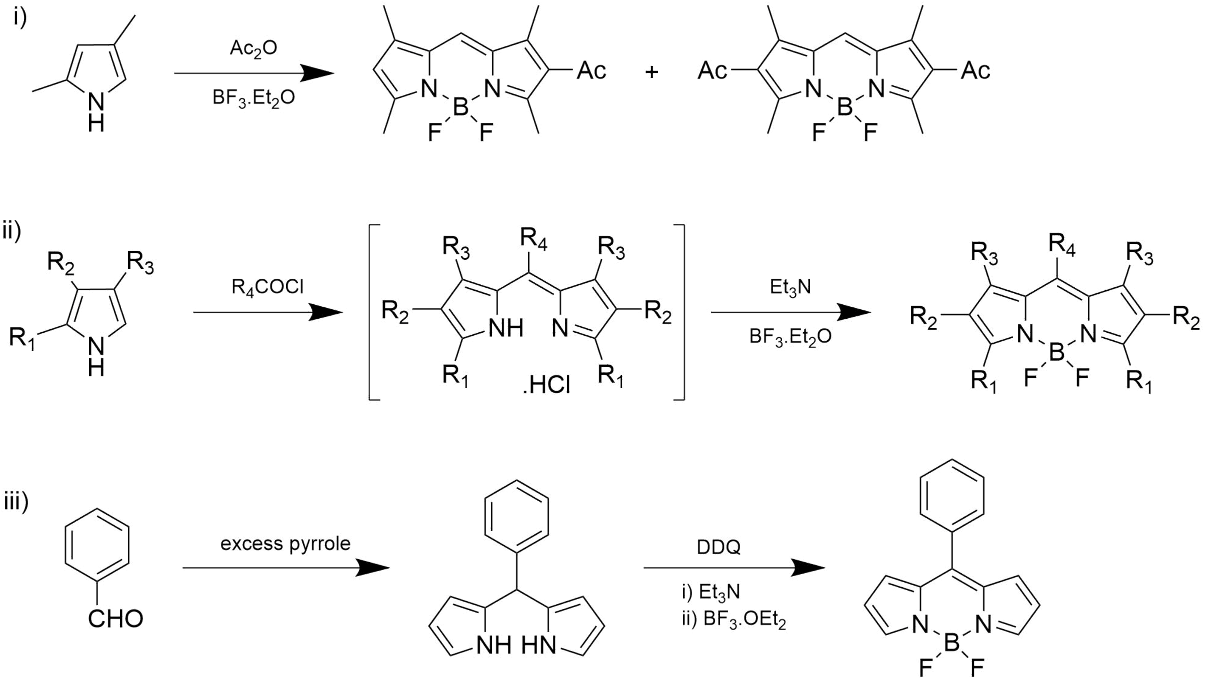

Figure 2.2: The main synthetic strategies towards BODIPY dyes. i) acid anhydride, ii) acid chloride iii) aldehyde

BODIPY Synthesis from aldehydes and pyrroles

One of the most popular methods of BODIPY synthesis via an aldehyde and pyrrole was developed from work on the synthesis of meso-porphyrins by Lindsey (Figure 2.3).[6] Briefly, an aldehyde can be subjected to acid catalysed condensation with two equivalents of α-substituted pyrrole to form the corresponding dipyrromethane in good yields.Subsequently, the dipyrromethane can be oxidised (with p-chloranil or DDQ) before chelation around the boron centre (typically with $BF_3.OEt_2$ boron trifluoride diethyletherate) mediated by an amine base (Et_3N, $^iPr_2NEt$) to form the symmetrical BODIPY dye. This method was designed around the use of α-substituted pyrroles, preventing higher orders of condensation and the formation of higher oligomeric structures, such as porphyrins.[7] The formation α-unsubstituted BODIPYs via the same method from an aldehyde and unsubstituted pyrrole results in extremely poor yields of the dipyrromethane. Lindsey offers an adapted "solventless" synthesis, whereby the reaction is carried out in a large excess of pyrrole and uses the pyrrole as a reaction medium for the condensation to occur. This high

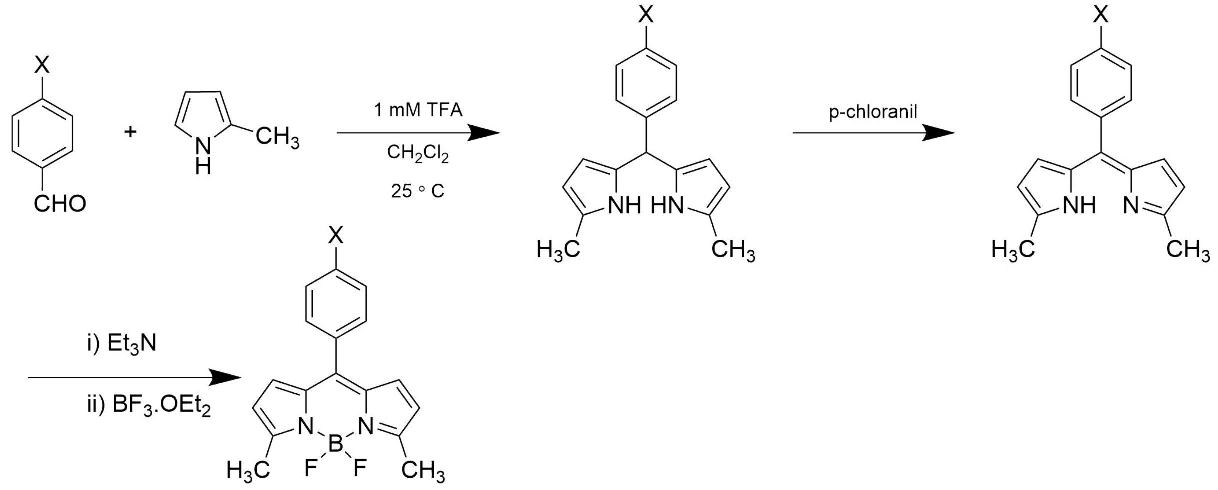

Figure 2.3: Formation of α-substituted BODIPY by Lindsey

dilution method ensures the formation of the higher oligomers during the reaction is minimised, before the symmetrical F-BODIPY is formed via complexation around the boron centre.[6] Dehaen further modified this reaction towards α-unsubstituted BODIPYs using near stoichiometric quantities of pyrrole and aldehyde and using water as the reaction medium.[8] This "greener" synthetic pathway has distinct benefits over the Lindsey method as over condensation is reduced due to selective precipitation of the dipyrromethane in the aqueous reaction medium, and smaller equivalents of pyrrole are required, with generally extremely high yields. One drawback of this method is the restricted range of aldehydes compatible with this reaction, limited to aryl-aldehydes. BODIPYs are stable to a wide range of chemical environments and are suitably reactive to undergo functionalization of the BODIPY core via a wide variety of substitution reactions. Introduction of synthetic handles onto the core opens up even more possible reactions to further derivatise the chromophore. Many articles have covered this subject, with more publications every year adding to the library of possible modifications to the BODIPY core.[19]

Synthesis of BODIPY dyes from pyrrole and aldehyde requires a free α-position on the heterocycle to undergo the acid catalysed condensation to the dipyrromethane intermediate. Blocking the other positions of the pyrrole ring generally increases the yields for the corresponding dipyrromethane. This can be attrituted to the inability of these substituted pyrroles to undergo side reactions and polymerizations during the reaction. The substitutions also have a dramatic effect on the photophysical and electrochemical properties of the BODIPY chromophore. Inspecting the reactions of unsubstituted pyrrole, 2,4-dimethyl pyrrole and 2,4-dimethyl-3-ethyl pyrrole into the corresponding BODIPY, it has been shown that increasing the number of aliphatic groups around the core induces a bathochronic shift in both absorbance and emission.[10] The fully substituted BODIPY also shows fully reversible Nernstian one-electron oxidation and reduction, with stable intermediate radical ions.[1011] An absence of substitution at positions 2,3,5 or 6 causes instability of the radical ions produced upon oxidation or reduction. Absence of substitution at position 8 (meso-) causes the radical anion produced upon reduction to be more reactive then its meso-substituted counterpart.[12] Both of these processes lead to rapid, irreversible redox processes at the BODIPY core.

BODIPY in DSSC

BODIPY dyes have been incorporated infrequently into n-type DSSC with moderate success, reaching PCE's of over 6%.[13] The first BODIPY photosensitizers reported for an n-type system were produced by Fukuzumi and co-workers, (Fig. 2.4, top) producing a PCE of 0.16 and 0.13 % respectively.[14]

More recently, Kubo and coworkers published a "butterfly" shaped BODIPY sensitizer series with PCE values up to 6.05%, noting that, in this work impressive performances came without an arylamine or carbazole based donor. The high J_{SC} values were attributed to the high light harvesting capabilities of these systems.[15] Research into BODIPY sensitizers for p-type systems is more limited, despite the versitile synthetic routes and tuneable absorption profile of this class of dyes are ideal for integration into tandem devices (ie. to optically match the photoanode).

Lefebvre and co-workers replaced the cyanovineline acceptor groups of P1 with BODIPY groups. The change in structure yielded an increase in absorption coefficient (P1; ϵ - 58 000 $dm^3mol^{-1}cm^{-1}$, P1-BOD; $\epsilon = 112\ 000\ dm^3mol^{-1}cm^{-1}$). There modifications also yielded a longer lived charge separated state when immobilized onto NiO (P1-BOD|NiO; $\tau = 180$ ns) in comparison to P1|NiO ($\tau = 200$ ps). The performance of the p-type devices

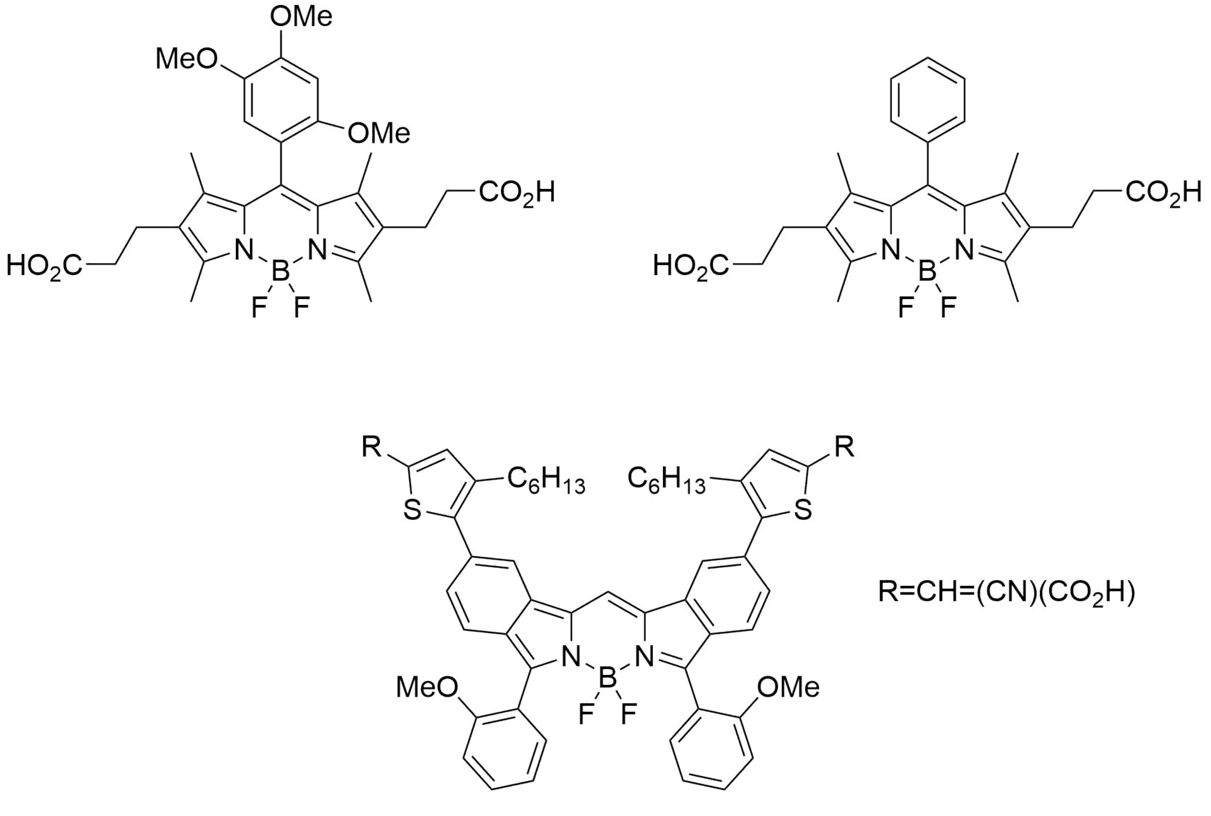

Figure 2.4: Structures of the two dyes published by Fukuzumi first incorporated into an n-type photoanode (top); Structure of the highest performance "butterfly" BODIPY by Kubo (bottom)

fabricated from P1-BOD were lower than that of P1 (P1-BOD; J_{SC} = 3.15 mA cm^{-1}, IPCE = 28%; P1; J_{SC} = 5.48 mA cm^{-1}, IPCE = 64%). Theoretical and experimental evidence suggested that the poor performance was due to poor electronic coupling between the BODIPY acceptors and the thiophene linkers caused by the aliphatic substituents in the 1,7 positions restricting rotation around the thiophene.

Summers later went on to synthesize a series of BODIPY sensitizers with two BODIPY acceptors with unsubstituted β-pyrrolic positions. The lack of substitution in the 1,7 positions allowed for unhindered rotation around the meso-substituent. GS1 showed increased photocurrent density when compared to P1-BOD (GS1; J_{SC} = 5.87 mA cm^{-1}, P1-BOD; J_{SC} = 3.15 mA cm^{-1}) which was accredited to improved electronic communication with the NiO. Upon further inspection of the device parameters and structures, the simple dye BOD1 performed similarly to more complicated TPA based donor-acceptor dyes (BOD1; J_{SC} = 1.48 mA cm^{-1}, 4; J_{SC} = 1.60 mA cm^{-1}, 6; 1.58 mA cm^{-1}).

Previous studies on BOD1

The BODIPY class of chromophores remains relatively unexplored in the field of p-DSSC. Previous studies have shown that even simple BODIPY dyes can achieve modest efficiencies. Summers highlighted the importance of good electronic communication between the dye and the semiconductor surface in order for high charge transfer efficiency and communication through the photocathode.

BOD1 performed well despite the simplicity of the dye (**BOD1**; J_{SC} = 1.48 mA cm^{-1}, **4**; J_{SC} = 1.60 mA cm^{-1}, **6**; 1.58 mA cm^{-1}), however inspection of the dye structure and properties shows that the structure is far from ideal for use as a sensitizer for p-type photocathodes,

Computational studies on BOD1 and other BODIPY dyes from this series investigated the dihedral angle between the BODIPY core and the aryl anchor group. Dihedral angles of 90^o give rise to a perpendicular configuration across the C2 axis between the BODIPY core and the anchor group, meaning there would be limited orbital overlap and the core

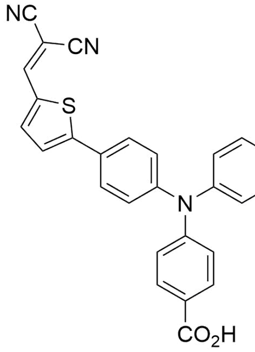

P1

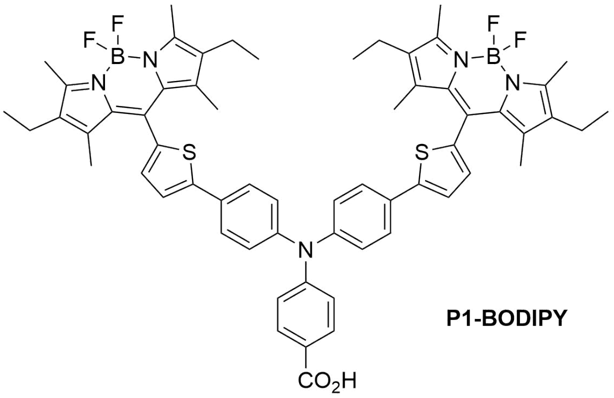

P1-BODIPY

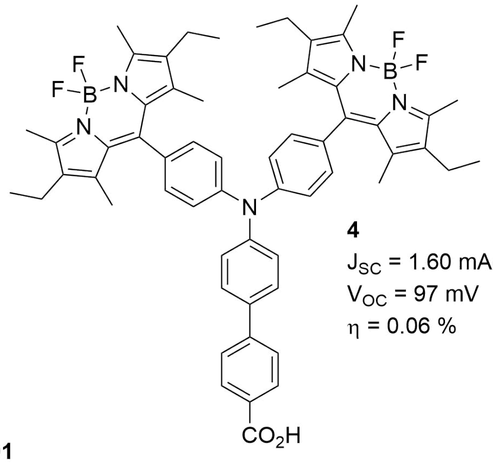

4
J_{SC} = 1.60 mAcm^{-2}
V_{OC} = 97 mV
η = 0.06 %

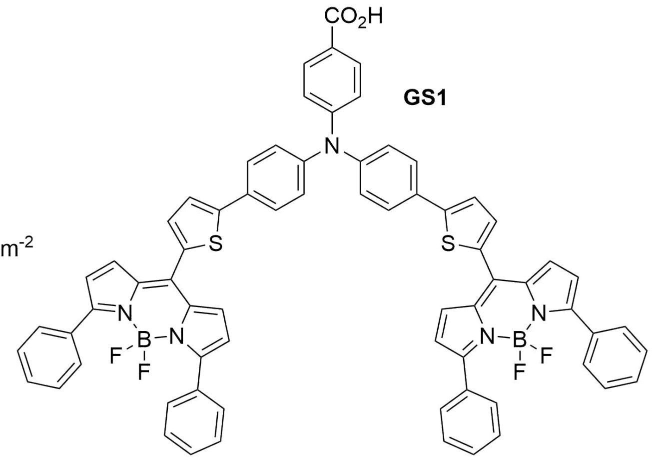

GS1

BOD1
J_{SC} = 1.48 mAcm^{-2}
V_{OC} = 95 mV
η = 0.05 %

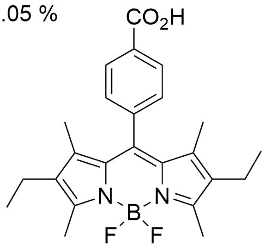

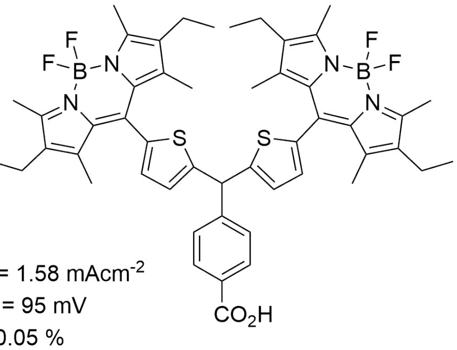

6
J_{SC} = 1.58 mAcm^{-2}
V_{OC} = 95 mV
η = 0.05 %

Figure 2.5: Structures of the P1 and P1-BODIPY studied by Lefebvre (top) and BODIPY dyes studied by Summers (bottom)

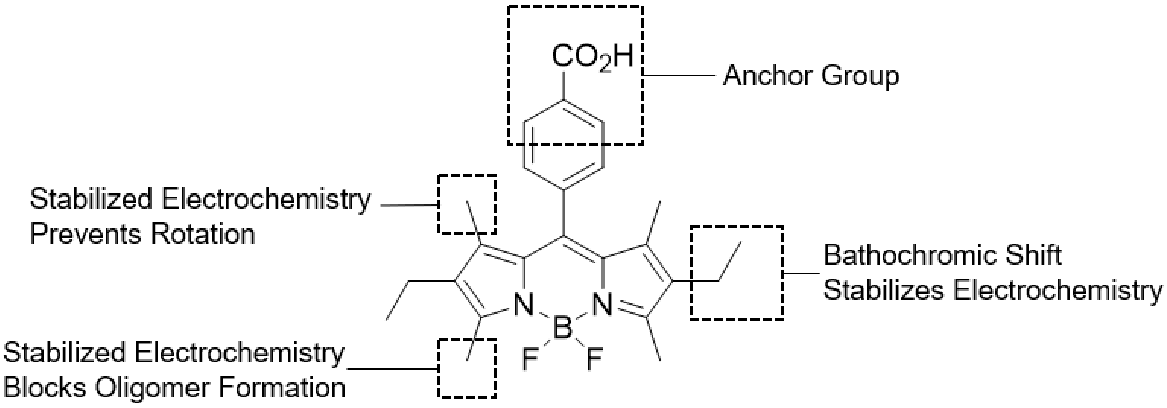

Figure 2.6: Structural features of BOD1

of the chromophore would be electronically decoupled from the semiconductor surface. A dihedral angle of 0^o places the phenyl ring of the anchor group co-planar with the BODIPY core giving the maximum electronic coupling between the chromophore and the semiconductor.

BOD1 was shown to have a dihedral angle of 90^o and was decoupled from the semiconductor. The methyl substituents at the 1,7 positions, although small, prevent rotation around the C2 axis. It was shown that removing the alkyl substituents or reducing the size of the aryl ring helps the BODIPY adopt a more planar conformation and increases the electronic communication through the dye.

Although BOD1 possessed favourable electrochemical properties, the absorbance profile (λ_{max} = 528 nm (CH_2Cl_2)) is not positioned to minimise spectral overlap in a tandem DSSC.

Synthetic Targets

The BODIPY core is robust to a wide range of reaction conditions and as such there is a wide variety of possible modifications available to the core. The introduction of halides onto the BODIPY core is a well established route to further derivitization. Regioselective halogenation can be carried out on either the 2,6- or the 3,5- positions, widening the scope of possible reactions to modify the core to include various substitutions and palladium catalyzed coupling reactions.[16–18] Hence, introduction of aromatic groups, directly coupled to the core can be achieved, increasing the π-conjugation of the system and generally resulting in a bathochromic shift in absoption. Two novel dye architectures have been synthesised for testing in a working p-type device to investigate how small structural changes to a simple chromophore affects the photochysical and electrochemical properties of the dye and investigating how these properties effect the output parameters of the working device. BOD2 (Figure 2.7) is based on the best performing dye in the series produced by Summers (GS1). The dihedral angle between the BODIPY core and the anchor group was significantly improved, leading to improved electronic communication with the semiconductor. Significant broadening of absorbance and emission profiles were observed when compared to the usual sharp electronic transitions found commonly in BODIPY dyes. This broadening is favourable for use in a DSSC to maximise light harvesting over a larger portion of the solar spectrum. However the bathochomic shift in absorbance by extension of the π-system was not as significant as expected, and the chromophore did not absorb in the red/NIR region of the solar spectrum. Ideally a sensitizer for p-type DSSC absorbs at a complimentary wavelength to that of the n-type photoanode in an ideal pn-tandem DSSC. In 1999, Burgess reported the first example of a tetradentate N,N,O,O BODIPY, where the BODIPY F atoms are displaced by intramolecular nucleophillic substitution from oxygen in the phenol groups, resulting in a chiral septacyclic BODIPY (BOD3, Figure 2.7) with a significant bathochromic shift in absorbance and emission.[19] Addition of the benzoic acid group in the meso position allows for the dye to bind to the NiO semiconductor for use in a DSSC. This method has been adapted and modified to produce a wide range of red abosrbing/NIR BODIPYs.[20–23]

By investigating the two dyes BOD2 and BOD3 (Figure 2.7), the structural modifications to two simple dye structures can be investigated and compared to existing values in the literature of a previously prepared BODIPY sensitizer (BOD1).

α-substituted BODIPYs

When designing dyes for p-type DSSC, stabilization of the chromophore during synthesis should be considered. Stabilization of the dye upon reduction is required to align with

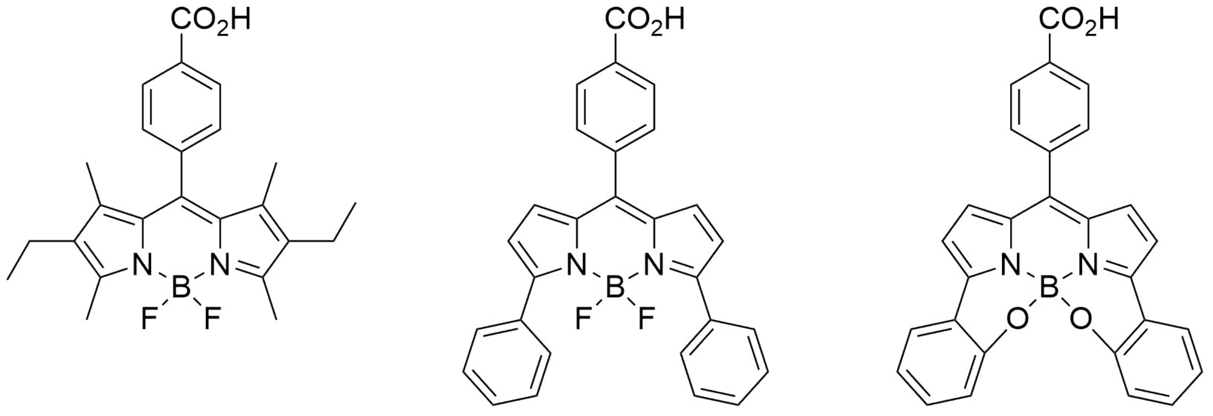

BOD1 **BOD2** **BOD3**

Figure 2.7: Synthetic Targets BOD1-3

the working principles of the device. Substitution at the α-position of the pyrrole has a two-fold benefit in this system. Modifying the pyrrole in this way blocks the formation of oligopyrroles, porphyrins and other higher condensed products during the acid catalysed condensation to form the dipyrromethane.[6] The radical ions formed upon charge transfer from the NiO semiconductor into the HOMO of the dye during photoinduced electron transfer are also stablilized by α-substitution of the BODIPY core. These radical cations when formed on an unsubstitited BODIPY core can lead to dimerization or substitution reactions upon reduction or oxidation as radical ions of unsubstituted BODIPY are known to be highly reactive.[12]

Many synthetic routes to α-BODIPYs have been published, mainly categorized into two synthetic strategies. Modification of a pyrrole before subjecting the mono-substituted pyrrole to condensation with aldehyde, or synthesis of the BODIPY core followed by modification post-complexation with BF_2.

Palladium cross-coupling remains one of the most useful tools in order to introduce C-C bonds in organic molecules. BODIPY dyes are no exception to this and many examples of these couplings on BODIPY can be found in literature including Suzuki–Miyaura[24–26] , Migita–Kosugi–Stille[23,24,27,28] , Mizoroki–Heck[23,24] and Sonogashira.[23,24,29,30] More recently Negishi couplings have also been reported in the 3,5 positions, expanding the library of

α-BODIPY further.[31]

Position	Reaction	Reagents	References
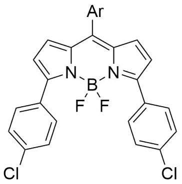	Suzuki–Miyaura	$Pd(PPh_3)_4$ / $ClC_6H_4B(OH)_2$	[24–26]
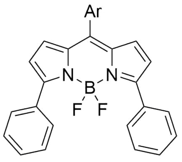	Migita–Kosugi–Stille	$Pd(PPh_3)_4$ / $Sn(Ph)_4$	[23,27,28]
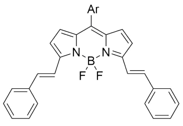	Mizoroki–Heck	Pd^{II} / PPh_3 / $C_6H_5C_2H_3$	[23,24]
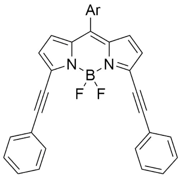	Sonogashira	$Pd(OAc)_2$ / PPh_3 / CuI / C_6H_5CCH	[23,24,29,30]
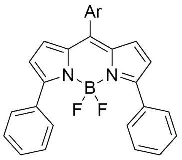	Negishi	PhZnBr / $Pd(PPh_3)_2Cl_2$	[31]

Table 2.1: Palladium catalyzed cross coupling reactions on 3,5 BODIPY, table adapted from Clarke et. al.[9]

The introduction of halides to the BODIPY core has been documented in many articles. Jiao reported an elegant study on the regioselectivity of the electrophillic aromatic substitution of the BODIPY core when subjected to varied equivalents of bromine (Figure 2.8).[17]

Briefly, stepwise regioselective bromination occurs preferentially on the 2,6 positions as they bear the least positive charge. Following this, increasing the equivalents of Br_2 yielded the tetrabromoBODIPY with substitution occurring at the α-positions (the tribromoBODIPY was seen on TLC but not isolated from the reaction mixture). A large excess of Br_2 (300 eq.) was required to form the hexabromoBODIPY.

Preferential substitution on the 3,5-positions can be achieved by electrophillic aromatic

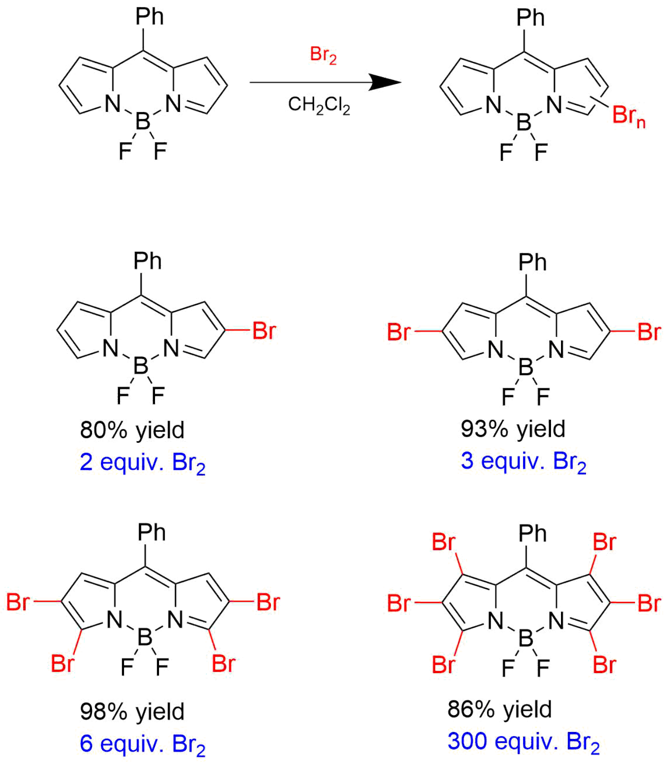

Figure 2.8: Jiao bromination BODIPY diagram

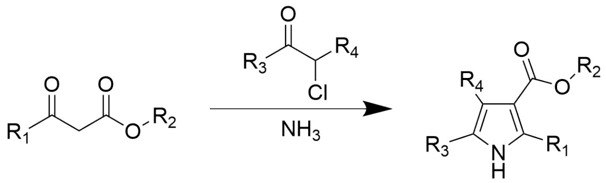

Figure 2.9: Overview of the Hantzch pyrrole synthesis

substitution reactions with N-halogen succinimide reagents (NCS, NBS, NIS) with the dipyrromethane precursor to the BODIPY as reported by Dehaen. Acting similarly to the pyrrole precursor, dipyrromethanes readily undergo electrophillic aromatic substitution reactions (SEAr) at the two α-positions and can be oxidised and coordinated around BF_2 to form the corresponding α,α-BODIPY.[32] A similar method has also been adapted for α,α-bromoBODIPYs.[33,34] Functionalized pyrroles are a deeply rich and diverse class of compounds, used for a wide variety of purposes. Commonly, multicomponent reactions (MCR) have been applied to form the desired heterocycles.

First noted in 1890, the Hantzsch pyrrole synthesis (Figure 2.9) began by reaction of "an equimolecular mixture of chloroacetone and aceto-acetic ester under reflux in concentrated aqueous ammonia" to afford the pyrrole derivative. Although recent developments have seen a wide range of pyrrole derivatives produced by MCRs, the complexity of this approach was not suitable for formation of mono-substituted pyrroles. Mono-substitution of pyrrole can be undertaken in various ways, the complexity of the synthesis and method being determined by the complexity of the pyrrole required.

2.3 Synthesis

The synthesis of BOD2 is based on synthesis of α-BODIPY based donor-acceptor dye GS1, which provides a facile synthetic route to α-BODIPY's with few reaction steps.[35] Briefly, this method is based on the direct arylation of a N-heteroarene developed by Yu et. al. (Fig 2.12), whereby a diaryliodinium salt is heated with pyrrole (using pyrrole as the solvent) to form the substituted arylpyrrole **2-3**.[36] Mechanistic studies carried out propose this arylation as a phenyl radical substitution pathway by decomposition of the diaryliodinium salt. The mono-substituted pyrrole can then be used as the pyrrollic starting material for condensation with an aryl aldehyde to form the dipyrromethane core of BOD2. Upon oxidation with DDQ or p-chloranil, deprotonation with $^{i}Pr_2NEt$ and complexation with $BF_3.OEt_2$ to introduce the boron core, the final BODIPY dye can be .

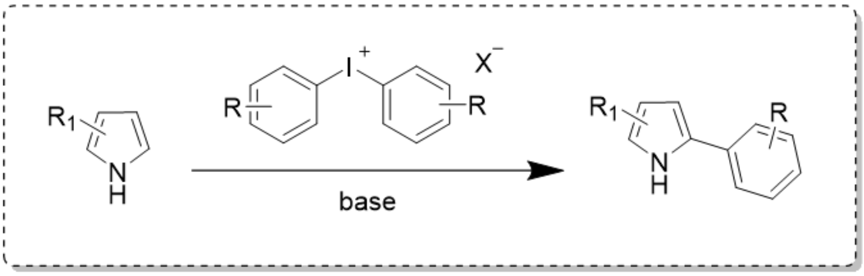

Figure 2.10: C2 Arylation of pyrrole with diaryliodinium salt

The diaryliodinium salt was prepared in a one-pot reaction as outlined by Olofsson et. al.[37] (Fig. 2.13) Iodobenzene **2-1** was coupled to benzene via the oxidation of **2-1** with 3-chloroperbenzoic acid into a reactive iodine (III) species, followed by ligand exchange with benzene. This reaction is mediated by trifluoromethanesulfonic acid and forms the di-phenyl iodinium triflate salt **2-2** in high yields.

2-2 was further reacted with pyrrole under basic conditions, forming the α-subsituted pyrrole **2-3**.

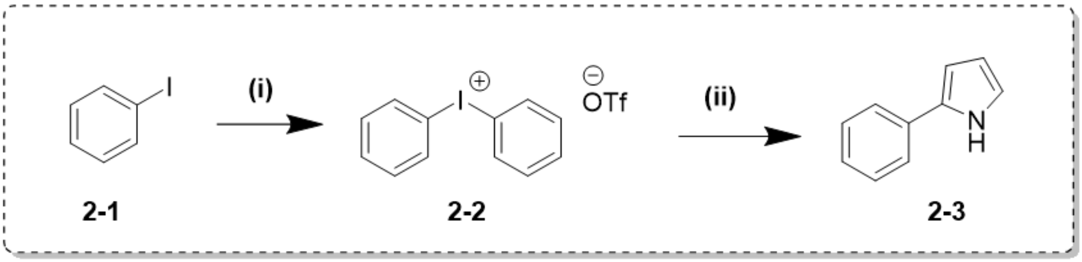

Figure 2.11: Reagents and conditions: (i) (a) mCPBA, benzene, CH_2Cl_2; (b) CF_3SO_3H (52 %); (ii) NaOH, pyrrole (65 %)

The arylpyrrole **2-3** was then condensed around an aromatic aldehyde (4-carboxy benzaldehyde) to form the intermediate dipyrromethane. This step also introduced a benzoic acid anchoring group to be used as the linker between the chromophore and the p-type semiconductor. The dipyrromethane was oxidised with p-chloranil to form the dipyrrin, before deprotonation of the remaining pyrrolic N-H proton by diisopropylethylamine (^{i}PrNEt$_2$) and insertion of the boron core using borontrifluoride diethyletherate ($BF_3.OEt_2$) to introduce the BF_2 motif into the BODIPY **BOD2**. The final three steps from arylpyrrole to BODIPY were carried out as a one-pot reaction, a common strategy for BODIPY synthesis due to the instability of many of the intermediates formed in the reaction. BOD2 was formed in moderate yields, although the unsubstituted beta-positions on the BODIPY core can be prone to side reactions during the synthesis, thus lowering the yield. The introduction of the carboxylic acid moiety and subsequent drop in solubility in common organic solvents can also be speculated as a cause for the reduced yields over the three steps.

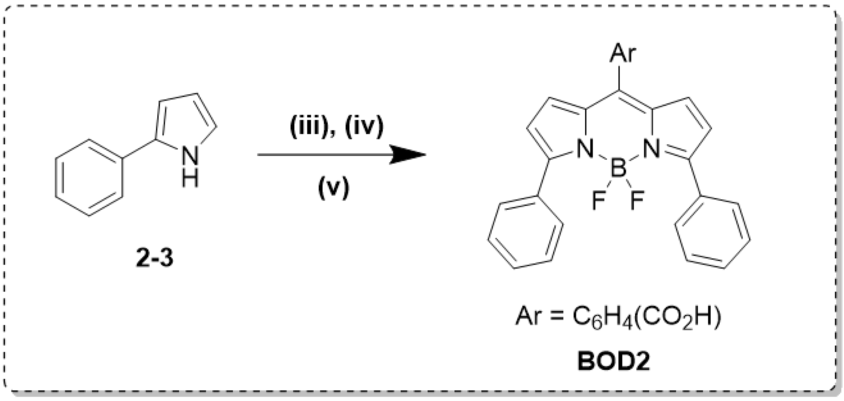

Figure 2.12: Reagents and conditions: (iii) 4-carboxybenzaldehyde, CH_2Cl_2, $C_2HF_3O_2$; (iv) p-chloranil; (v) ${}^iPr_2NEt$, $BF_3.Et_2O$ (16 %)

The synthesis of **BOD3** was initially attempted based on synthetic work by Burgess[8,19] and the modifications by Alnoman.[34] A general reaction scheme is outlined in Fig. 2.13.

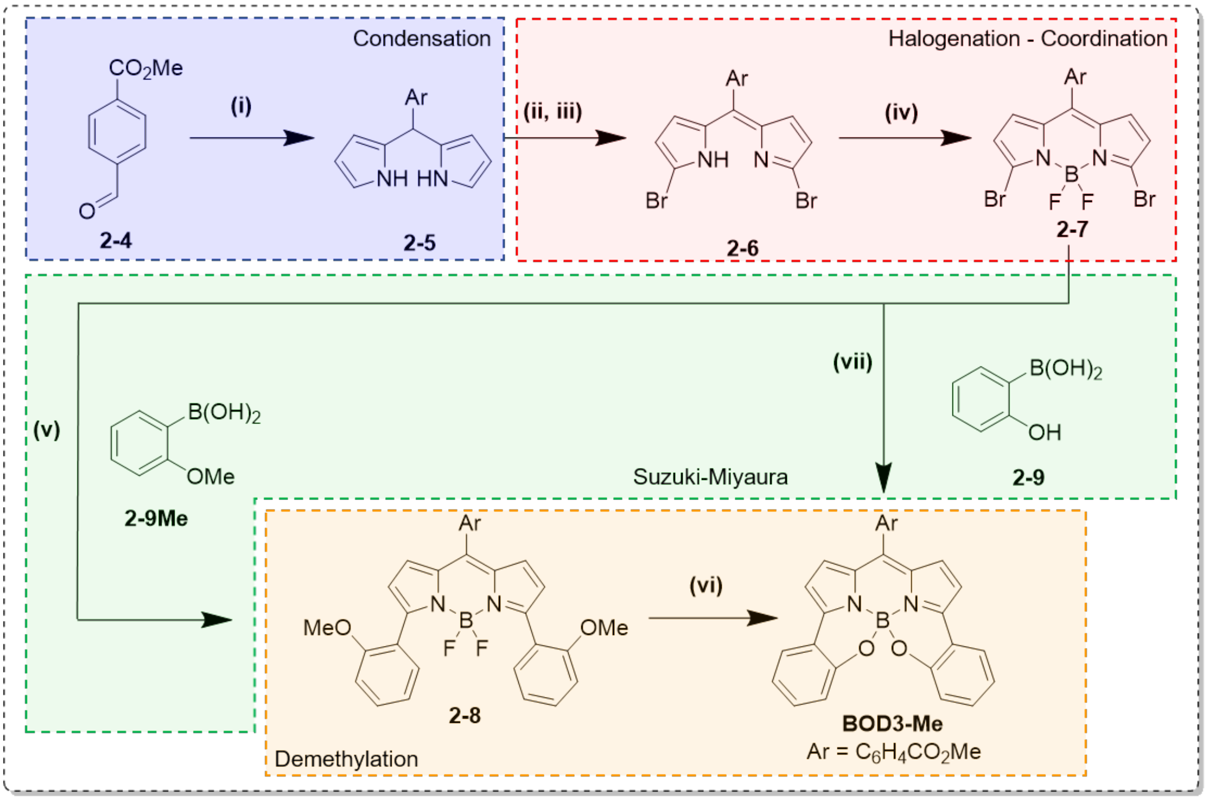

Figure 2.13: Overview of two synthetic routes to NP-01-05a

Methyl-4-formyl benzoate **2-4** underwent condensation around two unsubsitituted pyrrole molecules via an acid catalysed condensation with [0.18M] hydrochloric acid in aqueous

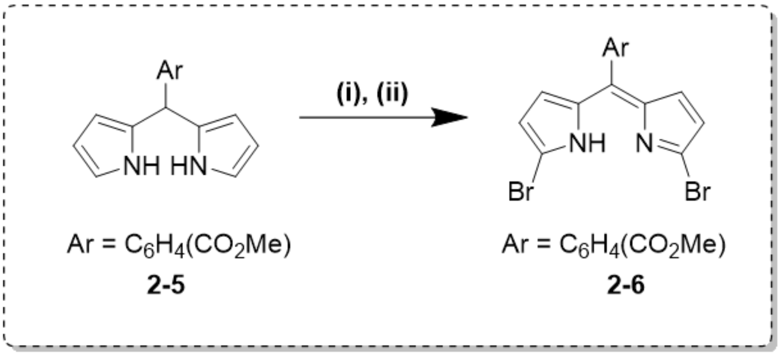

Figure 2.15: Reagents and conditions: (ii) NBS, THF, -78 ^{o}C, 1h; (iii) DDQ, -78 ^{o}C to rt, 30 min (51 %)

media. The resulting dipyrromethane **2-5** precipitated from the reaction upon formation, acting as a thermodynamic sink in the reaction, resulting in a high yield, high purity and facile synthetic route to this dipyrromethane by eliminating the possibility of higher oligopyrromethanes or porphyrins from forming in the reaction.

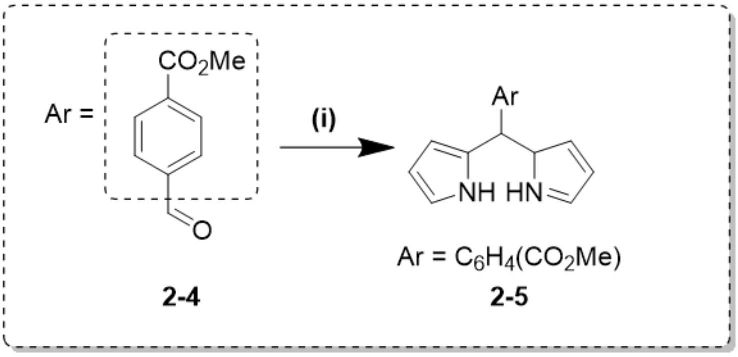

Figure 2.14: Reagents and conditions: (i) pyrrole, $HCl_{(aq)}$ [0.18]M, rt, 4h, (84 %)

The dihalogenated dipyrromethane **2-6** was formed by regioleslective bromination with N-bromo succinimide at -78 ^{o}C. The decrease in temperature was to disfavour multiple subsequent bromination reactions at the other pyrrolic positions that are succeptible to nucleophillic aromatic substitution. Even with the decreased temperature the reaction remained time sensitive and the yields of the reaction varied between reactions.

This halogenated dipyrromethane can be purified, however it is generally unstable to the acidic conditions found in silica based column chromatography, and so the next two steps were carried out in a one pot method. The first oxidation was performed with DDQ to

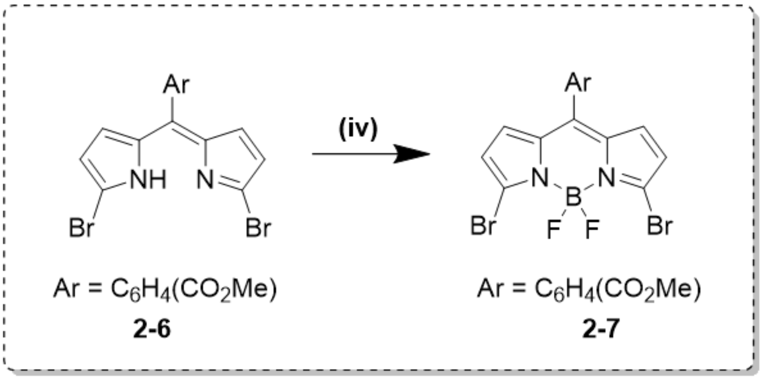

Figure 2.16: Reagents and conditions: (iv) ${}^{i}Pr_2NEt$, $BF_3.OEt_2$, CH_2Cl_2, 1h (77 %)

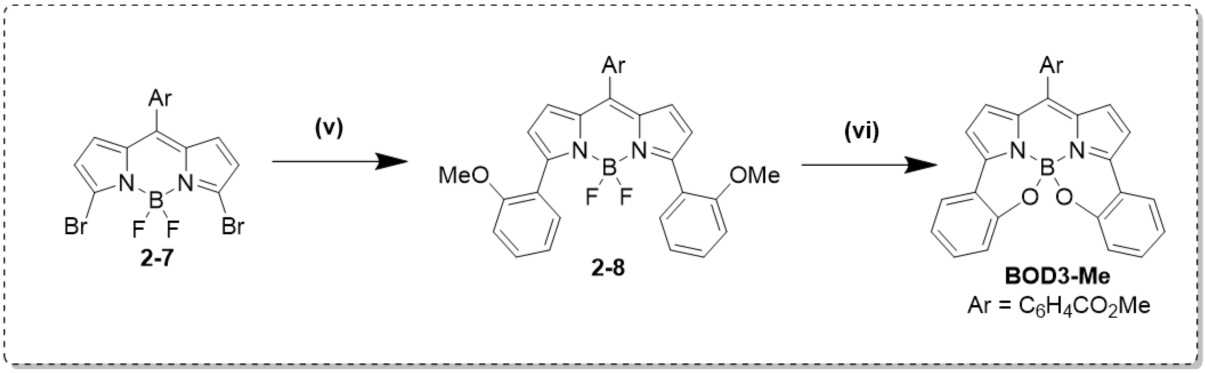

Figure 2.17: Reagents and conditions: (v) 2-methoxyphenyl boronic acid, $Pd(PPh_3)_4$ (5 mol %), K_3PO_4, toluene, 1,4-dioxane, 90 ^{o}C, 1 h 30 min (77 %); (vi) BBr_3, CH_2Cl_2, 0 ^{o}C, quantative

form the Br−2-dipyrromethene **2-6** followed by deprotonation of the remaining pyrrolic N-H proton with ${}^{i}Pr_2NEt$. Once deprotonated the dipyrromethene anion was chelated around the boron centre with $BF_3.OEt_2$ to form the Br_2-BODIPY **2-7**

Following the original procedure outlined by Burgess,[19] the 3,5 dihalogenated BODIPY was subjected to Suzuki coupling with 2-methoxyphenylboronic acid (**2-9Me**. Tetrakis(triphenylphosphine)palladium(0) was used as the catalyst at 5 mol% catalyst loading. K_3PO_4 was used to form the boronate complex in situ. The aryl ether BODIPY **2-8** was formed as a deep purple solid. Treatment with BBr_3 caused demethylation of the aryl ether substituents to the phenol groups, followed by an intramolecular cyclization. Displacement of the fluorines by the phenolic -OH groups on the α-positions on BODIPY formed the septacyclic **BOD3-Me**.

The Suzuki reaction was performed again substituting 2-hydroxyphenylboronic acid in

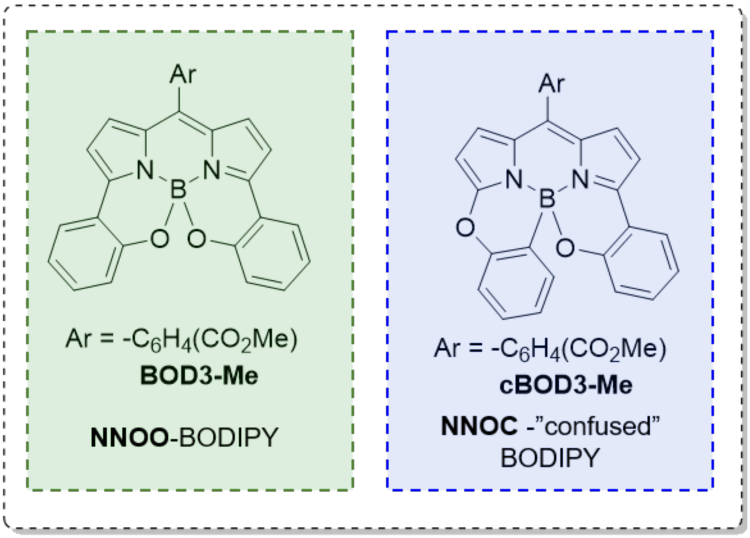

Figure 2.18: Structures of the two structural isomers isolated from the Suzuki coupling reaction, **BOD3-Me** and the "confused" **cBOD3-Me**

place of 2-methoxyphenyl boronic acid as the substrate to undergo coupling to the α-positions of the BODIPY core. This method has the benefit of removing the requirement for demethylation of **2-8** and instead forming **BOD3-Me** directly from the coupling reaction. BODIPY **2-7** was subjected to Suzuki coupling under the same conditions, bar the boronic acid used. This method leads to the formation of two structural isomers. Clarke et. al. has previously isolated and characterised the "confused" N,N,O,C-septacyclic BODIPY **cBOD3-Me**.[38] They postulate that these molecules may be formed via nucleophillic aromatic substitution of the halide by the phenol group, followed by the Suzuki coupling on the unreacted halide on the second α-position. The first nucleophillic substitution reaction appears to be in competition with the palladium coupling reaction and as such the reaction produces a mixture of the two isomers **BOD3-Me** and **cBOD3-Me**.

Hydrolysis of the methyl ester in the meso- position of **BOD3-Me** under basic conditions (NaOH in methanol) were repeatedly unsuccessful, therefore other synthetic routes to the final BODIPY chromophore were examined. **BOD3** can also be formed via functionalization of a pyrrole followed by formation of the BODIPY core, to introduce and α-phenol groups before the condensation reaction to form the dipyrromethane.

Following literature procedures, pyrrole was regioselectively brominated and immediately

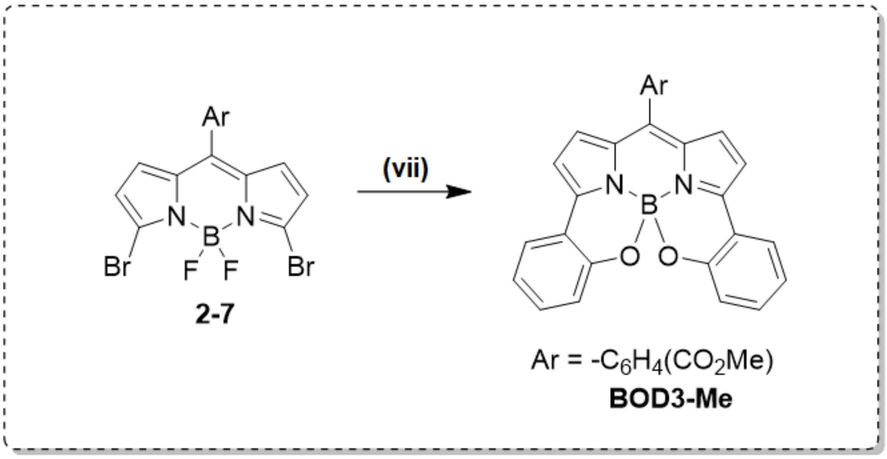

Figure 2.19: Reagents and conditions: (vii) 2-hydroxyphenyl boronic acid, $Pd(PPh_3)_4$ (5 mol %), K_3PO_4, toluene, 1,4-dioxane, 90 ^{o}C, 1 h 30 min (53 %)

protected with a boc group, to increase stability to form N-boc-2-bromo pyrrole (**2-10**) in good yields (68%). The bromo-pyrrole (**2-10**) was then coupled to 2-hydroxyphenyl boronic acid (**2-9**), and the product underwent an intramolecular cyclization to form cyclic carbamate **2-11**. The carbamate ring was then opened under mild hydrolysis conditions to yield the mono-functionalized pyrrole **2-12**. Changing the functional groups on the pyrrole and the phenyl ring, by using 2-bromophenol **2-13** and N-boc-pyrrole-2-boronic acid **2-14** as the catalysis reagents, the reaction occurred in the same way, however the intermediate carbamate **2-11** was only formed in small quantities and the major product is the ring opened functionalized pyrrole **2-12**. Due to the loss of the boc- protecting group it can be assumed that the carbamate formation and subsequent hydrolysis happens in situ.

2-bromophenol (**2-13**) and N-boc-pyrrole-2-boronic acid (**2-14**) underwent a palladium catalyzed Suzuki coupling reaction mediated by Pd(XPhos) with K_3PO_4 being used as the inorganic base. As previously mentioned the major product was the mono-substituted pyrrole **2-12** in good yields and with the two-fold benefit of direct synthesis of **2-12** without the need for further deprotection reactions.

Following literature procedures, **BOD1** was synthesized via a standard one-pot condensation of 4-carboxybenzaldehye and 2,4-dimethyl-3-ethyl pyrrole (**2-15**) with trifluo-

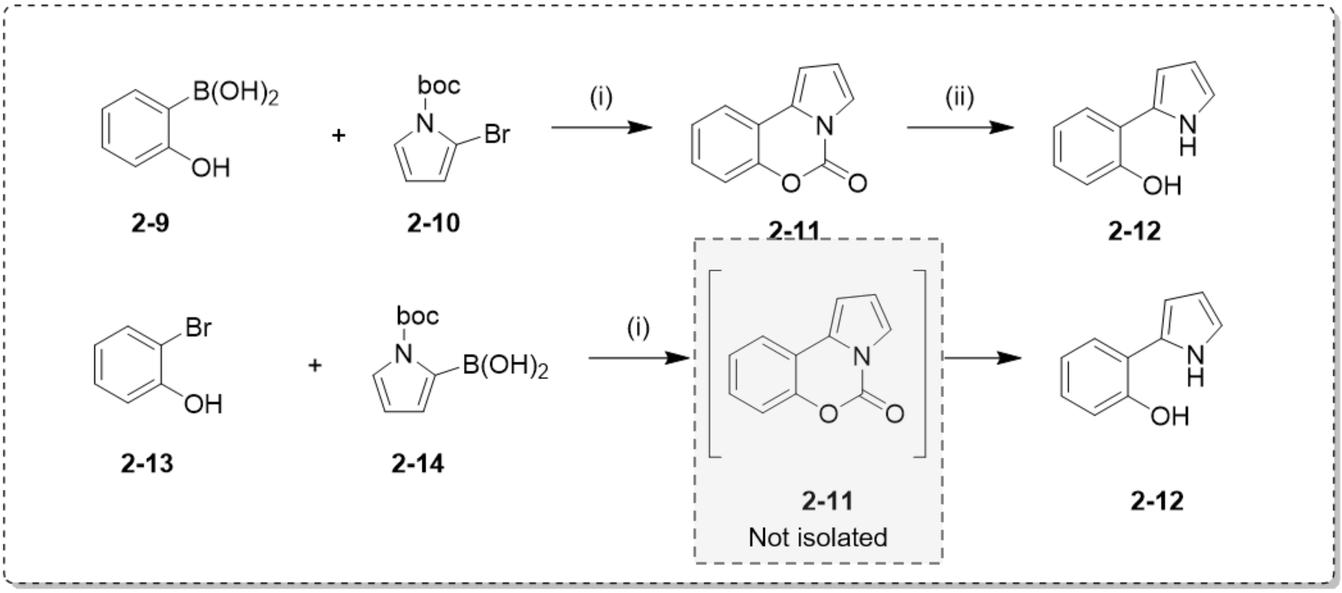

Figure 2.20: Two synthetic methods to 2-(1H-pyrrol-2-yl)phenol. Reagents and conditions: (top) (i) $Pd(PPh_3)_4$ (5 mol %), K_2CO_3, toluene/EtOH/H_2O (45 %); (ii) NaOH, EtOH, 1 h (56 %). (bottom) (i) Pd(XPhos), K_3PO_4, THF/H_2O, 24 h (68 %)

roacetic acid in dichloromethane, followed by oxidation with 2,3-dichloro-5,6-dicyano-1,4-benzoquinone (DDQ) to form the dipyrrin. This intermediate dipyrrin was deprotonated by $^iPr_2NEt$ and subjected to complexation with $BF_3.OEt_2$ to form **BOD1** in moderate yields.

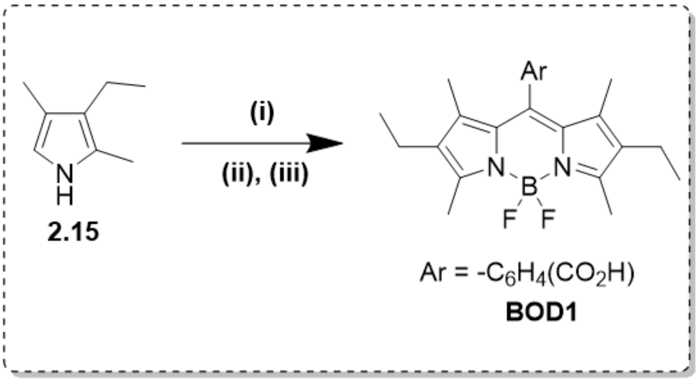

Figure 2.21: Synthesis of BOD1. (i) 4-carboxybenzaldehyde, CF_3CO_2H, CH_2Cl_2; (ii) p-chloranil; (iii) $^iPr_2NEt$, $BF_3.OEt_2$ (51 %)

2.4 Structural Characterization - NMR

BOD1, **BOD2** and **BOD3** have been structurally characterised by ^{1}H NMR, alongside the methyl protected **BOD3-Me** . The ^{1}H NMR assignments for **BOD1** are summarised in Table 2.2 with protons labelled as shown in Figure 2.22. These values are in good agreement with previously published data on this compound.[35]

H_x	m, H	δ (ppm)	J (Hz)
1	-	-	-
2	d, 2H	8.25	8.4
3	d, 2H	7.45	8.4
4	s, 6H	1.27	-
5	q, 4H	2.30	7.5
6	t, 6H	0.98	7.5
7	s, 6H	2.54	-

Table 2.2: ^{1}H NMR assignments for **BOD1** in $CDCl_3$

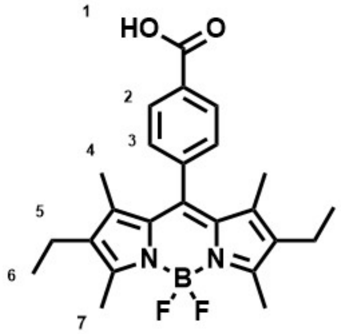

Figure 2.22: Structure of **BOD1** with proton assignment numbers corresponding to Table 2.1

The ^{1}H NMR assignments for **BOD2** are summarised in Table 2.3 with protons labelled as shown in Figure 2.23.

The ^{1}H NMR assignments for **BOD3-Me** and **BOD3** are summarised in Table 2.4, with protons labelled in Figure 2.25. Structurally the two compounds are almost identical, with BOD3-Me being the methyl ester derivative featuring a 3H singlet at 3.99 ppm from the $-CH_3$ group of the ester. This peak is absent in BOD3 indicating the free carboxylic acid group. The acidic $-CO_2H$ proton is absent in the spectrum of **BOD3**. The carboxylic

H_x	m, H	δ (ppm)	J (Hz)
1	br, s, 1H	6.90	-
2	d, 2H	8.27	9
3	d, 2H	7.72	9
4	d, 2H	6.87	6
5	d, 2H	6.67	-
6	m, 4H	7.94 - 7.86	-
7	m, 4H	6.48 - 6.42	-
8	m, 2H	6.48 - 6.42	-
9	m, 4H	6.48 - 6.42	-
10	m, 4H	7.94 - 7.86	

Table 2.3: ^{1}H NMR assignments for BOD2 in $CDCl_3$

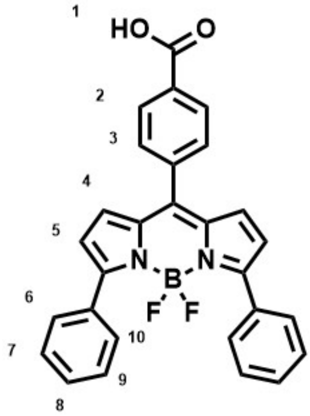

Figure 2.23: Structure of BOD2 with proton assignment numbers corresponding to Table 2.4

acid moiety has a higher inductive effect than the methyl ester analog, and therefore the protons closest to this group show significant change in chemical shift. The A-B doublet pair arising from the para substituted phenyl ring at the meso- position has been shifted downfield due to the difference in the shielding influences from a -CO_2Me vs a -CO_2H group. The protons found further from the para-carboxylate/carboxylic acid group do not appear to be influenced by the change in electronegativity with very similar chemical shifts and identical splitting patterns.

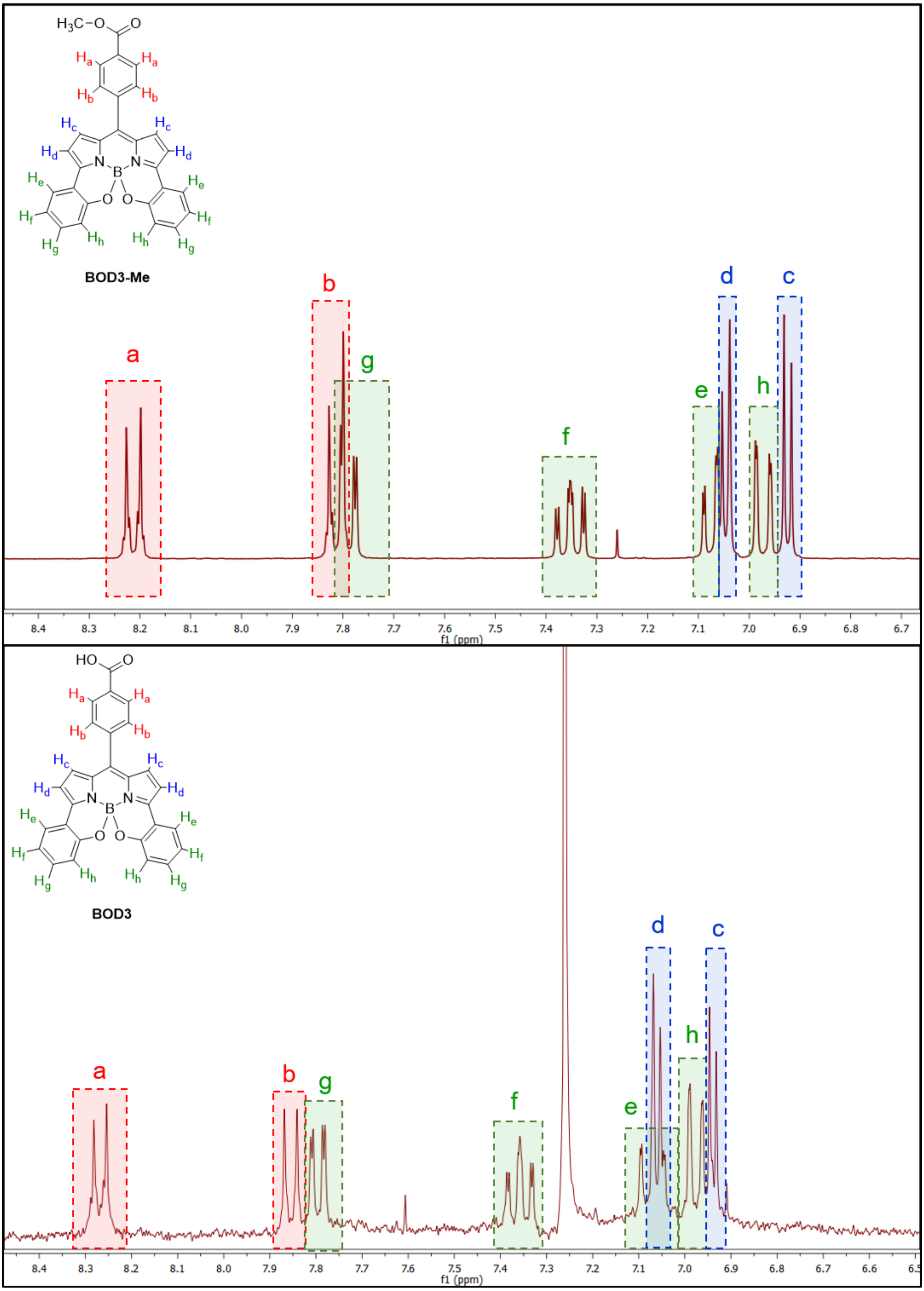

Figure 2.24: Expansion of the aromatic region of the ^{1}H NMR spectra of **BOD3-Me** (top) and **BOD3** (bottom)

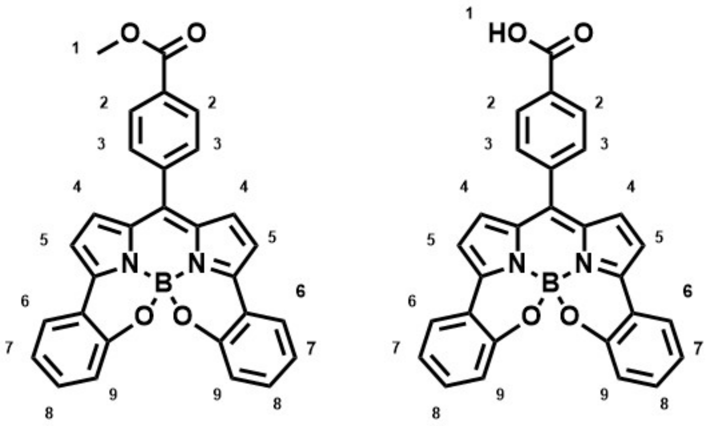

Figure 2.25: Structures of BOD3-Me and BOD3 with proton assignment numbers corresponding to Table 2.4

BOD3-Me				BOD3			
H_x	m, H	δ (ppm)	J (Hz)	H_x	m, H	δ (ppm)	J (Hz)
1	s, 3H	3.99	-	1	-	-	-
2	d, 2H	8.23	9	2	d, 2H	8.28	9
3	m, 4H	7.85 - 7.75	-	3	d, 2H	7.85	9
4	d, 2H	6.92	3	4	d, 2H	7.01 - 6.92	-
5	m, 4H	7.09 - 7.03	-	5	d, 2H	7.11 - 7.03	-
6	m, 4H	7.09 - 7.03		6	m, 4H	7.11 - 7.03	
7	t, 2H	7.35	6	7	t, 2H	7.36	6
8	m, 4H	7.85 - 7.25	-	8	d, 2H	7.80	9, 1.8
9	d, 2H	6.97	-	9	d, 4H	7.01 - 6.92	-

Table 2.4: ^{1}H NMR assignments for BOD3-Me (left) and BOD3 (right) in $CDCl_3$

2.5 Conclusions

This chapter outlines the synthesis of three BODIPY sensitizers via previously published literature methods towards alpha substituted BODIPYs. Although initial attempts using regioselective halogenation of the BODIPY core and subsequent deprotection of the methyl ester protecting group were unsuccesful, a reworked synthesis pathway yielded two novel BODIPY dyes with benzoic acid anchor groups suitable for use in a DSSC.

References

(1) Loudet, A.; Burgess, K. *Chem. Rev* **2007**, *107*, 4891–4932.

(2) Sola-Llano, R.; Bañuelos, J. In *BODIPY Dyes - A Privilege Molecular Scaffold with Tunable Properties*; IntechOpen: 2019.

(3) Treibs, V. A.; Kreuzer, F.-H. *Liebigs Ann. Chem.* **1968**, *223*, 208–223.

(4) Ulrich, G.; Ziessel, R.; Harriman, A. *Angewandte Chemistry International Edition* **2008**, *47*, 1184–1201.

(5) Shah, M.; Thangaraj, K.; Soong, M.-l.; Wolford, L. T.; Boyep, J. H.; Pavlopoulos, T. G. *Heteroatom Chemistry* **1990**, *1*, 389–399.

(6) Wagner, R. W.; Lindsey, J. S. *Pure & Applied Chemistry* **1996**, *68*, 1373–1380.

(7) Littler, B. J.; Miller, M. A.; Hung, C.-H.; Wagner, R. W.; Shea, D. F. O.; Boyle, P. D.; Lindsey, J. S.; Carolina, N. *Journal of Organic Chemistry* **1999**, 1391–1396.

(8) Rohand, T.; Dolusic, E.; Ngo, T. H.; Maes, W.; Dehaen, W. *Arkivoc* **2007**, 307–324.

(9) Clarke, R. G.; Hall, M. J., *Recent developments in the synthesis of the BODIPY dyes*, 1st ed.; Elsevier Inc.: 2019, pp 1–81.

(10) Nepomnyashchii, A. B.; Cho, S.; Rossky, P. J.; Bard, A. J. *Journal of the American Chemical Society* **2010**, 17550–17559.

(11) Nepomnyashchii, A.; Bröring, M.; Ahrens, J.; Bard, A. J. *Journal of the American Chemical Society* **2011**, 8633–8645.

(12) Nepomnyashchii, A. B.; Bard, A. J. *Accounts of Chemical Research* **2012**, *45*, 1844–1853.

(13) Singh, S. P.; Gayathri, T. *European Journal of Organic Chemistry* **2014**, 4689–4707.

(14) Hattori, S.; Ohkubo, K.; Urano, Y.; Sunahara, H.; Nagano, T.; Wada, Y.; Tkachenko, N. V.; Lemmetyinen, H.; Fukuzumi, S. *Journal of Physical Chemistry B* **2005**, *109*, 15368–15375.

(15) Kubo, Y.; Eguchi, D.; Matsumoto, A.; Nishiyabu, R.; Yakushiji, H.; Shigaki, K.; Kaneko, M. *Journal of Materials Chemistry A* **2014**, *2*, 5204–5211.

(16) Zhou, X.; Yu, C.; Feng, Z.; Yu, Y.; Wang, J.; Hao, E.; Wei, Y.; Mu, X.; Jiao, L. *Organic Letters* **2015**, *17*, 4632–4635.

(17) Jiao, L.; Pang, W.; Zhou, J.; Wei, Y.; Mu, X.; Bai, G.; Hao, E. *Journal of Organic Chemistry* **2011**, *76*, 9988–9996.

(18) Xi, L.; Huang Shufang; Hu, Y. *Organic & Biomolecular Chemistry* **2012**, *10*, 2369–2372.

(19) Kim, H.; Burghart, A.; Welch, M. B.; Reibenspies, J.; Burgess, K. *Chem. Commun.* **1999**, 1889–1890.

(20) Kubo, Y.; Minowa, Y.; Shoda, T.; Takeshita, K. *Tetrahedron Letters* **2010**, *51*, 1600–1602.

(21) Tomimori, Y.; Okujima, T.; Yano, T.; Mori, S.; Ono, N. *Tetrahedron* **2011**, *67*, 3187–3193.

(22) Kubo, Y.; Watanabe, K.; Nishiyabu, R.; Hata, R.; Murakami, A.; Shoda, T.; Ota, H. *Organic Letters* **2011**, *13*, 4508–4511.

(23) Feng, Z.; Jiao, L.; Feng, Y.; Yu, C.; Chen, N.; Wei, Y.; Mu, X.; Hao, E. *Journal of Organic Chemistry* **2016**, *81*, 6281–6291.

(24) Rohand, T.; Qin, W.; Boens, N.; Dehaen, W. *European Journal of Organic Chemistry* **2006**, 4658–4663.

(25) Taguchi, D.; Nakamura, T.; Horiuchi, H.; Saikawa, M.; Nabeshima, T. *The Journal of Organic Chemistry* **2018**, *83*, 5331–5337.

(26) Savoldelli, A.; Meng, Q.; Paolesse, R.; Fronczek, F. R.; Smith, K. M. *Journal of Organic Chemistry* **2018**, *83*, 6498–6507.

(27) Xuan, S.; Zhao, N.; Ke, X.; Zhou, Z.; Fronczek, F. R.; Kadish, K. M.; Smith, K. M.; Grac, M.; Vicente, H. *Journal of Organic Chemistry* **2017**, *82*, 2545–2557.

(28) Huaulmé, Q.; Sutter, A.; Fall, S.; Jacquemin, D.; Lévêque, P.; Retailleau, P.; Ulrich, G.; Leclerc, N. *Journal of Materials Chemistry C* **2018**, *6*, 9925–9931.

(29) Rao, M. R.; Mobin, S. M.; Ravikanth, M. *Tetrahedron* **2010**, *66*, 1728–1734.

(30) Liu, X.-L.; Niu, L.-Y.; Chen, Y.-Z.; Zheng, M.-L.; Yang, Y.; Yang, Q.-Z. *Organic & Biomolecular Chemistry* **2016**, *15*, 1072–1075.

(31) Duran-sampedro, G.; Palao, E.; Agarrabeitia, A. R. *RSC Advances* **2014**, *4*, 19210–19213.

(32) Rohand, T.; Baruah, M.; Qin, W. *Chem. Commun.* **2006**, 266–268.

(33) Rihn, S.; Retailleau, P.; Bugsaliewicz, N.; Nicola, A. D.; Ziessel, R. *Tetrahedron Letters* **2009**, *50*, 7008–7013.

(34) Alnoman, R. B.; Rihn, S.; Connor, D. C. O.; Black, F. A.; Costello, B.; Waddell, P. G.; Clegg, W.; Peacock, R. D.; Herrebout, W.; Knight, J. G.; Hall, M. J. *Chemistry A European Journal* **2016**, *22*, 93–96.

(35) Wood, C. J.; Summers, G. H.; Gibson, E. A. *Chem Commun* **2015**, *51*, 3915–3918.

(36) Wen, J.; Zhang, R.-Y.; Chen, S.-Y.; Zhang, J.; Yu, X.-Q. *Journal of Organic Chemistry* **2012**, *77*, 766–771.

(37) Bielawski, M.; Zhu, M.; Olofsson, B. *Advanced Synthesis & Catalysis* **2007**, *349*, 2610–2618.

(38) Clarke, R.; Ho, K. L.; Alsimaree, A. A.; Woodford, O. J.; Waddell, P. G.; Bogaerts, J.; Herrebout, W.; Knight, J. G.; Pal, R.; Penfold, T. J.; Hall, M. J. *ChemPhotoChem* **2017**, *1*, 513–517.

Chapter 3

Experimental

3.0.1 Experimental Details

Anhydrous solvents were used for electrolyte solutions, dye baths, electrochemical measurements, spectroelectrochemical measurements, time-resolved spectroscopy and synthesis. Anhydrous acetonitrile was purchased from Fisher Scientific (99.9 %, over molecularsieves). Dichloromethane was distilled over calcium hydride. Deuterated solvents were purchased from Fluorochem. All other reagents and chemicals were purchased from Sigma-Aldrich unless stated otherwise

Products were characterised by ^{1}H NMR and ^{13}C NMR spectroscopy using a Bruker 300 MHz spectrometer at 25°C; chemical shifts (δ) are reported in parts per million (ppm) from low to high field and referenced to residual non-deuterated solvent. Standard abbreviations indicating multiplicity are used as follows: s = singlet; d = doublet; t = triplet; m = multiplet. Infrared spectroscopy was performed using a Varian 800 FT-IR spectrometer.

UV-visible absorption spectroscopy measurements in solution were recorded on either a Perkin Elmer Lambda 25 UV-visible spectrometer, an Ocean Optics USB2000+ VISNIR fibre optic spectrometer or a Shimadzu UV-1800 UV spectrophotometer. All measurements were performed using a quartz cuvette with a path length of 1 cm.

Photoluminescence spectroscopy measurements in solution were recorded on a Shimadzu RF-6000 spectrofluorophotometer. All measurements were performed using a quartz cuvette with a path length of 1 cm.

Electrochemical studies were carried out using an IviumStat potentiostat controlled using IviumSoft. Redox potentials were determined using cyclic voltammetry and differential pulse voltammetry. All electrochemistry was performed under a nitrogen atmosphere, using a three-electrode setup, in a single compartment cell. A glassy carbon working electrode, a Pt wire secondary electrode and a saturated calomel or Ag/Ag+ (0.01 M $AgNO_3$ in acetonitrile) reference electrode were used. Measurements were typically carried out in anhydrous acetonitrile that had been purged with nitrogen. The sample had a concentration of 0.1 mM and 0.1 - 0.5 M supporting electrolyte was used. TBA ClO_4, Li ClO_4 or TBA PF_6 were used as supporting electrolytes. All redox potentials are quoted against the Fc/Fc^+ couple used as an internal standard.

UV-visible absorption spectra of the dyes adsorbed onto NiO films were recorded using an Ocean Optics USB2000+ VIS-NIR fibre-optic spectrophotometer. Current-voltage measurements were performed using an Ivium CompactStat or IviumStat potentiostat under simulated sunlight (AM1.5) from an Oriel VeraSol-2 Class AAA LED Solar Simulator, with an intensity of 100 mW cm$^{˘2}$. To determine the photocurrent density and photovoltage for a particular system, an average of three solar cells were fabricated and tested.

Femtosecond (fs) transient absorption measurements of dyes BOD1-3 in solution and grafted on NiO surface were carried out using a customized pump-probe laser setup based on an amplified Ti:Sapphire oscillator (Libra, Coherent Inc). The pump pulses exciting the sample were spectrally centered at 537 and 600 nm (TOPASwhite, Lightconversion Ltd.) for dyes BOD1-2 and BOD3 with a pump-pulse energy of 1 J. A white light continuum (350 nm $< \lambda < 750nm)generatedbyfocusingonarotatingCaF_2$ windows was used to probe the samples with typical probe intensities in the range of hundred nJ. The pump beam was delayed in time (Δt up to 2 ns) with respect to the probe beam using an optical delay line and the mutual polarization between pump and probe beam was set to magic angle (54.7º). The transient absorption data ΔA(λ,Δt) data was chirp corrected and analyzed by global fitting to a sum of exponentials. A spectral band of ± 20 nm around the pump wavelength was neglected from analysis due to pump-scattering effect in this spectral region. In addition, the pulse overlap region, i.e. ± 250 fs around time-zero, was excluded from the data fitting procedure to avoid prominent contributions from coherent artifacts.39,40 For fs transient absorption measurements of dyes BOD1-3 in solution, the optical density of each dye was adjusted to 0.2 (in a quartz cuvette with 1 mm optical path length) in dried acetonitrile at the respective excitation wavelength. For fs transient absorption measurements of dyes BOD1-3 on NiO, the BOD1-3 sensitized NiO films were prepared by immersing NiO films on FTO glass with an active area of 0.5 × 1.5 cm^2 in 0.5 mM BOD1-3 solution for 12 h. The BOD1-3 sensitized NiO films were thoroughly rinsed with acetonitrile to remove physisorbed dyes. All measurements were undertaken in sandwiched NiO cells with redox and inert electrolyte and thin film Pt-coated FTO as counter electrode. The I_3/I redox electrolyte contained 0.5 M tetrabutylammonium iodide, 0.1 M Lithium iodide, 0.1 M iodine and 0.5 M 4-tert-butylpyridine in acetonitrile while the inert electrolyte was 0.1M Lithium bis(trifluoromethanesulfonyl)imide (LiTFSI) in acetonitrile. To prevent any possible degradation on the BOD1-3 sensitized NiO film, the sample was moved during the pump-probe experiments.

BOD1

4-carboxybenzaldehyde (50 mg, 0.33 mmol) was loaded into a Schlenk flask and placed under an N_2 atmosphere. 2,4-dimethyl-3-ethylpyrrole (**2-15**) (0.1 mL, 0.73 mmol) and anhydrous dichloromethane (2 mL) were added, followed by trifluoroacetic acid (2 drops). The reaction mixture was stirred in the dark for 3 h before p-chloranil (90 mg, 0.37 mmol) was added and the reaction was stirred for a further 45 minutes. Diisopropylethylamine (1 mL, 5.7 mmol) was added and the reaction was left to stir for 5 minutes before boron trifluoride diethyl etherate 0.83 mL, 6.73 mmol) was added dropwise via a syringe before the reaction was left to stir at room temperature for a further hour. The crude reaction mixture was diluted with dichloromethane and washed with water. The organic extracts were dried over sodium sulphate and the excess organic solvent was removed under reduced pressure. The crude product was purified by column chromatography (DCM:MeOH 98:2) to afford **BOD1** (72 mg, 51%) as a dark red solid. 1H NMR (300 MHz, CDCl3): δ 8.25 (d, J = 8.4 Hz, 2H), 7.45 (d, J = 8.4 Hz, 2H), 2.54 (s, 6H), 2.30 (q, J = 7.5 Hz, 4H), 1.27 (s, 6H), 0.98 (t, J = 7.5 Hz, 6H). 13C NMR (100 MHz, CDCl3): δ 171.8, 156.4, 154.5, 141.8, 138.6, 138.2, 133.3, 131.1, 130.3, 129.0, 17.2, 14.7, 12.7, 12.0.

IR (neat): max/cm-1 2982, 1734, 739

2-2 - Diphenyliodinium triflate

3-Chloroperbenzoic acid (1.54 g, 8.9 mmol) was added to a solution of iodobenzene (**2-1**) (0.9 mL, 8.1 mmol) in dichloromethane (100 mL). Benzene (0.79 mL, 8.84 mmol) was added followed by dropwise addition of trifluoromethanesulfonic acid (2.14 mL) and left to stir for 30 minutes. The crude reaction mixture was concentrated under reduced pressure. Addition of diethyl ether precipitated the product **2-2** (1.822 g, 52 %) as an off-white crystalline powder which was filtered and washed with diethyl ether. 1H NMR (300 MHz, Chloroform-d) δ 8.02 – 7.92 (m, 2H), 7.70 – 7.59 (m, 1H), 7.49 (dd, J = 8.3, 7.1 Hz, 2H). 13C NMR (75 MHz, Chloroform-d) δ 135.09, 132.74, 132.46 121.80. IR (neat): max/cm-1 745, 728

2-3 - 2-phenyl-1*H*pyrrole

2-2 (527 mg, 1.23 mmol) and sodium hydroxide (74 mg, 1.85 mmol) were loaded into a Schlenk tube and degassed with N_2. Pyrrole was added and the mixture was heated to 80 ^{o}C and stirred overnight. The reaction mixture was cooled to room temperature and the excess pyrrole was removed under reduced pressure. The crude solid was redissolved in ethyl acetate and washed with water, the combined organic layers were dried with $MgSO_4$ and the excess solvent was removed under reduced pressure. The product was purified by silica gel chromatography (2:1 petroleum ether:ethyl acetate) to afford **2-3** as a beige solid (115 mg, 65 %) 1H NMR (300 MHz, Chloroform-d) δ 8.44 (s, 1H), 7.53 – 7.44 (m, 2H), 7.43 – 7.31 (m, 2H), 7.27 – 7.15 (m, 1H), 6.87 (td, J = 2.7, 1.5 Hz, 1H), 6.53 (ddd, J = 3.5, 2.6, 1.5 Hz, 1H), 6.31 (dt, J = 3.5, 2.6 Hz, 1H). 13C NMR (75 MHz, Chloroform-d)

δ 132.80, 132.16, 128.90, 126.22, 123.87, 118.83, 110.14, 105.96. IR (neat): max/cm-1 755, 716, 691

BOD2 - 4-(5,5-difluoro-3,7-diphenyl-5H-4λ^4,5λ^4-dipyrrolo [1,2-c:2',1'-*f*][1,3,2]diazaborinin-10-yl)benzoic acid

2-3 (90 mg 0.733 mmol), 4-carboxybenzaldehyde (51 mg, 0.333 mmol) were loaded into a Schlenk tube and placed under an N_2 atmosphere. Dry dichloromethane (10 mL) was then added and the mixture was left to stir until the reactants had fully dissolved. Trifluoroacetic acid (2 drops) was added and the reaction was left to stir for 3 hours. p-chloranil (90 mg, 0.366 mmol) was then added with continued stirring for 10 minutes, before diisopropylethylamine (1 mL) followed by boron trifluoride diethyletherate (1 mL). The reaction was then left to stir for 12 h in the dark, before dilution with dichloromethane and washing with $NaHCO_3$. The organic layers were combined and the excess solvent was removed under reduced pressure. The crude product was purified by silica gel chromatography (99:0.9:0.1 dichloromethane:methanol:acetic acid) before recrystallization by slow diffusion of pentane into dichloromethane to afford **BOD2** as a red solid (25 mg, 16%). 1H NMR (300 MHz, Chloroform-d) δ 8.27 (d, J = 8.5 Hz, 1H), 7.94 – 7.86 (m, 2H), 7.72 (d, J = 8.5 Hz, 1H), 7.45 (dd, J = 5.0, 1.9 Hz, 3H), 6.90 (s (broad), 1H), 6.87 (d, J = 3.6 Hz, 2H), 6.67 (d, J = 3.6 Hz, 2H). IR (neat): max/cm-1 3159, 1704

2-5 - methyl 4-((1H-pyrrol-2-yl)(2H-1λ^4-pyrrol-2-yl)methyl)benzoate

Methyl-4-formylbenzoate (**2-4**) (2.00g, 12 mmol) was suspended in an aqueous solution of [0.18] M HCl (100 mL) and left to stir for 20 minutes. Pyrrole (2.3 mL, 39 mmol) was then added dropwise via syringe over 5 minutes before stirring continued for a further 4 hours. The pale pink precipitate was filtered and washed with distilled H_2O and petroleum ether to afford the dipyrromethene **2-5** (2.82 g, 84%). 1H NMR (300 MHz, Chloroform-d) δ 7.98 (d, J = 8.4 Hz, 2H), 7.29 (d, J = 8.5 Hz, 3H), 6.72 (td, J = 2.7, 1.5 Hz, 1H), 6.20 – 6.12 (m, 1H), 5.89 (m, 2H), 5.53 (s, 1H), 3.91 (s, 3H).

2-6 - methyl (Z)-4-((5-bromo-1*H*-pyrrol-2-yl)(5-bromo-2*H*-pyrrol-2-ylidene) methyl)benzoate

2-5 (2.00 g, 8.48 mmol) was dissolved in dry THF (200 ml) under an N_2 atmosphere and cooled to -78 ^{o}C. Once cooled, N-bromosuccinimide 3.04 g, 17.08 mmol) was added as a solid in one portion and the reaction was left to stir for 1 h. Following this 2,3-dichloro-5,6-dicyano-1,4-benzoquinone (2.00 g, 6.8 mmol) was added at -78 ^{o}C and the reaction was left to warm to room temperature, before the crude mixture was diluted with dichloromethane and extracted with a saturated sodium sulphite solution and water. The organic layers were combined and dried over $MgSO_4$ and the solvent was removed under reduced pressure. The crude product was purified by silica gel column chromatography (1:1 DCM : petrol 40-60) to give **2-6** (1.89 g, 51%) IR (neat): max/cm-1 1716, 1434, 1357

2-7 - methyl 4-(3,7-dibromo-5,5-difluoro-5*H*-4λ^4,5λ^4-dipyrrolo[1,2-c:2',1'-*f*] [1,3,2]diazabo 10-yl)benzoate

The crude mixture of **2-6** (0.43 g, 1 mmol) was dissolved in dichloromethane (5 mL) and placed under a N2 atmosphere. Diisopropyl ethylamine (0.43 mL, 2.5 mmol) was added and the reaction was left to stir for 5 minutes before boron diflouorodiethyl etherate (0.25 mL, 2 mmol) was added slowly dropwise and the mixture was left to stir at room temperature for 1 hour. The crude mixture was washed with sodium hydroxide (0.1 M, 50 mL) and hydrochloric acid (0.1 M, 50 mL). The organic extracts were combined and dried with sodium sulfate and the excess solvent was removed under reduced pressure. The crude produce was purified by column chromatography (1:1 dichloromethane:toluene) to afford **2-7**. (0.37 g, 77%) 1H NMR (300 MHz, Chloroform-d) δ 8.18 (d, J = 8.5 Hz, 2H), 7.57 (d, J = 8.5 Hz, 2H), 6.74 (d, J = 4.3 Hz, 2H), 6.55 (d, J = 4.3 Hz, 2H), 3.98 (s, 3H). 13C NMR (75 MHz, Chloroform-d) 166.65, 142.06, 137.19, 135.85, 134.14, 132.88, 132.02, 130.90, 130.26, 123.71, 53.15 IR (neat): max/cm-1 1722, 1545, 726

BOD3-Me + cBOD3-Me

2-7 (50 mg, 0.1 mmol), Tetrakis(triphenylphosphine)palladium(0) (6 mg, 0.005 mmol 5 mol%), potassium phosphate(130 mg, 0.6 mmol) and 2-hydroxyphenyl boronic acid (**2-9**)(100 mg, 0.73 mmol) were loaded into a Schlenk flask and degassed thoroughly. A 1:1 mixture of toluene (1 mL) and 1,4-dioxane (1 mL) were added to the flask and the solution was heated to 90 ^oC for 90 minutes. Once finished the reaction was left to cool to room temperature before being diluted with dichloromethane (5 mL) and washed with water. The organic extracts were dried over sodium sulfate and excess solvent was removed under reduced pressure. The crude product was purified by column chromatography (6:1 petroleum ether:ethyl acetate) to afford **BOD3-Me** and **cBOD3-Me**. (25.8 mg, 53% and 6.8 mg, 14% respectively.) **BOD3-Me** 1H NMR (300 MHz, Chloroform-d) δ 8.21 (d, J = 8.4 Hz, 2H), 7.85 – 7.75 (m, 4H), 7.35 (ddd, J = 8.3, 7.3, 1.7 Hz, 2H), 7.09 (d, J = 1.1 Hz, 1H), 7.07 – 7.03 (m, 3H), 6.97 (dd, J = 8.3, 1.1 Hz, 2H), 6.92 (d, J = 4.4 Hz, 2H), 3.99 (s, 3H). 13C NMR (75 MHz, Chloroform-d) δ 166.5, 154.4, 150.6, 138.5, 137.1, 134.2, 132.6, 132.0, 130.6, 130.0, 129.9, 126.0, 120.7, 119.9, 119.7, 116.9, 52.6. **cBOD3-Me** 1H NMR (300 MHz, Chloroform-d) δ 8.23 – 8.17 (m, 2H), 7.80 – 7.70 (m, 3H), 7.31 (ddd, J = 8.0, 1.1, 0.6 Hz, 1H), 7.25 – 7.15 (m, 3H), 7.00 (dd, J = 4.5, 3.8 Hz, 2H), 6.98 – 6.90 (m, 2H), 6.86 (d, J = 4.3 Hz, 1H), 6.77 (dd, J = 8.3, 1.0 Hz, 1H), 6.43 (d, J = 4.6 Hz, 1H), 3.99 (s, 3H). 13C NMR (75 MHz, Chloroform-d) δ 166.6, 163.2, 156.9, 154.6, 148.4, 138.2, 137.3, 132.3, 131.9, 131.5, 130.5, 130.3, 129.9, 129.5, 128.4, 127.7, 127.5, 125.2, 124.6, 121.5, 120.4, 120.3, 117.0, 115.7, 107.9, 52.6.

IR (neat): max/cm-1 1721, 1270, 744

2-8 - methyl 4-(5,5-difluoro-3,7-bis(2-methoxyphenyl)-5*H*-4λ^4,5λ^4-dipyrrolo[1,2-c:2',1'-*f*][1,3,2]diazaborinin-10-yl)benzoate

2-7 (50 mg, 0.1 mmol), Tetrakis(triphenylphosphine)palladium(0) (6 mg, 0.005 mmol (5 mol%), potassium phosphate (130 mg, 0.6 mmol) and 2-methoxyphenylboronic acid (**2-9Me**) (120 mg, 0.79 mmol) were added to a Schlenk flask and placed under a N_2 atmosphere. A 1:1 mixture of toluene:dioxane were added to the flask and the reaction was heated to 90 ^oC for 90 minutes. The reaction was then left to cool to room temperature before being diluted with dichloromethane and washed with water. The organic extracts were combined and dried with sodium sulfate, and the excess solvent was removed under reduced pressure before purification by column chromatography (6:1 petroleum ether:ethyl acetate) to afford **2-8** (38 mg, 77%) 1H NMR (300 MHz, Chloroform-d) δ 8.20 (d, J =

8.5 Hz, 2H), 7.78 – 7.65 (m, 4H), 7.40 – 7.28 (m, 2H), 7.05 – 6.88 (m, 4H), 6.78 (d, J = 4.9 Hz, 2H), 6.60 (d, J = 4.5 Hz, 2H), 4.00 (s, 3H), 3.78 (s, 6H). 13C NMR (75 MHz, Chloroform-d) δ 157.56, 139.04, 135.16, 130.73, 130.54, 129.39, 121.86, 120.28, 110.96, 55.80. IR (neat): max/cm-1 1721, 1270, 754

2-12 - 2-(1*H*-pyrrol-2-yl)phenol

In a Schlenk tube was loaded 2-bromophenol (**2-13**) (0.50 g, 2.89 mmol), N-boc-pyrrole-2-boronic acid (**2-14**) (0.914 g, 4.34 mmol), Pd(XPhos) (44 mg, 0.058 mmol) and K_3PO_4 (1.15g, mmol) and placed under a N_2 atmosphere. The solids were then dissolved in THF (10 mL) and H_2O (5 mL) and the reaction was heated to 75 ^{o}C and stirred continuously for 24 h. The reaction mixture was cooled to room temperature and diluted with dichloromethane (20 mL) and washed with water (2 x 30 mL). The organic layers were dried over $MgSO_4$ and the excess solvent was removed under reduced pressure. The crude product was purified by silica gel column chromatography (3:1 hexane:dichloromethane) to afford **2-12** (0.31 g, 68 %) 1H NMR (300 MHz, Chloroform-d) δ 9.42 (1H, br s), 7.54 (1H, dd, J = 7.8, 1.5 Hz), 7.10 (1H, td, J = 7.8, 1.5 Hz), 6.97 (1H, td, J = 7.5, 1.1 Hz), 6.89-6.91 (1H, m), 6.84 (1H, dd, J = 7.8, 1.0 Hz), 6.59-6.57 (1H, m), 6.34-6.31 (1H, m). 13C NMR (75 MHz, Chloroform-d) δ 151.13, 128.90, 127.33, 127.18, 121.55, 119.79, 118.63, 116.39, 109.36, 106.36. IR (neat): max/cm-1 3425, 744

BOD3

2-12 (90 mg 0.733 mmol), 4-carboxybenzaldehyde (51 mg, 0.333 mmol) were loaded into a Schlenk tube and placed under an N_2 atmosphere. Dry dichloromethane (10 mL) was then added and the mixture was left to stir until the reactants had fully dissolved. Trifluoroacetic acid (2 drops) was added and the reaction was left to stir for 3 hours. p-chloranil (90 mg, 0.366 mmol) was then added with continued stirring for 10 minutes, before diisopropylethylamine (1 mL) followed by boron trifluoride diethyletherate (1 mL). The reaction was then left to stir for 12 h in the dark, before dilution with dichloromethane and washing with $NaHCO_3$. The organic layers were combined and the excess solvent was removed under reduced pressure. The crude product was purified by silica gel chromatography (99:0.9:0.1 dichloromethane:methanol:acetic acid) before recrystallization by slow diffusion of pentane into dichloromethane to afford **BOD3** (11 mg, 7%). 1H NMR (300 MHz, Chloroform-d) δ 8.27 (d, J = 8.4 Hz, 2H), 7.85 (d, J = 8.4 Hz, 2H), 7.80 (dd, J = 7.7, 1.7 Hz, 2H), 7.36 (ddd, J = 8.3, 7.3, 1.7 Hz, 2H), 7.11 – 7.03 (m, 4H), 7.01 – 6.92 (m, 4H). IR (neat): max/cm-1 2983, 1736, 746

Chapter 4

Spectroscopy

4.1 Aims

The photophysical and electrochemical properties of three BODIPY sensitizers (BOD1-3) were studied to assess their suitability for use in a p-DSSC. Using UV-Visible spectroscopy and cyclic voltammetry the frontier orbital energies were calculated and key driving forces in the electron transfer pathway in a p-DSSC (ΔG_{inj} and ΔG_{reg}) were estimated. The three dyes were studied in a working p-DSSC and the solar cell characteristics were reported.

4.2 Experimental Methods

4.2.1 Steady State Ultraviolet-visible Spectroscopy

The solar spectrum has a maximum irradiance in the visible region between 1.4 - 4.0 eV. Valence electron transitions (from p, d and π-orbitals) upon irradiation of the molecule can be monitored with visible light. UV-visible spectroscopy produces a cross section of the absorption of a molecule and quantifies the proportion of light absorbed at a particular wavelength or energy. Absorption can be quantified by the Beer-Lambert Law and is described at the molar absorption coefficient (ϵ, dm^3 mol^{-1} cm^{-1}) which is describes how well the molecule absorbs incoming radiation.[1]

$$log_{10}\frac{I_0}{I} = \epsilon cl \tag{4.1}$$

Where I_0 is the intensity of incident light, I is the intensity of transmitted light, ϵ is the molar absorption coefficient. c is the concentration of analyte in solution and l is the path length through which the light passes through the sample.

4.2.2 Photoluminesence Spectroscopy

Photoluminesence (or Fluoresence) spectroscopy probes the radiative decay processes from a photogenerated excited state. These processes are important to characterise in DSSC as the charge transfer processes associated with the working mechanism of these cells occur in the excited state. When a molecule absorbs a photon, an electron from the ground state is promoted to a higher energy singlet excited state. This energy is then released via radiative and non-radiative decay processes to relax back to the ground state. These radiative and non-radiative decay processes are outlined in Fig. 4.1. Internal conversion and vibrational relaxation happen on a shorter timescale than fluoresence, therefore fluoresence only occurs from the lowest energy singlet state ($S_1 \rightarrow \mathrm{S}_0$). This is described by Kashas Rule.[2] Two types of PL spectra have been used in this thesis. Emission spectra measure the fluoresence intensity over a range of wavelengths, following monochromatic excitation. Excitation spectra measure the emission intensity at a fixed wavelength as a function of the excitation wavelength. Both the UV-Visible spectra and the photoluminesence spectra have been used to estimate the zero-zero energy (E_{0-0}), defined as the intercept between the normalised emission and absorption spectra.

4.2.3 Cyclic Voltammetry

Cyclic voltammetry has been used in this thesis to understand the redox properties of the dyes used in DSSC. During a cyclic voltammetry experiment the voltage is increased or decreased to a user defined potential before reversal of the scan direction returning to the origin potential, whilst continuously measuring current.

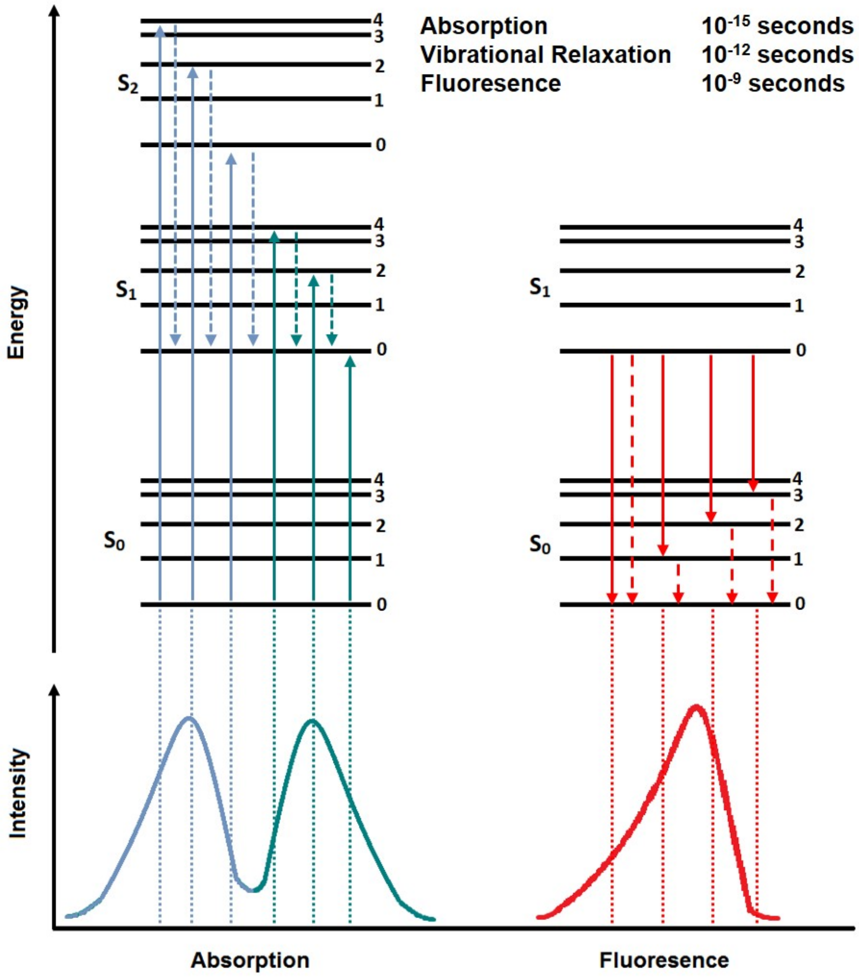

Figure 4.1: Jablonski Diagram representing energy levels and associated spectra. Solid arrows indicate radiative processes during absorption (blue, green) or emission (red). Dashed arrows indicate non-radiative processes (blue, green, red). Below the diagram absorption and emission spectra are shown.

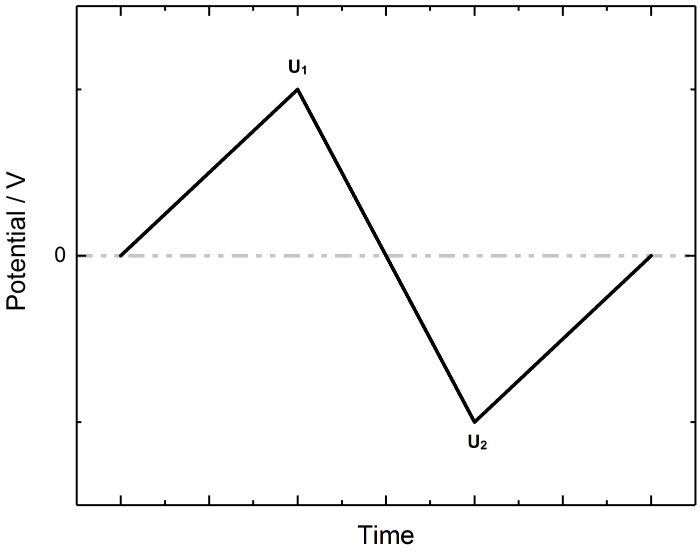

Figure 4.2: Example waveform for a cyclic voltammogram: U_1 shows the first switching potential, U_2 shows the second switching potential

In a three electrode setup, a potential is applied at the working electrode in relation to an internal reference electrode. The current flowing between the working electrode and the counter electrode through the supporting electrolyte is measured. Fig 4.2 shows a typical waveform for a cyclic voltammetry setup, Fig 4.3 shows an example cyclic voltammogram produced from waveform 4.2.

The redox potential of an analyte at the working electrode is given by the Nernst Equation.

$$E = E^0_{redox} - k_B T ln(\frac{C_{OX}}{C_{RED}}) \tag{4.2}$$

Initially when scanning in a positive direction, non-faradaic or charging processes are observed. When E^0_{redox} is reached, the processes at the electrode become faradaic processes involving oxidation and reduction of the analyte at the working electrode. The current increases as the concentration of the analyte at the surface of the working electrode reaches a maximum until the peak anodic current (U_{pa}) is reached. Scanning to further positive potentials shows a decrease in current as the species at the electrode is consumed and the

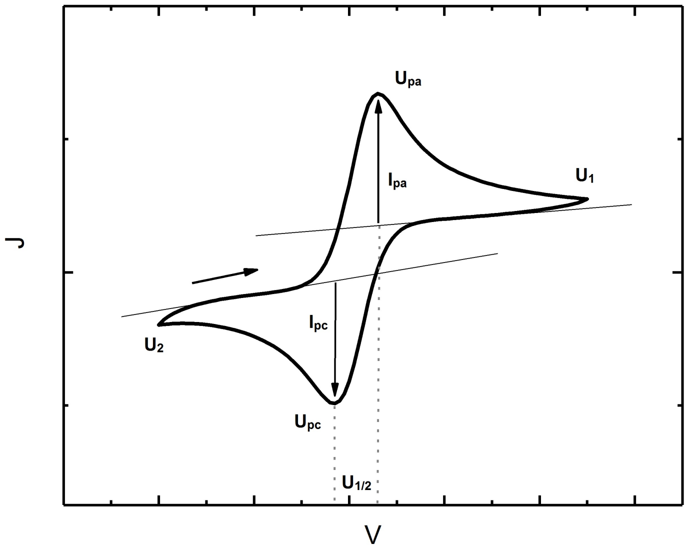

Figure 4.3: Example cyclic voltammogram for a one electron reversible electrochemical reaction. U$_1$ shows the first switching potential. U$_2$ shows the second switching potential U$_{pa}$ and U$_{pc}$ show the peak anodic and cathodic currents respectively. I$_{pa}$ shows the cathodic current

faradaic processes stop.

For a reversible reaction, upon reversal of scan direction, the reverse faradaic process can be observed, leading to an increase in cathodic current. Upon reaching the peak cathodic current (U$_{pc}$) and scanning back towards the origin, the analyte is depleted at the electrode surface and the cathodic current decreases again.

For organic dyes, such as the ones presented in this thesis, the oxidation potential is the potential where an electron is removed from the HOMO of the dye. The reduction potential is the potential at which an electron is accepted into the LUMO. As such, using cyclic voltammetry, the HOMO-LUMO energies can be estimated. When coupled with UV-vis and emission spectroscopy the excited state redox potentials can be estimated.

Current Voltage Characteristics

In order to determine the solar cell device efficiency, the current-voltage (J-V) measurements must be recorded (Fig. 4.4). All J-V measurements were performed under 1 sun

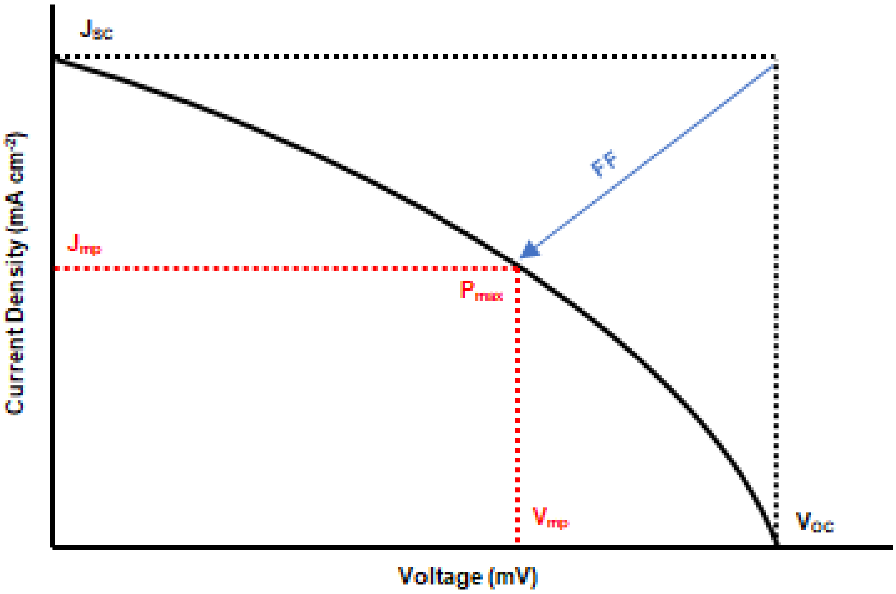

Figure 4.4: Sample JV curve for a p-DSSC. Key solar cell parameters are labelled.

(AM 1.5) illumination. There characteristics of the device are monitored under irradiation under a variable external load, from zero (short-circuit conditions) to infinite load (open-circuit conditions).

The maximum power (P$_{max}$) is found at the point where the product of the current and voltage is highest. The solar cell efficiency (η) is calculated by taking the ratio between P$_{max}$ and the power of the incident light placed on the cell (P$_{in}$ = 1000 W m^{-2}). Equation 4.3 is used to calculate η

$$\eta = \frac{P_{max}}{P_{in}} = \frac{J_{SC}.V_{OC}.FF}{P_{in}} \tag{4.3}$$

The Fill Factor (FF) (Equation 4.4) is the ratio between the maximum power and the product of J$_{SC}$ and V$_{OC}$ and reflects the squared shape of the JV curve.

$$FF = \frac{J_{max}.V_{max}}{J_{SC}.V_{OC}} \tag{4.4}$$

By measuring the J-V characteristics without illumination, information about recombination with the redox electrolyte can be obtained, as in the dark no interactions with the electronically excited dye occur within the device.

4.2.4 Device Fabrication

Preparation of NiO electrode

NiO electrodes were prepared according to established literature procedures.[3]

Anyhydrous Nickel (II) Chloride (1 g) was dissolved in ethanol (7.6 mL) and distilled water (6 mL). To this was added a templating ploymer (Pluronic® F108, poly(ethylene glycol)-block-propylene-glycol)-block-(polyethylene glycol) (1 g) and the solution was stirred overnight. The solution was left in the fridge for two weeks and centrifuged immediately prior to every use. Fluorine-doped tin oxide (FTO) coated glass (Pilkington, TEC 15, 15 Ω /sq) was used as the conductive substrate to support the electrode. The coated glass substrate was cleaned by immersion into soapy water (15 min), 0.1 M HCl in ethanol (5 mins) and ethanol (15 min) under sonication in an ultrasonic bath before drying at room temperature. A mask of Scotch® Magic ™ Tape (0.25 cm^2, circular) was applied. One drop of the nickel (II) chloride solution was placed and spread over the masked substrate (doctor-blading). The solution was left to dry for 5 minutes before the mask was removed and the electrodes were sintered in a muffle furnace (Nabertherm) at 450 ^{o}C for 30 minutes. The furnace was set to a ramp time of 30 minutes (15^{o}C/min). The sintering process anneals the NiO nanoparticles and establishes electrical connections between the nanoparticles and between the nanoparticles and the conductive substrate. Additional layers were applied and annealed between each layer until the the films were between 1 - 2 μ m. Whilst warm (ca. 80 ^{o}C) the electrodes were immersed in a solution of the dye (ca. 3 mM in CH_3CN).

Preparation of the counter electrode

Platinum counter electrodes were constructed from FTO coated glass (Pilkington, TEC 8, 8Ω /sq). A 1 mm hole was drilled into the corner of the electrode. The electrode was cleaned with the same procedure outlined above for the working electrode. 1 μ l of chloroplatnic acid (H_2PtCl_6, 4.8 mM) in ethanol was applied over the surface of the electrode and the counter electrode was annealed at 450 ^{o}C for 15 minutes (ramp time 15 min, 30 ^{o}C/min).

4.3 Electronic Absorption and Emission

The UV-Visible absorption spectrum of BOD1-3 were recorded in degassed, dry acetonitrile solution to determine the effect of the different alpha substitutions on the electronic structure of the three dyes. The photophysical properties of the three dyes are detailed in Table 4.1.

BOD1 exhibits absorption and emission profiles typical for a BODIPY based chromophore (Figure 4.5). It shows a narrow absorption band with absorption maxima over 500 nm, with a shoulder at a higher energy, characteristic of a BODIPY S_0 to S_1 transition. A less intense broad absorption band around 400 nm arises from contributions of the meso-aryl ring system lying perpendicular to the plane of the BODIPY core.

	$\lambda_{abs}(nm)$	$\lambda_{em}(nm)$	$\epsilon(dm^3mol^{-1}cm^{-1})$	$E_{0-0}(eV)$
BOD1	528	536	20 425	2.33
BOD2	515	541	14 325	2.35
BOD3	625	654	24 846	1.93

Table 4.1: Photophysical properties of BOD1, BOD2 and BOD3. The absorption (λ_{abs}) and emission (λ_{em}) maxima, the absorption coefficient (ϵ) determined in acetonitrile solution. E_{0-0} is calculated from the wavelength of the intersection between the normalized absorption and emission spectra λ_{int}: $E_{0-0} = 1240/\lambda_{int}$

BODIPY dyes generally show narrow emission bands, which appear as the mirror image of the absorption band. BODIPY dyes generally have small Stokes shifts, the rigid core of the chromophore show small amounts of structural change in the molecule during excitation and subsequent relaxation.[4] BOD1 has a narrow well defined emission profile in acetonitrile with an emission maxima (λ_{em}) at 536 nm and Stokes shift of 280 cm^{-1}.

BOD2 has a much broader and less well defined absorption spectrum then BOD1 (Figure

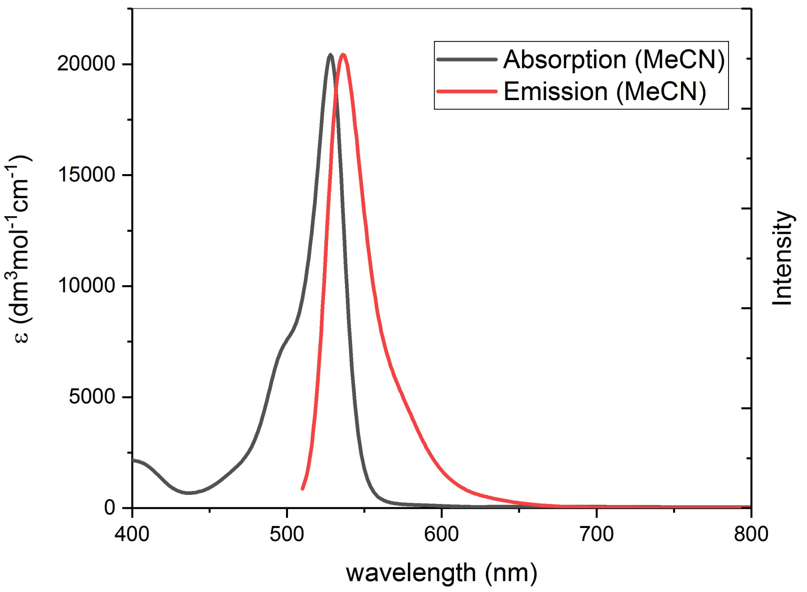

Figure 4.5: Normalised absorption (black line) and emission (red line) of BOD1 in acetonitrile solution. Excitation wavelength (λ_{ex}) = 510 nm

4.6). A hypsochromic shift of ca. 13 nm is observed for BOD2 vs BOD1 when the alkyl substituents are removed and replaced with α-phenyl substituents. It also features a reduction in the absorption coefficient (ϵ) when compared to BOD1. This band broadening and change to the extinction coefficient values can be seen as moving away from a π - π * transition towards a charge transfer transition. These effects mirror trends found in BODIPY's previously made by Summers, whereby removal of the alkyl substituents from the pyrrolic positions of BODIPY and increasing electronic communication between the BODIPY core and the meso substituents appeared to reduce the BODIPY π - π * transitions in favour of a charge transfer transition.

Inspection of the emission spectra of BOD2 shows two broad emission bands, with different intensities. Broadening of the emission profile of BOD2 can be attributed to an increase in non-radiative deactivation pathways introduced by the α-phenyl substituents. The low emission for this dye arises from free rotation of the aryl groups and reduction in rigidity in the system. Similar reports of α-phenyl BODIPY systems with rotating meso- and α-substituents agree with this.[5] The excitation spectra associated with these two peaks show

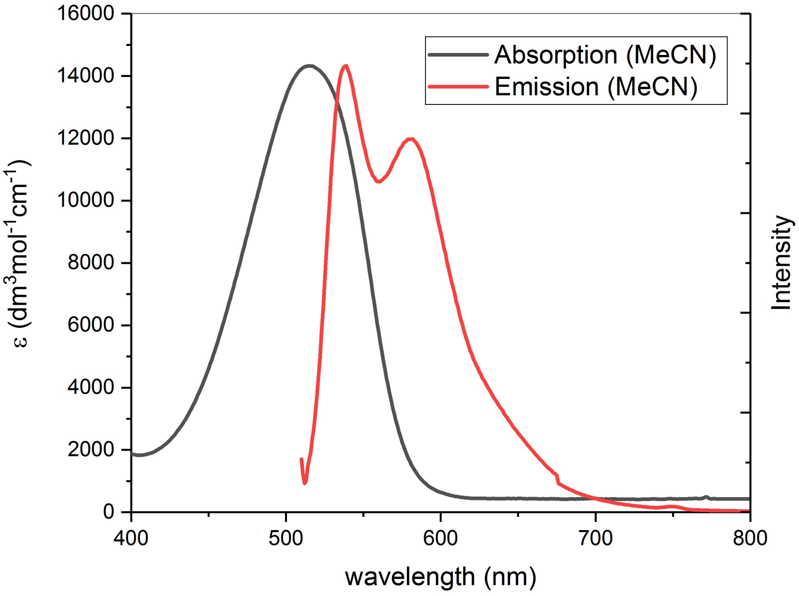

Figure 4.6: Normalised absorption (black line) and emission (red line) of BOD2 in acetonitrile solution. Excitation wavelength (λ_{ex}) = 500 nm

two emissive species in solution (Figure 4.7). The higher energy emission peak gives rise to an excitation spectrum of a typical BODIPY with narrow absorption with a shoulder at higher energy. The lower energy emission band gives rise to a broad featureless excitation spectrum, with lower intensity and bathochromically shifted by 8 nm. Planar organic dyes like BODIPY are prone to π-stacking with the planes of the molecule laying parallel to one another and thus aggregate in solution. The displacement of these planes, defined as the slip angle between the dye units defines the nature of the aggregate.[6] At a slip angle of 54.7°the aggregate and monomers have degenerate excited states and fluoresce as normal. At a slip angle of lower than 54.7°a J-aggregate can form, characterized by a red-shift in absorption and emission when compared to the monomer, with small Stokes shifts and sharpened spectral features.[7] At slip angles higher than 54.7°H-aggregates can be formed and the upper excited state is accessible leading to a high-energy transition and hence a hypsochromic shift in absorption and emission, with very low fluoresence quantum yields.[6,8] Since a red shift is observed between the two species, it should not be ruled out that BOD2 forms J-aggregates in solution, however the broadening of the

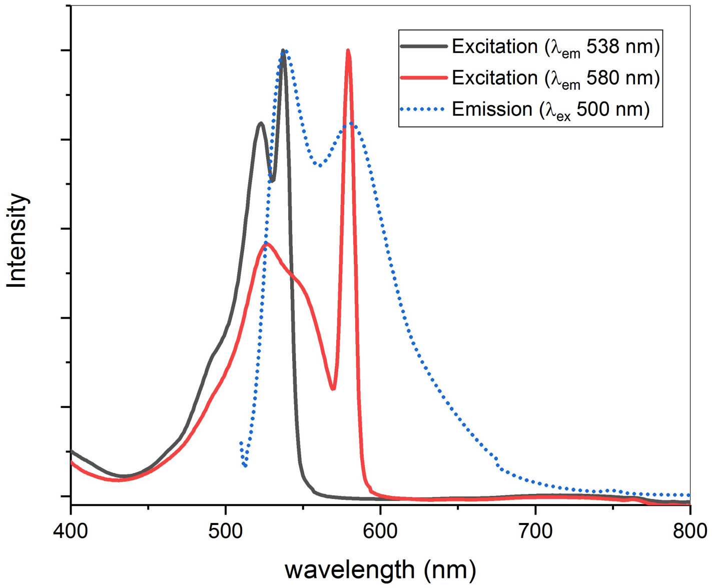

Figure 4.7: Emission spectrum (blue) and excitation spectra associated to the emission bands at 538 nm (black) and 580 nm (red) for BOD2

absorbance and emission profiles for this species indicates that the rotational effects of the substituted phenyl groups may cause the observed photophysical properties rather than any aggregate formation.

The formation of aggregates in solution usually leads to lower device performance in a DSC, due to aggregation on the surface on the NiO semiconductor surface. This multilayer of dye leads to competition for the absorption of irradiated photons and non-radiative recombination. As only the first monolayer of dye is electronically coupled to the surface of the semiconductor via the carboxylic acid anchor group, any excitation of the other dye species in the system causes loss of potential photocurrent that could be generated by dyes bound to the surface of the semiconductor. Dye aggregates on the surface can also lead to recombinative losses by quenching of the charge separated state, by recombination of the photogenerated holes localized in the semiconductor. Despite the addition of the two phenyl substituents to the alpha position and the extended conjugation of BOD2, the UV-Vis absorption and emission of the molecule are not significantly bathochromically shifted. This can presumably be attributed to the phenyl rings, although coupled directly

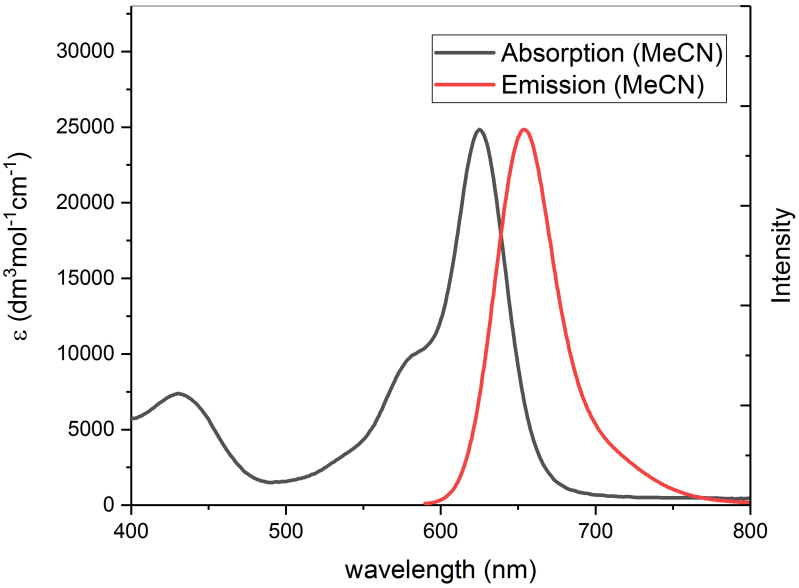

Figure 4.8: Normalised absorption (black line) and emission (red line) of BOD3 in acetonitrile solution. Excitation wavelength (λ_{ex}) = 585 nm

to the core of the chromophore, which lie orthogonal to the plane of dipyrromethane nucleus and do not contribute to an extended π system.

BOD3 shows a significant bathochromic shift in both absorption and emission compared to both BOD1 and BOD2 (Figure 4.8) consistent with previous reports of cyclicly contrained BODIPY.[9] The BNO hexacyclic ring formed between the alpha phenolic units and the BF_2 unit leads to a constrained cyclic system which causes the α-substituents to be forced closer to planarity with the dipyrromethane nucleus of the chromophore. BOD3 does not show any aggregation behaviours in solution, both the absorption and emission are well defined and display typical BODIPY-like features, however the spectra are slightly broadened.

A comparison of the steady state UV-Visible spectrum for dyes BOD1-3 can be seen in Figure 4.9. The overall broadening of the absorption profile of BOD3 vs. BOD1, alongside the increased contribution of the higher energy absorbance band at ca. 425 nm support the theory that the meso-phenyl group and 1,7 substituted phenyl groups in

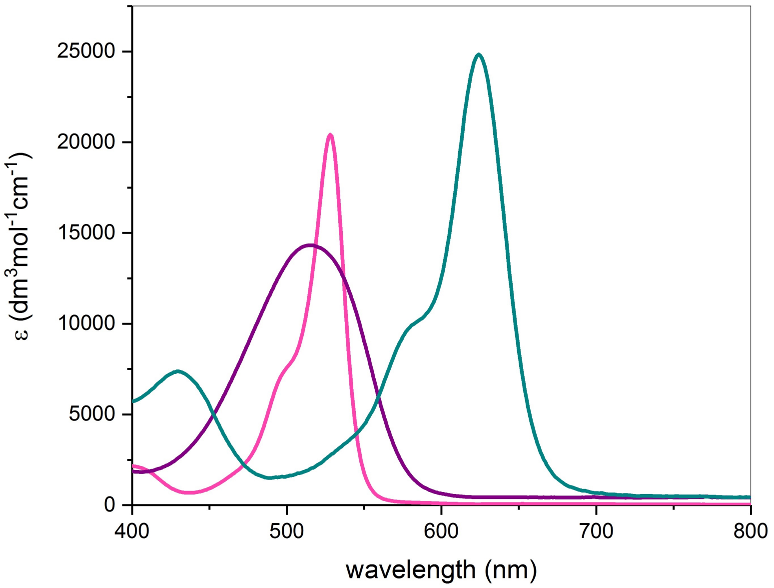

Figure 4.9: UV-Visible absorption spectra of BOD1 (pink), BOD2 (purple) and BOD3 (green) recorded in dry, degassed acetonitrile.

BOD3 are more electronically coupled to the BODIPY core and therefore has increased electronic communication between the two sub-units. This is reinforced by comparing the structures of the two dyes, specifically at the 1,7- positions. Many reports have shown that BODIPY containing alkyl-substituents on the 1,7-position with a meso-aryl substituent force the geometry of the meso-group to lie orthogonal to the plane of the core. BOD1 has two alkyl substituents preventing the free rotation of the meso-aryl ring around the C2 axis of the dye, this hindering any electronic communication between the core and the anchor group. BOD3 conversely has no substituents in the 1,7- positions, the ability for uinhindered rotation and therefore a more planar geometry is enhanced and overall electronic communication between the core and anchor group is increased.

The emission is also bathochromically shifted, to both BOD2 and BOD1 due to the constrained multi ring system contributing to a larger π-system located over the whole molecule. The stokes shift is increased to ca. 29 nm (vs. 8 nm for BOD1 and 26 nm for BOD2) indicating higher reorganisation energy in the excited state leading to radiative energy loss to vibrational relaxation pathways or to the surrounding solvent. In summary, BOD1 and BOD3 exhibit typical characteristics of BODIPY dyes, with large extinction coefficients, small Stokes shifts and narrow and well defined absorbance profiles, with emission spectra close to the mirror image of the absorption. BOD3 is bathochromically shifted in both absorption and emission vs BOD1 by ca. 103 nm (absorption) and 118 nm (emission). Band broadening observed in both absorption and emission of BOD3, alongside a larger contribution of the higher energy absorption band at ca. 425 nm indicate a higher degree of electronic communication between the BODIPY core and the benzoic anchor group. BOD2 shows aggregation behaviour in solution, indicated by the broad featureless absorption and two emissive species in solution. BOD2 is also hypsochromically shifted to both BOD1 and BOD3. The pendant phenyl groups in the α-position do not contribute to the extended π-system and therefore do not reduce the HOMO-LUMO gap and subsequentlyhave limited influence to the $_{max}$ of the dye . As the phenyl groups are free to rotate and are not constrained as in BOD3, emission appears to be quenched by vibrational and/or rotational relaxation pathways from the excited state.

4.4 Electrochemistry

The electrochemical properties of all three dyes (BOD1-3) were measured in acetonitrile to determine the oxidation and reduction potentials of the dyes to asses their suitability for use in a p-DSSC (Figures 4.10 - 4.13). These results are summarised in Table 4.2. The driving forces for injection into the p-type semiconductor and dye regeneration by the redox electrolyte (ΔG_{inj} and ΔG_{reg}) can then be estimated. A three electrode setup consisting of a glassy carbon working electrode, a platinum wire counter electrode and an Ag/Ag$^+$ reference electrode were used. The Ag/Ag$^+$ reference electrode was comprised of a silver wire immersed in a solution of the supporting electrolyte with a small amount of silver nitrate, separated from the sample solution by a Vycor glass frit. The supporting electrolyte was 0.5M tetrabutylammonium perchlorate. The electrodes were calibrated by using ferrocene as internal standard and determining the potential of the ferrocene/ferrocenium redox couple by cyclic voltammetry.

Figure 4.10 shows the oxidative cyclic voltammogram and differential pulse voltammogram

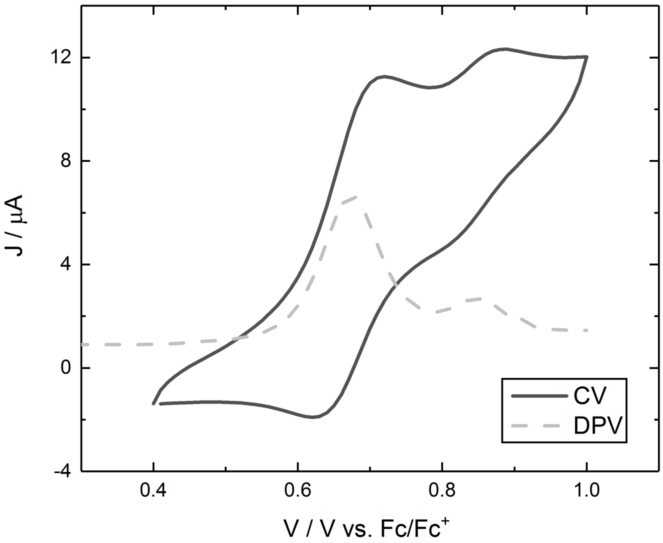

Figure 4.10: Oxidative cyclic voltammogram (100 mV s^{-1}) and differential pulse voltammogram (100 mV s^{-1}) of BOD1 (1 mM) measured in acetonitrile with 500 mM supporting electrolyte ($TBAClO_4$). A glassy carbon working electrode, platinum wire counter electrode and Ag/Ag^+ reference electrode were used.

(DPV) of BOD1 in 0.5M $TBAClO_4$ in acetonitrile as the supporting electrolyte. The oxidative scan was started close to 0.4 V vs Fc/Fc^+. Earlier in the scan from 0-0.4 V almost no current flowed. At 0.57 V vs. Fc/Fc^+ an anodic current appeared attributed to the oxidation of the analyte BOD1 to the $BOD1^+$ cation. This current increased as the scan was taken to more positive potentials as the concentration of $BOD1^+$ at the glassy carbon electrode increased. Slightly past the redox potential of BOD1/$BOD1^+$ as the concentration of BOD1 was depleted on the surface of the electrode the current decreased again. At more positive potentials the current increases again indicating a second oxidative process occurring at the electrode attributed to oxidation of $BOD1^+$ to $BOD1^{++}$. As before the current begins to decrease as the concentration of $BOD1^+$ cations at the electrode decrease. Upon reversal of the scan a small cathodic peak formed at 0.83 V that is difficult to resolve. At a more negative potential on the reverse sweep another cathodic peak appears at 0.64 V indicating the reduction of $BOD1^+$ back to BOD1.

The reductive scan of BOD1 (Fig. 4.11) began at -1.0V vs Fc/Fc^+ and the reduction

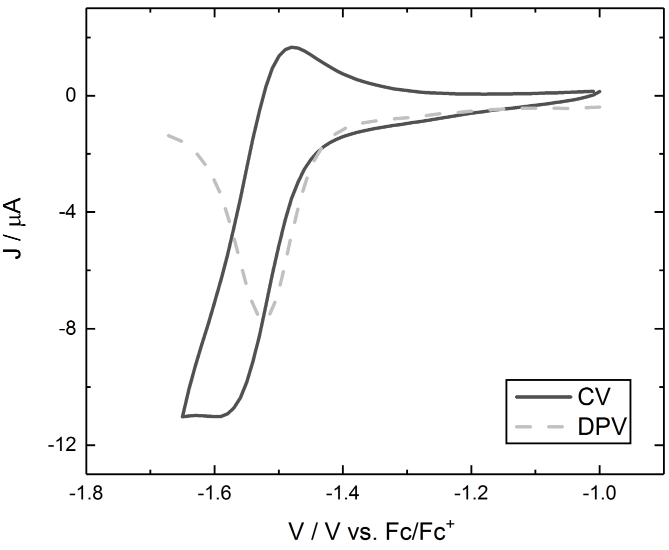

Figure 4.11: Reductive cyclic voltammogram (100 mV s^{-1}) and differential pulse voltammogram (100 mV s^{-1}) of BOD1 (1 mM) measured in acetonitrile with 500 mM supporting electrolyte (TBAClO$_4$). A glassy carbon working electrode, platinum wire counter electrode and Ag/Ag$^+$ reference electrode were used.

of BOD1 to BOD1$^-$ was indicated by an increase in cathodic current at approx -1.35 V vs Fc/Fc$^+$. As the concentration of BOD1 at the electrode decreased and eventually depletes, the cathodic current decreases. No further reduction processes were observed within the solvent window.

Figure 4.12 shows the reductive differential pulse voltammagram and reductive cyclic voltammogram for BOD2. The onset of the cathodic current occured at ca. -0.9 V vs Fc/Fc$^+$ and peaked at ca. 1.2 V vs Fc/Fc$^+$. Reversing the scan produced an anodic current associated with the reoxidation of the reduced species at the electrode at ca. -1.35 V vs Fc/Fc$^+$.

Figure 4.13 shows the reductive cyclic voltammogram of BOD3 overlaid with the differential pulse voltammogram reductive scan. The onset of the cathodic current begins at ca. -1.1 V vs Fc/Fc$^+$ and peaks at -1.29 V vs Fc/Fc$^+$. Upon reversal of the scan the anodic peak current is observed. The peak analysis data for the three dyes are presented

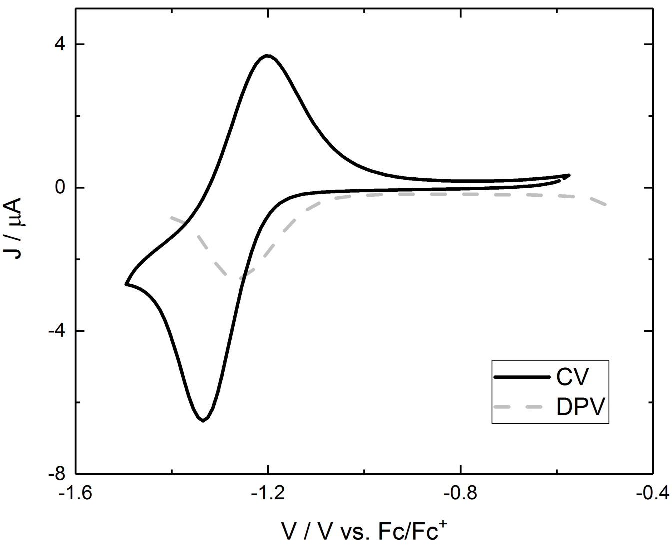

Figure 4.12: Reductive cyclic voltammogram (100 mV s^{-1}) and differential pulse voltammogram (100 mV s^{-1}) of BOD2 (1 mM) measured in acetonitrile with 500 mM supporting electrolyte ($TBAClO_4$). A glassy carbon working electrode, platinum wire counter electrode and Ag/Ag^+ reference electrode were used.

in Table 4.3.

For a reaction to be fully reversible the peak position ($U_{1/2}$) should be independent of scan rate and the peak separation between the anodic peak current and the cathodic peak current should be approximately 59 mV at 298 K.[10] Figure 4.14 shows the peak analysis of BOD1-3 vs the scanrate. The exact values are detailed in Table 4.3. For all three systems the peak separation was smaller than 59 mV with BOD2 and BOD3 increasing in peak separation with scanrate. The $U_{1/2}$ peak position remains independent of scanrate, with small variations being attributed to diffusion limitations at the electrode at slower scan rates.

For all three dyes the reduction has been shown to be reversible, as is characteristic of BODIPY chromophores and suitably makes them good candidates for use in p-type DSC. For longevity of device performance the dye must be readily capable of receiving an electron from the NiO valence band in order to propagate current though the electrochemical

	D^+/D / V	D/D^- / V	D^*/D^- / V	E_{0-0} / eV
BOD1	0.62	-1.54	0.79	2.33
BOD2	0.67	-1.28	1.07	2.35
BOD3	0.69	-1.29	0.64	1.93

Table 4.2: Electrochemical properties of BOD1-3 in acetonitrile solution with 500 mM $TBAClO_4$. D^+/D (ground state oxidation potential) and D/D^- (ground state reduction potential) were determined from the differential pulse voltammograms. D^*/D^- (excited state reduction potential) was calculated using $D^*/D^- = D/D^- + E_{0-0}$.

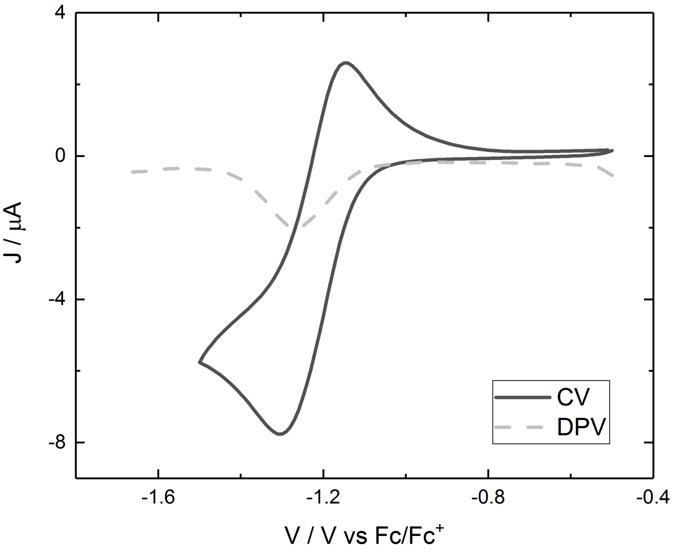

Figure 4.13: Reductive cyclic voltammogram (100 mV s^{-1}) and differential pulse voltammogram (100 mV s^{-1}) of BOD3 (1 mM) measured in acetonitrile with 500 mM supporting electrolyte ($TBAClO_4$). A glassy carbon working electrode, platinum wire counter electrode and Ag/Ag^+ reference electrode were used.

BOD1			
Scanrate / V s^{-1}	U_{pa}	U_{pc}	$U_{1/2}$
0.05	-1.48	-1.60	-1.54
0.1	-1.48	-1.59	-1.54
0.2	-1.48	-1.58	-1.53
0.5	-1.48	-1.58	-1.53
1.0	-1.48	-1.58	-1.53
BOD2			
Scanrate / V s^{-1}	U_{pa}	U_{pc}	$U_{1/2}$
0.05	-1.11	-1.24	-1.18
0.1	-1.05	-1.29	-1.17
0.2	-1.01	-1.32	-1.17
0.5	-0.96	-1.38	-1.17
1.0	-0.98	-1.38	-1.18
BOD3			
Scanrate / V s^{-1}	U_{pa}	U_{pc}	$U_{1/2}$
0.05	-1.14	-1.32	-1.23
0.1	-1.15	-1.30	-1.23
0.2	-1.12	-1.35	-1.24
0.5	-1.09	-1.40	-1.24
1.0	-1.12	-1.38	-1.25

Table 4.3: Peak analysis data for BOD1-3. All values are taken from the reductive cyclic voltammograms and reported in V vs. Fc/Fc^{+}

system.

Only BOD1 shows reversible oxidation in solution. It has been well documented that the oxidation to the BODIPY radical anion can be stabilised with alkyl substituents in the free pyrrolic positions.[11] Without these substituents the reacting BODIPY radical anion is prone to side reactions rendering the oxidation irreversible as seen for both dyes BOD2 and BOD3. The formation of the reactive radical cation on the pyrrolic core can undergo dimerization reactions on the BODIPY core and lead to formation of oligomeric structures.[12]Although the unsubstituted BODIPY is more prone to these dimerization reactions, Heiland and coworkers have shown that 2,6-substituted BODIPY dyes are still prone to dimerization upon oxidation through the loss of a substituent.[13]

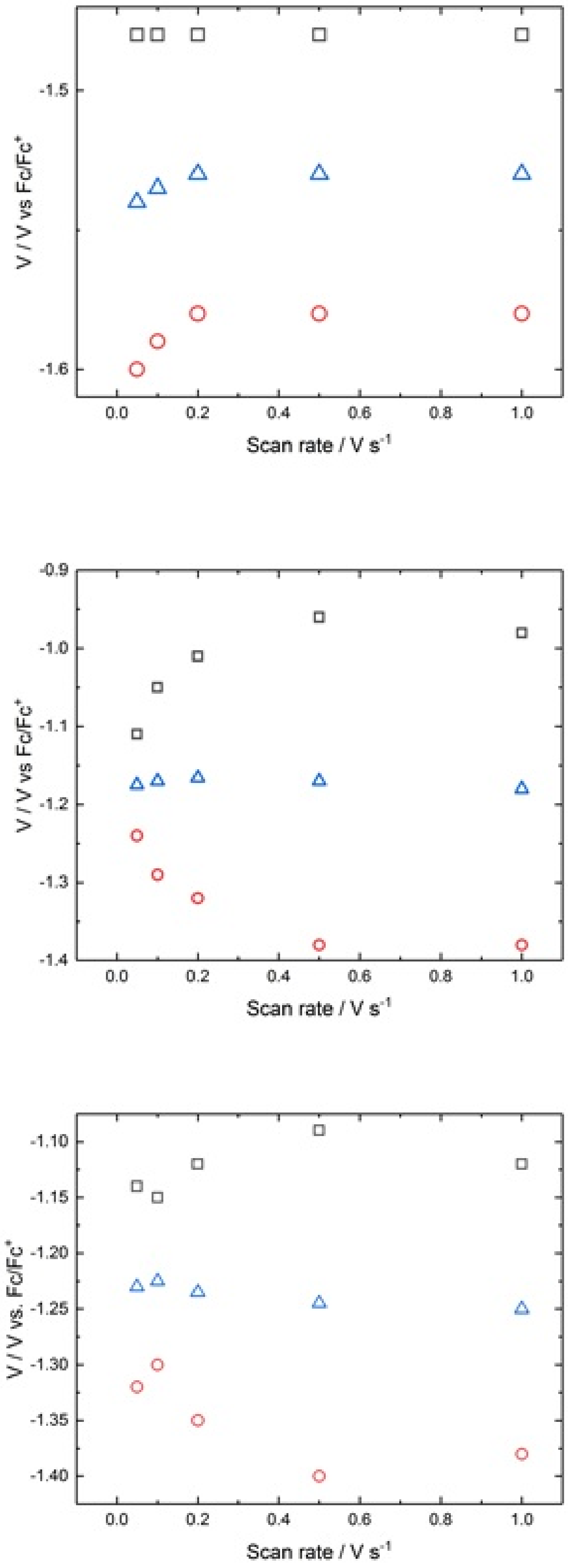

Figure 4.14: Peak analysis of BOD1 (top), BOD2 (middle) and BOD3 (bottom) at different scan rates. Peak voltages: U_{pa} (squares); U_{pc} (circles) and $U_{1/2}$ (triangles.)

	$E_{red}(S/S^-)$ / V	E_{0-0} / eV	$E_{red}(S^*/S^-)$ / V	ΔG_{inj} / V	ΔG_{reg} / V
BOD1	-1.54	2.33	0.79	-0.91	-0.72
BOD2	-1.28	2.35	1.07	-1.19	-0.46
BOD3	-1.29	1.93	0.64	-0.76	-0.47

Table 4.4: Calculated driving forces for electron transfer processes within p-DSC device. All potentials are reported vs Fc/Fc+. Where E_{red} is the reduction potential; E_{0-0} is the zero-zero energy; $E_{red}(S^*/S^*)$ is the excited state potential.

4.5 Analysing Driving Forces in p-DSSC

The redox potentials can be used to estimate the driving force for charge transfer between the dye and the semiconductor. The driving force for injection of an electron from an electron donor, here NiO, and an electron acceptor, here the dye molecule, is taken from the Rehm-Weller equation.[14] The driving force for photoinduced electron transfer can then be calculated using the excited state reduction potential (D*/D-) which is derived from the ground state reduction potential and the zero-zero energy. e = electronic charge and E_{VB}(NiO) = 0.54 V vs. NHE[15]

$$\Delta G_{inj} = e[E_{VB}(NiO) - E_{red}(D^*/D^-)] \tag{4.5}$$

$$E_{red}(D^*/D^-) = E_{red}(D/D^-) + E_{0-0} \tag{4.6}$$

The driving force for regeneration of the dye by the redox electrolyte can also be calculated using the ground state reduction of the dye and the redox potential of the electrolyte. Where $E(I_3^-/I_2^{\cdot -})$ = -0.19 V vs NHE.[16,17]

$$\Delta G_{reg} = e[E(I_3^-/I_2^{\cdot -}) - E_{red}(S/S^-)] \tag{4.7}$$

ΔG_{reg} was lowest for the two dyes without alkyl substituents on the BODIPY core BOD2 (-0.46 V) and BOD3 (-0.47 V). Whereas the alkyl substituted BOD1 had an increased

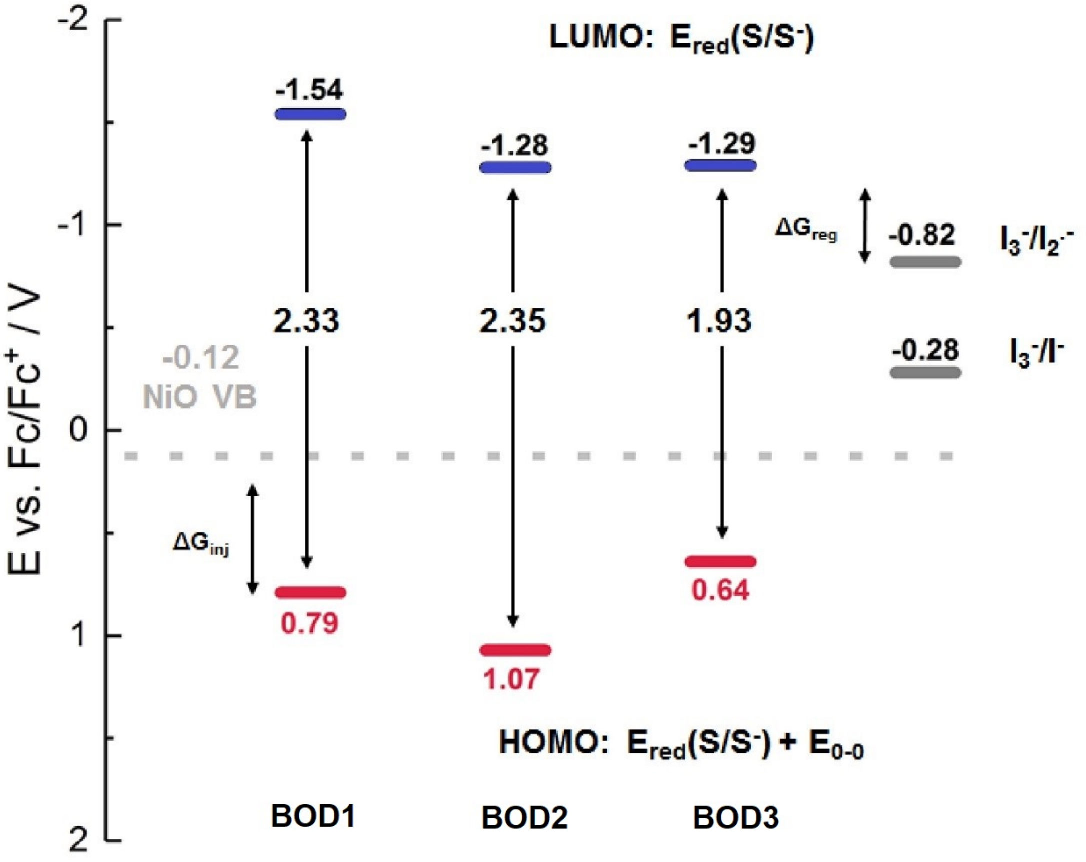

Figure 4.15: HOMO/LUMO energy level diagram for BOD1, BOD2 and BOD3 with driving forces for injection (Δ G$_{inj}$) and regeneration (Δ G$_{reg}$)

LUMO energy (-0.72). As the LUMO shifts to more negative potentials the driving force for regeneration increases, indicating BOD1 would have the most efficient regeneration by the redox electrolyte. As all Δ G_{reg} values were found to be negative it is likely that all three dyes would have thermodynamically favourable dye regeneration in an operating p-DSC.

ΔG_{inj} was found to be highest for BOD2 (-1.19 V) and lowest for BOD3 (-0.76 V). BOD1 lay between these two values (-0.91 V). Liu conducted a study correlating ΔG_{inj} and charge injection quantum yield and reported that 0.8 V of hole injection driving force is needed to achieve relatively high hole injection quantum yields for NiO based p-DSC.[18] Both BOD2 and BOD1 are above this value, however BOD3 has the closest Δ G_{inj} to this theoretical optimum value, laying 0.04 V below this postulated optimum.

4.5.1 Solar Cell Characteristics

Nickel oxide dye-sensitized solar cells were fabricated with dyes BOD1-3 to assess the photovoltaic performance of the three sensitizers in a complete device. NiO thin films were prepared as outlined in Section 4.2.4. The films were sensitized in dye baths containing 0.3 mM of the dye in CH_3CN. The photocathodes were paired with a platinum counter electrode and the empty cells were filled with a iodide/triiodide electrolyte containing either 0.1 M iodine (I_2) and 1 M lithium iodide (LiI) or 0.5 M I_2 and 1 M LiI. JV curves were taken to determine the short circuit current density (J_{SC}) and the open circuit voltage (V_{OC}). These values were used to calculate the fill factor and overall solar power conversion efficiency (PCE). For reference, p-DSC with P1 as the sensitizer were fabricated to check the consistency of the fabrication methods. The UV-Visible spectrum of the dyes were recorded on the NiO film to inspect how conjugation to the semiconductor affected the electronic absorption profile.

The UV-Visible spectra of the three BODIPY dyes in NiO thin film are presented in Fig. 4.16. All three dyes experience broadening of the absorbance profile when immobilized on a NiO thin film due to interactions between the chromophore and the semiconductor.

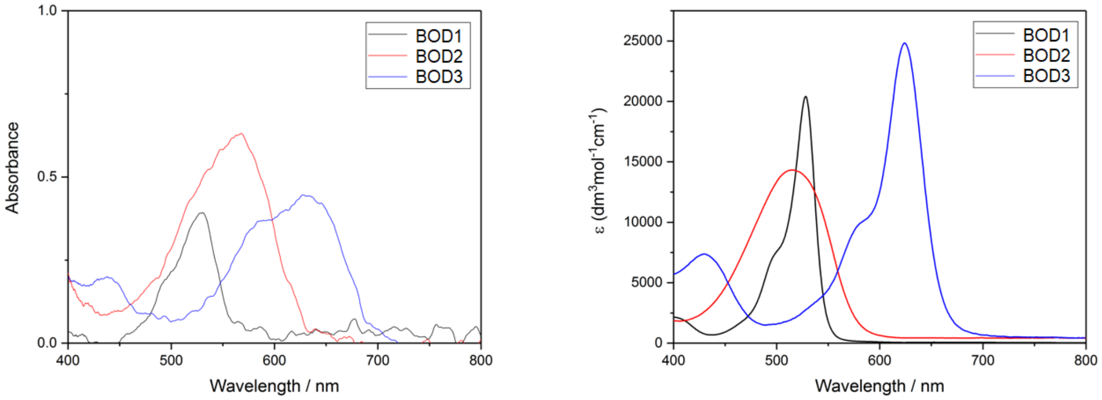

Figure 4.16: Absorbance spectra of BOD1 (black), BOD2 (red) and BOD3 (blue) in solution (right) and adsorbed onto NiO film (left)

When adsorbed onto NiO, P1 absorbs broadly from 400 nm - 600 nm. BOD3 is the most red shifted on NiO film, which agrees with the solution based experiments. BOD2 showed the highest absorbance on film.

The LHE (Light Harvesting Efficiency) for a dye adsorbed onto a semiconductor can be calculated using equation 4.8, where A is the absorbance at λ_{max}.

$$LHE = 1 - 10^{-A} \tag{4.8}$$

Based on the differences in the LHE for the three BODIPY dyes (BOD1 = 55.3%, BOD2 = 74.9%, BOD3 = 64.5%), it would be expected to see approximately a 10% increase in photocurrent (J_{SC}) between BOD1 and BOD3, and a similar increase in photocurrent between BOD3 and BOD2.

The solar cell characteristics of BOD1, BOD2 and BOD3 are shown in Table 3.1. The highest J_{SC} of the three BODIPY sensitizers was obtained by BOD2 (0.48 mA cm^{-2}). As this dye had the lowest absorption coefficient in solution and exhibits the highest absorbance on film, it appears that that BOD2 has the highest loading of dye on the surface of the semiconductor. BOD1 showed the lowest short circuit current and lowest absorbance on film.

	J_{SC} (mA cm^{-2})	V_{OC} (V)	η (%)	FF (%)
BOD1	0.12	0.07	0.004	36.90
BOD2	0.48	0.04	0.006	28.92
BOD3	0.21	0.06	0.003	29.37
P1	2.12	0.12	0.080	31.86

Table 4.5: Photovoltaic performance of nickel oxide dye-sensitised solar cells containing the three BODIPY dyes, with an electrolyte containing 0.1 M I_2 and 1.0 M LiI in CH_3CN. FF is the fill factor; η is the solar conversion efficiency

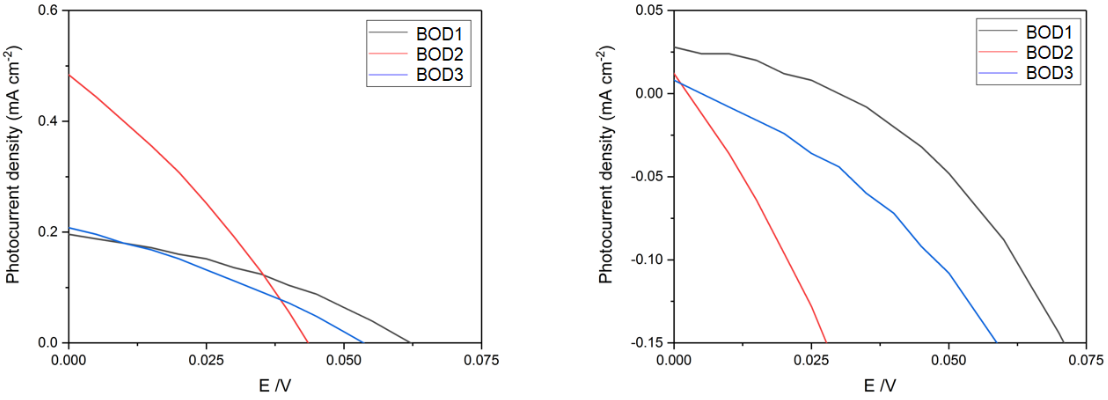

Figure 4.17: Photocurrent density-voltage curves for the NiO DSSC with BOD1 (black), BOD2 (red) and BOD3 (blue) under 1 sun illumination (left) and in the dark (right). Electrolyte: 0.1 M I_2 and 1.0 M LiI in CH_3CN.

Increasing the concentration of I_2 to [0.5 M] in the electrolyte shows an increase in the J_{SC} values for all the BODIPY sensitizers. This is attributed to the increase in concentration of the I_3^- in solution, providing more efficient regeneration of the reduced dye species at the electrode.

The V_{OC} for BOD2 and BOD3 p-DSSC is reduced with increased I_2 concentrations, BOD1 showed no change in V_{OC}. The aforementioned rise in J_{SC} comes with a reduction in V_{OC} as recombination between the increased concentration of I^- and the holes in the VB of NiO also increases. The filling of trap states near the VB edge contributes to a raising of the quasi-Fermi level and therefore a reduction in the maximum possible V_{OC} possible for the device. The presence of recombination sources (i.e I^- from the electrolyte) close to

	J_{SC} (mA cm^{-2})	V_{OC} (V)	η (%)	FF (%)
BOD1	0.56	0.07	0.015	37.84
BOD2	0.58	0.02	0.003	28.49
BOD3	0.42	0.02	0.002	28.84
P1	2.26	0.11	0.080	32.77

Table 4.6: Photovoltaic performance of nickel oxide dye-sensitised solar cells containing BOD1-3, with an electrolyte containing 0.5 M I_2 and 1.0 M LiI in CH_3CN. FF is the fill factor; η is the solar conversion efficiency

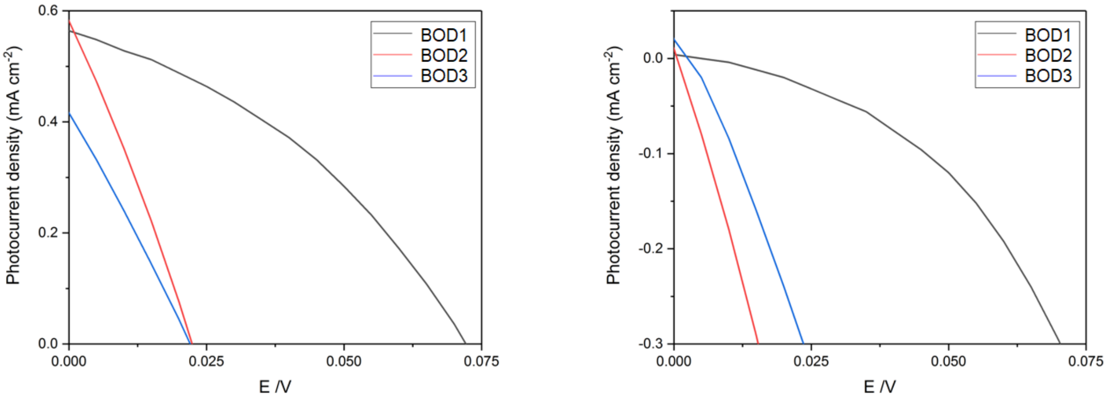

Figure 4.18: Photocurrent density-voltage curves for the NiO DSSC with BOD1 (black), BOD2 (red) and BOD3 (blue) under 1 sun illumination (left) and in the dark (right). Electrolyte: 0.5 M I_2 and 1.0 M LiI in CH_3CN.

the NiO|Dye interface causes rapid recombination and is shown in the JV measurements of the p-DSSC in the dark.

The performance of the solar cells with higher concentrations of I_2 showed a similar trend between the J_{SC} and the LHE. The light harvesting efficiencies of the dyes showed BOD2 > BOD3 > BOD1, and the J_{SC} values for the three p-DSC also show BOD2 > BOD3 > BOD1. The variance between the J_{SC} values for the p-DSC with lower iodine concentrations is much greater than those with higher concentrations of iodine. It appears that other factors may dominate the performance of the cell under low electrolyte concentrations, mainly the regeneration of the dye by the redox electrolyte and the charge injection from the valence band of the NiO to the excited dye. As V_{OC} is proportional to

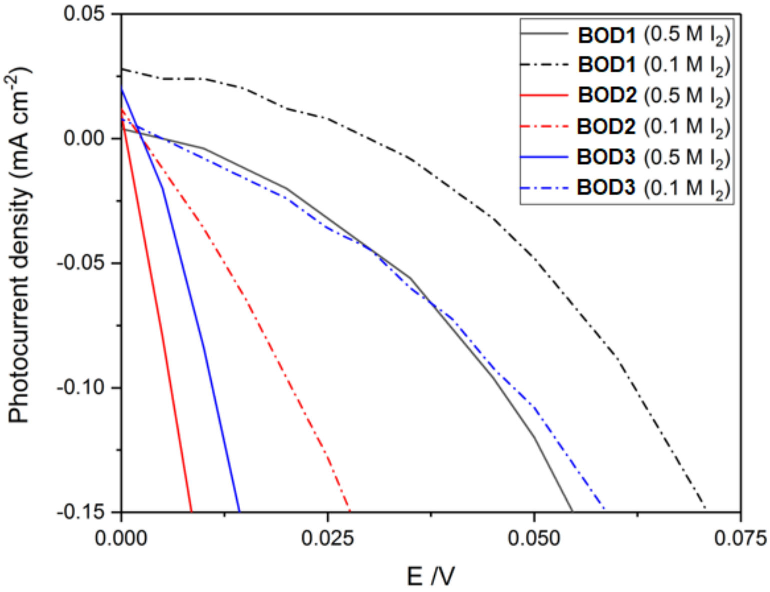

Figure 4.19: Photocurrent density-voltage curves for the NiO DSSC with BOD1 (black), BOD2 (red) and BOD3 (blue) in the dark with two different electrolyte compositions. (0.1 M I_2, 1.0 M LiI (dashed) 0.5 M I_2, 1.0 M LiI (solid)

carrier concentration, an increase in charge injection should lead to a higher V_{OC} meaning an increase in current should also lead to an increase in the V_{OC} of the DSSC. For all three dyes, there is an increase in the dark current for the devices with higher concentrations of triiodide, with more recombination at the electrolyte/electrode interface.

4.6 Conclusions

In this chapter, the optical and electrochemical properties have been reported for BOD1-3. Despite an extended π-system BOD2 did not exhibit a significant bathochromic shift, however BOD3 achieved absorbance into the red region of the visible spectrum. This shift should reduce the the spectral overlap of BOD3 with many dyes used in n-type systems, achieving one of the main goals put forward for an ideal p-type dye. All three dyes showed reversible reduction in a three electrode cyclic voltammetry setup. By pairing these two spectroscopic techniques, the driving forces for injection and regeneration have been estimated and shown that for all three dyes there is significant driving force for injection to promote charge transfer in a p-type DSSC. The structures of dyes BOD2 and BOD3 allow for further tuning via the unsubstituted β-positions on the BODIPY core, as well as the investigations of how changing the functional groups on the α-aryl groups could affect solar cell performance. By diversifying the dye series, the solubility issues present in both dyes could be overcome, allowing for higher yielding synthetic pathways and fine-tuning of the frontier orbitals. Although a moderate performance was seen for all three dyes there appears to be significant limitations on the J_{SC} at both high and low concentration of electrolyte. By reducing the concentration of I_2 in the electrolyte it appears that poor regeneration of the dye is a key factor in the limited J_{SC} for the dye series. In order to understand how the electron transfer processes occur in the device, a kinetic study of the dyes on NiO must be conducted to observe the recombination pathways in the p-DSSC. These findings should reinforce design of future dyes for p-DSSC.

References

(1) Swinehart, D. F. *Journal of Chemical Education* **1962**, *39*, 333.

(2) Kasha, M. *Discussions of the Faraday Society* **1950**, *9*, 14.

(3) Wood, C. J.; Summers, G. H.; Gibson, E. A. *Chem Commun* **2015**, *51*, 3915–3918.

(4) Bittel, A. M.; Davis, A. M.; Wang, L.; Nederlof, M. A.; Escobedo, J. O.; Strongin, R. M.; Gibbs, S. L. *Scientific Reports* **2018**, *8*.

(5) Saino, S.; Saikawa, M.; Nakamura, T.; Yamamura, M.; Nabeshima, T. *Tetrahedron Letters* **2016**, *57*, 1629–1634.

(6) Vu, T. T.; Dvorko, M.; Schmidt, E. Y.; Audibert, J.-F.; Retailleau, P.; Trofimov, B. A.; Pansu, R. B.; Clavier, G.; Méallet-Renault, R. *The Journal of Physical Chemistry C* **2013**, *117*, 5373–5385.

(7) Edwin E, J. *Nature* **1937**, *139*, 631–631.

(8) Fennel, F.; Gershberg, J.; Stolte, M.; Würthner, F. *Physical Chemistry Chemical Physics* **2018**, *20*, 7612–7620.

(9) Kim, H.; Burghart, A.; Welch, M. B.; Reibenspies, J.; Burgess, K. *Chem. Commun.* **1999**, 1889–1890.

(10) Elgrishi, N.; Rountree, K. J.; McCarthy, B. D.; Rountree, E. S.; Eisenhart, T. T.; Dempsey, J. L. *Journal of Chemical Education* **2017**, *95*, 197–206.

(11) Nepomnyashchii, A. B.; Bard, A. J. *Accounts of Chemical Research* **2012**, *45*, 1844–1853.

(12) Thompson, B. L.; Heiden, Z., *Redox Chemistry of BODIPY Dyes*; IntechOpen: 2019.

(13) Heiland, N.; Cidarér, C.; Rohr, C.; Piescheck, M.; Ahrens, J.; Bröring, M.; Schröder, U. *ChemSusChem* **2017**, *10*, 4215–4222.

(14) Nič, M.; Jirát, J.; Košata, B.; Jenkins, A.; McNaught, A., *IUPAC Compendium of Chemical Terminology*; IUPAC: 2009.

(15) Zhu, H.; Hagfeldt, A.; Boschloo, G. *The Journal of Physical Chemistry C* **2007**, *111*, 17455–17458.

(16) Boschloo, G.; Hagfeldt, A. *Accounts of Chemical Research* **2009**, *42*, 1819–1826.

(17) Hagfeldt, A.; Boschloo, G.; Sun, L.; Kloo, L.; Pettersson, H. *Chemical Reviews* **2010**, *110*, 6595–6663.

(18) Liu, Z.; Xiong, D.; Xu, X.; Arooj, Q.; Wang, H.; Yin, L.; Li, W.; Wu, H.; Zhao, Z.; Chen, W.; Wang, M.; Wang, F.; Cheng, Y.-B.; He, H. *ACS Applied Materials & Interfaces* **2014**, *6*, 3448–3454.

Part III

Probing the dye-semiconductor interface in p-type DSSC

Chapter 5

Probing dye-NiO interfaces using X-Ray Photoelectron Spectroscopy

5.1 Aims

Studying the dye-semiconductor interface in a DSSC is an important method of understanding the relative orbtial energies and orbital overlap present in an electron transfer pathway. Using X-ray photoelectron spectroscopy (PES) at varied X-ray excitation energies, it is possible to probe the same sample at various depths to understand how adsorption of a dye effects the bulk semiconductor material alongside the interface between the two materials. In this chapter a study of three BODIPY dyes (BOD1-3) has been conducted to assess their suitability for use in a p-DSSC. In previous chapters, information about the dye (HOMO/LUMO energies) have been estimated in solution. In this chapter the three dyes were studied in an environment that is closer to that of a working p-DSSC. The core orbitals of the dye molecule have been investigated and structural changes in the dye were observed at two different X-ray excitation energies. The changes in binding energy for these orbitals have been related to the structural changes seen in BOD1-3. The core levels for the NiO semiconductor have also been studied and a comparison of the unsensitized and senzitised semiconductor has been discussed. Finally the valence orbitals for the NiO semiconductor have been measured and compared to the HOMO of the dye to reassess key driving fores in the p-DSSC.

5.2 Experimental Methods

5.2.1 Photoelectron Spectroscopy

Photoelectron Spectroscopy (PES) is a characterization technique used for surface characterization of materials. The technique is based on the photoelectron effect which was first experimentally reported by Hertz in 1887 which describes the emission of electrons from a material when irradiated with photons of a certain energy. The photoelectric emission process is described in Equation 5.1, where hv is the photon energy, E_B is the binding energy, and E_X is the kinetic energy of the released electrons.

$$hv = E_B + E_X \tag{5.1}$$

In metals, the binding energy is referred to as the Fermi Level and therefore, in the case of sufficiently conducting materials, a new term ψ is introduced to describe the work function, here defined as the minimum energy required to remove an electron from a metal to a point immediately outside the solid surface to the vacuum surrounding the sample (Equation 5.2).

$$hv = E_B + E_X + \psi \tag{5.2}$$

In photoelectron spectroscopy the sample is irradiated with high energy photons and the kinetic energy of the emitted electrons are measured, then the binding energy of the electron can be calculated using Equations 5.1 and 5.2. By using a monochromatic source of photons at a set photon energy, a PES spectrum can be obtained.

Each element in a compound has a specific well defined binding energy, spread out over a wide range. Element specific binding energies can be measured and information about compound can be obtained by investigation over a small range of binding energies and analysing the changes in the peak positions of one element. Measurements on the valence band and Fermi level of a compound can be more complex and are composed of the bond forming electrons in a compound. They generally present as the lowest binding energy and form complex band structures from multiple atoms in a sample.

Using PES, important information can be obtained about the energy level alignment between the dyes and semiconductor in DSSC. As discussed previously, good orbital overlap between the frontier orbitals (HOMO or LUMO) and the semiconductor is required for efficient electron injection following photo-excitation processes in the DSSC. By mapping energy levels found in a DSSC these transfer processes can be understood and optimized.

Previous studies show that atoms in specific chemical states can be resolved in the core level spectra, acting as indicators for charge redistribution in the chromophore.[1] Hahlin reported dyes D9L2A1, D5A2L1 and D5L2A3 with two nonequivalent nitrogen atoms, found in the donor ($N1s_D$) and the acceptor ($N1s_A$). Both can be assigned to a core level peak in the PE spectrum and binding geometry can be obtained by the inspection of the changes in intensity at different probe wavelengths.[1] Srinivas also presented a study relating the DOS at the TiO_2 band edges with the electron withdrawing properties of cyanoacrylic and malonic acid anchor groups in TiO_2 based DSSC and approximates binding energy changes with various simulated adsorption configurations.[2] Other reports of structural ordering on multilayer films and on a TiO_2 surface come from O'Shea who has published multiple studies on the spatial distribution of molecules on a surface and the relationship at the interface between adsorbant and surface.[3] Rensmo utilized the X-ray PES to study semiconductor senzitized solar cells and valence band overlap between various metal sulfides, TiO_2 and some common polymers used for hole transport in these devices.[4]

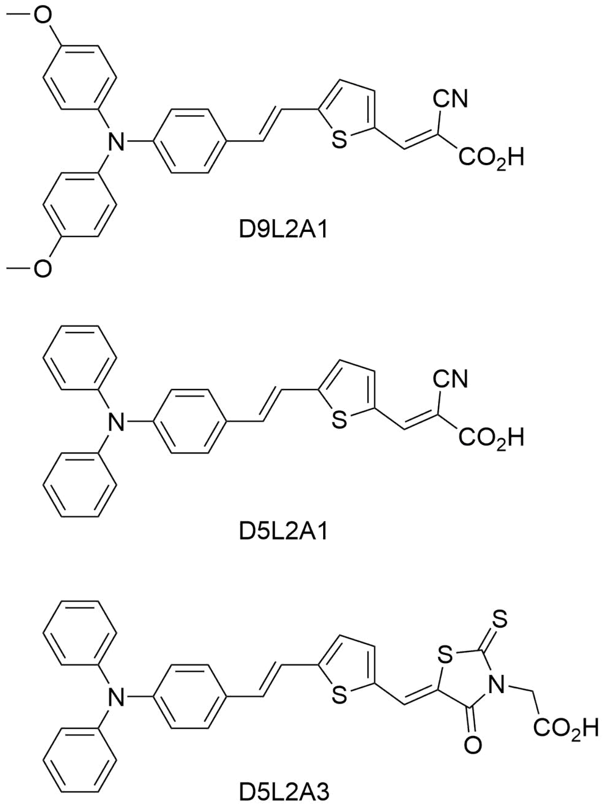

Figure 5.1: Molecular structures of D9L2A1, D5L2A1 and D5L2A3. The molecules are built up by three units, the donor unit (diphenylamine moiety), the linker group (thiophene moiety) andthe anchor unit (cyanoacetic moiety for D9L2A1 and D5L2A1 and rhodanine moiety for D5L2A3).

X-ray PES is routinely used to characterise the dye-semiconductor interface is n-type TiO_2 based devices, however studies involving p-type NiO are less common. Recently, Poldme reports studies of photocatalyst degradation on NiO films for a series of platinum and palladium catalysts, tracking the effects of the catalytic activity on the core levels of both the catalyst and the NiO semiconductor.[5] Previously, the energy levels for BOD1, BOD2 and BOD3 have been estimated in isolation (by electrochemistry and UV-Visible spectroscopy in solution), however to fully understand the alignment of the components in a DSSC it is important to study the dye when adsorbed onto the semiconductor and detail any changes in the core level or valence band to gain insight on any interactions post dye adsorption.

5.2.2 Experimental Details

All samples were run on the Diamond Lightsource IO9 Beamline. Mesoporous samples of NiO were mounted onto a Fluorine-doped Tin Oxide (FTO) substrate. These samples were either measured directly or sensitized with the three dyes BOD1, BOD2 and BOD3. Reference samples were prepared by immersing cleaned FTO glass into the dye solution to create multilayers of the dye to investigate the core levels of the dyes in absence of the semiconductor. The samples were attached to the sample holder with carbon tape to ensure electrical connection between the sample plate and the FTO substrate. Energy calibration was carried out by measuring the Au4f or Fermi level (84.00 eV and 0.00 eV respectively). All samples were measured under various X-ray excitation energies to probe the sample at different depths and chemical sensitivities. Core level measurements were carried out at 830, 835 or 2200 eV. Valence band spectra were measured with photon energies of 2200 eV, 830 eV, 250 eV or 120 eV. The undulator gap was detuned during measurements in order to reduce the X-ray intensity and prevent sample damage. The PES spectra were evaluated using Igor Pro 8.1 and all fits were performed with a Gaussian/Lorentzian profile with a ratio of 70% to 30%.

5.3 Results

5.3.1 Core Level Analysis

The electronic and molecular properties of dyes BOD1, BOD2 and BOD3 were studied using photoelectron spectroscopy. The peaks were assigned using the NIST database and the Handbook of XPS.[6] The N1s, O1s, F1s and B1s core level energies for the dye samples on FTO are summarised in Table 5.1.

The XPS results reflect the difference in coordination centre for the three dyes, with the sp3 hybridized boron centre in BOD3 bound to two nitrogen atoms and two oxygen atoms, whereas BOD1 and BOD2 both contain boron bound to two nitrogen and two fluorine atoms.

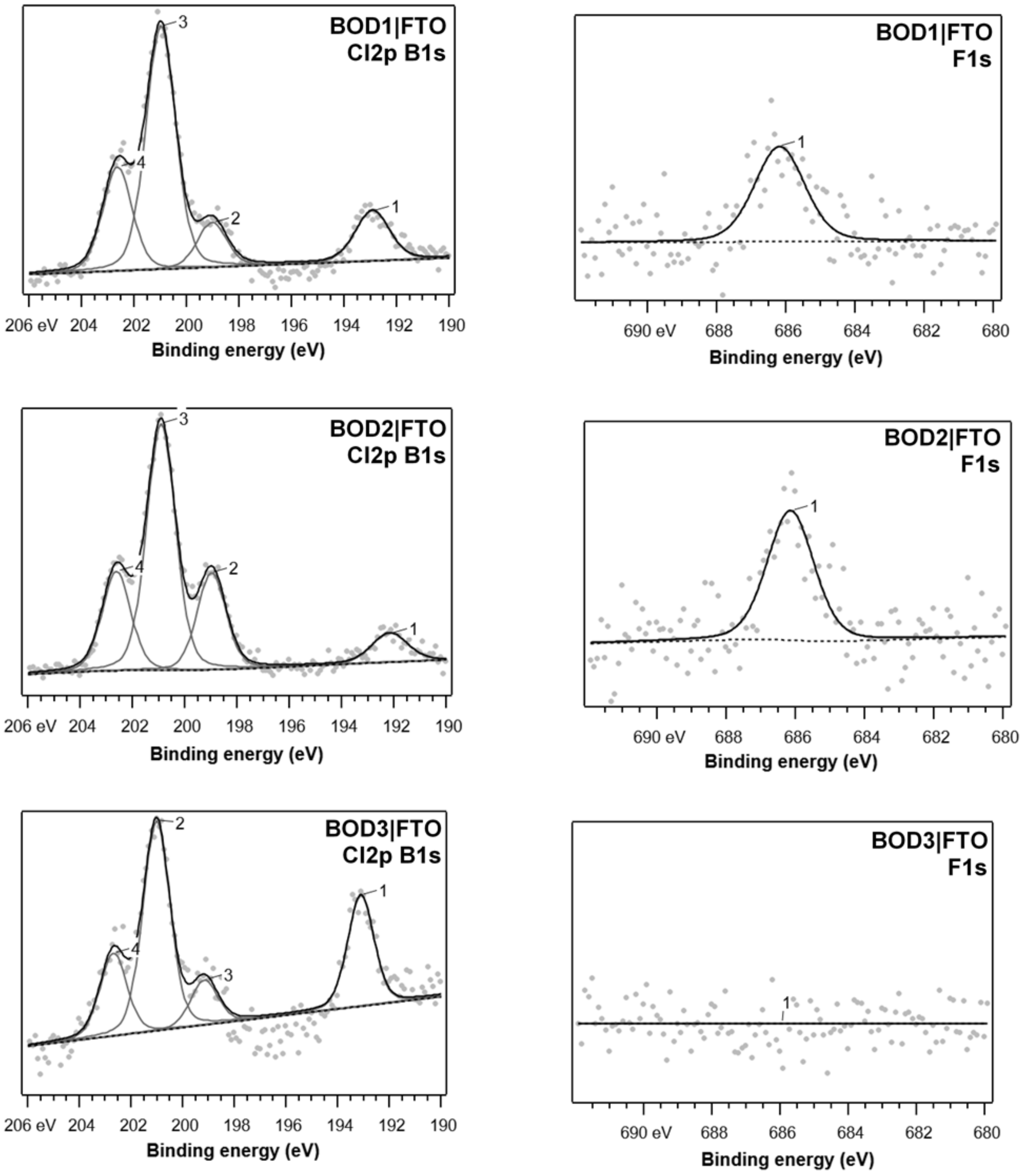

Figure 5.2: The Cl2p and B1s (left) and F1s (right) core level energies for BOD1-3 dye multilayer samples on FTO measured with a photon energy of 835 eV. The spectra were normalised to the Sn3d peak and calibrated against an external Au reference.

Core Level	BOD1/ eV	BOD2/ eV	BOD3/ eV
N1s	400.10	399.85	400.07
O1s $_{C=O}$ (CO_2H)	531.95	531.85	531.77
O1s $_{OH}$	532.98	532.94	532.59
O1s $_{NBO}$	-	-	533.92
O1s SnO_2	530.95	530.94	530.92
F1s	686.18	686.14	-
B1s	193.01	193.10	192.15

Table 5.1: Measured core level binding energies for dyes BOD1, BOD2 and BOD3 - B1s and F1s core level spectra were measured at 835 eV X-ray excitation energy, N1s, and O1s core level spectra were measured at 2200 eV X-ray excitation energy.

The B1s core level binding energies (Fig 5.2, left) show significant shifts in binding energy for BOD3 (192.15 eV) when compared to BOD1 and BOD2 (193.01 and 193.10 eV respectively) consistent with the change in bonding environment for BOD3. This is a promising result as previous attempts by groups to detect the B1s core level of BODIPY dyes have been unsuccessful due to the low sensitivity of the peak.[7]

The F1s spectra of the three dyes also reflect the difference in structure (Fig 5.2, right). The F1s core levels are present at similar binding energies (686.18, 686.14 eV) in both the BOD1 and BOD2 spectra, and are absent in the spectra of BOD3, which is consistent with the displacement of the fluorine atoms by the phenolic groups of BOD3. All three BODIPY dyes contain two equivalent nitrogen atoms which appear as one peak in the N1s core level spectrum (Figure 5.3, left). This peak is not affected by the coordination environment of the boron and is, instead, present at similar binding energies throughout the series. This is in agreement with the literature values of N1s core level binding energies for BODIPY dyes.[7]

The O1s spectra for the Dye|FTO samples (Fig 5.4, left) show three core level environments for dyes BOD1 and BOD2, which are assigned to the SnO_2 (ca. 530.95 eV[8]), and the two inequivalent oxygen environments found in the carboxyl anchor group (O1s$_{(C=O)}$ and O1s$_{(-OH)}$). Typically the hydroxyl group presents at higher binding energies than the

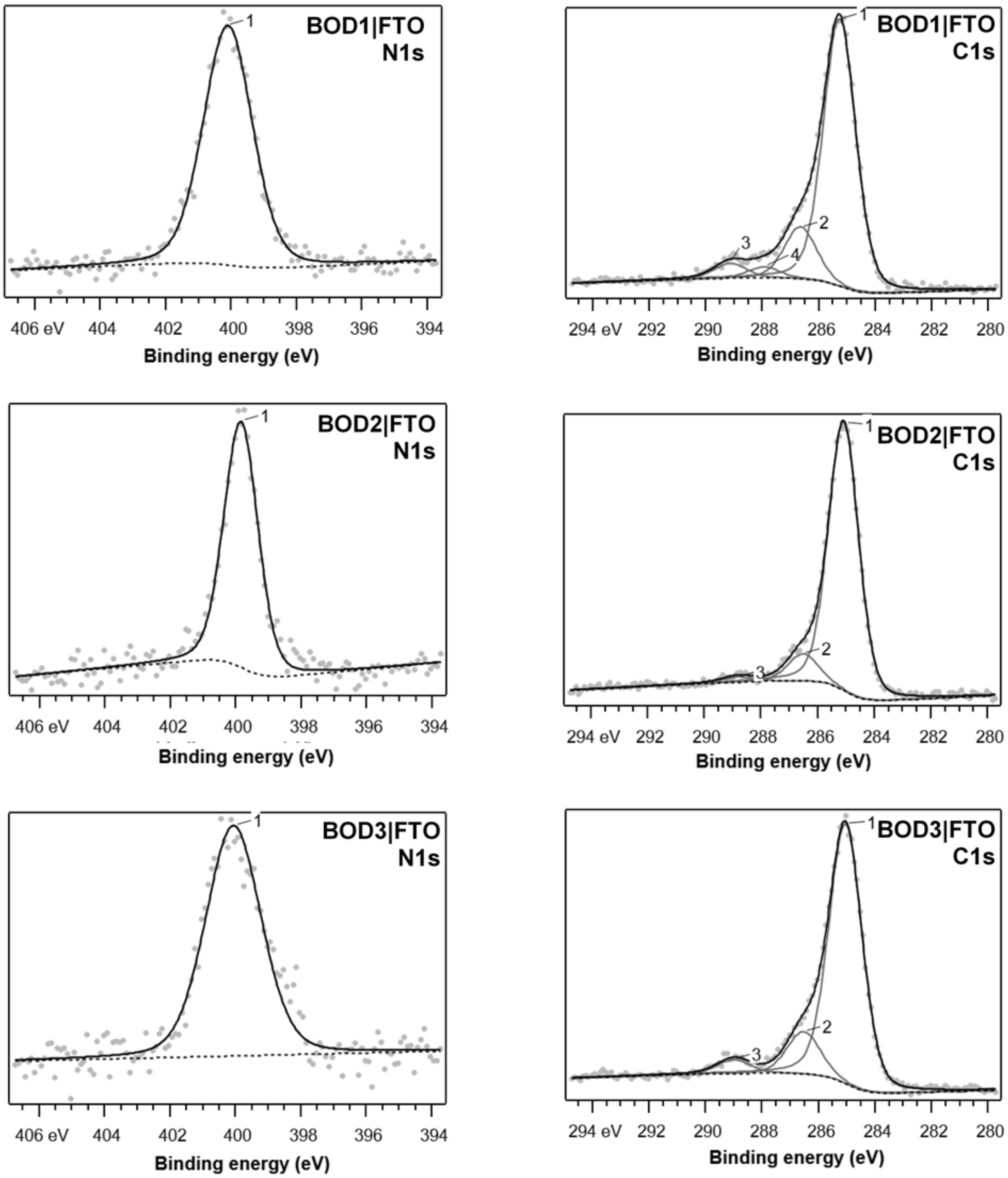

Figure 5.3: The N1s (left) and C1s (right) core level energies for BOD1-3 dye multilayer samples on FTO measured with a photon energy of 2200 eV. The spectra were normalised to the Sn3d peak and calibrated against an external Au reference.

carbonyl oxygen so the peaks can be fully assigned.[9] The remaining core level peak can be assigned to SnO_2. These three features are also present in the O1s spectra of BOD3, together with an additional O1s environment in the NNBOO tetrahedral B-coordination centre of the chromophore. In the spectra for the dye-sensitized NiO samples (Fig. 5.4, right), the NiO substrate O1s peak can be observed at lower binding energies than the SnO_2 peak. Consistent with the Dye|FTO spectra, the carboxylic acid O1s peaks are present at higher binding energies, however detailed analysis of the O1s spectra originating from the carboxylic acid groups is difficult, as the ex-situ preaparations also may introduce small amount of surface contamination, such as water or ethanol. Due to the resulting complexity of the spectra, the binding geometry and orientation for this dye series cannot be shown by these experiments.

	FTO /eV	NiO /eV	ΔBE /eV
BOD1			
O1s SnO_2	530.95	530.71	0.24
O1s NiO	-	529.24	-
O1s C=O	531.95	531.39	0.56
O1s -OH	532.98	532.41	0.57
BOD2			
O1s SnO_2	530.94	530.66	0.26
O1s NiO	-	529.28	-
O1s C=O	531.87	531.21	0.66
O1s -OH	532.94	531.96	0.02
BOD3			
O1s SnO_2	530.92	530.76	0.16
O1s NiO	-	529.30	-
O1s C=O	531.77	531.44	0.33
O1s -OH	532.59	532.30	0.29
O1s -NBO	533.60	533.33	0.27

Table 5.2: Comparison of the O1s core level binding energies of dyes BOD1-3 adsorbed onto FTO or NiO measured with 2200eV X-ray excitation energy. The spectra were normalised to the Sn4d (FTO) or Ni2p (NiO) and calibrated against an external Au reference.

The C1s core level spectra (Fig 5.3, right) show multiple carbon environments in the dye multilayer which persist when bonded to NiO as well as when deposited on FTO. This is consistent with the dye being adsorbed onto the NiO surface. A carbon atom bound to a carboxyl (C=O) rather than another carbon atom (C-C) experiences an increase of binding energy of ca. 4.5 eV.[10] Johanssen shows similar findings in a study of simple carboxylic acids on a variety of metal oxide substrates.[11] However detailed analysis of the carbon environments when adsorbed onto the substrate is difficult as the dye may be present in different configurations on the surface in addition to contamination during preparations of the sample leave surface residues which overlap with the C1s peaks arising from the dye multilayer.

X-ray photoelectron spectroscopy measurements were also carried out to study the effects of adsorption of the dye onto the core and valence orbitals of the NiO substrate. The NiO spectra for the blank and sensitized spectra can be seen in Figure 5.5.

There was no significant changes in the peak shape or peak ratios between the blank and sensitized NiO samples, indicating there were no substantial changes to the NiO upon adsorption of the dye. The unsensitized NiO thin film shows typical peaks seen for a nanocrystaline film. The Ni^{3+} and Ni^{2+} (1 and 2, Fig 5.5, top) mixed valence signals resulting from the annealing process can be seen at lower binding energies, as well as the corresponding satellite peaks (3).[12,13] Previous reports show the presence of $Ni^{(0)}$ metal in samples from incomplete oxidation of the $Ni^{(0)}$ metal during the annealing of the NiO films, however, this is not present at lower binding energies in these samples.[14] A comparison of the three dye sensitized NiO films to the blank NiO shows identical features for all 4 samples, indicating no significant changes to the Ni2p orbitals post dye adsorption (Fig. 5.5, bottom).

5.3.2 Valence Band Analysis - FTO

This section outlines overviews of the valence band spectra of the dye samples on FTO and adsorbed onto a NiO film. Expansions to the valence band and calculated values for

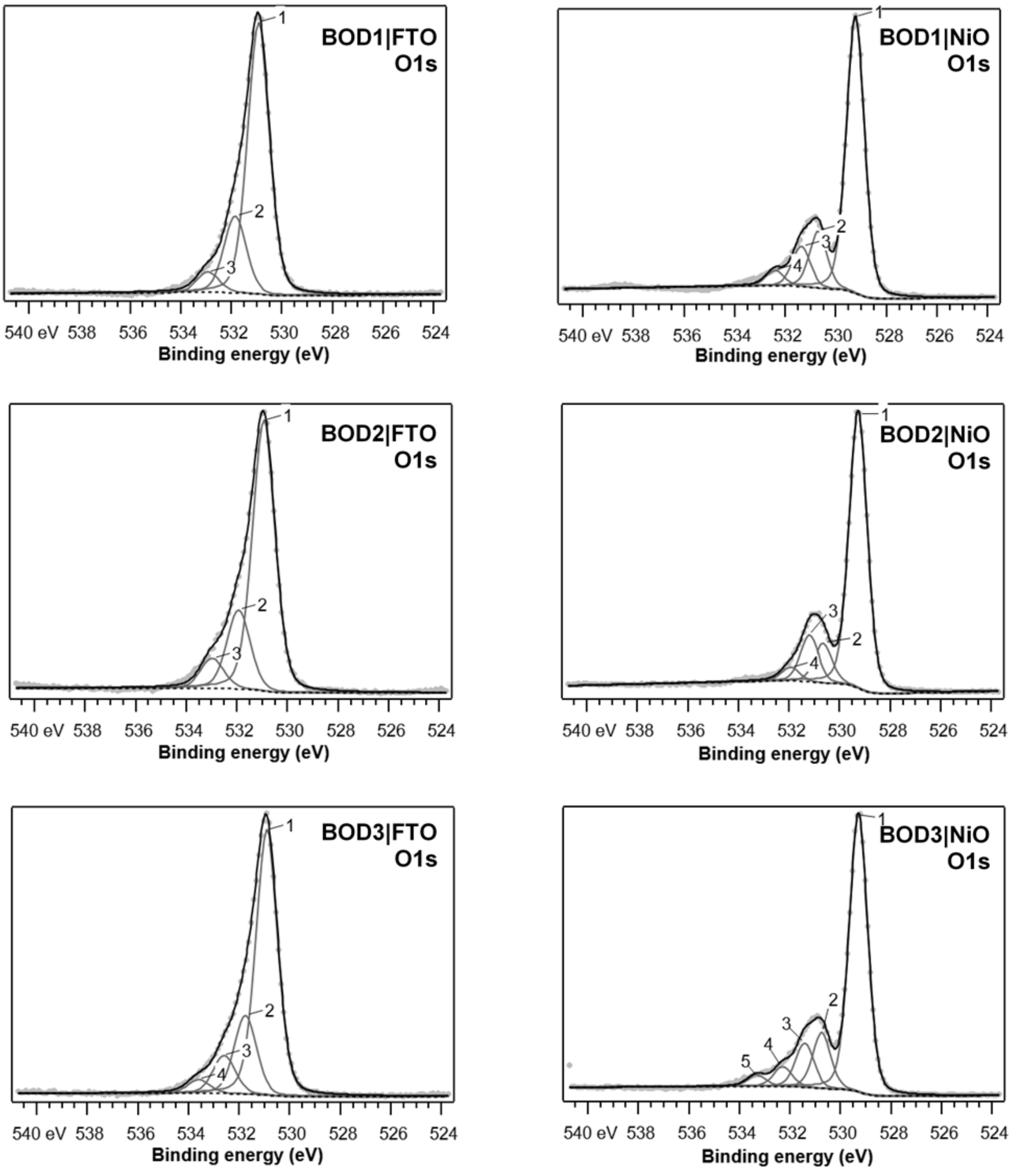

Figure 5.4: The O1s core level energies for BOD1-3 samples on FTO (left) and absorbed onto NiO (right) measured with a photon energy of 835 eV. The spectra were normalised to the Sn4d peak and calibrated against an external Au reference.

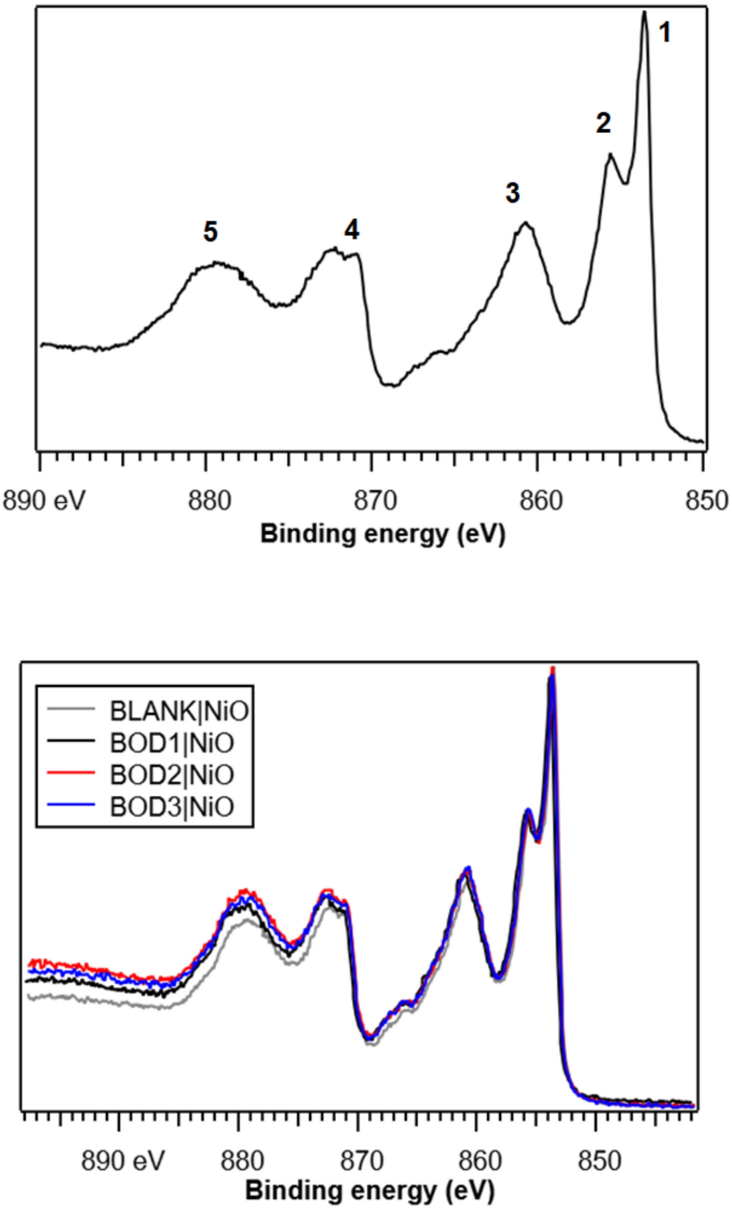

Figure 5.5: The Ni2p core level energies for the blank reference NiO sample (top) and dye-sensitized samples (bottom). Peak assignments - (1) - Ni^{2+} $2p_{(3/2)}$; (2) - Ni^{3+} $2p_{(3/2)}$; (3) - $Ni^{2+/3+}$ $2p_{(3/2)}$ satellite; (4) - Ni $2p_{(1/2)}$; (5) - Ni $2p_{(1/2)}$ satellite - ; The spectra were normalised to the Sn3d peak and calibrated against an external Au reference.

the Fermi level will be discussed in Section 5.3.4.

The valence photoelectron spectra for the dye multilayers on FTO, and the dye adsorbed onto a NiO thin film can be used to experimentally probe the character of the highest occupied energy states in the system. The valence spectra of FTO and the dye multilayers were probed using three different X-ray excitation energies to gather information about the bulk semiconductor materials and the interface between the dye and semiconductor.

Fig. 5.6 shows the valence photoelectron spectra for the FTO reference sample and the three dyes deposited on FTO at 2200 eV X-ray excitation energy. The major contribution to this spectra is the Sn4d peak (1) at 26.4 eV originating from the SnO_2 coating of the glass substrate. (Literature value Sn4d = 26.8 eV[15] The valence spectra for all four samples show identical features at this X-ray excitation energy, with the VB edge (2) clearly visible at 3 eV. Filled band gap states (3) can be observed at binding energies lower than the VB edge arising from the n-doping present in the FTO.

Inspection of the valence photoelectron spectra of the same samples at 250 eV (Figure 5.7) shows peaks in the spectra of the dye multilayers that are not present in the blank FTO reference sample, indicating that these features are contributions from the dyes in the valence spectra. (4, 5). The Sn4d orbital (appears at the same binding energy as the spectra under higher X-ray intensity, however the ratio between the Sn4d and valence orbitals decreases. The HOMO of the dye is difficult to see and is masked by the VB edge - the VB edge also becomes less defined at this X-ray excitation energy in comparison to the higher excitation energy spectra.

The valence photoelectron spectra of the dyes on FTO at 120 eV X-ray excitation energy (Figure 5.8) penetrates least far into the sample, causing a larger contribution from the dye orbitals compared to the FTO. The peaks previously seen fron the 250 eV X-ray excitation spectra of the valence band region persist to this X-ray excitation energy and the ratio of the Sn4d peak vs. the VB edge of FTO further decreases, confirming that these spectra are probing closer to the interface between the dye and the semiconductor than previously. The HOMO of the dye is largely masked by the FTO VB edge, however

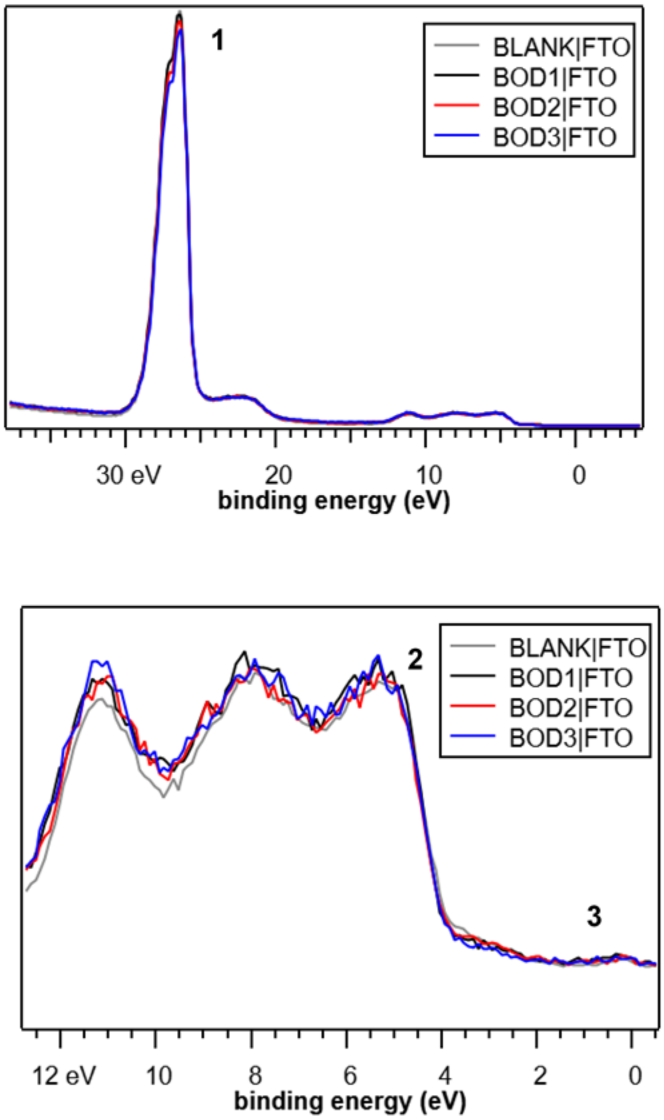

Figure 5.6: The valence levels of the FTO/BOD1, FTO/BOD2, FTO/BOD3 and FTO/BLANK reference samples measured with a photon energy of 2200 eV. (top) Expansion of the lower valence region 0-12 eV (bottom) of the four samples. The spectra were normalised to the Sn4d peak and calibrated against an external Au reference.

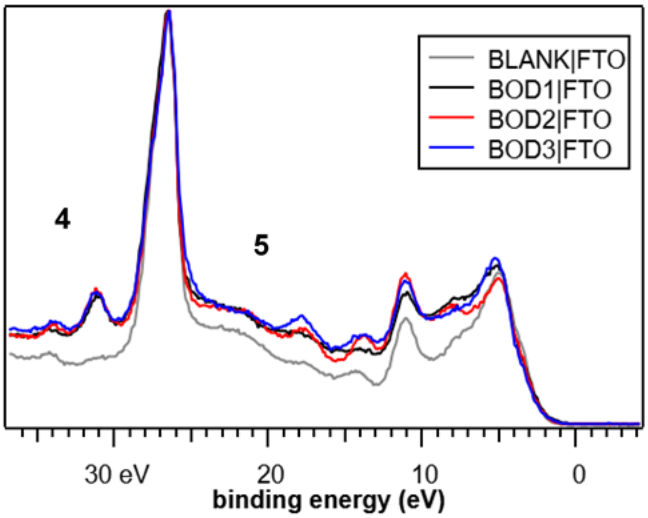

Figure 5.7: The valence levels of the FTO/BOD1, FTO/BOD2, FTO/BOD3 and FTO/BLANK reference samples measured with a photon energy of 250 eV. The spectra were normalised to the Sn4d peak and calibrated against an external Au reference.

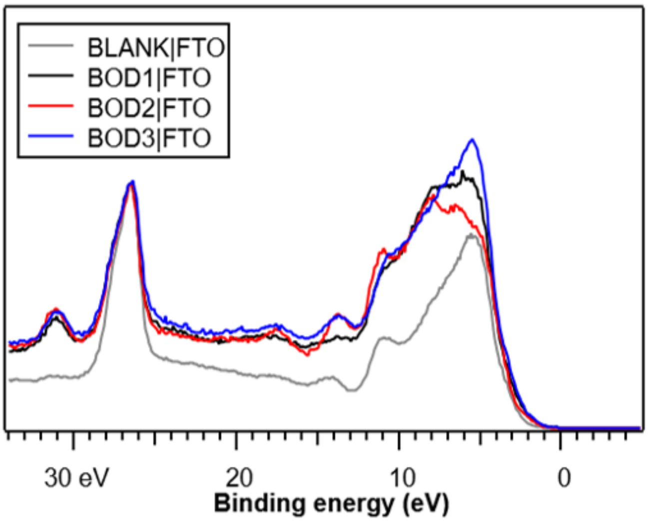

Figure 5.8: The valence levels of the FTO/BOD1, FTO/BOD2, FTO/BOD3 and FTO/BLANK reference samples measured with a photon energy of 120 eV. The spectra were normalised to the Sn4d peak and calibrated against an external Au reference.

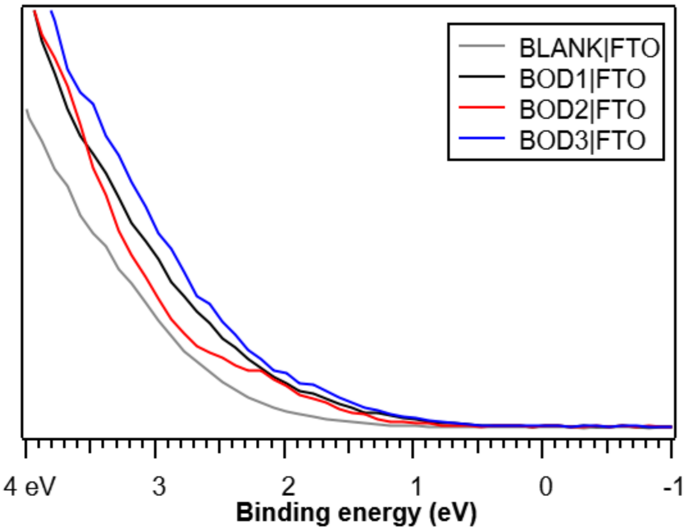

Figure 5.9: Expansion of the lower valence region -1 - 4 eV of the BOD1-3 multilayers on FTO with the blank reference sample measured with a photon energy of 120 eV. The spectra were normalised to the Sn4d peak and calibrated against an external Au reference.

a small signal extending past the VB edge can be seen at lower binding energies (Fig. 5.9). The energy level of the HOMO of BOD1, BOD2 and BOD3 have been calculated and discussed in Section 5.3.4.

5.3.3 Valence Band Analysis - NiO

The dye-sensitized NiO valence photoelectron spectra at 2200 eV X-ray excitation energy (Figure 5.10) have similar features, and the major contributions are the FTO substrate and the VB and Ni3p orbital of NiO.

As the dyes bind there are no significant changes to the NiO bulk material under these experimental conditions. The Sn4d peak is present for all samples except for BOD2, suggesting that the film thickness for the NiO may have been greater for the area probed in the BOD2-coated sample compared to the area probed in the other samples. As the X-rays did not penetrate far enough into the sample to the FTO substrate below the Sn4d peak cannot be seen in this spectrum. Another possible explanation could be the area of the film irradiated for the reference sample, BOD1 and BOD3 samples may contain crack

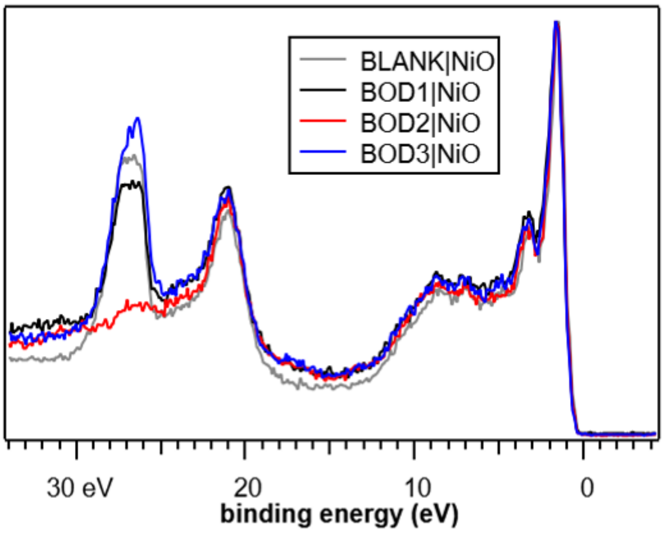

Figure 5.10: The valence levels of the NiO/BOD1, NiO/BOD2, NiO/BOD3 and NiO/BLANK reference samples measured with a photon energy of 2200 eV. The spectra were normalised to the Ni3p peak and calibrated against an external Au reference.

or imperfections in the NiO film, exposing the FTO below.

The valence photoelectron spectra for the dyes and the blank reference samples at 250 eV X-ray excitation energy (Figure 5.11) have largely the same features, with the main contribution coming from the Ni3p orbital, with some peaks originating from the dye being present in the spectra. The Sn4d orbital is no longer present at this X-ray energy due to the NiO film being deposited over the surface of the substrate. The peaks which have been assigned as contributions of the dye appear at similar binding energies to those seen for the dye samples on FTO. Dye adsorption onto a semiconductor is routinely modelled using a Langmuir isotherm, which assumes a monolayer of adsorbent onto the solid surface.[16,17] Contributions from the dye monolayer can still be seen on the valence spectra of the dyes adsorbed onto NiO, however the signals are much less defined due to the low amount of dye present in the sample when compared to the dye multilayers on FTO. All four sample show very similar features close to the VB edge, however a shift in the valence band position can be seen towards a more positive binding energy can be seen for all three of the dyed NiO films. (Fig 5.11.). The changes to the valence band upon

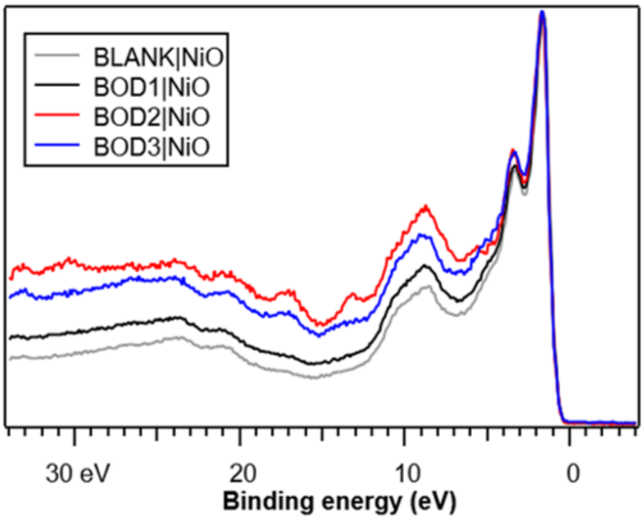

Figure 5.11: The valence levels of the NiO/BOD1, NiO/BOD2, NiO/BOD3 and NiO/BLANK reference samples measured with a photon energy of 250 eV. The spectra were normalised to the Ni3p peak and calibrated against an external Au reference.

dye adsorption are compared and discussed later.

The contributions from the dyes on the valence photoelectron spectra can be seen most clearly at 120 eV X-ray excitation energy (Figure 5.12), as the dye monolayer is found mostly on the surface of the semiconductor film, although as the annealing process forms a mesoporous later of NiO, some dye sits inside the pores of the sample and hence can be seen deeper into the sample.,[1819] The NiO VB can clearly be seen alongside contributions from the dye frontier orbitals. The HOMOs of the three dyes are fully masked by the NiO VB, indicating the frontier orbitals lie well within the valence band and are positioned well for electron injection from the VB of the semiconductor in a functioning p-type DSSC. (Fig. 1.12). As before the VB edge shows a shift to higher binding energies for all three samples upon dye adsorption (Figure 5.14).

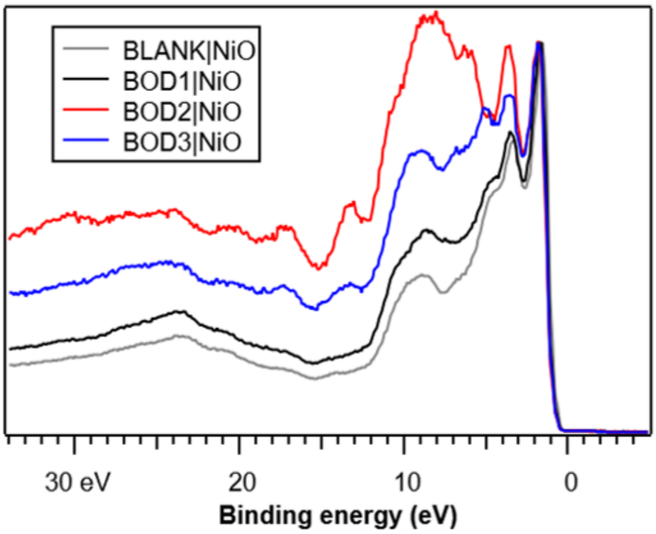

Figure 5.12: The valence levels of the NiO/BOD1, NiO/BOD2, NiO/BOD3 and NiO/BLANK reference samples measured with a photon energy of 120 eV. The spectra were normalised to the Ni3p peak and calibrated against an external Au reference.

5.3.4 Mapping Energy Levels in p-type DSSC

Dye HOMO Calculations

The positions for the HOMOs for the three dyes were taken from the valence PES spectra at 120 eV X-ray excitation energy. Although the valence PES spectra contain multiple features arising from contributions to the dye close to the VB edge, the calculations are taken from the binding energy region 0-4 eV. An expansion of the outermost occupied energy region for all three dyes alongside the blank NiO reference sample is shown in Figure 5.15. In this region the HOMO can be seen protruding past the VB edge for the FTO substrate. Although partially masked, it can be observed that the outermost energy structure for all three dyes differ in position and shape, a distinct shoulder can be seen for BOD2 and no such shoulder can be seen for BOD1 and BOD3.

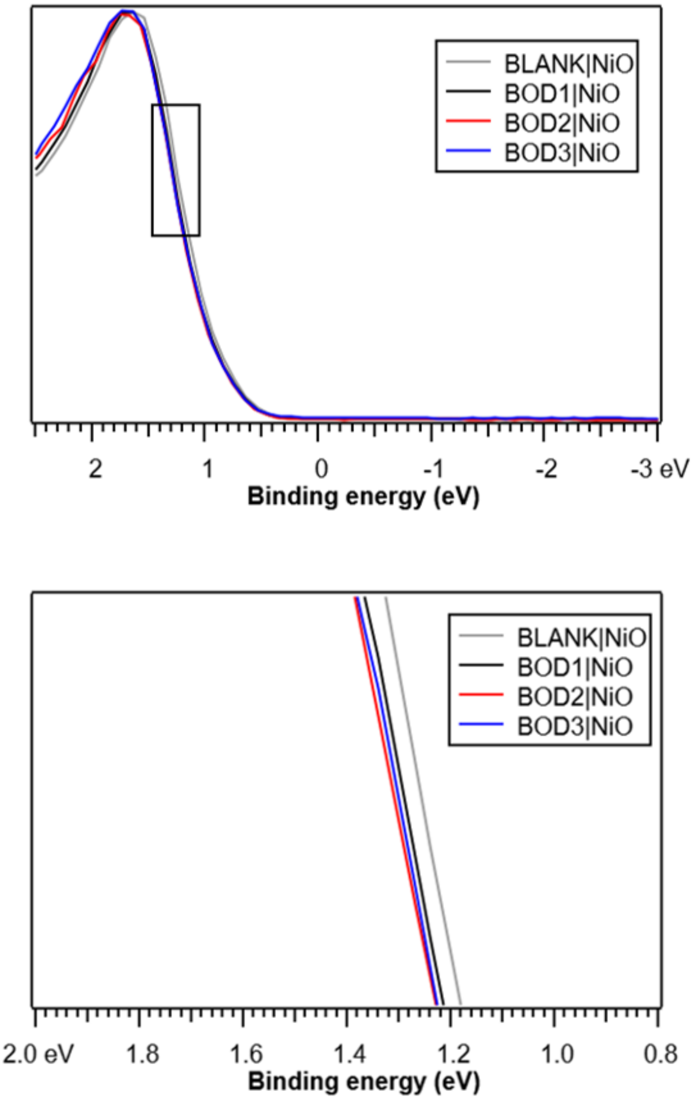

[H]

Figure 5.13: Valence spectra of the different NiO samples (top) measured at 250 eV photon energy. Expansion of the valence band edge shift (bottom). The spectra were normalised to the Ni3p peak and calibrated against an external Au reference.

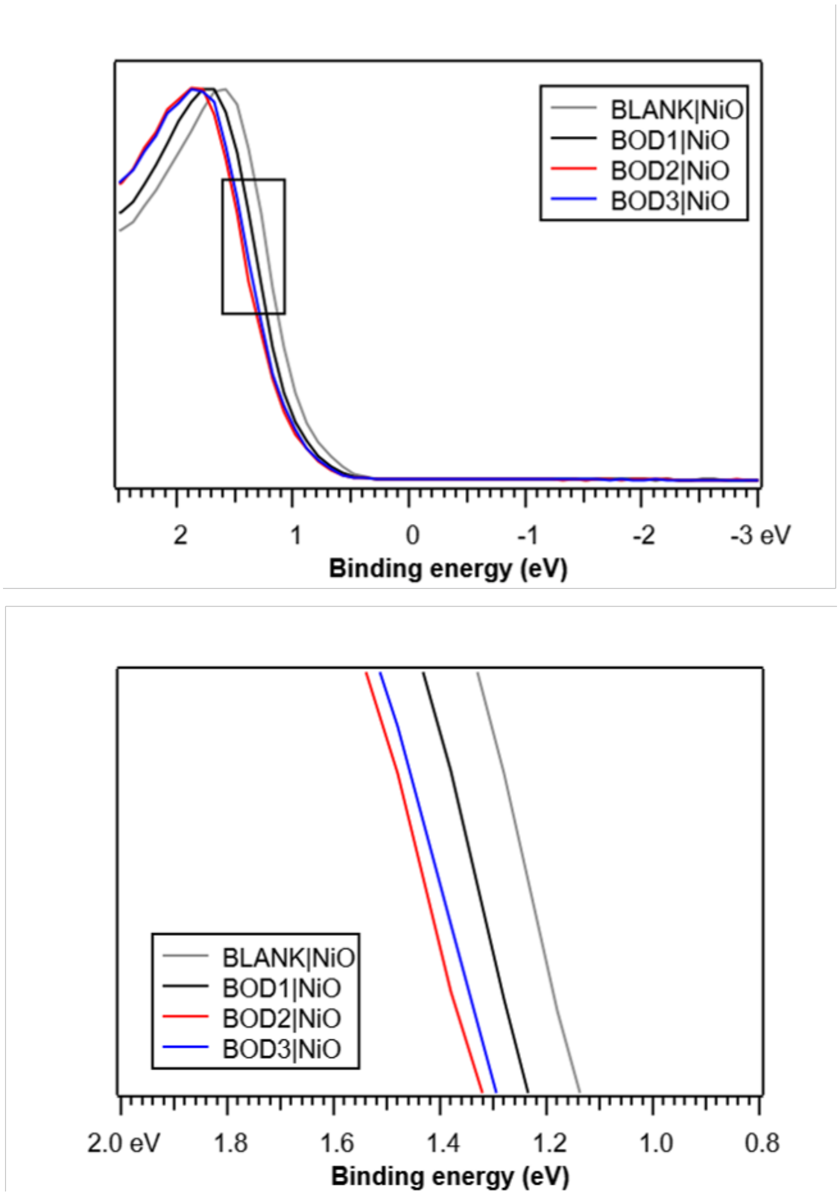

[H]

Figure 5.14: Valence spectra of the different NiO samples (top) measured at 120 eV photon energy. Expansion of the valence band edge shift (bottom). The spectra were normalised to the Ni3p peak and calibrated against an external Au reference.

	BOD1/eV	BOD2/eV	BOD3/eV
HOMO	0.85	1.16	0.73

Table 5.3: Experimentally calculated HOMO binding energies for dyes BOD1-3 measured at 120 eV X-ray excitation energy.

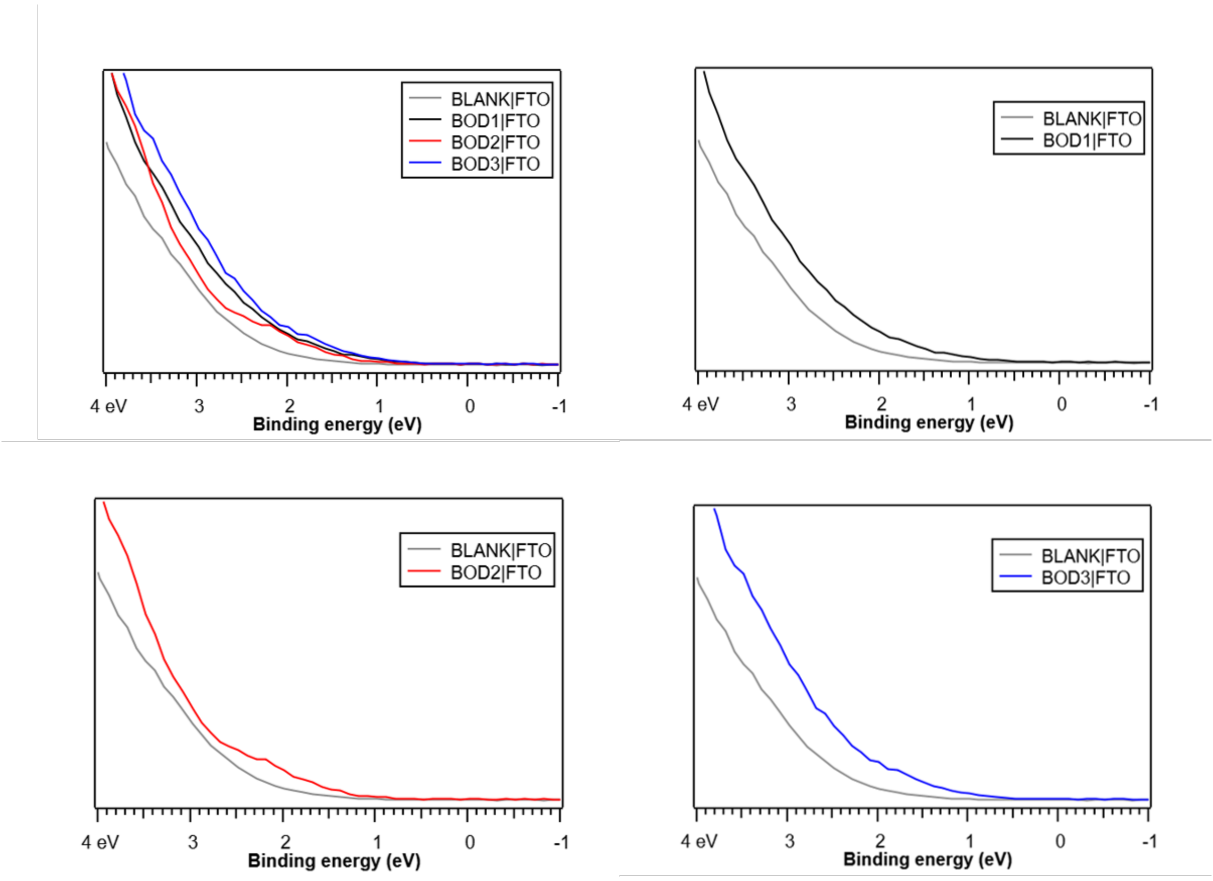

Figure 5.15: Overlays of the lower binding energy region of the BOD1-3/FTO spectra showing the HOMO protruding past the FTO VB edge. The spectra were measured at 120 eV, normalised to the Ni3p peak and calibrated against an external Au reference.

As the HOMO was partially masked by the FTO valence band position, the values were taken from the onset of the peak corresponding for the HOMO of dyes BOD1-3. The experimentally calculated positions for the HOMO of BOD1-3 are presented in Table 5.3. From the difference in binding energy for BOD3 compared to BOD2 (ΔBE = 0.43 eV) confirms an increase in conjugation from the phenolic groups forming the constrained ring system pushes the HOMO of BOD3 to lower binding energies. The electron donating properties of the aliphatic chains of BOD1 also destabilize the HOMO of the molecule, raising the energy of the HOMO and pushing it to lower binding energy. These results are in agreement with the solution based studies conducted in Chapter 2 where it was calculated that the trend in HOMO energies was BOD3«BOD1«BOD2.

	E_F NiO /eV	
	250 eV	120 eV
BLANK	0.68	0.28
BOD1	0.71	0.48
BOD2	0.76	0.56
BOD3	0.74	0.56

Table 5.4: Measured Fermi levels for NiO thin film sensitized with BOD1-3 with a blank reference sample measured with 120 eV and 250 eV X-ray excitation energies.

NiO VB Changes

The VB spectra for the dyed NiO films and the blank reference sample contain similar features close to the VB edge, however a distinct shift can be observed for the core level peaks and the valence band with respect to the Fermi level. (Figure 5.13, Figure 5.14). Such shifts in the VB position have been documented previously and is generally attributed to changes at the dye/semiconductor interface, such as chemical reduction of high valence Ni states (Ni^{3+}, Ni^{4+}) in the NiO nanoparticle leading to a decrease in p-type doping.[20] Other studies describe shifting of the VB as a result of modifications to the surface hydroxyl residues and a subsequent change in the work function of the material. In both cases the shift is defined as a Fermi level shift rather than a VB potential movement.[21][22]

Adsorption of the dye in all three samples results in a Fermi level shift to higher binding energies and can be seen at both X-ray excitation energies (120 eV and 250 eV). The magnitude of these changes is reduced at the higher X-ray excitation energies. A summary of the changes in binding energies is outlined Table 5.5.

	ΔBE vs. BLANK /eV	
	250 eV	120 eV
BOD1	0.033	0.10
BOD2	0.052	0.17
BOD3	0.077	0.14

Table 5.5: Binding energy difference (ΔBE) for the Fermi level of NiO for BOD1-3 adsorbed onto NiO vs. a blank reference sample, measured at 120 eV and 250 eV X-ray excitation energy.

As previously outlined, the Fermi level of the NiO semiconductor is a key factor in determining the solar cell performance and theoretical maximum efficiency of the device. Table 5.6 outlines the positions of the Fermi level under the experimental conditions for the blank reference sample and dyes BOD1-3. As the electron transfer in a DSSC relies on efficient electron injection from the VB of the semiconductor into the HOMO of the dye, these shift in Fermi level position will determine how efficiently the electron injection step occurs.

	E_F NiO /eV	HOMO /eV	ΔG_{inj} /eV
BLANK	0.28	-	-
BOD1	0.48	0.85	0.37
BOD2	0.56	1.16	0.60
BOD3	0.56	0.73	0.17

Table 5.6: Measured Fermi levels for NiO, HOMO energies for dyes BOD1-3 and calculated E_{inj} from valence PES measurements at 120 eV X-ray excitation energy.

A comparison of these results with the solution based studies presented in Chapter 3 shows the change in driving force for hole injection across the dye series. Although the three dyes still maintain sufficient driving force for hole injection (ΔG_{inj} is positive, therefore hole injection is encouraged), none of the dyes contain a driving force for charge injection close to the postulated optimum proposed by Liu (0.8 V).[23] BOD2 was found to have the highest driving force for hole injection to the semiconductor and was also shown to perform best in a working p-type DSSC. (Chapter 3.).

5.4 Conclusions

In summary, these results outline how X-ray Photoelectron Spectroscopy can be used as a tool to characterise the core level orbitals of organic dyes for DSSC and observe how structural modifications can be evaluated by inspection of the changes to the core level spectra. The ΔBE induced by these structural changes can be observed on both the dye multilayer deposited on FTO and as a monolayer adsorbed onto a NiO thin film. The Ni2p shows no changes in peak ratio or intensity upon dye adsorption, indicating that no significant changes to the bulk NiO upon dye adsorption. The film has been shown not to contain any $\mathrm{Ni}^{(0)}$ metal regions as previously described in literature. The HOMO of the three dyes have been measured and at low X-ray excitation energies, these orbitals can be seen just below the VB edge for FTO. The VB edge of NiO has been measured and upon dye adsorption a shift to higher BE has been reported for all three dyes, this change has been quantified and shows that assembly of the dye monolayer has a significant effect on the energy overlap at the dye|semiconductor interface. Under the conditions found in a working p-type NiO DSSC it has been shown that none of the three dyes operate with the postulated optimum driving force for electron injection ($\Delta\mathrm{G}_{inj}$), although all three dyes possess sufficient driving force for electron injection from the VB of NiO. The recalculated $\Delta\mathrm{G}_{inj}$ reflect the trend in DSSC performance where BOD2 performed best in a working device and was also shown to have the highest $\Delta\mathrm{G}_{inj}$ by XPS. This work highlights the importance of studying the interface between the dye and semiconductor under the conditions found in a working device.

References

(1) Hahlin, M.; Johansson, E. M. J.; Plogmaker, S.; Odelius, M. *Physical Chemistry Chemical Physics* **2010**, 1507–1517.

(2) Srinivas, K.; Yesudas, K.; Bhanuprakash, K.; Rao, V. J.; Giribabu, L. *Journal of Physical Chemistry C* **2009**, 20117–20126.

(3) O'Shea, J. N.; Swarbrick, J. C.; Nilson, K.; Puglia, C.; Brena, B.; Luo, Y.; Dhanak, V. R. *The Journal of Chemical Physics* **2004**, *121*, 10203–10208.

(4) Lindblad, R.; Cappel, U. B.; Mahony, F. T. F. O.; Siegbahn, H.; Johansson, E. M. J.; Haque, A.; Rensmo, H. *Physical Chemistry Chemical Physics* **2014**, 17099–17107.

(5) Põldme, N.; O'Reilly, L.; Fletcher, I.; Portoles, J.; Sazanovich, I. V.; Towrie, M.; Long, C.; Vos, J. G.; Pryce, M. T.; Gibson, E. A. *Chem. Sci.* **2019**, *10*, 99–112.

(6) Moulder, J.; Chastain, J., *Handbook of X-ray Photoelectron Spectroscopy: A Reference Book of Standard Spectra for Identification and Interpretation of XPS Data*; Physical Electronics Division, Perkin-Elmer Corporation: 1992.

(7) Ambroz, F.; Donnelly, J. L.; Wilden, J. D.; Macdonald, T. J.; Parkin, I. P. *Nanomaterials* **2019**, *9*, 1346.

(8) Barreca, D.; Garon, S.; Tondello, E.; Zanella, P.; Barreca, D.; Loredan, V.; Tondello, E.; Loredan, V. *Surface Science Spectra* **2000**, *7*, 81–85.

(9) Tawil, N.; Sacher, E.; Boulais, E.; Mandeville, R.; Meunier, M. *Journal of Physical Chemistry C* **2013**, 20656–20655.

(10) Van den Berg, J. *Surface and Interface Analysis* **1993**, *20*, 1081–1082.

(11) Johansson, E.; Nyborg, L. *Surface and Interface Analysis* **2003**, *35*, 375–381.

(12) Biesinger, M. C.; Payne, B. P.; Lau, L. W. M.; Gerson, A.; Smart, R. S. C. *Surface and Interface Analysis* **2009**, *41*, 324–332.

(13) Grosvenor, A. P.; Biesinger, M. C.; Smart, R. S.; McIntyre, N. S. *Surface Science* **2006**, *600*, 1771–1779.

(14) Renaud, A.; Chavillon, B.; Cario, L.; Pleux, L. L.; Szuwarski, N.; Pellegrin, Y.; Blart, E.; Gautron, E.; Odobel, F.; Jobic, S. *The Journal of Physical Chemistry C* **2013**, *117*, 22478–22483.

(15) Stranick, M. A.; Moskwa, A. *Surface Science Spectra* **1993**, *2*, 50–54.

(16) Benazzi, E.; Mallows, J.; Summers, G. H.; Black, F. A.; Gibson, E. A. *Journal of Materials Chemistry C* **2019**, *7*, 10409–10445.

(17) Ooyama, Y.; Yamaguchi, N.; Ohshita, J.; Harima, Y. *Physical Chemistry Chemical Physics* **2016**, *18*, 32992–32998.

(18) Yuasa, T.; Kawakami, R.; Sato, Y.; Mori, Y.; Adachi, M.; Yoshikado, S. *Solar Energy Materials and Solar Cells* **2012**, *102*, 2–7.

(19) Pazoki, M.; Lohse, P. W.; Taghavinia, N.; Hagfeldt, A.; Boschloo, G. *Physical Chemistry Chemical Physics* **2014**, *16*, 8503.

(20) D'Amario, L.; Jiang, R.; Cappel, U. B.; Gibson, E. A.; Boschloo, G.; Rensmo, H.; Sun, L.; Hammarström, L.; Tian, H. *ACS Applied Materials & Interfaces* **2017**, *9*, 33470–33477.

(21) Ratcliff, E. L.; Meyer, J.; Steirer, K. X.; Garcia, A.; Berry, J. J.; Ginley, D. S.; Olson, D. C.; Kahn, A.; Armstrong, N. R. *Chemistry of Materials* **2011**, *23*, 4988–5000.

(22) Irwin, M. D.; Servaites, J. D.; Buchholz, D. B.; Leever, B. J.; Liu, J.; Emery, J. D.; Zhang, M.; Song, J.-H.; Durstock, M. F.; Freeman, A. J.; Bedzyk, M. J.; Hersam, M. C.; Chang, R. P. H.; Ratner, M. A.; Marks, T. J. *Chemistry of Materials* **2011**, *23*, 2218–2226.

(23) Liu, Z.; Xiong, D.; Xu, X.; Arooj, Q.; Wang, H.; Yin, L.; Li, W.; Wu, H.; Zhao, Z.; Chen, W.; Wang, M.; Wang, F.; Cheng, Y.-B.; He, H. *ACS Applied Materials & Interfaces* **2014**, *6*, 3448–3454.

Chapter 6

Probing electron transfer in p-type DSC

6.1 Aims

The aim of this chapter was to probe the electron transfer pathways for the three dyes when adsorbed onto p-type NiO. By inspecting the system using ps-resolved transient absorption spectroscopy and characterising key intermediates in the electron transfer pathway it is possible to estimate charge separated state lifetimes of the three dyes to understand the limiting factors to efficiency for the three dyes when fabricated into a p-DSSC. To understand the system, information regarding some of the transient species found in the electron transport pathway were observed by spectroelectrochemical techniques. Pairing this information with ultrafast time-resolved spectroscopy allows for calculation of time constants associated with key electron transfer processes in a working DSSC.

6.2 Introduction

6.2.1 Kinetics

The kinetics of the electron transfer within a working dye-sensitized solar cell is a complex pathway of competing productive or recombination processes. The typical lifetimes for

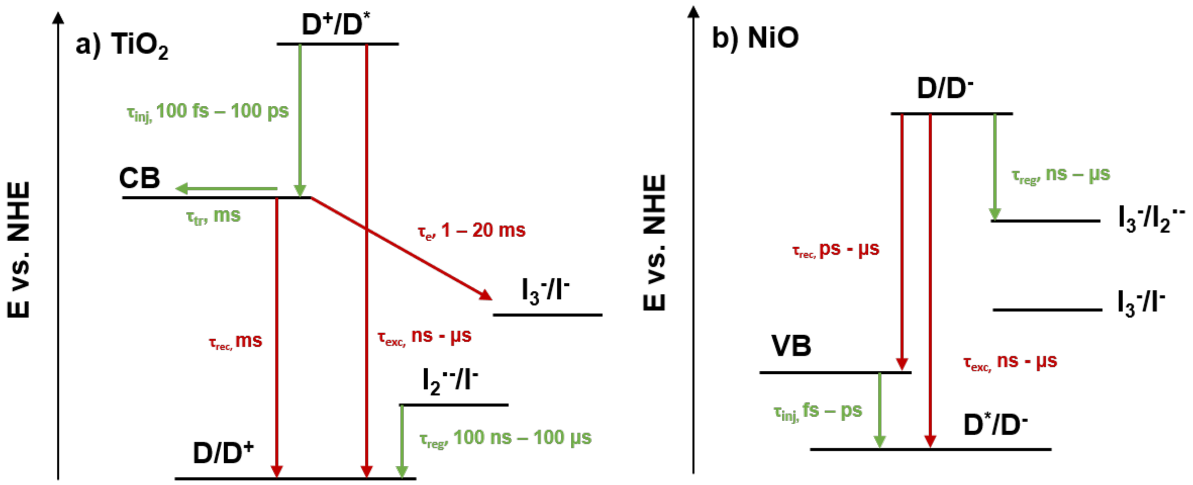

Figure 6.1: Energy Level diagram for an a) TiO_2 and b) NiO based dye-sensitized solar cell showing the relevant time scales of each process.

these processes are outlined in Fig 3.1 for both TiO_2 and NiO based devices.

τ_{inj} typically occurs on a 100 fs - 100 ps timescale in TiO_2 based systems, and must be over an order of magnitude faster than the excited state lifetime of the dye, which occurs on a ns - ms timescale, for a working device.[1–3] The electron transport through the semiconductor, τ_{tr} is fast enough to compete with recombination between the semiconductor and electrolyte at the liquid junction, τ_e 1 - 20 ms).[4] For TiO_2, this constitutes the main recombination loss mechanism within the device and is in direct competition with regeneration of the oxidised dye species.[1] For p-type devices, the dye$^-$|NiO$^+$ recombination, τ_{rec} occurs on an extremely fast time scale (ps - ns) compared to dye$^+$|TiO_2^- (ms) and competes with regeneration of the reduced dye (τ_{reg} ns - ms).,[5]

Dye regeneration in p-type systems has been reported from ns - ms timescales, the latter leading to poorly performing solar cells.[6] Engineering of donor-acceptor dye systems has allowed for charge separated state lifetimes of up to ms to be produced in an attempt to reduce the effect of the dye|semiconductor recombination in the solar cell.[7–9] The fast charge recombination at the NiO|dye interface may be a result of low hole mobility through the NiO[10] or the presence of electronic vacancies or defects above the valence band edge. For NiO, charge transport through the semiconductor has been proposed to proceed by a "hole-hopping" mechanism, which also is thought to promote semiconductor|electrolyte recombination. The hole hopping in NiO is thought to originate from "trap states" caused by the presence of Ni^{3+} and Ni^{4+} defects formed in the annealing process.[10,11]

Fast recombination of the dye|NiO charge-separated state has been highlighted as a major limitation on the performance of p-type DSSC.[12,13] For a p-type DSSC to operate efficiently, the DYE|NiO charge-separated state must be generated faster than the recombination of the dye excited state and the charge separated state must also be longer lived than τ_{reg}. Charge recombination is believed to occur over a range of timescales due to holes present in different states in the semiconductor, some reports reflect this by assigning multiple lifetimes to this process.[5,14,15]

6.3 Experimental Methods

6.3.1 Spectroelectrochemistry

The oxidized and reduced forms of dye molecules usually have different optical spectra to the ground state of the dye molecule. Therefore the formation of intermediate charged species, such as intramolecular charge separated states and dye semiconductor charge separated conjugates can be monitored by inspection changes in the UV-Visible spectrum during an electrochemical measurement. These electrochemical methods allow for simulation of the charge separated state in solution which can then aid in assignment of features in the transient absorption experiments. Spectroelectrochemistry can aid in assigning faradaic processes within an electrochemical measurement. It can also indicate the reversibility of an electrochemical reaction and monitor the recovery of ground state species following electrochemical oxidation or reduction. A spectroelectrochemical experiment involves step-wise potential increase via a chronoampometric waveform (Fig 6.2). Simultaneously at each potential step a UV-Vis spectrum is recorded. As the ground state of the analyte is depleted at the working electrode, any transitions associated with the ground state transitions of the analyte will also be depleted. During the experiment, any species generated in situ with different optical properties will be observed. As absorbance

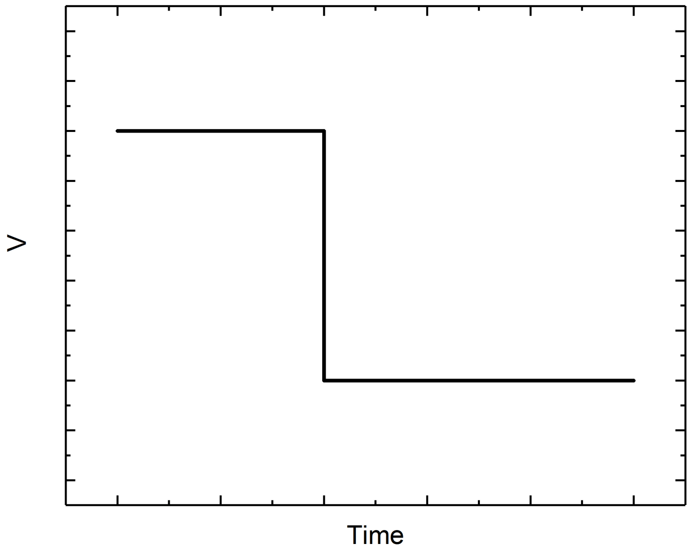

Figure 6.2: An example chronoampometric potential waveform.

(A) is proportional to the concentration of the analyte in solution, at the oxidation or reduction potential for the analyte, the ground state species at the working electrode will be consumed and therefore the changes in the UV-Visible spectrum can be attributed to the oxidized or reduced form of the dye respectively.

6.3.2 Chronoamperometry

Chronoamperometry is an electrochemical technique in which the potential between the working and counter electrode is varied in a step-wise manner. The current arising from faradaic processes at the working electrode is recorded as a function of time. Fig 6.2 shows the standard waveform used in a chronoamperometry (CA) experiment, Fig 6.3 shows the response waveform generated from the potential waveform in Fig 6.2.[16]

At time X (determined by the experimental setup), the voltage is increased by a step (E_X) predefined by the experimental conditions, if this reaches the required voltage for a faradaic process to begin the analyte at the surface of the electrode undergoes the redox process. As the analyte is consumed at the surface of the electrode, the current decreases

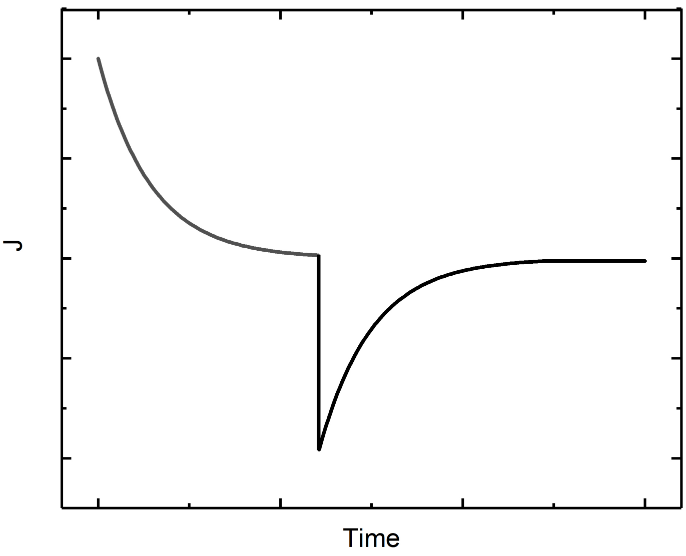

Figure 6.3: An example chronoampometric response waveform.

proportionally until the current plateaus.

6.3.3 Transient Absorption Spectroscopy

Measuring lifetimes and extracting kinetic data associated with charge injection and charge recombination processes can be investigated using flash photolysis or time-resolved spectroscopy. Time resolved spectroscopy monitors the evolution and decay of transient species after excitation of a sample with a laser pulse. The transient species then decay via radiative or non-radiative decay pathways. Briefly, the sample is excited with a pump beam (typically in the visible region). The excited samples are probed across the visible spectrum by a broadband pump beam (white light) and spectra are recorded at various time delays. As previously mentioned the dye|NiO recombination can occur over multiple timescales, therefore multi exponential decay functions are commonly used to fit multiple time constants to the decay profiles.[7,10,17]

In this thesis, the NiO|dye and solution based spectra underwent single point analysis to extract kinetic information from the time-resolved spectroscopy data. In the case of overlapping signals or multiple species present in the sample, global analysis techniques were employed. Global analysis fits the data to multiple time components, the amplitude of each component is then plotted against the detection wavelength.[18,19]

6.4 Results

6.4.1 Spectroelectrochemistry

Spectroelectrochemical studies in the visible region were carried out to characterise the reduced forms of the dyes for comparison with the transient absorption measurements.

The spectrum of BOD1$^-$ was broader and red shifted in comparison to BOD1 (Figure 6.4). It contained additional absorption bands at 400-570 nm and 550-575 nm which grow in during the experiment.

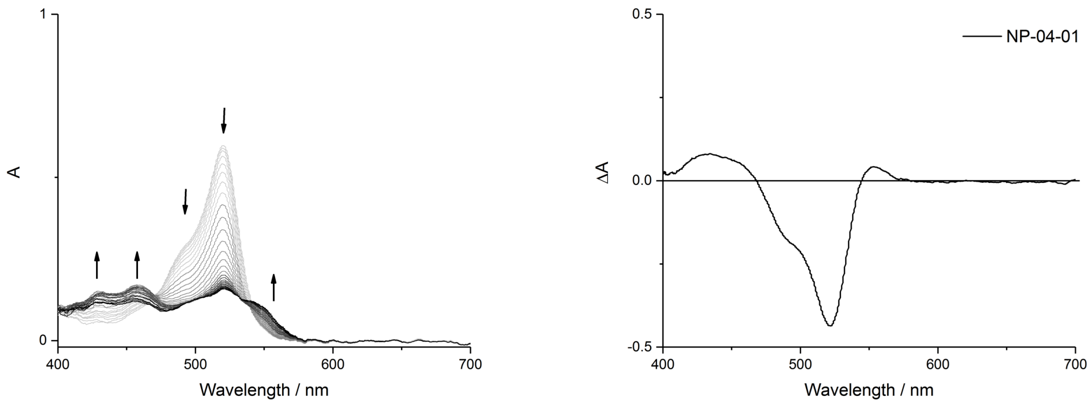

Figure 6.4: Left: absorbance spectra in the visible region of BOD1 under a negative bias with 0.1 M TBAClO$_4$ in CH$_3$CN as the supporting electrolyte. Right: absorbance difference spectrum of BOD1 under a negative bias (-1.7 V vs. Fc/Fc$^+$, 600 s)

BOD2$^-$ shows a slight blue shift compared to BOD2 in the chronoamperometry experiment (Figure 6.5). A bleach in the main absorption band can be observed, however no positive absorption signal can be seen. During the experiment an insoluble byproduct was formed upon application of the cathodic potential.

Electrocatalyzed reactions and dimerisations of BODIPYs have been well characterized

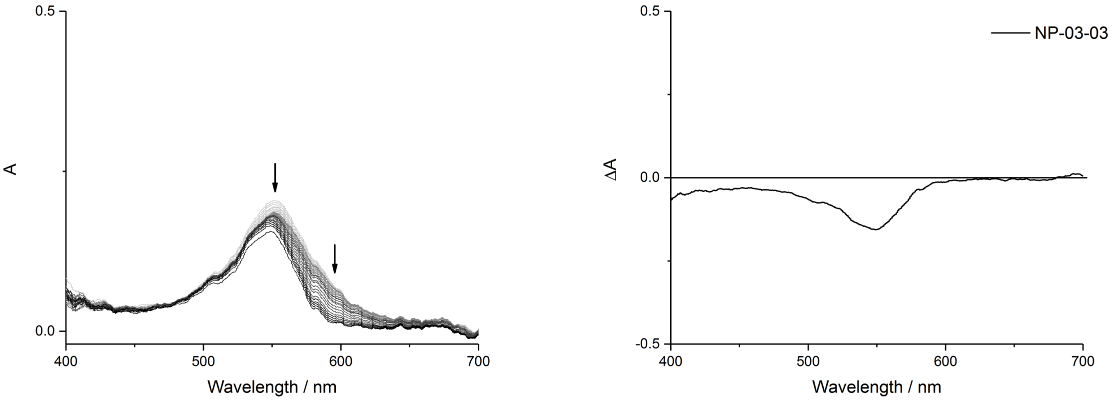

Figure 6.5: Left: absorbance spectra in the visible region of BOD2 under a negative bias with 0.1 M TBAClO$_4$ in CH$_3$CN as the supporting electrolyte. Right: absorbance difference spectrum of BOD2 under a negative bias (-1.6 V vs. Fc/Fc$^+$, 600 s)

in literature.[20,21] The radical anion produced upon reduction of the chromophore can be stabilized when the α, β and meso- positions, which are susceptible to electrophillic and nucleophillic attack are blocked. BOD2 contains two free β-pyrrolic positions and appears to undergo electrocatalyzed reactions under the experimental conditions.

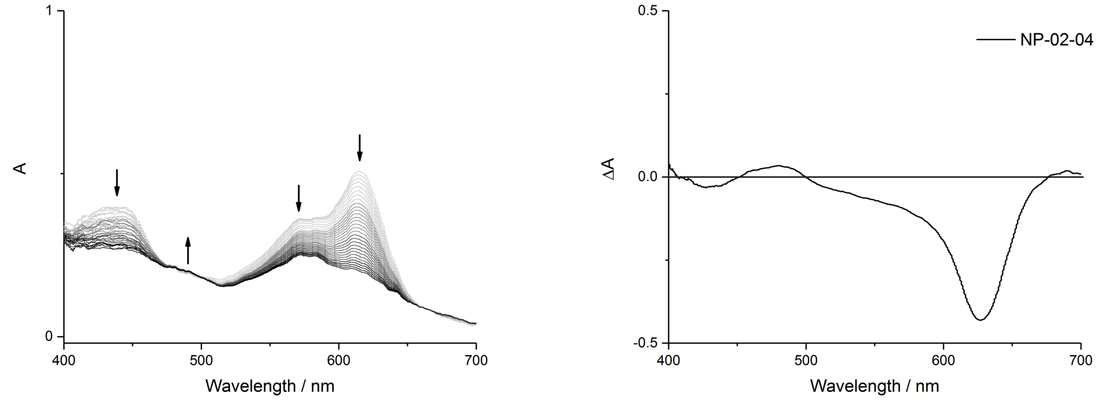

Figure 6.6: Left: absorbance spectra in the visible region of BOD3 under a negative bias with 0.1 M TBAClO$_4$ in CH$_3$CN as the supporting electrolyte. Right: absorbance difference spectrum of BOD3 under a negative bias (-1.7 V vs. Fc/Fc$^+$, 600 s)

BOD3 also features a bleach under the experimental conditions - only small absorbance features can be seen at ca. 500 nm and 690 nm (Figure 6.6). The absence of a significant absorbance indicates that BOD3 may also undergo electrocatalyzed reactions at the free β-pyrrolic positions.

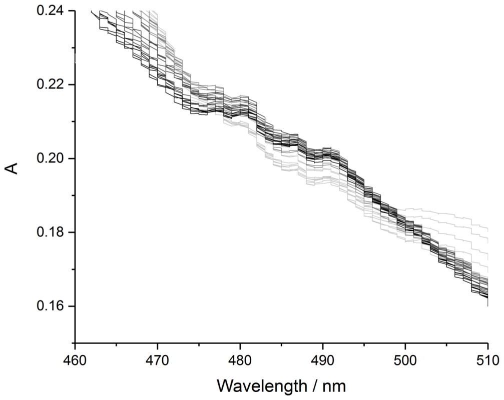

Figure 6.7: Expansion of the spectroelectrochemical trace for BOD3 between 400 - 510 nm.

A small absorbance feature can be seen at 470-500 nm, suggesting that the absorbance of the reduced dye BOD3$^-$ may be similar to BOD1$^-$ (Figure 6.7).

6.4.2 Transient Absorption Spectroscopy

As previously outlined, the sample (dye in solution or dye associated to the NiO film) was excited with a short laser pulse, subsequently the electronic absorption spectrum was probed using white light at various time delays in order to understand the kinetic pathways of an electron within the system. The data was analysed using single point analysis where the change in optical density of the sample at a specific wavelength was fit to either a single or multi-exponential decay function to interpret the lifetimes of the processes.

The transient absorption spectra of BOD1, BOD2 and BOD3 in acetonitrile solution and immobilized on a NiO film are shown in Fig. 6.8, with the lifetimes from single point analysis given in Table 6.1.

Figure 6.8 shows the fs-TAS measurements of the three dyes in CH_3CN (left) and immobilized on a NiO film (right). In solution, BOD1 and BOD3 did not decay within the timescale of the experiment, consistent with the typical excited state lifetime of the

BODIPY dye (≈6 ns).[22] The exception to this is BOD2 which decays fully within the 1 ns time resolution of the experiment and has a lifetime of 0.5 ns. This is consistent with the observation in Chapter 2 where this compound was shown to have weaker emission when compared to the other two dyes.

BOD2 shows a broad ground state bleach (GSB) between 500-600 nm, consistent with the steady state UV-Visible spectrum (Chapter 2). The GSB is partially masked by the laser pump pulse which has been removed from the spectrum for clarity. An absorbance feature can be seen between 400-500 nm which has been assigned to the singlet BODIPY excited state. Both processes evolve on similar time scales and within the resolution of the experiment, the excited state lifetime for dye BOD2 is therefore 0.5 ns. Stimulated emission from the dye is also seen, however the signal decays quickly which is consistent with the weak fluoresence observed in solution.

Femtosecond transient absorption spectroscopy was also used to investigate the formation and decay of the dye^{-}|NiO^{+} charge separated state when the dyes were adsorbed onto a NiO thin film.

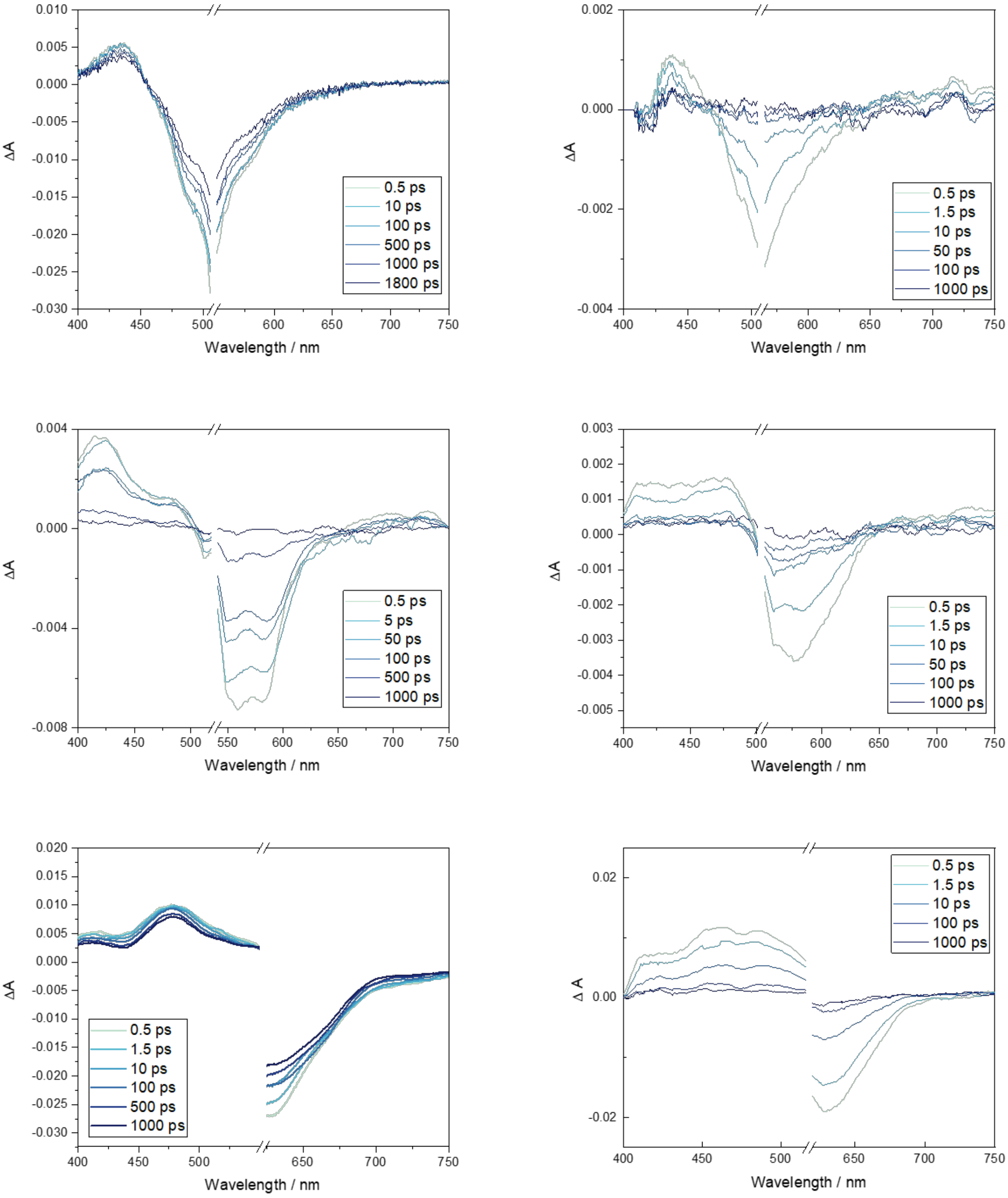

Figure 6.8: Femtosecond resolution transient absorption spectra of BOD1 (top), BOD2 (middle) and BOD3 (bottom) at selected time delays. Left - in CH$_3$CN solution, right - adsorbed onto NiO film. (λ $_{ex}$: BOD1, BOD2 - 537 nm; BOD3 - 600 nm

	Lifetime, ps	
	CH_3CN	NiO
		$\tau_{435} = 18.4 \pm 8.5$
BOD1	$\tau > 1ns$	$\tau_{485} = 5.01 \pm 1.4$
		$\tau_{575} = 14.4 \pm 3.4$ (2%), 1.06 ± 0.23 (98%)
	$\tau_{425} = 69.3 \pm 71.6$ (15%), 326.0 ± 87.8 (85%)	$\tau_{430} = 1.18 \pm 0.18$ (98 %), 417.07 ± 336.25 (2%)
BOD2	$\tau_{475} = 101.6 \pm 413.8$ (15%), 403.2 ± 347.4 (91%)	$\tau_{565} = 0.79 \pm 0.11$ (75 %), 37.66 ± 6.09 (25%)
	$\tau_{555} = 1.22 \pm 0.3$ (56%), 221.3 ± 20 (44%)	$\tau_{585} = 4.34 \pm 0.5$
	$\tau_{575} = 366 \pm 1014$ (81%), 201.1 ± 1731 (19%)	$\tau_{725} = 67.44 \pm 219.8$ (6 %), 1.39 ± 1.55 (94 %)
		$\tau_{450} = 3.79 \pm 0.27$ (80 %), 95.1 ± 12.7 (20 %)
BOD3		$\tau_{480} = 4.01 \pm 0.3$ (68 %), 51.46 ± 5.7 (32 %)
	$\tau > 1ns$	$\tau_{640} = 1.39 \pm 0.13$ (88 %), 21.05 ± 2.01 (12 %)
		$\tau_{700} = 1.61 \pm 0.35$

Table 6.1: Single point analysis of the fs-TA measurements on BOD1-3 in solution (CH_3CN) and adsorbed onto a NiO film.

When BOD1, BOD2 and BOD3 were immobilized on NiO the excited species were generated and decayed within the time resolution of the experiment, indicating a new electron decay pathway was present.

BOD1 exhibits faster kinetics on film than in solution with the ground state bleach being recovered within the time frame of the experiment. The ground state bleach was fit to a mono-exponential decay function $\tau_{485} = 5$ ps. Stimulated emission is seen at 625 nm, arising from the interaction between the laser probe pulse and the excited dye molecule resulting in the release of a photon. The broad absorption at ca. 400-475 nm has been assigned to the charge separated state of the dye, where hole injection to the NiO has occurred and the reduced dye is the transient species appended to the NiO surface. The charge separated state has a blue-shifted absorption by ca. 10 nm compared to BOD1 in solution. The charge separated state lifetime was fit to a mono-exponential decay function $\tau_{435} = 18$ ps, indicating a much faster recovery to the ground state on NiO film than in acetonitrile solution. The spectrum of BOD1 also contains a broad absorption from 620 nm across the rest of the measured spectrum to 700 nm, which is characteristic of holes in NiO.[23]

BOD3 displays similar changes in kinetics as BOD1 when imobilized on a NiO film. A reduction of the lifetime of the slower component of the ground state bleach at 640 nm (CH_3CN: $\tau_1 = 1.2$ ps, $\tau_2 = 529$ ps, $\tau_3 = \infty$; NiO|Dye $\tau_1 = 1.4$ ps, $\tau_2 = 21$ ps) is observed when comparing the recovery of the ground state bleach. A broad absorption feature attributed to the charge separated state from ca. 400-520 nm is seen composed of two time components ($\tau_1 = 4$ ps, $\tau_2 = 51$ ps). A broad feature attributed to holes on NiO can be seen at the lower energy region of the spectra ($\tau_{700} = 1.6$ ps). All three processes evolved within the timescale of the experiment.

BOD2 also exhibits shorter ground state bleach lifetimes on NiO than in acetonitrile solution (CH_3CN: $\tau_1 = 1.2$ ps, $\tau_2 = 221$ ps; NiO|Dye: $\tau_1 = 0.79$ ps, $\tau_2 = 37$ ps). The absorption at ca. 400-500 nm has been fit to a bi-exponential decay function ($\tau_1 = 1.2$ ps, $\tau_2 = 417$ ps) indicating that the charge separated state lifetime is extremely short.

Again a broad absorption feature at the lower energy portion of the spectrum indicates holes present on NiO which also decay on a very short timescale.

Global analysis was used to extract the lifetimes of the main features of the fs-transient absorption spectra where the species overlap. In solution, the decay-associated spectra (DAS) of BOD1 (Fig. 6.9, (top)) and BOD3 (Fig. 6.11, (top)) both contain an infinite component, consistent with the findings from the single point analysis of the TA data. BOD2 shows two main components in the DAS in acetonitrile. The fast component (1.2 ps) is assigned to thermalization of the excited electron from a higher energetic state than S_1. The slower component (278 ps) is assigned to the excited state lifetime, and is in agreement with the single point analysis. The decay of the excited state for BOD2 appears to be much shorter than that of a typical BODIPY dye, however the pendant α-phenyl groups are free to rotate, which opens up new non-radiative decay pathways leading to reduction of the excited state lifetime. When BOD1 is adsorbed onto NiO (Fig 6.9, middle) the components seen are related to the excited state and stimulated emission and no new features appear from 1.3 ps to 30 ps. As both stimulated emission and excited state absorption are seen, the components are both assigned to the excited state formation. As there are no components seen corresponding to the reduced dye (Fig. 6.4) it is implied that if charge separation occurs between the semiconductor and dye, recombination of the excited electron back to the ground state is in competition with the charge separation process. When an iodine electrolyte is introduced to the system (Fig. 6.9, bottom) the components show very different features. At 1.3 ps, the decay associated spectra (DAS) looks very similar to the features seen in absence of electrolyte. At 36 ps the spectrum has evolved and a new transient absorption feature is seen at 470 nm, consistent with the absorption profile of the reduced dye seen by spectroelectrochemistry. A broad signal from 550 nm that extends to the red region of the spectrum is seen which persists to longer timescales during the experiment is indicative of holes being present on NiO, affirming that charge separation is taking place between the dye and semiconductor. At 2120 ps, the holes on NiO are still present and the signal originating from the excited state has reduced in amplitude. No change in signal at the wavelengths corresponding to stimulated emission is observed at 2120 ps and the feature assigned to the GSB feature is still present, indicating that the system has not reached the ground state completely.

The DAS for BOD2 (Fig. 6.10, middle) immobilized on NiO shows similar features as BOD1. At 1.2 ps the features correspond to the formation of the excited state of the dye however a blue shift in the signal at 14 ps and the evolution of a broad absorption feature extending to the red region is once again characteristic of hole generation on the NiO, this feature is still present at 661 ps and demonstrates that BOD2 experiences charge separation between the dye and semiconductor in the absence of the iodine electrolyte. When the electrolyte is introduced to the system (Fig. 6.10, bottom) the excited state component has a lifetime of 1.6 ps, which persists to 34 ps, the latter shoes contributions from both the excited and charge separated states. At 3430 ps the holes generated on NiO can still be seen at the red region of the spectrum, and the ground state bleach is not fully recovered. As with BOD1 these signals live much longer with the electrolyte present indicating the rate of recombination for the regeneration of the ground state have slowed down.

BOD3|NiO (Fig. 6.11, middle), shows features consistent with the solution based experiments (Fig. 6.11, top), the excited state formation occurring within 1.7 ps. This feature is red-shifted at 20 ps, agreeing with the bathochromic shift seen in spectroelectrochemical measurements, with the absorption of the reduced dye molecule being red-shifted to the ground state absorption. When compared to BOD1 and BOD2 immobilized on NiO, the transient species last much longer for BOD3, by 1603 ps the features have reduced in intensity but the ground state is not fully recovered. When the electrolyte is added to the system, BOD3 does not fully recover to the ground state within the time resolution of the experiment indicating that, similarly to the other dyes in the series, when the electrolyte is present the lifetime of the reduced dye increases.

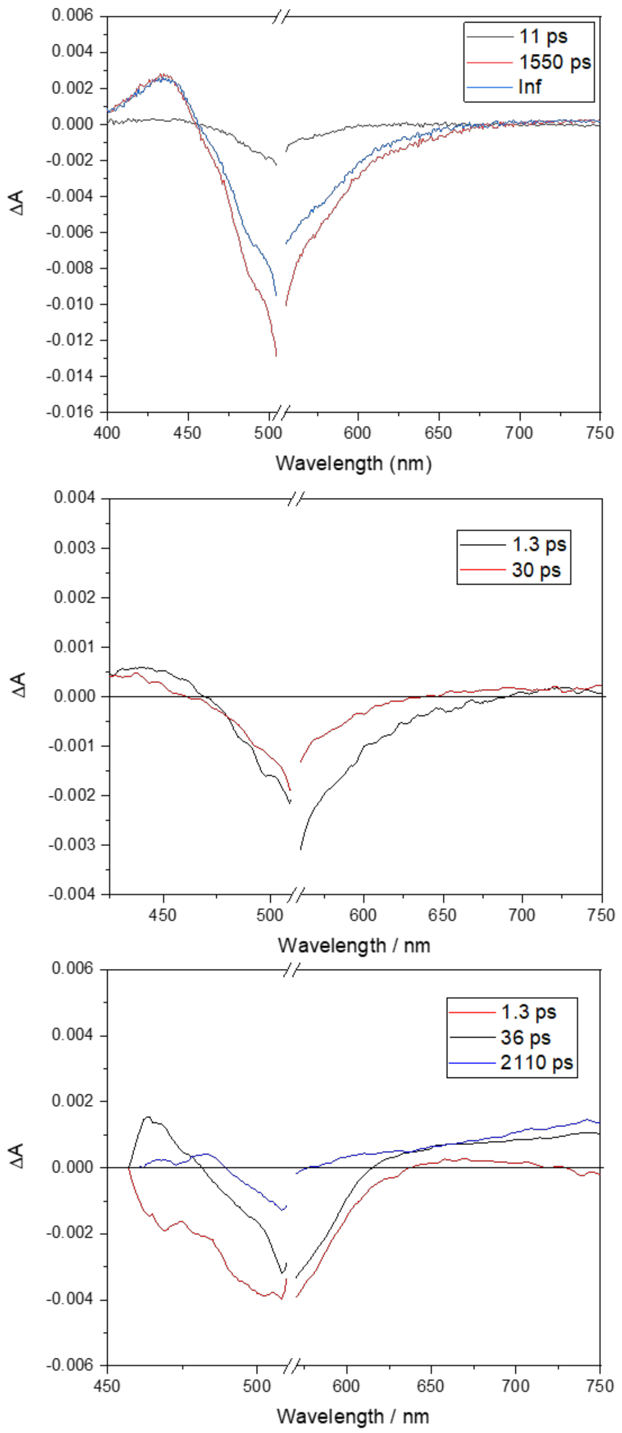

Figure 6.9: Global analysis decay associated spectra of transient absorbance spectra of BOD1 in acetonitrile (top), on NiO with a LiTFSI in acetonitrile (middle), on NiO with an iodine electrolyte (bottom)

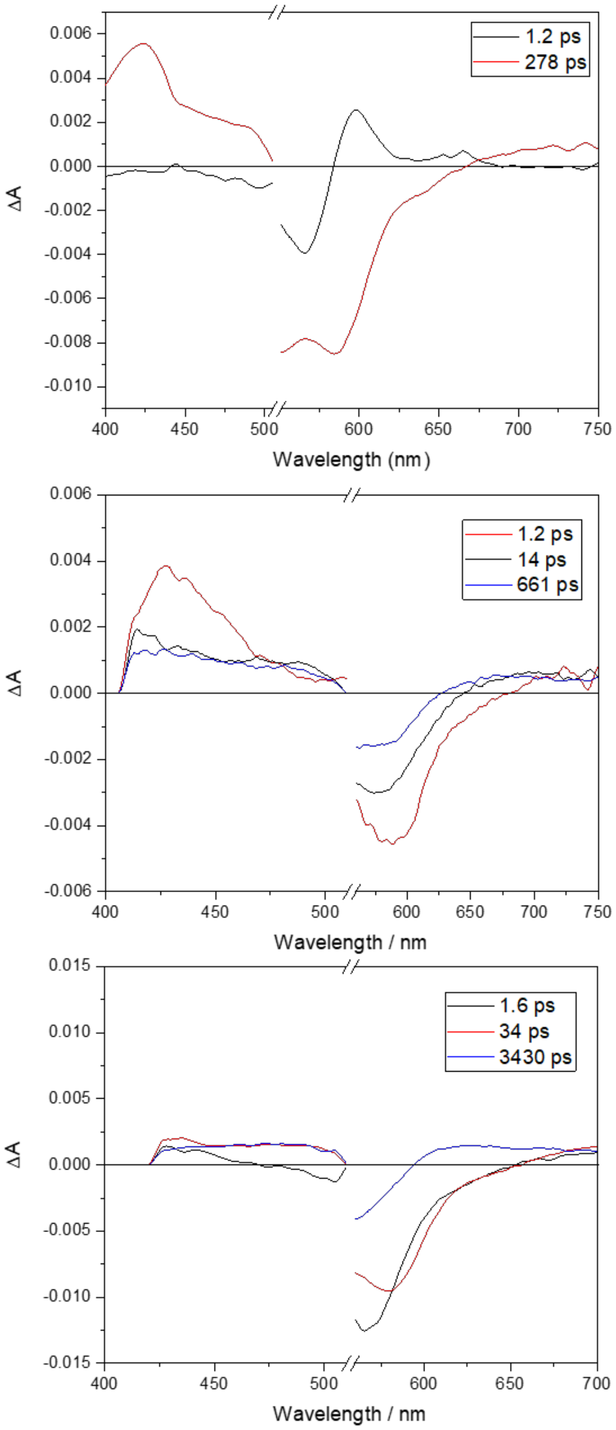

Figure 6.10: Global analysis decay associated spectra of transient absorbance spectra of BOD2 in acetonitrile (top), on NiO with a LiTFSI in acetonitrile (middle), on NiO with an iodine electrolyte (bottom)

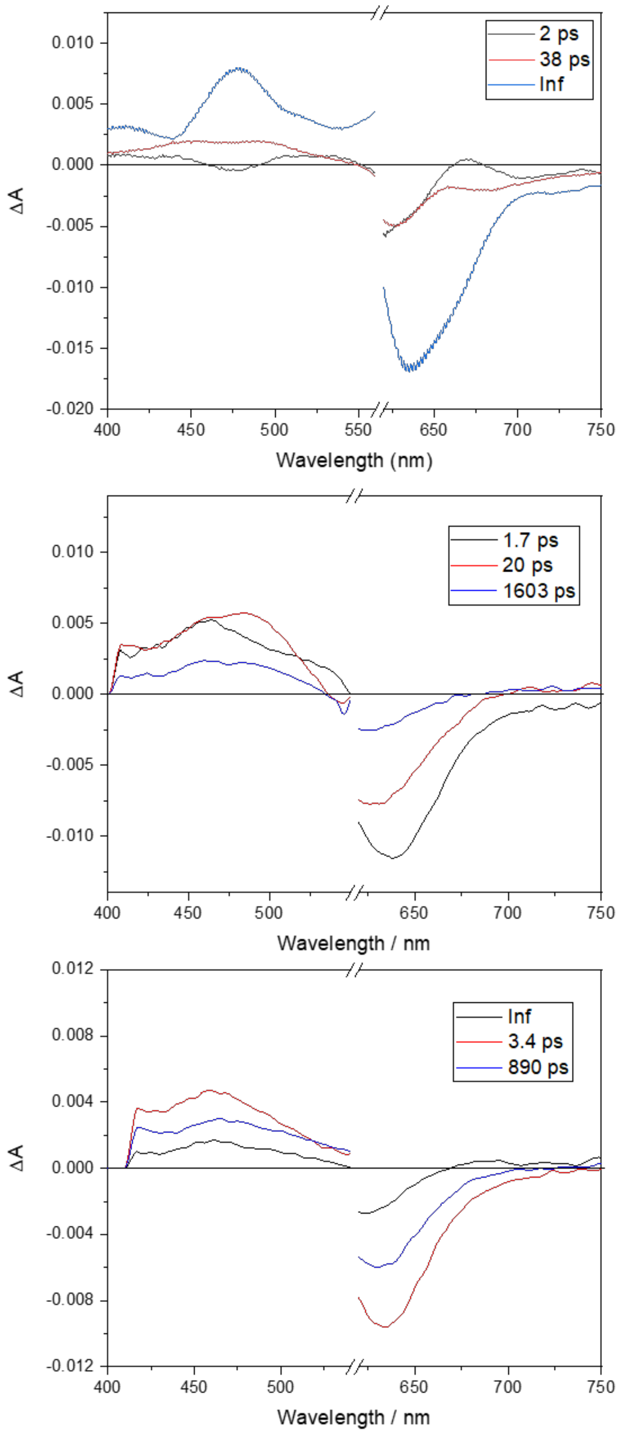

Figure 6.11: Global analysis decay associated spectra of transient absorbance spectra of BOD3 in acetonitrile (top), on NiO with a LiTFSI in acetonitrile (middle), on NiO with an iodine electrolyte (bottom)

6.4.3 Conclusions

For all three dyes, charge injection (τ_{inj}) occurs on similar timescales (1.2 - 5 ps) each being more than an order of magnitude faster than the excited state lifetime for the three dyes. In Chapter 4, it was shown that all three dyes have sufficient driving force for electron injection from the valence band of NiO to the HOMO of the dye, the findings from the transient absorption data reflect this indicating that the charge injection process is favourable for all three dyes. The calculated driving forces for charge injection from XPS (Table 4.5) are lower than the optimum proposed by Liu et.al.[24] Inspection of the DAS indicates that the initial charge separation process is very fast and may not require a large driving force, however in absence of electrolyte the recombination is also very fast and the reduced dye is immediately quenched. It appears that the larger overpotential quoted by Liu may be required to form sufficient reduced dye molecules on the surface of NiO to compete with the recombination of the reduced dye.

Interestingly, the lifetime of the reduced dye appears to increase in the presence of the redox electrolyte. It is expected that the lifetime of the reduced dye would be quenched restoring the ground state and reducing the electrolyte. Previous work has shown that interactions at the electrode/electrolyte interface catalyze the oxidation of iodide to triiodide and causing a reduction at the surface of the NiO electrode. Dini reports characterization of the density of states (DOS) of NiO thin films and attributes their findings to presence of high valence states (Ni^{2+}, Ni^{3+}, Ni^{4+}).[25] Gibson et. al. demonstrated this catalytic behaviour; when immersed in a solution of LiI, the NiO showed catalytic properties in forming triiodide in situ and postulated the surface defects in the NiO acting as catalytic sites for this oxidation reaction and reducing $Ni3^{+}$ residues. The addition of iodide to a NiO film results in formation of triiodide and a reduction at the surface of NiO. The suggested pathway for this reaction is described in equations 6.1-6.3.[26]

$$I^{-} + S = I(S) + e^{-} \tag{6.1}$$

$$I(S) + I^{-} = I_2 + S + e^{-} \tag{6.2}$$

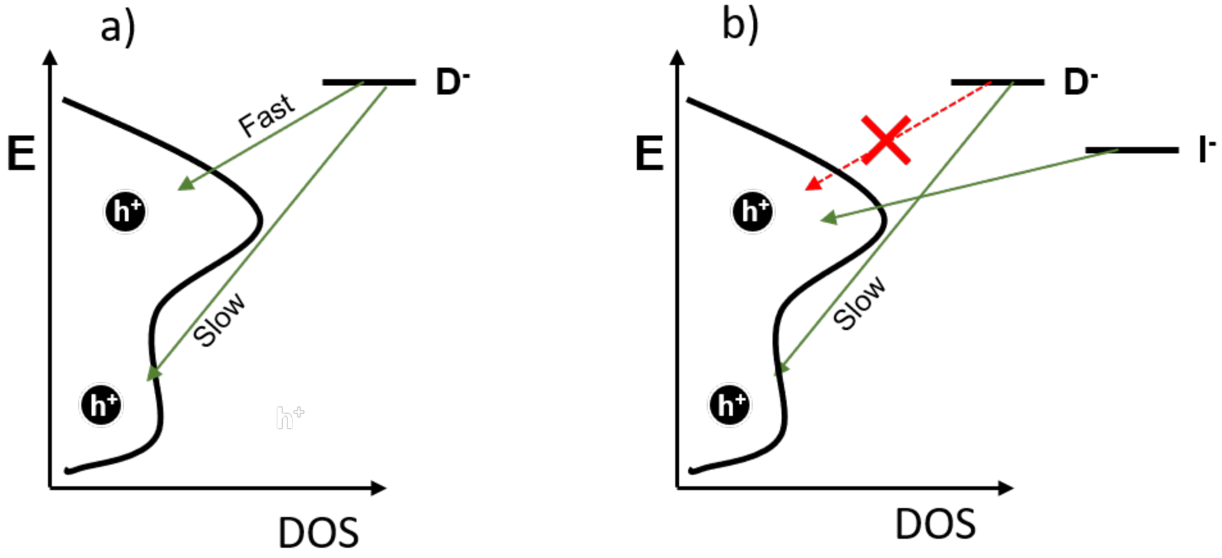

Figure 6.12: A qualitative schematization of the VB edge of NiO in a p-DSSC; a) without iodine electrolyte; b) with iodine electrolyte demonstrating the suggested recombination pathways leading to an increased reduced dye lifetime.

$$I_2 + I^- = I_3^- \tag{6.3}$$

This is in agreement with other studies on the surface of a NiO thin film, Haining et. al describe reduction of surface states of NiO, using sodium borahydride as a chemical reductant.[10] By doing so, not only can it be observed that a change to the Fermi level of the material occurs upon reduction of the surface, it provides insight into other recombination pathways inside a p-DSSC.

We suggest here that due to the iodide reducing the surface states on NiO, this could compete with the recombination of the reduced dye and the electrolyte. As the density of the surface states causing recombination is reduced by the interactions with the electrolyte, the rate of recombination is slower. On this basis, the increase in the lifetime of the reduced dye can be rationalised, the I_3^- in the electrolyte that is available to recombine with the reduced dye is converted to triiodide at the electrode/electrolyte interface, which is presented as an increase in the lifetime of the reduced dye in the fs-TA measurements.

NiO typically has a positively charged surface which is compensated by a layer of hydroxyl residues at the surface, therefore it has been suggested that I^- could be adsorbed onto NiO more easily than TiO_2 therefore these recombination pathways are not seen in n-type DSSC.[27,28]

BOD2 was the only dye of the series to decay on the time scale of the instrument, indicating that the regeneration of the dye was the most efficient for this system. This is in agreement with the solar cell results where it was shown that, under low electrolyte concentrations where dye regeneration is expected to be the limited by the triiodide concentration, BOD2 generated a photocurrent more than double those of BOD3 and four times that of BOD1,

References

(1) Boschloo, G.; Hagfeldt, A. *Accounts of Chemical Research* **2009**, *42*, 1819–1826.

(2) Ardo, S.; Meyer, G. J. *Chem. Soc. Rev* **2009**, *38*, 115–164.

(3) Anderson, N. A.; Lian, T. *Annu. Rev. Phys. Chem* **2005**, *60*, 491–519.

(4) Zaban, A.; Greenshtein, M.; Bisquert, J. *ChemPhysChem* **2003**, *4*, 859–864.

(5) Qin, P.; Wiberg, J.; Gibson, E. A.; Linder, M.; Li, L.; Brinck, T.; Hagfeldt, A.; Albinsson, B.; Sun, L. *Journal of Physical Chemistry C* **2010**, *114*, 4738–4748.

(6) Le Pleux, L.; Odobel, F.; Smeigh, A. L.; Gibson, E.; Pellegrin, Y.; Blart, E.; Boschloo, G.; Hagfeldt, A.; Hammarstr, L. *Energy and Environmental Science* **2011**, 2075–2084.

(7) Zhang, L.; Favereaub, L.; Farré, Y.; Mijangosa, E.; Pellegrin, Y.; Blart, E.; Hammarström, L.; Fabrice, O. *Physical Chemistry Chemical Physics* **2016**, *18*, 18515–18527.

(8) Haque, S. A.; Palomares, E.; Cho, B. M.; Green, A. N. M.; Hirata, N.; Klug, D. R.; Durrant, J. R. *Journal of the American Chemical Society* **2005**, *127*, 3456–3462.

(9) Gennari, M.; Légalité, F.; Zhang, L.; Pellegrin, Y.; Blart, E.; Fortage, J.; Brown, A. M.; Deronzier, A.; Collomb, M.-N.; Boujtita, M.; Jacquemin, D.; Hammarström, L.; Odobel, F. *The Journal of Physical Chemistry Letters* **2014**, *5*, 2254–2258.

(10) D'Amario, L.; Jiang, R.; Cappel, U. B.; Gibson, E. A.; Boschloo, G.; Rensmo, H.; Sun, L.; Hammarström, L.; Tian, H. *ACS Applied Materials & Interfaces* **2017**, *9*, 33470–33477.

(11) Dillon, R. J.; Alibabaei, L.; Meyer, T. J.; Papanikolas, J. M.; Dillon, R. J.; Alibabaei, L.; Meyer, T. J.; Papanikolas, J. M. *ACS Applied Materials & Interfaces* **2017**, *9*, 26786–26796.

(12) Benazzi, E.; Mallows, J.; Summers, G. H.; Black, F. A.; Gibson, E. A. *Journal of Materials Chemistry C* **2019**, *7*, 10409–10445.

(13) Odobel, F.; Pellegrin, Y.; Gibson, E. A.; Hagfeldt, A.; Smeigh, A. L.; Hammarström, L. *Coordination Chemistry Reviews* **2012**, *256*, 2414–2423.

(14) Lefebvre, J.-F.; Sun, X.-Z.; Calladine, J. A.; George, M. W.; Gibson, E. A. *Chem. Commun.* **2014**, *50*, 5258–5260.

(15) Smeigh, A. L.; Pleux, L. L.; Fortage, J.; Pellegrin, Y.; Blart, E.; Odobel, F.; Hammarström, L. *Chem. Commun.* **2012**, *48*, 678–680.

(16) Bard, A. J.; Faulkner, L. R., *Electrochemical Methods: Fundamentals and Applications*, 2nd; Wiley: 2001.

(17) Odobel, F.; Pellegrin, Y. *Journal of Physical Chemistry Letters* **2013**, *4*, 2551–2564.

(18) Van Stokkum, I. H.; Larsen, D. S.; van Grondelle, R. *Biochimica et Biophysica Acta (BBA) - Bioenergetics* **2004**, *1657*, 82–104.

(19) Berera, R.; van Grondelle, R.; Kennis, J. T. M. *Photosynthesis Research* **2009**, *101*, 105–118.

(20) Nepomnyashchii, A.; Bröring, M.; Ahrens, J.; Bard, A. J. *Journal of the American Chemical Society* **2011**, 8633–8645.

(21) Nepomnyashchii, A. B.; Bard, A. J. *Accounts of Chemical Research* **2012**, *45*, 1844–1853.

(22) Zhao, J.; Xu, K.; Yang, W.; Wang, Z.; Zhong, F. *Chemical Society Reviews* **2015**, *44*, 8904–8939.

(23) D'Amario, L.; Föhlinger, J.; Boschloo, G.; Hammarström, L. *Chemical Science* **2018**, *9*, 223–230.

(24) Liu, Z.; Xiong, D.; Xu, X.; Arooj, Q.; Wang, H.; Yin, L.; Li, W.; Wu, H.; Zhao, Z.; Chen, W.; Wang, M.; Wang, F.; Cheng, Y.-B.; He, H. *ACS Applied Materials & Interfaces* **2014**, *6*, 3448–3454.

(25) Marrani, A. G.; Novelli, V.; Sheehan, S.; Dowling, D. P.; Dini, D. *ACS Applied Materials & Interfaces* **2013**, *6*, 143–152.

(26) Macagno, V.; Giordano, M.; Arvıa, A. *Electrochimica Acta* **1969**, *14*, 335–357.

(27) McIntyre, N. S.; Cook, M. G. *Analytical Chemistry* **1975**, *47*, 2208–2213.

(28) Hernández, N.; Moreno, R.; Sánchez-Herencia, A. J.; Fierro, J. L. G. *The Journal of Physical Chemistry B* **2005**, *109*, 4470–4474.

Part IV

Final Remarks

The work presented in this thesis outlines a multidisciplinary approach to inspection of the charge transfer mechanisms at the dye-semiconductor interface in a p-type dye sensitized solar cell. Three small molecule BODIPY dyes have been synthesized and characterized by many common photophysical and electrochemical spectroscopic techniques. These values were then compared to newer experimental techniques designed to characterise the p-type photocathode directly at the interface where the charge transfer processes occur. Combining these techniques with a kinetic study of the lifetimes of the charge transfer processes occuring on the photocathode results in a relative energy map of the photocathode under working conditions along with lifetimes for the associated charge transfer processes.

A series of small molecule BODIPY dyes (BOD1-3) were synthesized to shift the frontier orbitals of the organic dyes to study the effects of fine tuning the energy levels in a p-type photocathode. (Chapter 2 - 4). Utilizing a wide range of chemistry, functionalized heterocycles were synthesized to differentiate the final dyes and applied to common synthetic conditions to form the BODIPY chromophore. The effects of these changes were evaluated by photophysical and electrochemical techniques commonly used for investigations of dyes in the field of DSSC. (Chapter 4). All three dyes showed potential for use in a p-DSSC, reversible electrochemistry in solution, high extinction coefficients and suitably placed frontier orbitals to promote hole injection into NiO from the dye and regeneration by the iodine electrolyte. Of the three dyes (BOD1-3) BOD3 absorbed furthest towards the red region of the visible spectrum (λ_{max}= 625 nm) and the calculated driving force for electron injection (ΔG_{inj} = -0.76 V was closest to that of the "optimum" value reported in literature for dyes for p-DSSC. Despite the promising values, the solar cell performance of BOD3 was worse than BOD2 with both electrolyte compositions. The J_{SC} values appeared to be limited by the dye regeneration in a system with low concentrations of iodide in the electrolyte. BOD2 was least affected by the reduction of iodine in the electrolyte composition indicating that the regeneration of BOD2 in the p-DSSC was most efficient out of the three dyes.

The work in Chapter 5 uses X-ray PES to create a map of the energy levels in a vaccum to assess the driving forces for electron transfer in a system closer to that of a working p-DSSC device. Previously the energy levels were approximated in solution based experiments; by studying the dye adsorbed onto NiO it was possible to discern any changes in the energy levels upon dye binding. The core level orbitals were examined and the structural changes in the dye can be seen and quantified in the XPS spectra of the dye multilayers on FTO. The lower valence band region of the photocathodes were measured at variable X-ray intensity to inspect the sample at differing probe depths and monitor changes in the spectral features in the bulk semiconductor material and towards the dye-semiconductor interface. At low X-ray excitation energies, the HOMO of the dyes can be seen at binding energies lower than that of the FTO substrate and the binding energies for the HOMO orbitals for all three dyes can be measured directly. Applying the same variable depth X-ray PES technique to the sensitized photocathode showed that further into the sample, dye binding does not have a significant effect on the Fermi position of the NiO but, closer to the interface, dye adsorption shifts the Fermi position to higher binding energies. The shift in Fermi level impacts the driving forces for electron transfer within the device and it was shown that when the dyes BOD1-3 are adsorbed onto the semiconductor, none of the three dyes maintained ΔG_{inj} values close to the postulated optimum values from literature. The recalculated values show BOD2 to have the highest driving force (ΔG_{inj} = 0.60 eV). This result aligns with the results from the solar cell testing where BOD2 was shown to be the most efficient dye from the series in a p-DSSC.

In Chapter 6, fs-TAS was used to investigate the kinetics of the electron transfer processes in the p-DSSC and characterise the transient species produced following photoexcitation of the dye. Single point analysis of the TA data show that for all three dyes, charge injection (τ_{inj}) occurs on a similar timescale for all three dyes, and happens more than an order of magnitude faster than the excited state lifetime. Global anaysis of the data indicated that the inital charge separation process was fast, however in the absence of the redox electrolyte the recombination of charges in the dye and semiconductor is also very fast. Addition of the redox electrolye increased the lifetime of the reduced dyes on the semiconductor. These findings give insight into interactions between the electrolyte and the semiconductor surface and align with previous reports of catalytic activity of NiO towards the conversion of iodide to triiodide. We postulate that interactions of the electrolyte with higher energy states close to the valence band cause deactivation of possible recombination pathways between the reduced dye and NiO and is expressed as an increase in the lifetime of the reduced dye.

The field of p-type DSSC still has some way to go to achieve efficiencies matching the n-type DSSC counterparts. The studies in this thesis should provide some guidelines on designing new dyes for p-DSSC. We suggest the next step to improve this dye series would be introduction of a dyad system to promote spatial separation of the dye. Commonly in dyes for p-DSSC this has been carried out using a TPA donor however multiple other donor-acceptor systems without TPA are published in literature.

The solar cell studies and subsequent kinetic studies highlight issues relating to using an iodide/triiodide electrolyte in DSSC. Other electrolytes have found success in emerging p-DSSC systems such as cobalt (II/III) and iron (II/III), however these electrolytes and the devices seem dependant on dye structure and as such the best electrolyte for p-DSSC is still undefined.

As the trend in research into p-DSSC moves towards looking for new p-type semiconducting materials to increase the performance of the devices, XPS can prove a valuable tool to investigate dye-semiconductor interfaces to understand the fine interactions that occur upon binding of a dye to a semiconductor. Studying the effects on the valence band position is crucial in order to create an efficient photocathode out of new p-type semiconductors.

Choosing a more suitable chromophore should enable studies to elucidate binding geometries of dye monolayers on semiconductor surfaces.

To conclude, this thesis has presented a study of small molecule BODIPY sensitizers for use in p-DSSC. We hope that the methods utilized in this thesis should help advance the field of p-DSSC and serve as guidelines on how to effectively study the interfaces found in these devices.

Appendix A

Appendix

A.1 Publications From The Author Not Included In This Thesis

As part of a GCRF grant, collaboration with the Indian Institute of Technology Hyderabad (IITH), new photocathode materials from Newcastle University were tested in a tandem pn-Quantum Dot Solar Cell alongside TiO_2 based photoanodes fabricated at IITH. The fabricated solar cells showed impressive PCE (7.99%) and exhibited photoelectrochromic properties under illumination.

Sustainable Energy & Fuels

PAPER

View Article Online
View Journal

Check for updates

Cite this: DOI: 10.1039/c8se00548f

A dual-function photoelectrochemical solar cell which assimilates light-harvesting, charge-transport and photoelectrochromic nanomaterials in a tandem design†

Ankita Kolay,[a] Nathan T. Z. Potts,[b] Kripasindhu Sardar,[b] Elizabeth A. Gibson[b] and Melepurath Deepa*[a]

Received 9th November 2018
Accepted 27th December 2018

DOI: 10.1039/c8se00548f

rsc.li/sustainable-energy

A multifunctional tandem cell has been fashioned by (i) replacing the conventional counter electrode in a n-type titanium dioxide-based quantum dot sensitized solar cell (QDSC) with a QD-sensitized p-type nickel oxide photocathode to harness maximum power-conversion efficiency, and (ii) by coating an electrochromic molybdenum oxide overlayer at the photoanode. Light harvesting In_2S_3 nano-flakes were deposited onto a mesoporous NiO semiconductor scaffold. On pairing with the n-QDSC, substantial gains in the photovoltaic performance were achieved owing to greater spectral utilization across the visible region. Improvements to the photoanode architecture were developed by embedding plasmonic Au NPs in the CdS QD-sensitized TiO_2 layer to augment the light absorption *via* plasmonic and scattering effects which translated to higher photocurrent densities. A thin film of MoO_3 was applied to the photoanode, which provided an electrochromic response upon illumination, due to the concurrent insertion of an electron and a cation in the MoO_3 matrix. The power conversion efficiency (PCE) achieved was 6.01% for the n-QDSC half-cell (TiO_2/CdS/Au/MoO_3-$nS^{2-}/S_n{}^{2-}$-C-fabric) and 0.047% for the p-QDSC half-cell (NiO/In_2S_3-$nS^{2-}/S_n{}^{2-}$-C-fabric). A stellar PCE value of 7.99% was attained when the two half-cells were co-assembled in a tandem device, in spite of the disparity in performance between the photoanode and photocathode. The maximum transmission modulation for the tandem device under 1 sun irradiance was 34% and the photocoloration efficiency was 16.4 $cm^2\ min^{-1}\ W^{-1}$ at 550 nm. The results highlight the potential opportunities for combining energy conversion and light management in photovoltaics based on nanotechnology.

Introduction

The performance of quantum-dot sensitized solar cells (QDSC)[1] has risen steadily over recent years to a maximum solar-to-electrical power conversion efficiency of around 12%. To induce a step-change in efficiency, to bring them in line with established PV technology, efforts are now dedicated to developing p/n tandem cells which contain both a photoanode (based on n-type TiO_2 or ZnO) and photocathode (typically based on p-type NiO) in a single device. Studies in the recent past have shown that experimentation centered around either the TiO_2-based n-type- or NiO-based p-type-QDSC, has the potential to yield very high efficiency.[2,3] Approaches undertaken to improve the performance of TiO_2-based QDSCs include using complementary QDs of different sizes or chemical composition, for panchromatic absorption of solar radiation, or integrating QDs with intrinsic electron or hole conductors that facilitate charge transport.[4,5] Further improvements to the QDSC performance have been achieved by embedding plasmonic metal nanoparticles on the QD sensitized TiO_2 photoanode.[6] In these systems, a match between the absorption wavelength of the QDs with the localized surface plasmon resonance peak of the noble metal nanoparticle increases the near-field electromagnetic intensity and, therefore, amplifies the photocurrent.[7,8] The electron accepting ability of metal nanoparticles, *via* an appositely positioned work function, 5.1 eV of Au NPs, augments the charge transfer to the current collector.[9] Building on this idea, in this work, plasmonic gold nanoparticles (Au NPs) have been deposited onto the surface of CdS-sensitized TiO_2 photoanodes, together with a thin layer of MoO_3. In organic photovoltaics, solution-processed MoO_3 thin films have been investigated as

---

[a] *Department of Chemistry, Indian Institute of Technology Hyderabad, Kandi, Sangareddy, Telangana 502285, India. E-mail: mdeepa@iith.ac.in*

[b] *Energy Materials Laboratory, Chemistry, School of Natural and Environmental Science, Newcastle University, Newcastle upon Tyne NE1 7RU, UK*

† Electronic supplementary information (ESI) available: BET–BJH plot for NiO, Mott–Schottky plot of In_2S_3, cyclic voltammograms of TiO_2, CdS, Au, MoO_3, NiO, In_2S_3; calculations of CB, VB positions with band gaps; a half-cell bode plot, IPCE *versus* wavelength plot and table of solar cell parameters. See DOI: 10.1039/c8se00548f

a versatile hole-injection layer.[10] The s-MoO_3 layer is very proficient in hole extraction because it possesses deep lying electronic states with a work function of 5.5 eV.[11] This non-toxic and n-type semiconducting transition-metal oxide shows distinct electrochromism. The transparent as-fabricated film darkens to appear blue in color when reduced to Na_xMoO_3 through concurrent injection of electrons and intercalation of charge-compensating cations into the MoO_3 lattice.[12,13]

$$\text{(Transparent) } MoO_3 + x(Na^+ + e^-) \rightarrow Na_xMo^{VI}_{(1-x)}Mo^{V}_xO_3 \text{ (deep blue)} \quad (1)$$

There have been many reports on NiO-based photoactive cathodes applied in dye-sensitized solar cells over the last few years,[14–16] but in the case of QDSCs, there is still immense scope for exploration.[17] Finding suitable QD-sensitized photocathodes would pave the way for the application of tandem QDSCs, which could, in theory, surpass the maximum attainable conversion efficiency of single-junction QDSCs. To achieve this, the photocurrent generated by the photocathode must match the photocurrent generated by the photoanode. However, to date, the efficiencies of "p-type" solar cells lag behind those of the more established "n-type" devices.

A promising strategy to obtain photocurrents in p-type photocathodes which are comparable to the n-type systems is to sensitize mesoporous wide band gap semiconductors, such as NiO, with light-absorbing QDs rather than dyes. The advantages of QD sensitizers include the ability to finely tune the visible response and position of the valence band (VB) edge by modulating both the QD size and composition. It is also possible to obtain higher photocurrents by boosting the hole injection through the phenomenon of multiple exciton generation.[18] In addition, such sensitizers have higher molar extinction coefficients than those of molecular dyes, which could enable thinner films to be used to compensate for the relatively short diffusion length in NiO compared to TiO_2.[19] Complementary to the photoanode, a photoexcited QD injects a hole into the VB of the NiO cathode which travels to the charge collector.[20] Indium sulfide (In_2S_3) is an example of a group III–VI compound semiconductor material which has shown merit as suitable QD material for n-QDSC,[21] and its use can potentially be extended to photocathodes. Depending upon the temperature and pressure, it exists in three crystallographic modifications: *viz.*, α, β and γ. Of these polymorphs, β-In_2S_3, with a tetragonal structure, is the most stable state below 693 K. Its direct bandgap varies between 2.0 and 2.45 eV, depending upon the composition and the NPs are light-absorbing in the visible region.[22] *In situ* growth techniques such as chemical bath deposition (CBD) provide a relatively inexpensive, simple and convenient route for large area deposition.[23] The electron injection rate from *in situ* grown QDs increases as the distance between electron donor and acceptor is progressively reduced.

Herein In_2S_3 sensitized NiO supported on a carbon (C)-fabric substrate was used as the photocathode. The C-fabric current collector is a cost-effective, highly conducting (with low sheet resistance) alternative to FTO glass, which requires no elaborate treatment prior to use. TiO_2/CdS/Au/MoO_3 was chosen for the photoanode assembly and, due to the use of QDs instead of dyes as the light harvester, an alkaline polysulfide redox couple gel electrolyte was incorporated. This architecture enhances the theoretical solar-to-electrical conversion efficiency by collecting photons on two photo-electrodes within a single device, thereby reducing the spectral losses. In addition, we present the possibility to improve the performance and open up new applications of the devices through the incorporation of a multifunctional MoO_3 coating.

Experimental

Chemicals

Fluorine doped tin oxide (FTO) glass with a sheet resistance of ~25 Ω cm^{-2} was purchased from Pilkington and cleaned consecutively in soap solution, 10% HCl solution, 10% NaOH solution, distilled water, acetone/ethanol (v/v: 1 : 1) and iso-propanol. TiO_2 (P25) and fumed silica were free gifts from Evonik and Cabosil respectively. Titanium chloride ($TiCl_4$), sodium hydroxide pellets (NaOH), hydrochloric acid (HCl), methanol, ethanol, iso-propanol, toluene, potassium chloride (KCl), sulfur powder were purchased from Merck; Triton X-100, gold(III) chloride solution ($HAuCl_4$, 99.99%), ammonium heptamolybdate tetrahydrate ($(NH_4)_6Mo_7O_{24}\cdot 4H_2O$), indium(III) chloride ($InCl_3$), thioacetamide, acetyl acetone, cadmium acetate [$Cd(CH_3COO)_2$], sodium sulfide (Na_2S), sodium borohydride ($NaBH_4$), oleylamine and tetraoctylammonium bromide (TOAB, 98%) were acquired from Sigma Aldrich. Carbon-fabric (sheet resistance ~10 Ω cm^{-2}) was procured from Alibaba Pvt. Ltd. Ultra-pure water with a resistivity of ~18.2 MΩ cm was obtained through a Millipore Direct-Q3 UV system.

Synthesis of oleylamine-capped Au nanoparticles

An aqueous solution of 10 mM $HAuCl_4$ was prepared in 25 mL of ultra-pure water and then mixed with 25 mL of a toluene solution containing 25 mM TOAB. Once the Au precursors were transferred into the toluene phase, the dense water phase was discarded. Oleylamine (1.65 mL) was added into the Au–TOAB in toluene solution. $NaBH_4$ (0.283 g) dissolved in 15 mL of deionized water was quickly added dropwise with vigorous stirring. The mixture turned deep red and was used without further purification.[24]

Synthesis of the MoO_3 solution

The MoO_3 solution was prepared by heating 0.4 g of $(NH_4)_6Mo_7O_{24}\cdot 4H_2O$ in distilled water (10 mL) at 80 °C for 1 h in air. The precursor decomposed to three components: MoO_3, NH_3 and H_2O, among which NH_3 evaporated, and MoO_3 was the only solute left in the solution. The resulting solution was diluted to 40 mL with deionized water.[25]

Photoanode preparation

A TiO_2 slurry was prepared by dispersing TiO_2 powder in a solution of 1.5 mL of acetyl acetone, 8.5 mL of ultrapure water and 20 mg of Triton X-100. A screen printing technique was employed to apply this slurry over a pre-cleaned FTO substrate.

The as-fabricated TiO_2 film was heated at 60 °C for 30 min, followed by annealing at 500 °C for another 30 min. This procedure was repeated to apply, heat and anneal a second layer of TiO_2. Finally, the TiO_2-coated FTO substrate was immersed in an aqueous $TiCl_4$ (40 mM) solution for 30 min at 70 °C, and the resulting TiO_2 film was rinsed in deionized water and annealed at 500 °C for 30 min. CdS QDs were deposited onto the TiO_2 film by a successive ionic layer adsorption and reaction (SILAR) process. Clear homogeneous solutions of 0.1 M cadmium acetate and 0.1 M sodium sulfide in methanol were taken in two separate beakers as the Cd^{2+} and S^{2-} ion precursors, respectively. The TiO_2 film was first dipped in the Cd^{2+} precursor for 2 min, rinsed in methanol to remove excess ions, and then dried at 60 °C in a hot air oven. The same film was subsequently immersed in the S^{2-} precursor solution for 2 min followed by rinsing in solvent and oven drying to form one layer of CdS over the TiO_2 film. These steps constitute one SILAR cycle. The TiO_2/CdS film was completed by performing five more SILAR cycles on the film, which was then oven dried for two days at 50 °C. Au nanoparticles were incorporated in the TiO_2/CdS electrodes by drop-casting the Au NPs in toluene solution and evaporating the solvent by drying in air. A very thin film of MoO_3 was formed over the TiO_2/CdS/Au electrode by adding one drop of the diluted solution and the TiO_2/CdS/Au/MoO_3 film was annealed on a hot plate at 150 °C for 10 min (Scheme 1).

Photocathode preparation

The NiO precursor solution was prepared by dissolving 1 g of anhydrous $NiCl_2$ and 1 g of Pluronic P123 (PEG-PPG-PEG) symmetric tri-block copolymer in a 6 : 5 (v/v) mixture of ethanol and ultrapure Milli-Q water. The solution was left at rest for 3 days at 30 °C, and then centrifuged. NiO electrodes were made by applying the supernatant solution onto C-fabric followed by sintering at 450 °C for 30 min.[26] Upon these C-fabric/NiO films, In_2S_3 nanoparticles were deposited by CBD. Anhydrous $InCl_3$ (0.35 g) and thioacetamide (0.18 g) were dissolved in 20 mL of distilled water. The C-fabric/NiO films and blank C-fabrics were dipped vertically in the solution and heated on a hot plate at 70 °C for 2 h with constant stirring (for different durations). The films were collected, washed with distilled water and finally dried at 60 °C in air.[27] The resulting films were labelled as C-fabric/NiO/In_2S_3 and C-fabric/In_2S_3 electrodes. Single layer NiO films sensitized with In_2S_3 were also prepared on FTO glass substrates for half-cell measurements, and for evaluating the photoelectrochromic response.

Device fabrication

Tandem devices used for photovoltaic measurements were assembled by sandwiching the photoanode (TiO_2/CdS/Au/MoO_3 or their other combinations) and the photocathode (C-fabric/NiO/In_2S_3 or C-fabric/In_2S_3) with their active areas facing each other and a 2 mm wide para-film spacer between them. The two electrodes were clamped together with binder clips after filling the gap between active sites with a polysulfide gel electrolyte. The electrolyte was prepared by vigorously mixing 1 M Na_2S and 1 M elemental sulfur powder in 10 mL ultrapure water until it turned into a clear dark-yellow colored solution. 4 wt% of fumed silica was dispersed by stirring to form a homogeneous polysulfide gel. Half-cells were assembled similarly with TiO_2/CdS/Au/MoO_3 or NiO/In_2S_3 as the photoanode and with a blank C-fabric substrate as the counter electrode.

Instrumental methods

XRD patterns were recorded on a PANalytical, X'PertPRO instrument with a Cu-K_α (λ = 1.5406 Å) radiation as the X-ray

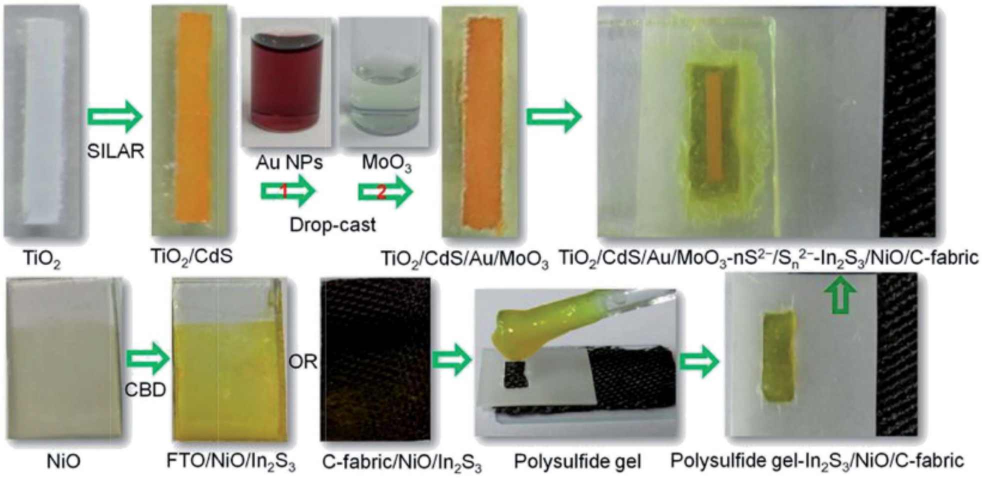

Scheme 1 Pictorial illustration of the preparation of photoanode, photocathode followed by tandem cell fabrication.

source. A field emission scanning electron microscope (Carl Zeiss Supra 40 FE-SEM) was used for imaging the surface morphology of the samples. Transmission electron microscopy (TEM) images were obtained for samples deposited on carbon coated copper grids (*via* suspension in acetone and evaporation) on a JEOL 2100 microscope operating at an accelerating voltage of 200 kV. The optical absorption and the transmission spectra of the films of were recorded on a UV-VIS-NIR spectrophotometer (T90+ of PG Instruments). A Horiba Fluoromax-4 spectrometer was used for recording fluorescence spectra of the photoactive films. Current *versus* potential (*I–V*) data of QDSCs were measured under 1 sun (100 mW cm^{-2}) illumination using a LOT-Oriel solar simulator equipped with a 150 W Xe lamp, an AM 1.5 filter, capable of delivering a collimated output beam of 25 mm diameter, coupled with a Metrohm Autolab PSTAT302N. The spatial uniformity of irradiance was confirmed by calibrating with a 2 cm × 2 cm Si reference cell and re-affirmed with an ILT1400 radiometer/photometer. Incident power to current conversion efficiency (IPCE) *versus* wavelength was measured on a Newport machine compliant to ASTM E1021-12 standard with a tunable xenon arc lamp (300 W) as the light source. Electrochemical impedance spectra (EIS) for photoanodes were recorded on an Autolab PGSTAT 302N equipped with a frequency response analyzer and a NOVA 1.11 software, under an ac amplitude of 20 mV over the frequency range of 1 MHz to 0.1 Hz. Photovoltage decay *versus* time and photocurrent *versus* time measurements were carried out by using a tungsten-halogen lamp as the light source coupled to an Autolab PGSTAT 302N, which recorded the chronopotentiometric as well as chronoamperometric data in dark. The Mott–Schottky plot of In_2S_3 was derived from dark EIS measurement with Pt and Ag/AgCl/KCl as counter and reference electrode respectively using 0.1 M KOH as the electrolyte. Cyclic voltammograms (CV) of pristine-TiO_2, CdS, Au, MoO_3, NiO and In_2S_3 deposited over FTO substrates were recorded in a three electrode cell, with the aforementioned as working electrodes, a Pt rod as the counter electrode and Ag/AgCl/KCl as the reference electrode in an aqueous 0.1 M KCl electrolyte solution at a scan rate of 20 mV s^{-1}.

Results and discussion

Photocathode assembly and structural characterisation of the photocathode components

Two types of mesoporous NiO cathodes were prepared. A C-fabric electrode was coated with NiO, by drop-casting a Ni salt-Pluronic 123 precursor, followed by annealing in air. The precursor was also deposited on FTO-coated glass by doctor blade and annealed. A semi-transparent photocathode was constructed from In_2S_3 nano-flakes tethered to the NiO film on FTO glass. The extent of deposition of In_2S_3 was optimized by varying the reaction time while monitoring the change in the optical band gap, which was deduced from the shift in the absorption band edge in the visible spectrum (see below).

The XRD pattern of the In_2S_3 nano-flakes (Fig. 1a), contains distinct peaks at 2θ = 27.42°, 33.22°, 43.59°, 47.67°, 56.58°, 60.77°,67.66°, 70.83° and 77.03° aligning with d = 3.25, 2.70, 2.07, 1.91, 1.63, 1.52, 1.38, 1.33 and 1.24 Å, corresponding to the (213), (220), (323), (400), (426), (431), (525), (444) and (606) planes of body-centered tetragonal In_2S_3. The XRD pattern of NiO (Fig. 1b) reveals well-defined peaks at 2θ = 37.25°, 43.28°, 62.86°, 75.40° and 79.39°, and they are attributed to the (111), (200), (220), (311), and (222) planes of NiO with a face centered cubic (fcc) crystal lattice (JCPDS: 711179). The SEM and TEM images of In_2S_3, displayed in Fig. 1c–f, show that the photosensitizer has a nano-flake-like morphology. Elongated fiber like shapes, 35 to 40 nm in length, interspersed with irregular shaped flaky structures are observed in the images. A lattice scale image (Fig. 1c), extracted from a nano-flake shows an inter-fringe distance of 0.33 nm, which matches an inter-planar spacing (*d*) of 3.25 Å, corresponding to the (213) plane of the body-centered tetragonal structure of In_2S_3 (JCPDS: 731366). The TEM image of NiO (Fig. 1g–i) illustrates that the oxide is made up of misshaped interconnected nanoparticles with indistinguishable grain boundaries. The selected area electron diffraction (SAED) pattern of NiO (inset of Fig. 1i) shows bright spots superimposed over diffuse rings, and these are assigned to the (111), (200) and (220) planes of fcc NiO corresponding to *d* values of 2.41, 2.09 and 1.48 Å. The particles are porous, an outcome of the templating method used for synthesizing NiO. Annealing the Ni salt-Pluronic 123 precursor film burns out the organic material and leaves behind voids or pores, which function as active sites for the In_2S_3 nano-flakes to anchor onto. A surface area of 47.6 m^2 g^{-1}, pore volume of 0.2 cm^3 g^{-1} and average pore size of 28.4 Å were determined from the N_2 adsorption–desorption isotherm of NiO (Fig. S1, ESI†).

SEM images of the NiO and NiO/In_2S_3 assembly tethered to the C-fabric substrate are shown in Fig. 2a–e. Pristine C-fabric is composed of inter-woven carbon fibers having a smooth texture (inset of Fig. 2c), which provides a high electroactive surface area for the anchoring of the photocathode components. The SEM images of the C-fabric/NiO electrode (Fig. 2a and b) show that the carbon fibers are uniformly coated with the oxide particles and the texture now appears to be rough. When the In_2S_3 layer is deposited on top of the NiO layer, the density of particles appears to increase, particularly in the gaps between the NiO coated carbon fibers, as can be judged from Fig. 2c and d. An enlarged view of the C-fabric/NiO/In_2S_3 assembly (Fig. 2e) shows aggregates of In_2S_3 flakes deposited over the NiO coated carbon fibers. The EDX spectrum and elemental mapping are shown in Fig. 2f. The elemental mapping over a 2.5-micron length region shows uniform coverage of In_2S_3 and NiO over carbon fibers, for all the four major elements, S, In, O and Ni are observed to be homogeneously distributed. The concentration of In_2S_3 is comparatively higher than that of NiO as can be seen from the EDX spectrum. The mass ratio of In_2S_3 and NiO is 2.3 : 1.

Optical properties of the photoanode components

The UV-visible absorption spectra of In_2S_3 nano-flakes were recorded at half-hour intervals during the deposition (0.5 h, 1 h, 1.5 h and 2 h) and are shown in Fig. 3a. The absorption edge shifts to longer wavelengths in the visible spectrum as a function of increasing deposition time, indicating that the

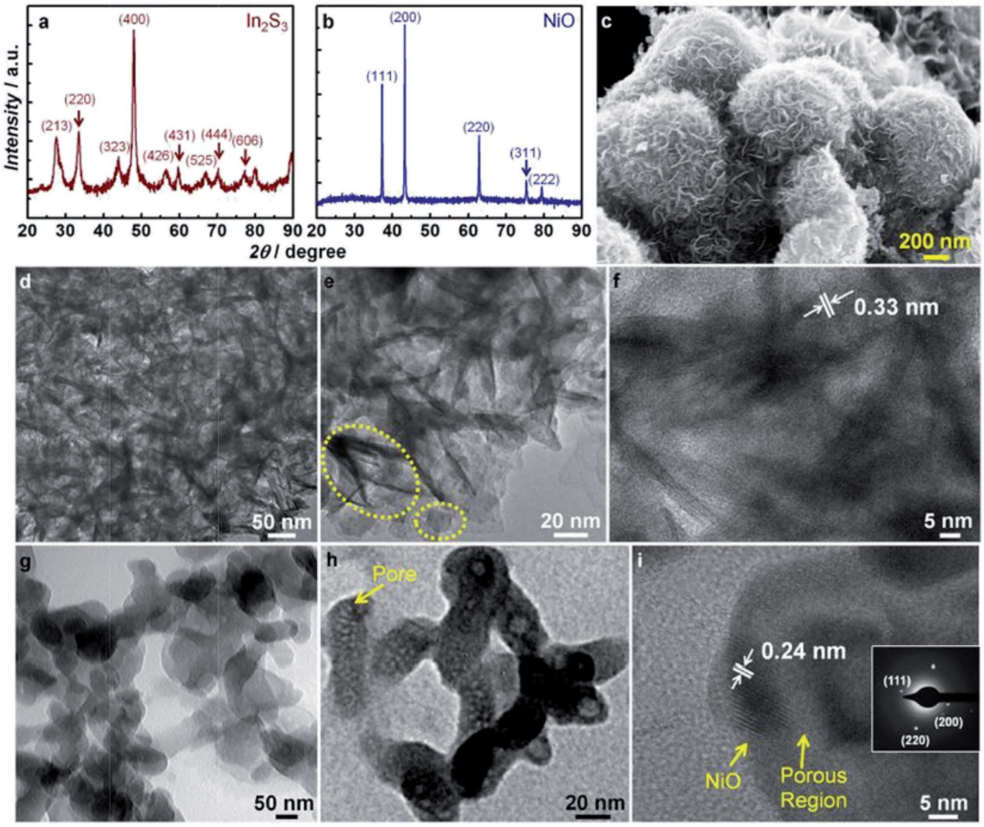

Fig. 1 XRD patterns of (a) In_2S_3 and (b) NiO. (c) SEM image of In_2S_3. (d and e) TEM- and (f) lattice scale-images of In_2S_3; (nano-needles and nanoparticles shown in yellow dotted circle and ellipse in (e)). (g and h) TEM- and (i) lattice scale-images of NiO; inset shows the corresponding SAED pattern.

dimensions of In_2S_3 are controlled by the duration of immersion. For the 2 h deposition time, the In_2S_3 light absorbers exhibited a broad absorption peak in the 315–430 nm wavelength range, corresponding to a band gap of 2.2 eV which is the closest to literature values.[28] The narrowing of the band gap indicates that the size of the nanostructures increases over time. During the deposition, In_2S_3 particles rearrange to form stable structures, and a combination of nano-needles and nanoparticles results at the end of 2 h. This film exhibited a broader spectral absorption and a lower band gap compared to the In_2S_3 obtained at the end of 0.5, 1 and 1.5 h immersion spans. Fig. 3b depicts the absorption spectra of pristine NiO and NiO/In_2S_3. The NiO spectrum contains shows a strong absorption in the UV region with a band gap of 3.6 eV and NiO/In_2S_3 films reflect the cumulative absorption features of both NiO (UV) and In_2S_3 (UV-visible).

The fluorescence spectra of pristine In_2S_3 and NiO/In_2S_3 films obtained at an excitation wavelength of 370 nm are presented in Fig. 3c. The emission from the photosensitizer, In_2S_3, alone was broad, and deconvolution gave two components, a strong one, centered at 564 nm, followed by a low intensity one at 617 nm. While the higher energy component is ascribed to band edge recombination, the lower energy one is assigned to radiative transitions between the intra-gap defect states. In the NiO/In_2S_3 film, the intensity of the band-edge emission of In_2S_3 was quenched by ~63%. This is consistent with light-induced electron transfer from the VB of NiO to the VB of In_2S_3. This experiment shows the ability of In_2S_3 to act as a photosensitizer for NiO, leaving holes in NiO which diffuse to the current collector, *e.g.* FTO or C-fabric.

Photoelectrochemistry of the photocathode half-cell

An energy band diagram for the half-cell, shown in Fig. 3f, illustrates the mechanism in the device. The energy levels of the In_2S_3 were determined from cyclic voltammetry; the CV plots

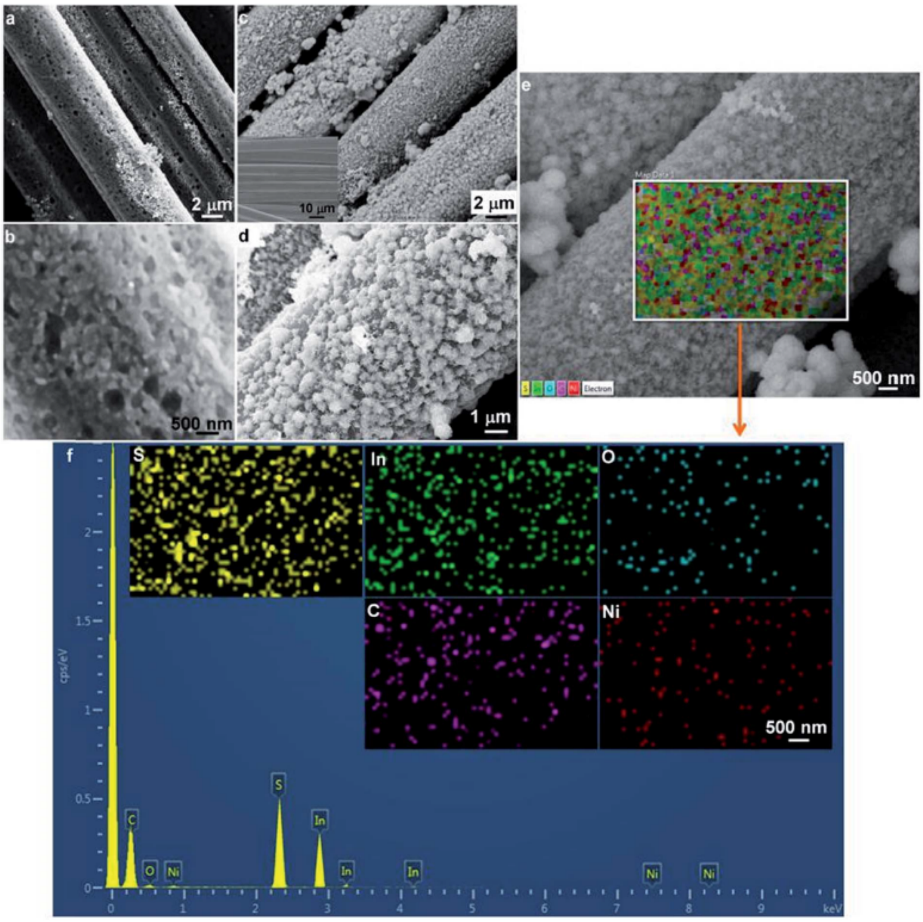

Fig. 2 SEM images of (a and b) C-fabric/NiO and (c and d) In_2S_3 coated over C-fabric/NiO. Inset of (c) is plain C-fabric. SEM image of (e) C-fabric/NiO/In_2S_3 and (f) the corresponding EDX plot and the elemental mapping images.

and the calculations are provided in ESI (Fig. S2 and Table S1†). The Mott–Schottky plot of In_2S_3 film on FTO, deposited by CBD for 2 h confirms the n-type nature of the absorber (Fig. S3, ESI†). The corresponding 1/(capacitance)^2 *versus* voltage profile yields a positive slope, consistent with data previously reported for β-In_2S_3 deposited by CBD.[29] NiO is a p-type semiconductor with a high-lying VB, above that of In_2S_3.[30] Upon excitation, the exciton which forms in the In_2S_3 can, therefore, extract an electron from the NiO valence band. The electron in the conduction band of In_2S_3 is transferred to the polysulfide redox mediator, and the reduced S^{2-} species diffuses to the C-fabric counter electrode to complete the circuit.

The potential for the NiO/In_2S_3 film to serve as a photocathode in photoelectrochemical solar cells was confirmed by recording the current *versus* time transients for the NiO/In_2S_3-nS^{2-}/S_n^{2-}-C-fabric half-cell during on–off cycles of white light with an irradiance of 25 mW cm^{-2}. Fig. 3d depicts that the NiO/In_2S_3-nS^{2-}/S_n^{2-}-C-fabric half-cell produces a reasonably stable photocurrent of 0.037 mA upon irradiation for 20 s intervals. In the dark, the current dropped steeply to nearly zero, and upon illumination, the same magnitude of photocurrent was reproduced, indicating the good photo-activity of this electrode.

The *J*–*V* characteristics of this half-cell (Fig. 3e) gave a PCE of 0.047% with a V_{OC} of 182 mV, J_{SC} of 0.84 mA cm^{-2} and FF of 30.53% under 1 sun irradiance. Although the NiO based half-cell delivers a much lower PCE compared to the PCE produced by typical TiO_2 based half-cells (discussed in the next section), below we show that the synergy between the two

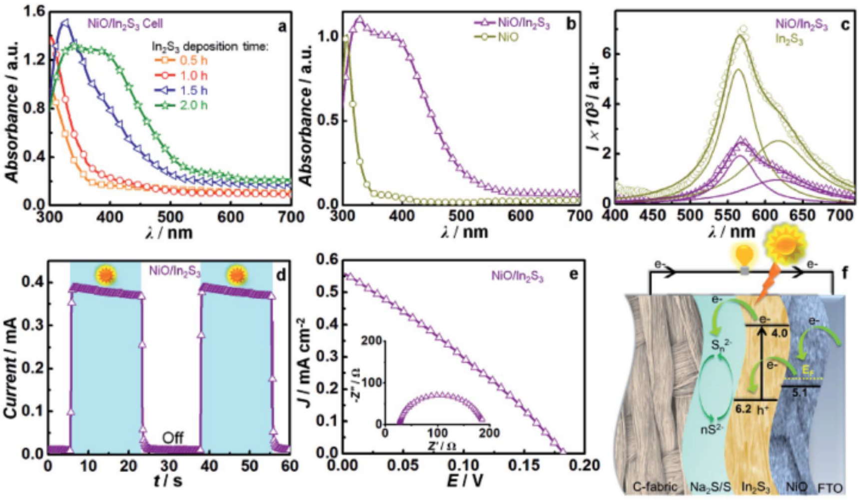

Fig. 3 (a) Absorbance spectra of In_2S_3 films grown for different deposition times. (b) Absorbance spectra of pristine NiO and NiO/In_2S_3 films. (c) Fluorescence spectra of In_2S_3 and NiO/In_2S_3 films, obtained at $\lambda_{ex} = 370$ nm. For the NiO/In_2S_3-nS^{2-}/S_n^{2-}-C-fabric half-cell, with NiO/In_2S_3 as the photoanode: (d) current *versus* time transients under white light irradiance, (e) *J*–*V* characteristics (under 1 sun illumination, AM 1.5), and inset is a Nyquist plot recorded in dark under an open-circuit dc voltage of −0.2 V (forward bias) and (f) energy band diagram of the half-cell, showing charge separation and transport.

components leads to a high PCE in the tandem cell, which exceeds the performance of the photocathode or photoanode when used alone. The ability of this half-cell to preferentially direct the photo-excited charge carriers to C-fabric, as opposed to competing unwanted recombination routes, was studied by EIS. Recombination resistance, R_{rec} is inversely proportional to the recombination rate and it is well established that R_{rec} in QDSCs reflects the interfacial charge recombination process. From the Nyquist plot, in the inset of Fig. 3e, the R_{rec} at the $(NiO/In_2S_3)/(nS^{2-}/S_n^{2-})$ interface was found to be 159 Ω. The R_{rec} value points to the probability of holes in the VB of both In_2S_3 and NiO recombining with reduced species in the electrolyte and surface trap state defects which hinders the performance of QDSC. From the Bode plot shown in ESI (Fig. S4†), the recombination lifetime was calculated using the equation $\tau_d = 1/2\pi f$, where *f* is the middle frequency peak. Recombination time (τ_d) is defined as the time taken by the excited state electron vacancy in the NiO/In_2S_3 electrode to recombine with the reduced species in the polysulfide electrolyte. The electron–hole recombination time is calculated to be 1.5 ms in the NiO/In_2S_3-nS^{2-}/S_n^{2-}-C-fabric cell.[31]

Photoanode assembly and structural characterisation of the photoanode components

The photoanode comprises of TiO_2, CdS, Au and MoO_3; of these, while the structures of TiO_2 and CdS have been reported in detail by us in the past,[32] Au and MoO_3 are investigated in detail here. XRD pattern of Au NPs (Fig. 4a) shows a sharp intense peak at $2\theta = 38.19°$, followed by multiple peaks at 44.39°, 64.58° and 77.57°, which are assigned to the (111), (200), (220) and (311) planes of Au with a fcc lattice structure (JCPDS: 652870). The corresponding TEM images (Fig. 4b and c) show a uniform distribution of discrete NPs with distinctive grain boundaries, with particle size in the range of 5–10 nm. Since the dimensions of the particles are less than 50 nm, it is anticipated that when they are employed in the photoanode, plasmonic effects as opposed to scattering effects will dominate. Scattering generally dominates at NP dimensions in excess of 50 nm. Thus, the near electric field enhancement of Au NPs upon excitation of the surface plasmon is expected to increase the effective light absorption cross-section of the solar cell. MoO_3, in the photoanode, functions as an additional hole transport layer, and as an electrochromic layer. The XRD pattern of MoO_3 (Fig. 4d) contains a prominent broad hump at low 2θ, which indicates that the layer is largely amorphous, with few indistinct peaks at 23.33°, 25.70°, 27.33° and 38.57° matching to the (110), (040), (021) and (131) planes of orthorhombic MoO_3 (JCPDS: 050508). The SEM image of the MoO_3 layer shows a featureless undulating morphology (Fig. 4e), and the TEM image (Fig. 4f) shows mingling particles with no unique shapes, and having no clear boundaries. The SAED pattern (inset of Fig. 4f) reveals diffuse concentric rings, with very faint spots, re-affirming the amorphous nature of the MoO_3 layer. The SEM image of the TiO_2/CdS electrode (Fig. 4g) shows a network of interconnected particles separated by pores (the latter having sizes of the order of few tens of nm), typical of P25 TiO_2, which is known to have a mesoscopic structure. Coating TiO_2/CdS with Au NPs, and

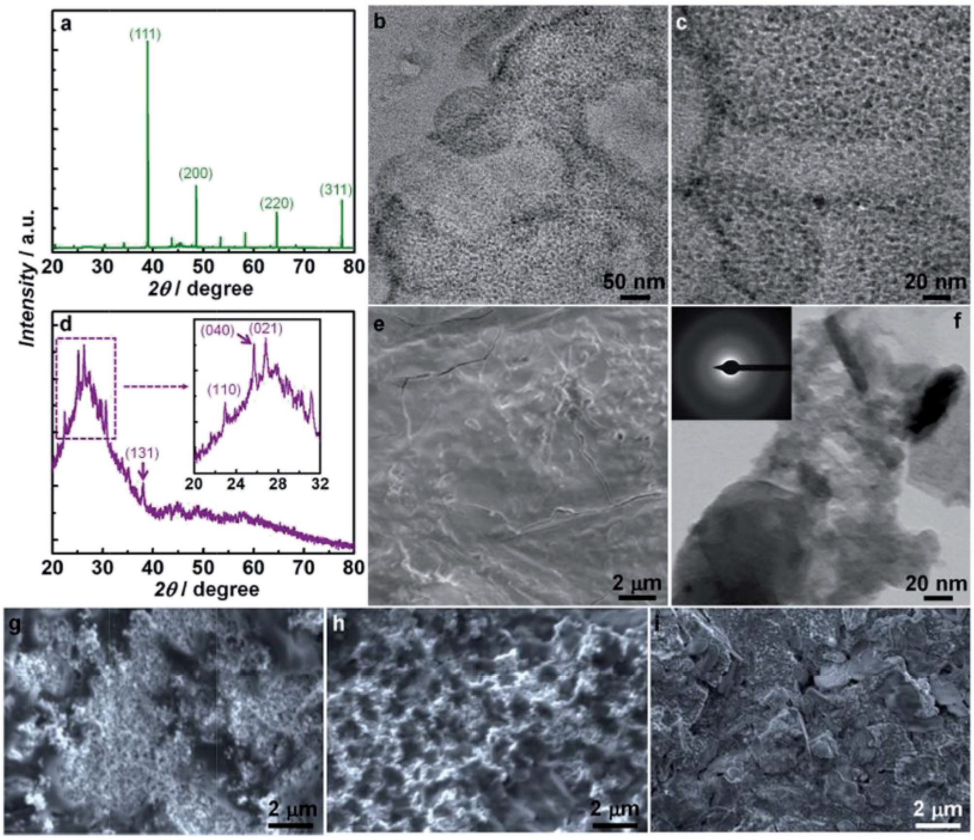

Fig. 4 (a) XRD pattern and (b and c) TEM images of Au NPs. (d) XRD pattern, (e) SEM image and (f) TEM image and SAED pattern (as inset) of MoO_3. SEM images of (g) TiO_2/CdS, (h) TiO_2/CdS/Au and (i) TiO_2/CdS/Au/MoO_3 electrodes.

then by MoO_3, led to some textural but unremarkable changes in the corresponding images (Fig. 4h and i).

Optical properties of the photoanode components

The absorbance and emission (recorded at $\lambda_{ex} = 370$ nm) plots of the photoanode components: CdS, Au and MoO_3 are shown in Fig. 5a–c. CdS QDs show a broad but featureless absorption extending from 310 to 460 nm, which tapers off at 540 nm and corresponds to a band gap of 2.29 eV (Fig. 5a). The CdS/glass film shows a highly intense emission peak above 470 nm with a λ_{max} at 536 nm which is largely due to band edge recombination. Au NPs show a localized surface plasmonic absorption peak at 520 nm (Fig. 5b) which is close to the λ_{max} of CdS QDs, and therefore when integrated with the photo-absorber, the metal nanoparticles further improve their light harvesting capability. The emission peak of Au NPs spans over a wavelength range of 400 to 500 nm, indicating that the high energy photons in the UV-region absorbed by Au NPs possibly induce electronic transitions from the Fermi level (E_F) of Au, and the emission is brought about when they revert to the E_F. MoO_3 shows an intense absorption peak in the UV region (Fig. 5c), which corresponds to a band gap of 3.42 eV. MoO_3 shows a strong emission peak with a λ_{max} at 430 nm. Although MoO_3 does not function as a photo-sensitizer, possibly due to fast recombination and poor electron injection efficiency, this observation shows it to be an emissive material. The inset of Fig. 5c depicts the absorption profile of pristine TiO_2 and the absorption edge, which tapers off at the onset of the visible region, is consistent with the optical band gap for TiO_2 of ~3.16 eV.

The optical properties and charge transfer studies on the photoactive films: TiO_2/CdS, TiO_2/CdS/Au and TiO_2/CdS/Au/MoO_3, are presented in Fig. 5d and e. The absorption features of TiO_2/CdS, TiO_2/CdS/Au and TiO_2/CdS/Au/MoO_3 films reveal the

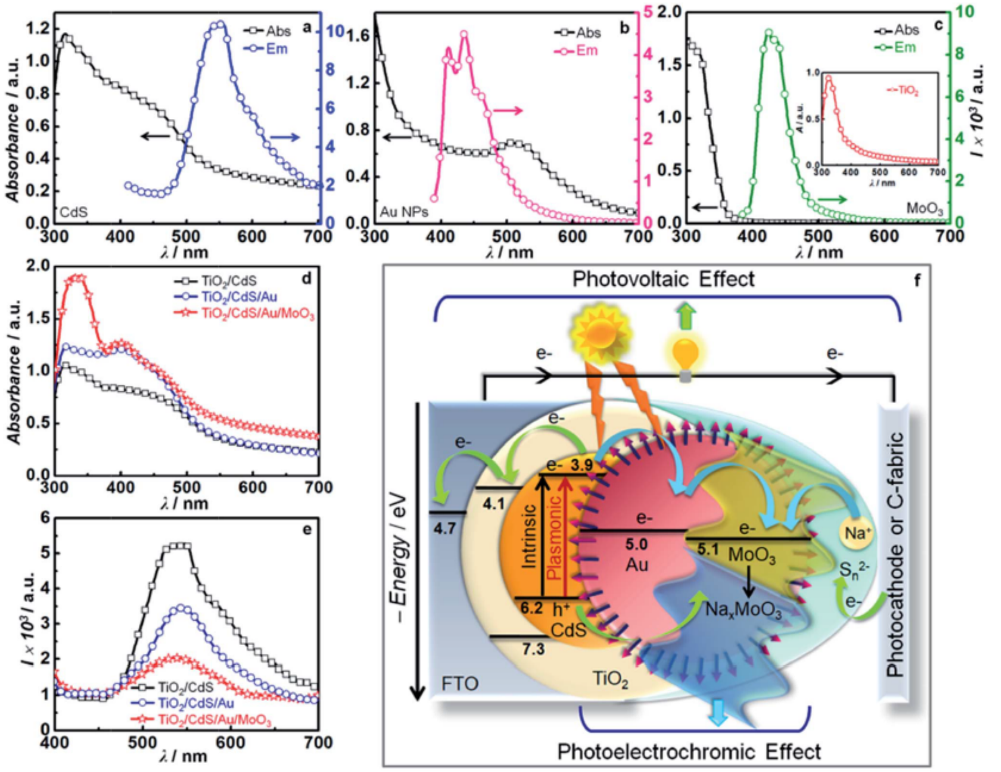

Fig. 5 Superimposed absorption and emission spectra (λ_{ex} = 370 nm) of (a) CdS, (b) Au NPs and (c) MoO$_3$. Inset of (c) shows the absorbance curve of pristine TiO$_2$. (d) Absorption spectra of photoanode films and (e) fluorescence spectra of photoanode films obtained at λ_{ex} of 370 nm. (f) Energy level diagram illustrating all possible electron transfer modes and photoelectrochromism in the TiO$_2$/CdS/Au/MoO$_3$ assembly.

combined effects of TiO$_2$ and CdS. All the three curves display a wide absorption band in the visible region over a wavelength range of 310–525 nm. Both TiO$_2$/CdS/Au and TiO$_2$/CdS/Au/MoO$_3$ films show an additional absorption hump in the visible region, spanning 380 to 510 nm which can be attributed to the plasmonic effect of Au NPs, which causes a surge in the absorption by CdS QDs. When light impinges on an Au NP smaller than 50 nm (as is the case here), the electric field component of the radiation interacts with the conduction band electrons, and induces a redistribution of the electron density in the NP. A restoring force then sets in a series of oscillations that decays in about 10 fs, at the end of which the photons are re-radiated, where the strength of the field decays rapidly with distance within the photoanode (TiO$_2$/CdS/Au). Thus, the vicinal semiconductor QDs, such as CdS here, undergo excitation by absorbing this energy, and show an enhanced absorption in the region of overlap with the SPR peak of the metal NP. Further, the inclusion of the MoO$_3$ layer does not eclipse the SPR effect, for the TiO$_2$/CdS/Au/MoO$_3$ film almost retraces the curve obtained for the TiO$_2$/CdS/Au film, except for a slight increment above 500 nm and an amplified absorption over 300–370 nm which are due to the absorption trends of MoO$_3$ in these wavelength regions.

The fluorescence spectra of TiO$_2$/CdS, TiO$_2$/CdS/Au and TiO$_2$/CdS/Au/MoO$_3$ electrodes, recorded at a fixed excitation wavelength of 370 nm, are analogous to that of CdS over a wide wavelength range of 470–610 nm, with λ_{max} centered around 540 nm (Fig. 5e). The emission intensity of CdS is quenched by ~50% when the CdS QDs are anchored to titania in the TiO$_2$/CdS electrode. The emission is quenched by a further 34% upon the incorporation of Au NPs. The TiO$_2$/CdS/Au/MoO$_3$ electrode retains about 39% of the emission intensity of TiO$_2$/CdS assembly devoid of Au and MoO$_3$. The quenching is consistent with a photoexcited electron cascade from the CB of CdS to the CB of TiO$_2$ in the TiO$_2$/CdS film or to the equilibrated Fermi level of the photoanode. Au and MoO$_3$ significantly contribute to the quenching of the exciton emission by providing channels for unhindered electron and hole transport in the TiO$_2$/CdS/Au/

MoO_3 assembly, respectively, which could improve the photoelectrochemical performance of the solar cell.

Photoelectrochemistry of the photoanode half-cell

The energy level diagram shown in Fig. 5f shows the proposed mechanism for the combined photovoltaic and photoelectrochromic effects. Intrinsic and plasmonic electron–hole pairs are generated in CdS, upon illumination of the TiO_2/CdS/Au/MoO_3 electrode. Some of the electrons are transferred to MoO_3, which forms blue colored Na_xMoO_3 (eqn (1)). Meanwhile, the bulk of the excited electrons are injected into TiO_2 and lead to the photocurrent response. Had this not been the case, the cell would have delivered a poor PCE. These electrons reach the CE *via* the external circuit, where they are consumed in the reduction of the S_n^{2-} species in the electrolyte.

Optimization of the Au NP content on the TiO_2/CdS electrode is of prime importance to exploit the plasmonic light trapping mechanism. Fig. 6a depicts the current density (J) *versus* voltage (V) curves for TiO_2/CdS/Au photoanodes with varying Au NP content, measured under 1 sun irradiance (100 mW cm^{-2}). The Au NP content was varied by adjusting the concentration of the Au stock solution in toluene, which was drop cast over the TiO_2/CdS photoanode, and the effect on the solar cell parameters is summarized in Table 1. An optimum Au NP dilution factor of 1 : 13 delivered a maximum PCE value of 6.11% for a TiO_2/CdS/Au-nS^{2-}/S_n^{2-}-C-fabric cell, with a better FF of 56.98% compared to other dilutions.

The photovoltaic parameters of the half-cells assembled with different photoanodes, TiO_2/CdS, TiO_2/CdS/Au and TiO_2/CdS/Au/MoO_3, and a bare C-fabric counter electrode are shown in Fig. 6b and the cell parameters are summarized in Table 2. Due to the localized SPR effects in the Au NPs, the CdS QDs in the vicinity pick up the localized optical energy, which augments the PCE. The TiO_2/CdS based half-cells exhibited an increasing trend in PCE from 4.47% to 5.90% with the addition of Au NPs. This was increased further to 6.01% with the thin coating of MoO_3 over the photoanode. While the J_{SC} of the cells with Au and with both Au and MoO_3 were almost equal, the V_{OC} was higher with the MoO_3 layer. MoO_3 permits efficient hole transport, resulting in improved charge separation and hence increased V_{OC}. This is ratified from EIS and chronopotentiometric studies.

The introduction of Au NPs and MoO_3 thin film in the CdS sensitized photoanode reduced the recombination rate of photogenerated electrons in TiO_2 with the oxidized S_n^{2-} species in the electrolyte and this increased the V_{OC} of the resultant QDSCs. Fig. 6c gives direct comparison of Nyquist plots between TiO_2/CdS, TiO_2/CdS/Au and TiO_2/CdS/Au/MoO_3 cells at a forward bias which corresponds to the V_{OC} values of the three cells. The R_{rec} value at the TiO_2/CdS/Au/MoO_3-nS^{2-}/S_n^{2-} interface was 216 Ω which was notably higher than that of 172 Ω for TiO_2/CdS/Au and nearly double the value of R_{rec} 115 Ω obtained for TiO_2/CdS. The TiO_2 film electrodes and redox electrolyte were identical for each device, so the direct electron loss at the metal oxide matrix with acceptor species in electrolyte between the concerned half-cells should remain unchanged. The disparity in the R_{rec} is ascribed to the suppression of the back electron transfer from TiO_2 to the photosensitizer and/or from the photosensitizer to electrolyte. Au plasmons not only energize electron propagation but can also assist the coloration in the electrochromic MoO_3 layer. The Bode plots of the cells (phase angle *versus* frequency) are shown in Fig. 6d. The phase angle peak located in the low frequency range shifted to a lower frequency, revealing an increase in the electron recombination time from 352 ms for the TiO_2/CdS cell to 445 ms for the TiO_2/CdS/Au cell with the polysulfide redox electrolyte where Au NPs contribute to rapid electron injection into FTO. The electron–hole recombination time increased to a maximum of 1318 ms in the presence of MoO_3, which is consistent with faster hole scavenging from the QDs by MoO_3 and, as a consequence, more efficient charge separation. These results are consistent with the trends in the photoluminescence of the electrodes.

The photocurrent *versus* time transients under illuminated (0.25 sun) and dark conditions, are shown in Fig. 6e. The highest photocurrent was delivered by the TiO_2/CdS/Au/MoO_3 cell which was closely followed by the TiO_2/CdS/Au cell. The photocurrent response of the TiO_2/CdS/Au/MoO_3 cell dropped slightly from 0.7 to 0.66 mA during irradiance over 20 s. The TiO_2/CdS cell maintained a stable value of ∼0.24 mA, which rose to 0.55 mA when Au NPs were incorporated. This improvement in the current response is consistent with the favourable plasmonic and light scattering effects. The photovoltage decay was monitored in the dark, after allowing the voltage to stabilize under light, and is shown in Fig. 6f. For the photovoltage to drop by the same extent, the cell based on the TiO_2/CdS/Au/MoO_3 electrode took 2.48 s, whereas cells based on the TiO_2/CdS and TiO_2/CdS/Au electrodes took 0.64 and 1.23 s, respectively. The longer decay time is attributed to the MoO_3 acting as hole-transport layer which is consistent with the higher V_{OC} registered for the TiO_2/CdS/Au/MoO_3 electrode based solar cell.

Characterisation of the gel electrolyte

The redox couple in the electrolyte serves to promote charge-separation by rapidly scavenging holes from the VB of CdS (*i.e.* the S^{2-} undergoes oxidation at the photoanode) and electrons from the In_2S_3 CB (*i.e.* S_n^{2-} is reduced at the photocathode), limiting recombination with the charge carriers in the NiO or TiO_2 electrodes, respectively. The reactions are shown below.

Photoanode:

$$S^{2-} + 2h^+ + S_{n-1}^{2-} \rightarrow S_n^{2-}\ (n = 2\text{–}5) \quad (2)$$

Photocathode:

$$S_n^{2-} + 2e^- \rightarrow S_{n-1}^{2-} + S^{2-} \quad (3)$$

Silica was added to the polysulfide electrolyte to form a gel, which combines the stability of solid state electrolytes with high charge transport ability of a liquid electrolyte, resulting in a quasi-solid-state QDSC with promising photovoltaic performance. The gel avoids the limitations posed by a fully aqueous

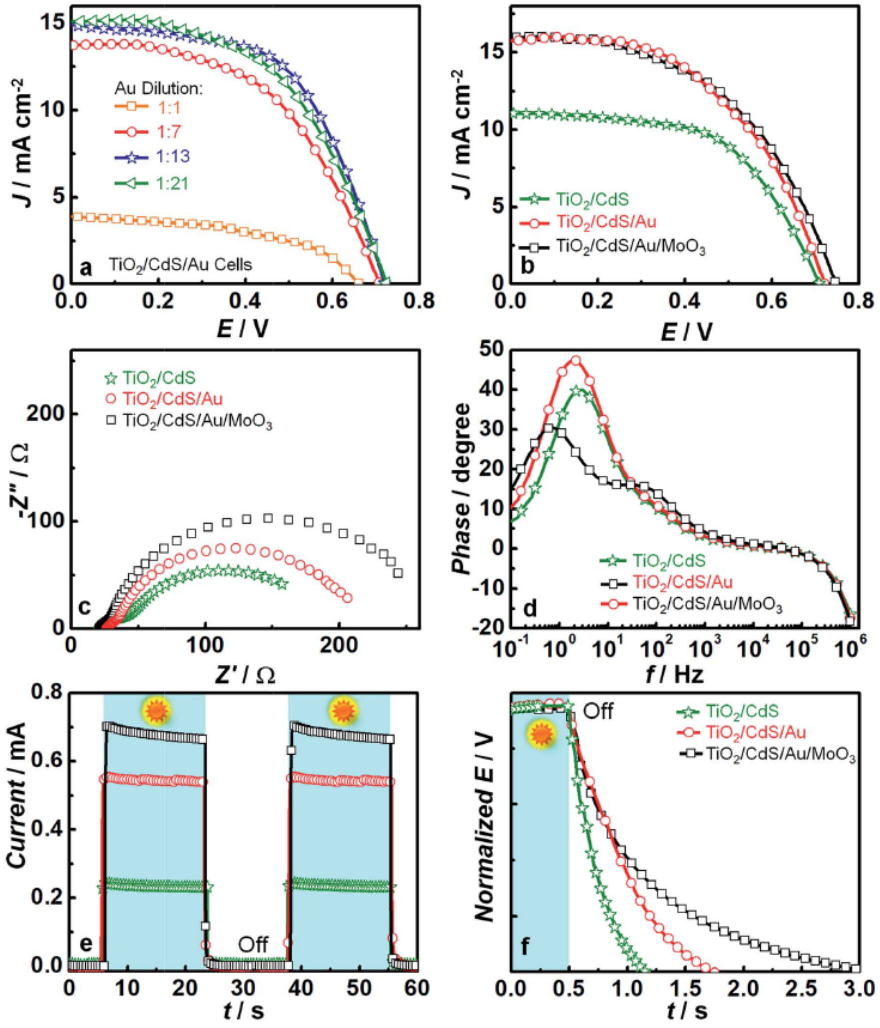

Fig. 6 (a) *J*–*V* curves of solar cells with TiO_2/CdS/Au photoanodes with varying Au NPs content achieved by changing dilution factor. (b) *J*–*V* characteristics of half-cells with different photoanodes: TiO_2/CdS, TiO_2/CdS/Au and TiO_2/CdS/Au/MoO_3, with C-fabric CE and nS^{2-}/S_n^{2-}gel electrolyte under a solar irradiance of 100 mW cm^{-2} (AM 1.5). (c) Nyquist and (d) Bode plots of QDSCs with the varying photoanodes, recorded at their respective V_{OC}, in dark and under an ac bias of 20 mV, over a frequency range of 1 MHz to 0.1 Hz. (e) Photovoltage- and (f) photocurrent-*versus* time plots for QDSCs with different photoanodes under white light irradiance.

liquid electrolyte, such as leakage and evaporation of solvent (water) from the sandwiched solar cell with time.[33] A comparison between the 1 M aqueous S^{2-}/S_n^{2-} liquid electrolyte and S^{2-}/S_n^{2-}-SiO_2 gel electrolyte with respect to the reduction of S_n^{2-} into S^{2-}, was performed using cyclic voltammetry and the results are provided in Fig. S5 of the ESI.† A more pronounced reduction peak with a lower onset potential was observed for the gel electrolyte compared to liquid electrolyte. This is consistent with facile propagation of reaction (3) in the polysulfide gel electrolyte, despite the higher viscosity. The stability of the tandem cells with aqueous polysulfide gel and liquid electrolyte was compared under continuous 1 sun illumination for 6 hours. The plot is included in the ESI (Fig. S5†). The TiO_2/CdS/Au/MoO_3-nS^{2-}/S_n^{2-} gel-In_2S_3/NiO/C-fabric cell exhibited a higher initial efficiency but also almost 3 times less degradation compared to the equivalent cell with liquid electrolyte at the end

Table 1 Solar cell parameters of cells under 1 sun illumination (100 mW cm^{-2}) with TiO_2/CdS/Au photoanode, C-fabric counter electrode and 1 M polysulfide gel electrolyte (active area: 0.10 cm^2)

Au NPs dilution factor	V_{OC} (V)	J_{SC} (mA cm^{-2})	FF (%)	Efficiency (η%)
1 : 1	0.660	3.903	48.37	1.247
1 : 7	0.707	13.722	51.67	5.013
1 : 13	0.719	14.921	56.98	6.112
1 : 21	0.724	15.094	52.29	5.714

Table 2 Solar cell parameters of half-cells with the listed photoanodes, 1 M polysulfide gel electrolyte and bare C-fabric substrate as the counter electrode, under an irradiance of 100 mW cm^{-2} (AM 1.5 spectrum) and exposed cell area: 0.12–0.15 cm^2

Photoanodes	V_{OC} (V)	J_{SC} (mA cm^{-2})	FF (%)	Efficiency (η%)
TiO_2/CdS	0.709	11.05	57.08	4.473
TiO_2/CdS/Au	0.721	15.75	51.97	5.902
TiO_2/CdS/Au/MoO_3	0.746	15.96	50.48	6.010

of 6 hours under irradiation. This stability is also due to the presence of SiO_2 nanoparticles in the electrolyte which induce a passivating effect and restrict the photocorrosion of QDs.[34]

Photoelectrochemistry of tandem cells

QDSCs were constructed using the photoanode, TiO_2/CdS/Au/MoO_3 paired with two different photoactive cathodes: C-fabric/In_2S_3 and C-fabric/NiO/In_2S_3. The tandem devices were assembled with the aqueous polysulfide gel electrolyte and a para-film spacer. The schematic in the inset of Fig. 7a illustrates the device configuration. The cells were illuminated from the rear-side (*i.e.* through the transparent FTO glass). *J*–*V* plots, obtained under 1 sun irradiance (100 mW cm^{-2}), are shown in Fig. 7a and the solar cell parameters are summarized in Tables 3 and S2.† The PCE for the tandem cell with a TiO_2/CdS/Au/MoO_3 photoanode was 6.79% with C-fabric/In_2S_3 counter electrode, and 7.99% with the C-fabric/NiO/In_2S_3 photocathode.

IPCE *versus* wavelength curves for each cell with different combinations of photoanodes and photocathodes are shown in Fig. S6 in the ESI.† The independent contributions of CdS, Au, In_2S_3 and the photocathode: NiO/In_2S_3 to solar energy conversion can be observed from the trends in IPCE spectra. The maximum IPCE value attained for the TiO_2/CdS-nS^{2-}/S_n^{2-}-C-fabric cell was ~34% in the 400–450 nm wavelength range, and the photocurrent onset, near 600 nm, was consistent with the absorption onset of the CdS QDs (Fig. 5a). Higher IPCEs of 49% and 50% at 450 nm were observed for the TiO_2/CdS/Au and TiO_2/CdS/Au/MoO_3 photoanodes with C-fabric CE, respectively. For these devices, a much broader spectral response was observed compared to the photoanodes without the Au NPs, with 4.5% IPCE at 700 nm, dropping to zero beyond 800 nm. This 15% enhancement in IPCE achieved over the breadth of the visible spectrum is consistent with the SPR effect proposed above. Higher IPCEs were observed for the tandem devices. TiO_2/CdS/Au/MoO_3 photoanode with C-fabric/In_2S_3 counter electrode achieved a maximum IPCE of 56% and that of the tandem cell with the same photoanode and C-fabric/NiO/In_2S_3 photocathode was increased further to 62%.

To examine the reason for the increase in performance of the tandem device containing the NiO layer between the photosensitizer and the C-fabric substrate, ac EIS was performed. The Nyquist plots of the tandem cell, TiO_2/CdS/Au/MoO_3-nS^{2-}/S_n^{2-}-In_2S_3/NiO/C-fabric under the applied open-circuit potential, both in dark and under 1 sun illumination are shown in Fig. 7c. Two skewed semicircles are present, one at high frequencies with a relatively small diameter and an incomplete large arc in the mid- to low frequency range. The full cell has a greater R_{rec} value of 236 Ω in the dark compared to 135 Ω under simulated sunlight. R_{rec} is related to the recombination of charges at the metal oxide/electrolyte interface. This resistance is sensitive to surface processes and exhibits a strong light-dependence owing to the increase in density of charge carriers in the metal oxide on illumination compared to in the dark. On illumination, R_{rec} is smaller than for the cell in the dark because the recombination rate is higher due to the higher carrier concentration. Additionally, a local increase in temperature under sunlight may also enhance the charge transfer kinetics and strongly reduce the size of the arcs.[35]

Tandem devices with the In_2S_3 sensitized p-type NiO photocathode boosted all the solar cell parameters, the V_{OC}, J_{SC} and FF, compared to only the photosensitizer, In_2S_3 on the C-fabric substrate. The presence of NiO drives the separation of the electron and hole pair by providing a downhill pathway for the electrons from the NiO valence band to the vacancy in the In_2S_3 sensitizer (*i.e.* it is the opposite of the process occurring at the photoanode, where the electron in the CdS CB is transferred to the lower lying CB in the TiO_2). This process overcomes the radiative recombination of the exciton (see photoluminescence experiment above) and enables the charges to be selectively extracted. Typically, charge-transfer at the interface between the QD and the metal oxide is much faster than charge-transfer to the redox electrolyte, which is diffusion limited. Accordingly, on illumination of the tandem cell, the Fermi level in the TiO_2 rises towards the conduction band edge, the Fermi level in the NiO falls to the valence band edge, and the difference in potential energy at the photocathode and photoanode leads to the V_{OC} (*i.e.* in a tandem cell, the V_{OC} should be the sum of the V_{OC} of the individual TiO_2 and NiO-based half cells), and therefore the conversion efficiency is increased. The increase in V_{OC} observed when NiO is introduced, is therefore attributed to the better charge-separation in the device compared to the device with only C-fabric/In_2S_3. The large charge-transfer resistance of the tandem device is consistent with the higher J_{SC} and FF. Once the charges are transferred to the metal oxide, they are insulated from the redox mediator by the absorber layer, leading to long charge lifetimes.

Photoelectrochromism in a tandem cell

The presence of MoO_3 in the photoanode of the tandem cell leads to a change in coloration upon illumination

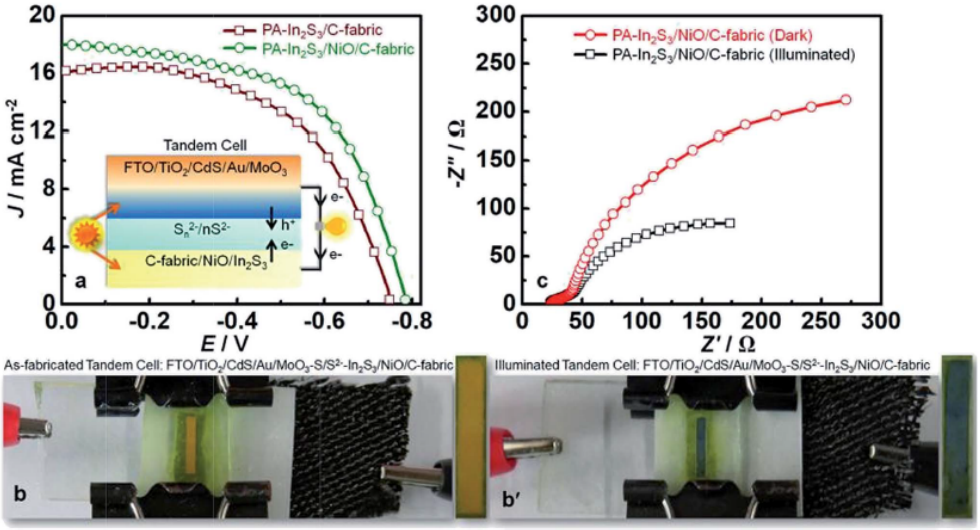

Fig. 7 (a) J–V characteristics for $TiO_2/CdS/Au/MoO_3$ photoanode (PA)-based cells with two different counter electrodes: C-fabric/In_2S_3 and C-fabric/NiO/In_2S_3, and a polysulfide gel electrolyte, under 1 sun illumination, AM 1.5. Inset of (a) is a schematic of the cell configuration. Photographs of PA-gel-In_2S_3/NiO/C-fabric tandem cell in (b) as-fabricated state or under dark and (b′) under 1 sun. (c) Nyquist plots for the PA-gel-In_2S_3/NiO/C-fabric cell at V_{OC}, in dark and under 0.1 sun light irradiance.

(photoelectrochromic effect) due to the formation of the sodium molybdenum bronze, as discussed above, in addition to delivering a high PCE (photovoltaic effect). Photographs of the as-fabricated tandem cell which is yellow in color, and the resulting blue colored tandem cell are shown in Fig. 7b and b′. To quantify the photoelectrochromic response, semi-transparent tandem cells were fabricated ($TiO_2/CdS/Au/MoO_3$-nS^{2-}/S_n^{2-}-In_2S_3/NiO/FTO) by substituting the C-fabric current collector in the photocathode with FTO. Photographs of the $TiO_2/CdS/Au/MoO_3$-nS^{2-}/S_n^{2-}-In_2S_3/NiO/FTO tandem cell before (yellow) and after (blue) irradiation with white light (AM1.5, 100 mW cm^{-2}) are shown in Fig. 8c and c′, respectively. The maximum transmittance (Fig. 8a) of the photocathode NiO/In_2S_3 film on FTO was 59% over the visible region (400 to 800 nm). The transmittance of the as-fabricated photoanode $TiO_2/CdS/Au/MoO_3$ film gradually increased from 5% to 61% over the same wavelength range. The transmittance of the tandem cell in its colored state, provided in Fig. 8b, varied from 0.5% to 16% in the visible region. When the light was switched off, the charge stored in the electrochromic layer drove the process in reverse, triggering the film to bleach and giving a maximum transmittance of 50%, while retaining spectral shape. The modulation in transmittance ($\Delta T(\lambda) = T_{\text{bleached}}(\lambda) - T_{\text{colored}}(\lambda)$) was 29% at 550 nm, the wavelength at which the human eye is most responsive, and 34% at 800 nm (Fig. 8b). The electrochromic contrast induced in the MoO_3 layer depends on the electronic charge that flows into the film upon illumination. The photocoloration efficiency (phCE) is the relationship between the modulation of the optical density (ΔOD) and the solar energy density absorbed by the QDs-sensitized plasmonic photoanode to initiate the color transition in MoO_3.[36] For this chromogenic device, the phCE was estimated using eqn (4):

$$\text{phCE} = \Delta\text{OD}(\lambda)/G_{\text{T}}t = \log[T_{\text{b}}(\lambda)/T_{\text{c}}(\lambda)]/G_{\text{T}}t \tag{4}$$

where G_T is the total solar intensity for incidence normal to the device (in W cm^{-2}), and t is the exposure time (in minutes). The magnitudes of T_b and T_c corresponding to the optical

Table 3 Solar cell parameters of cells with 1 M polysulfide/silica gel electrolyte, under 1 sun illumination (AM 1.5, 100 mW cm^{-2}) with the listed combinations of photoanodes and photocathodes, exposed cell area: 0.12–0.15 cm^2

Cells	V_{OC} (V)	J_{SC} (mA cm^{-2})	FF (%)	Efficiency (η%)
$TiO_2/CdS/Au/MoO_3$–In_2S_3/NiO/FTO	0.647	11.38	42.27	3.112
$TiO_2/CdS/Au/MoO_3$–In_2S_3/C-fabric	0.750	16.15	56.12	6.793
$TiO_2/CdS/Au/MoO_3$–In_2S_3/NiO/C-fabric	0.785	17.99	56.54	7.987

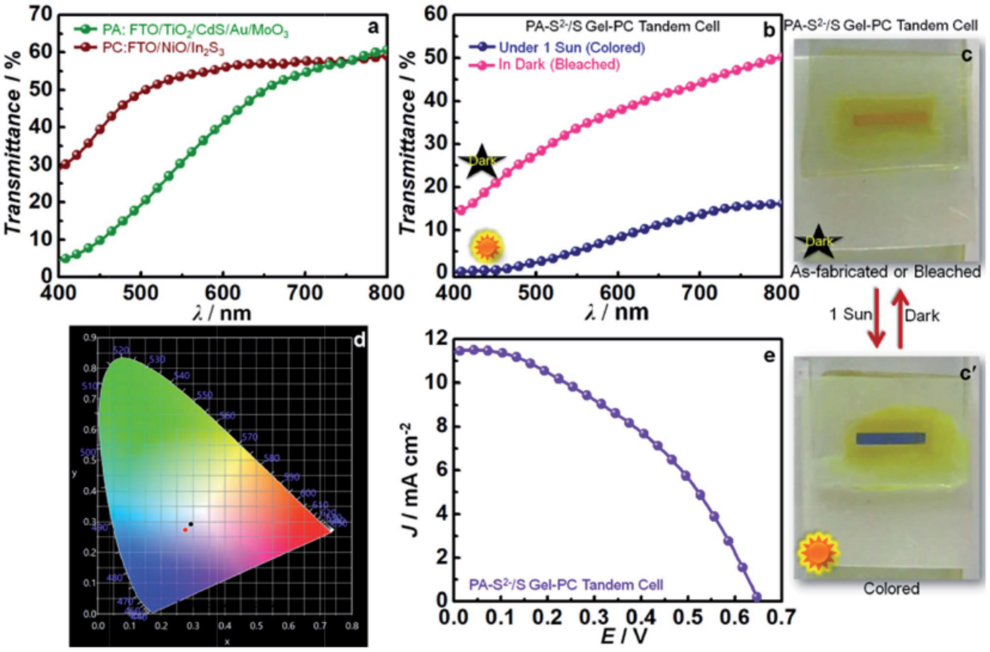

Fig. 8 Transmittance *versus* wavelength spectra of (a) PA: $TiO_2/CdS/Au/MoO_3$ and PC: NiO/In_2S_3 films in their as-fabricated states, (b) the FTO/$TiO_2/CdS/Au/MoO_3$-nS^{2-}/S_n^{2-}-In_2S_3/NiO/FTO tandem cell in colored state (under illumination) and bleached state (under dark or as-fabricated). Photographs of the PA-gel-PC tandem cell in (c) as-fabricated state or under dark and (c′) under 1 sun. (d) CIE 1931 chromaticity diagram of the photoelectrochromic tandem cell. (e) *J*–*V* curve of the tandem cell: $TiO_2/CdS/Au/MoO_3$-nS^{2-}/S_n^{2-}-In_2S_3/NiO/FTO under 100 mW cm^{-2}.

transmittance in the bleached and colored states are 33.7 and 5.1% respectively (at $\lambda = 550$ nm). A photocoloration efficiency of 16.4 cm^2 min^{-1} W^{-1} at a wavelength of 550 nm was obtained under exposure to AM1.5 white light, 100 mW cm^{-2} intensity, for 30 seconds.

The CIE-1931 color chromaticity parameters L^*, a, b for colored and bleached films were estimated at 2° observer using D-65 illumination source. The generated chromaticity diagram for the $TiO_2/CdS/Au/MoO_3$ photoanode in the tandem device is as shown in Fig. 8d. The values of L^*, a and b parameters for the bleached state of the MoO_3 layer were 53.9, 4.4 and −8.7, respectively. These parameters changed to 74.7, 6.4 and −19.6 after illumination, which clearly indicates an enhancement in blue coloration.[37] The electrocatalytic effect of Au is seen in the noticeable electrochromism of the MoO_3 film in the solar cell.[38] A PCE of 3.11% with a J_{SC} of 11.4 mA cm^{-2} was recorded for the tandem QDSC assembled with the $TiO_2/CdS/Au/MoO_3$ photoanode, polysulfide gel electrolyte and NiO/In_2S_3 over FTO glass substrate photocathode (Fig. 8e), which was somewhat lower than the photocurrent obtained for the device with the highly conductive C-fabric as the photocathode substrate. However, it was sufficient to induce the desired electrochromic switching.

Conclusions

Coupling of a $TiO_2/CdS/Au/MoO_3$ photoanode with a C-fabric/NiO/In_2S_3 photocathode maximized the light absorption range afforded by CdS–Au NPs on one side and In_2S_3 on the other. The PCEs achieved were 6.01% for the $TiO_2/CdS/Au/MoO_3$ photoanode based half-cell, 0.047% for the NiO/In_2S_3 photocathode based half-cell and 7.99% for the tandem QDSC, $TiO_2/CdS/Au/MoO_3$-nS^{2-}/S_n^{2-}-In_2S_3/NiO/C-fabric measured under a light intensity of 1 sun. The latter is one of the best solar cell efficiencies reported to date for tandem QDSCs. In addition, device also exhibits electro-optical switching and the MoO_3 layer in the photoanode plays a dual role, serving both as a hole conduit as well as an electrochrome. The maximum light-induced modulation of the transmission was 34% upon chromatic switching between the bleached state and blue-colored state induced in MoO_3 film, for the tandem device with optically transparent current collectors (FTO glass). This work demonstrates the improvements in solar cell efficiency which can be made through the tandem cell architecture and opens up new avenues for research by incorporating nanomaterials with multiple functions in the photoelectrochemical solar cells. Because of the modular system, there remains much scope for optimising the synergy between the photoactive electrodes to capture and convert more of the solar spectrum more efficiently.

Conflicts of interest

There are no conflicts to declare.

Acknowledgements

We thank the EPSRC Global Challenges Research Fund (GCRF) grant BH173540, for providing financial support for the exchange of students and also for carrying out this research work; EAG thanks Newcastle University for a studentship for N. P; ERC starting grant pTYPE 715354; EPSRC ISCF North East Centre for Energy Materials EP/R021503. Author A. K. is thankful to University Grants Commission (UGC) of India for the grant of a junior research fellowship.

References

1 S. Jiao, J. Du, Z. Du, D. Long, W. Jiang, Z. Pan, Y. Li and X. Zhong, *J. Phys. Chem. Lett.*, 2017, 8, 559–564.

2 J. Du, Z. Du, J.-S. Hu, Z. Pan, Q. Shen, J. Sun, D. Long, H. Dong, L. Sun, X. Zhong and L.-J. Wan, *J. Am. Chem. Soc.*, 2016, 138, 4201–4209.

3 W. Kong, S. Li, Z. Chen, C. Wei, W. Li, T. Li, Y. Yan, X. Jia, B. Xu and W. Zhang, *Part. Part. Syst. Charact.*, 2015, 32, 1078–1082.

4 P. N. Kumar, S. Mandal, M. Deepa, A. K. Srivastava and A. G. Joshi, *J. Phys. Chem. C*, 2014, 118, 18924–18937.

5 J. Qian, Q.-S. Liu, G. Li, K.-J. Jiang, L.-M. Yang and Y. Song, *Chem. Commun.*, 2011, 47, 6461–6463.

6 P. N. Kumar, M. Deepa and A. K. Srivastava, *Phys. Chem. Chem. Phys.*, 2015, 17, 10040–10052.

7 X. Dang, J. Qi, M. T. Klug, P.-Y. Chen, D. S. Yun, N. X. Fang, P. T. Hammond and A. M. Belcher, *Nano Lett.*, 2013, 13, 637–642.

8 M. D. Brown, T. Suteewong, R. S. S. Kumar, V. D'Innocenzo, A. Petrozza, M. M. Lee, U. Wiesner and H. J. Snaith, *Nano Lett.*, 2011, 11, 438–445.

9 P. N. Kumar, R. Narayanan, M. Deepa and A. K. Srivastava, *J. Mater. Chem. A*, 2014, 2, 9771–9783.

10 C. Girotto, E. Voroshazi, D. Cheyns, P. Heremans and B. P. Rand, *ACS Appl. Mater. Interfaces*, 2011, 3, 3244–3247.

11 W. Zhang, W. Lan, M. H. Lee, J. Singh and F. Zhu, *Org. Electron.*, 2018, 52, 1–6.

12 C.-S. Hsu, C.-C. Chan, H.-T. Huang, C.-H. Peng and W.-C. Hsu, *Thin Solid Films*, 2008, 516, 4839–4844.

13 T. M. Mcevoy, K. J. Stevenson, J. T. Hupp and X. Dang, *Langmuir*, 2003, 19, 4316–4326.

14 E. A. Gibson, A. L. Smeigh, L. Le Pleux, J. Fortage, G. Boschloo, E. Blart, Y. Pellegrin, F. Odobel, A. Hagfeldt and L. Hammarström, *Angew. Chem.*, 2009, 121, 4466–4469.

15 A. Nattestad, A. J. Mozer, M. K. R. Fischer, Y.-B. Cheng, A. Mishra, P. Bäuerle and U. Bach, *Nat. Mater.*, 2009, 9, 31–35.

16 C. J. Wood, G. H. Summers and E. A. Gibson, *Chem. Commun.*, 2015, 51, 3915–3918.

17 A. Kolay, R. K. Kokal, A. Kalluri, I. Macwan, P. K. Patra, P. Ghosal and M. Deepa, *ACS Appl. Mater. Interfaces*, 2017, 9, 34915–34926.

18 J. B. Sambur, T. Novet and B. A. Parkinson, *Science*, 2010, 330, 63–66.

19 F. Odobel, Y. Pellegrin, E. A. Gibson, A. Hagfeldt, A. L. Smeigh and L. Hammarström, *Coord. Chem. Rev.*, 2012, 256, 2414–2423.

20 I. Barceló, E. Guillén, T. Lana-Villarreal and R. Gómez, *J. Phys. Chem. C*, 2013, 117, 22509–22517.

21 J. Duan, Q. Tang, B. He and L. Yu, *Electrochim. Acta*, 2014, 139, 381–385.

22 R. Ranjith, T. T. John, C. S. Kartha, K. P. Vijayakumar, T. Abe and Y. Kashiwaba, *Mater. Sci. Semicond. Process.*, 2007, 10, 49–55.

23 C. D. Lokhande, A. Ennaoui, P. S. Patil, M. Giersig, K. Diesner, M. Muller and H. Tributsch, *Thin Solid Films*, 1999, 340, 18–23.

24 H. Choi, W. T. Chen and P. V. Kamat, *ACS Nano*, 2012, 6, 4418–4427.

25 S. Murase and Y. Yang, *Adv. Mater.*, 2012, 24, 2459–2462.

26 C. J. Wood, G. H. Summers, C. A. Clark, N. Kaeffer, M. Braeutigam, L. R. Carbone, L. D'Amario, K. Fan, Y. Farre, S. Narbey, F. Oswald, L. A. Stevens, C. D. J. Parmenter, M. W. Fay, A. La Torre, C. E. Snape, B. Dietzek, D. Dini, L. Hammarström, Y. Pellegrin, F. Odobel, L. C. Sun, V. Artero and E. A. Gibson, *Phys. Chem. Chem. Phys.*, 2016, 18, 10727–10738.

27 C. Gao, J. Li, Z. Shan, F. Huang and H. Shen, *Mater. Chem. Phys.*, 2010, 122, 183–187.

28 M. G. Sandoval-Paz, M. Sotelo-Lerma, J. J. Valenzuela-Jáuregui, M. Flores-Acosta and R. Ramírez-Bon, *Thin Solid Films*, 2005, 472, 5–10.

29 Y. J. Hsiao, C. H. Lu, L. W. Ji, T. H. Meen, Y. L. Chen and H. P. Chi, *Nanoscale Res. Lett.*, 2014, 9, 32.

30 J. He, H. Lindstro, A. Hagfeldt and S.-E. Lindquist, *J. Phys. Chem. B*, 1999, 103, 8940–8943.

31 S. H. Kang, K. Zhu, N. R. Neale and A. J. Frank, *Chem. Commun.*, 2011, 47, 10419–10421.

32 P. N. Kumar, A. Kolay, S. K. Kumar, P. Patra, A. Aphale, A. K. Srivastava and M. Deepa, *ACS Appl. Mater. Interfaces*, 2016, 8, 27688–27700.

33 J. Duan, Q. Tang, R. Li, B. He, L. Yu and P. Yang, *J. Power Sources*, 2015, 284, 369–376.

34 K. Zhao, Z. Pan, I. Mora-Seró, E. Cánovas, H. Wang, Y. Song, X. Gong, J. Wang, M. Bonn, J. Bisquert and X. Zhong, *J. Am. Chem. Soc.*, 2015, 137, 5602–5609.

35 S. Gimenez, H. K. Dunn, P. Rodenas, F. Fabregat-santiago, S. G. Miralles, E. M. Barea, R. Trevisan, A. Guerrero and J. Bisquert, *J. Electroanal. Chem.*, 2012, 668, 119–125.

36 A. Cannavale, M. Manca, L. De Marco, R. Grisorio, S. Carallo, G. P. Suranna and G. Gigli, *ACS Appl. Mater. Interfaces*, 2014, 6, 2415–2422.

37 D. S. Dalavi, R. S. Devan, R. A. Patil, R. S. Patil, Y.-R. Ma, S. B. Sadale, I. Kim, J.-H. Kim and P. S. Patil, *J. Mater. Chem. C*, 2013, 1, 3722–3728.

38 J. N. Yao, Y. A. Yang and B. H. Loo, *J. Phys. Chem. B*, 1998, 102, 1856–1860.